

**REDOX-ACTIVE ORGANOMETALLIC DIMERS AS DOPANTS
AND SURFACE MODIFIERS IN OPTOELECTRONICS**

A Dissertation
Presented to
The Academic Faculty

by

Federico Pulvirenti

In Partial Fulfillment
of the Requirements for the Degree
Doctor of Philosophy in the
School of Chemistry and Biochemistry

Georgia Institute of Technology
May 2019

COPYRIGHT © 2019 BY FEDERICO PULVIRENTI

REDOX-ACTIVE ORGANOMETALLIC DIMERS AS DOPANTS AND SURFACE MODIFIERS IN OPTOELECTRONICS

Approved by:

Dr. Seth R. Marder, Advisor
School of Chemistry and Biochemistry
Georgia Institute of Technology

Dr. Bernard Kippelen
School of Electrical and Computer
Engineering
Georgia Institute of Technology

Dr. Carlos Silva Acuña
School of Chemistry and Biochemistry
Georgia Institute of Technology

Dr. Elsa Reichmanis
School of Chemical and Biomolecular
Engineering
Georgia Institute of Technology

Dr. Jean-Luc Brédas
School of Chemistry and Biochemistry
Georgia Institute of Technology

Date Approved: [Month dd, 2019]

To my family on both sides of the Atlantic Ocean, and my teachers

ACKNOWLEDGEMENTS

I would like to thank the people who played a key role in shaping not only the scientist, but the person I have become over the last six years. I would like to thank Prof. Francesco Stellacci for guiding me through the process of choosing the academic institution where to perform my graduate studies, and of identifying a rigorous advisor who would tirelessly incite me to push the boundaries of knowledge, while supporting my career interests. I would like to thank Prof. Seth R. Marder for being that type of advisor, and help me make the transition from a purely engineering background to chemistry. Such transition has been a tortuous path, one more challenging than originally expected but well worth the struggle. It is thanks to Seth's support that not only I was able to build a greater understanding of the fundamental concepts behind my research, but I was able to pursue enriching opportunities, such as performing research abroad, investigating issues at the interface of science and policy through the Sam Nunn Security Fellowship, and becoming a leadership coach. I am immensely grateful for the help, patience and dedication of Dr. Stephen Barlow, with whom I have had uncountable insightful discussions during my Ph.D. Steve's input has been invaluable towards drafting my publications, my research reviews and this dissertation. I would like to acknowledge and thank Dr. Timothy Parker, Dr. Raghunath R. Dasari, Dr. Yadong Zhang, Dr. Junxiang Zhang, Dr. Elena Longhi, Dr. Sebastian Fürer, Dr. Kartikay Moudgil, Dr. Anthony J. Giordano and Dr. Swagat Mohapatra for providing instruction, support and friendship. I will cherish the friendship developed over the years with previous and current members of the Marder group, specifically Dr. Annabelle Scarpaci, Dr. Rebecca B. M. Hill, Dr. Matthew Cooper, Dr.

Samik Jhulki, Marie-Hélène Tremblay and Khaled Al-Kurdi. The support provided by Dr. Denise H. Bale, Dr. Kenyetta A. Johnson, Dr. Cameron Tyson, Teresa W. Jonsson, Amy E. Hartley and Walaa Compton in making my graduate experience successful cannot be understated. A special thanks goes to Dr. Karen C. Adams and Dr. Erin M. Weaver, who assisted me in revising uncountable applications and stimulated me to pursue what seemed impossible dreams, by tirelessly pushing me to improve my writing skills.

I owe a great debt of gratitude to Prof. Bernard Kippelen, for granting me access to his facilities and the expertise of his group members. Therefore, I must acknowledge Dr. Canek Fuentes Hernandez, Dr. Talha M. Khan, and Xiaojia Jia for fruitful discussions and assistance in the design and fabrication of proof-of-principle diodes and samples for conductivity measurements. I must recognize Prof. Jean-Luc Brédas, Prof. Elsa Reichmanis, Prof. Carlos Silva Acuña and Prof. Joseph W. Perry for serving on my committee and providing perspective to my research.

My thanks go to my collaborators outside of Georgia Tech whom, have welcomed me in their laboratories for an extensive period of time. In particular, I am grateful to Prof. Henry J. Snaith and Prof. Norbert Koch for providing an exciting thirteen-month-long deep-dive into topics (perovskites) and techniques (photoelectron spectroscopy) that I was not too familiar with. I will forever remember my stay in Oxford and Berlin as one of the most scientifically and personally enriching times of my life, particularly because of the people I had the opportunity to interact and discuss science with. Hence, words cannot express my gratitude to Dr. Nakita K. Noel, who not only helped me review parts of this dissertation, but also played a major role in building my confidence in my own skills as a scientist, and was there for me in and outside of the lab. I would like to thank Dr.

Maximilian Hoerantner, Dr. David P. McMeekin, Dr. Alba Pellaroque, Dr. Giulio Mazzotta, Dr. Jay B. Patel, Dr. JongChul Lim, Dr. Mark G. Christoforo, Dr. Severin Habisreutinger, Dr. Berthold Wegner and Dr. Thorsten Schultz for making lab work fun everyday.

I would like to acknowledge the Center for the Science and Technology of Advanced Materials and Interfaces (STAMI) for the graduate fellowship and the travel funds I was awarded, which gave me the opportunity to learn from experts in the field of optoelectronics at three major international conferences.

I would like to express my gratitude to Prof. Margaret E. Kosal for accepting me in the Sam Nunn Security Program, for sharing her expertise and network in the policy community, and for stimulating me to apply the scientific method while investigating international security issues.

I am grateful to Dr. Wes Wynens and Stacey Doremus for inspiring me to become a better leader and a better person with their Leadership Education and Development program at Georgia Tech. Through the latter I was able to meet Dr. Brandy Blake, whom I would like to thank for granting me access to the Communication Center, where most of this dissertation was written.

I would like to thank the Student Alumni Association for their Mentor Jackets Program, through which I have been able to meet the people that have help me shape my professional path. Therefore, I must recognize Sonny Chaffin for his thought leadership and willingness to listen over the years.

Last but not least, I cannot express enough my gratitude for the role that my life-long friends and my family members on both sides of the Atlantic Ocean have played over

this long journey. Getting from the beginning to the end of the Ph.D. has not been an easy ride, but my husband Daniel H. Weaver has certainly made it a worthwhile experience. I would like to thank all the members of the Pulvirenti, Weaver and Mecaslin families for providing me with a solid support system while I pursued my scientific aspirations. And a special thanks goes to my mother, the person who taught me how to fight while spreading kindness and keeping my head up.

TABLE OF CONTENTS

ACKNOWLEDGEMENTS	iv
LIST OF TABLES	xi
LIST OF FIGURES	xiv
LIST OF SYMBOLS AND ABBREVIATIONS	xxiv
SUMMARY	xxviii
CHAPTER 1. Introduction	xxviii
1.1 Motivation and Significance	1
1.2 Energy Level and Associated Terminology Definitions	4
1.2.1 Vacuum Level (E_{vac})	4
1.2.2 Valence Band (VB)	4
1.2.3 Conduction Band (CB)	5
1.2.4 Fermi Level (E_{F})	5
1.2.5 Work Function (WF)	8
1.2.6 Ionization Energy (IE)	8
1.2.7 Electron Affinity (EA)	9
1.3 Semiconductors	9
1.4 Redox-Active Organometallic Dimers	12
1.5 Transparent Conducting Oxides (TCOs)	14
1.5.1 Indium Tin Oxide (ITO)	14
1.5.2 Fluorinated Tin Oxide (FTO)	15
1.6 Surface Modification of Transparent Conducting Oxides	16
1.7 Analytical Methods for Examining Surface Modifiers and Redox-Active Species	18
1.7.1 Ultraviolet Photoelectron Spectroscopy (UPS)	19
1.7.2 Inverse Photoemission Spectroscopy (IPES)	21
1.7.3 X-ray Photoelectron Spectroscopy (XPS)	22
1.7.4 Kelvin Probe (KP)	23
1.7.5 Mobility Measurements Techniques	25
1.7.6 Electrical Conductivity Measurements	26
1.7.7 UV-vis-NIR Absorption Spectroscopy	29
1.8 Thesis Structure and Overview	30
CHAPTER 2. Surface modification of indium tin oxide with dimeric reductants	33
2.1 Introduction	33
2.2 Stability of the Work Function Modification Induced by Organometallic Dopants	36
2.2.1 Stability of the Work Function Modification to Temperature	37
2.2.2 Stability of the Work Function Modification to Solvent Washing	38
2.3 Electrical Behavior of Surface-Modified ITO	39

2.3.1	Diode Fabrication with Vacuum-Deposited Organic Semiconductors	40
2.3.2	Diode Fabrication with Solution-Processed Organic Semiconductors	49
2.4	Phosphonic Acids to Prevent Dopant Washing During Solution Processing of Organic Semiconductors	52
2.5	Conclusions	54
2.6	Experimental	55
2.6.1	Materials	55
2.6.2	Sample Preparation	60
2.6.3	Surface Characterization	61
2.6.4	Diode Fabrication	62
CHAPTER 3.	Modification of the fluorinated tin oxide/electron/transporting material interface in perovskite solar cells	64
3.1	Introduction	64
3.2	Surface Modification of FTO using Vacuum-Deposited (RhCp* Cp)₂	67
3.3	Electronic Alignment at the FTO/ETM Interface	70
3.4	Interfacial Doping of the ETM	75
3.4.1	Discussion of the XPS Rh 3d Peak Assignment	80
3.5	PTCBI as ETM in Perovskite Solar Cells and the Impact of FTO Surface Treatment with (RhCp* Cp)₂	82
3.6	Conclusions	86
3.7	Experimental	87
3.7.1	Materials Synthesis and Purification	87
3.7.2	Photoelectron Spectroscopy	87
3.7.3	Solar Cell Fabrication	88
3.7.4	Current Density-Voltage Characterization	89
3.7.5	UV-vis-NIR Absorption Spectroscopy	90
CHAPTER 4.	Interfacial doping of C₆₀ and its implication for high-performance perovskite solar cells	91
4.1	Introduction	91
4.2	Surface Modification of FTO	94
4.2.1	Surface Modification of FTO using (RhCp* Cp) ₂ Solutions	94
4.2.2	Surface Modification of FTO using TBABH ₄ solutions	97
4.3	Impact of Surface Treatments on in-Plane Electrical Conductivity of C₆₀	101
4.4	Through-Plane Electrical Behavior of Surface-Modified FTO	104
4.5	Impact of FTO Surface Treatments on Perovskite Solar Cells	107
4.6	Conclusions	110
4.7	Experimental	111
4.7.1	Materials Synthesis and Purification	111
4.7.2	Sample Preparation	112
4.7.3	Surface Characterization	112
4.7.4	Transmission Line Measurements	113
4.7.5	Diode Fabrication	114
4.7.6	Solar Cell Fabrication	114

CHAPTER 5. <i>n</i>-Doping of a Fullerene That Can Be Thermally Insolubilized as an Electron-Transporting Material for Metal Halide Perovskite Solar Cells	116
5.1 Introduction	116
5.2 Doping of PCBCB using (IrCp*<i>Cp</i>)₂	120
5.2.1 Doping of PCBCB Solutions	120
5.2.2 Doping of (PCBCB) _{<i>n</i>} Films	122
5.3 Electrical Conductivity Measurements	124
5.3.1 Impact of Doping on in-Plane Electrical Conductivity of (PCBCB) _{<i>n</i>}	124
5.3.2 Impact of Crosslinking on in-Plane Conductivity of Doped (PCBCB) _{<i>n</i>}	127
5.4 Stability of Doping of (PCBCB)_{<i>n</i>} Films to Solvent Washing	129
5.5 Diffusion Studies of (IrCp*<i>Cp</i>)⁺ in (PCBCB)_{<i>n</i>} upon Thermal Annealing	132
5.6 The Effect of Dopant and Crosslinker Addition to (PCBCB)_{<i>n</i>} ETMs in Perovskite Solar Cells (PSCs)	134
5.6.1 Stability of Perovskite Solar Cells upon the Introduction of <i>n</i> -Dopant and Crosslinker	142
5.7 Conclusions	146
5.8 Experimental	148
5.8.1 Materials Synthesis	148
5.8.2 UV-vis-NIR Absorption Spectroscopy	153
5.8.3 Photoelectron Spectroscopy	153
5.8.4 Transmission Line Measurements	153
5.8.5 Solar Cell Fabrication	154
CHAPTER 6. Conclusions and Outlook	158
APPENDIX A. List of Publications	169
REFERENCES	171

LIST OF TABLES

Table 3.1	XPS positions and peak ratios for (RhCp*Cp) ₂ -covered piranha-cleaned FTO. All values are in eV (except ratios). The position of the Rh ^{III} 3d peaks was fixed to be at a distance of 1.3 eV from Rh ^I 3d peaks to allow consistent fitting. ¹²² ^a XPS core shifts are discussed at length in section 3.4.1. ^b FTO modified by dipping for 10 min in a 2 mM solution of (RhCp*Cp) ₂ in toluene, followed by three rinsing cycles with pure toluene.	69
Table 3.2	XPS peak ratios for (RhCp*Cp) ₂ -covered piranha-cleaned FTO. All values are in eV (except ratios). ^b FTO modified by dipping for 10 min in a 2 mM solution of (RhCp*Cp) ₂ in toluene, followed by three rinsing cycles with pure toluene.	70
Table 3.3	XPS binding energies for C ₆₀ , bilayers of (RhCp*Cp) ₂ and C ₆₀ , and coevaporated C ₆₀ and dopant. ^a XPS core shifts are discussed at length in section 3.4.1.	71
Table 3.4	XPS peak ratios for C ₆₀ , bilayers of (RhCp*Cp) ₂ and C ₆₀ , and coevaporated C ₆₀ and dopant. The Rh/C ratio of 0.003 for the coevaporated ETM and dopant was used to calculate the actual doping concentration of 10%.	72
Table 3.5	XPS binding energies for PTCBI, bilayers of (RhCp*Cp) ₂ and PTCBI, and coevaporated PTCBI and dopant. ^a XPS core shifts are discussed at length in section 3.4.1.	73
Table 3.6	XPS peak ratios for PTCBI, bilayers of (RhCp*Cp) ₂ and PTCBI, and coevaporated PTCBI and dopant. The Rh/N ratio of 0.04 for the coevaporated ETM and dopant was used to calculate the actual doping concentration of 8%.	73
Table 3.7	Device performance parameters averaged over five solar cells with evaporated CH ₃ NH ₃ PbI ₃ .	82
Table 3.8	Device performance parameters of best-performing solar cells with solution-processed CH ₃ NH ₃ PbI ₃ .	86
Table 4.1	XPS positions and peak ratios for (RhCp*Cp) ₂ -covered piranha-cleaned FTO. FTO was modified by dipping in 2 mM solutions of the <i>n</i> -dopant for different amount of time, followed by three rinsing cycles with pure toluene. All values are in eV (except ratios). The position of the Rh ^{III} 3d peaks was fixed to be at a distance of 1.3 eV from Rh ^I 3d peaks to allow consistent fitting. ¹²²	97

Table 4.2	XPS positions for TBABH ₄ -dropcast FTO immediately analyzed after modification and analyzed after being stored for two days at 10 ⁻¹⁰ mbar. FTO was modified by dipping in 10 mM solutions of the ammonium salt for 10 min, without rinsing. All values are in eV.	101
Table 4.3	Peak ratios of XPS signals for TBABH ₄ -dropcast FTO immediately analyzed after modification and analyzed after being stored for two days at 10 ⁻¹⁰ mbar. FTO was modified by dipping in 10 mM solutions of the ammonium salt for 10 min, without rinsing.	101
Table 4.4	Sheet resistance of C ₆₀ and resistance at the C ₆₀ /silver contact as a function of surface treatments on glass.	102
Table 4.5	Resistivity and conductivity of C ₆₀ as a function of surface treatments on glass.	102
Table 4.6	Device performance parameters averaged over twelve solar cells with evaporated CH ₃ NH ₃ PbI ₃ .	109
Table 5.1	XPS positions and peak ratios for pristine or doped (PCBCB) _n films on FTO. All values are in eV (except ratios). All XPS signals were normalized to the one of Sn 3d _{5/2} . (IrCp*Cp) ₂ content is reported as a function of molar percentage of monomer cations (IrCp*Cp) ⁺ relative to the host.	124
Table 5.2	Sheet resistance of (PCBCB) _n and resistance at the (PCBCB) _n /silver contact as a function of (IrCp*Cp) ⁺ content (molar percentage). The sheet resistance of PCBM and resistance at the PCBM/Ag contact are reported for comparison.	125
Table 5.3	Resistivity and conductivity of (PCBCB) _n as a function of (IrCp*Cp) ⁺ content (molar percentage). The resistivity and conductivity of PCBM are reported for comparison.	125
Table 5.4	Sheet resistance of doped (PCBCB) _n and resistance at the doped (PCBCB) _n /silver contact as a function of crosslinker concentration. The (IrCp*Cp) ⁺ concentration was fixed to 3 mol%.	127
Table 5.5	Resistivity and conductivity of (PCBCB) _n as a function of crosslinker concentration. The (IrCp*Cp) ⁺ concentration was fixed to 3 mol %.	128
Table 5.6	Device performance parameters averaged over thirteen solar cells with solution-processed (HC(NH ₂) ₂) _{0.83} Cs _{0.17} Pb(I _{0.8} Br _{0.2}) ₃ as a function of the dopant concentration in (PCBCB) _n films. Reference devices were made with PCBM as the organic ETM. All solar cells	137

were made using tin oxide nanoparticles as a buffer layer between the fullerene derivative and FTO.

- Table 5.7 Device performance parameters averaged over five solar cells with solution-processed $(\text{HC}(\text{NH}_2)_2)_{0.83}\text{Cs}_{0.17}\text{Pb}(\text{I}_{0.8}\text{Br}_{0.2})_3$ as a function of the PMHBCB crosslinker concentration in $(\text{PCBCB})_n$ films. The reference solar cell was made using compact-layer SnO_2 covered with PCBM as the ETM. 139
- Table 5.8 Device performance parameters averaged over seven solar cells with solution-processed $(\text{HC}(\text{NH}_2)_2)_{0.83}\text{Cs}_{0.17}\text{Pb}(\text{I}_{0.8}\text{Br}_{0.2})_3$ and different ETMs. The reference solar cells were made using compact-layer SnO_2 covered with PCBM as ETM. 0.2 mol% $(\text{IrCp}^*\text{Cp})^+$ and 1 mol% PMHBCB were used in the films of $(\text{PCBCB})_n$ that were doped, crosslinked or both. 141

LIST OF FIGURES

Figure 1.1	Representation of energetic disorder in an amorphous film of an organic semiconductor. The HOMO consists of a collection of energetically disordered localized states, which can be described by a Gaussian distribution. Charge carriers (holes) hop between these states. Figure adapted from the literature. ³²	11
Figure 1.2	Chemical structure of molecular <i>n</i> -dopants used in this dissertation.	12
Figure 1.3	Two mechanisms by which electron transfer using organometallic dimers can take place. ³³⁻³⁴	13
Figure 1.4	Energy diagram of ITO adapted from the literature. ⁴⁵	15
Figure 1.5	Chemical structure of TDAE, MV(0), AOB and PEIE.	18
Figure 1.6	Sample UPS spectrum of ITO modified with a phosphonic acid (discussed in section 2.4), where the intensity is plotted as a function of the binding energy (E_B) with respect to the Fermi level (E_F , $E_B = 0$ eV). The secondary electron cut-off (SECO), the valence band onset (VB_{onset}) and the ionization energy (IE) are clearly marked. The WF of the sample is calculated as the difference between the energy of the incident radiation [21.22 eV for He (I)] and the SECO (see equation 19).	20
Figure 1.7	Sample XPS spectrum of phenylC ₆₁ butyric acid benzocyclobutene ester <i>n</i> -doped with (IrCp*Cp) ₂ (discussed in section 5.2.2), showing the Ir 4f ionization split into a doublet by spin-orbit coupling. The doublet is deconvoluted into two sets of peaks corresponding to iridium species with oxidation states +3 at higher E_B , and +1 at lower E_B , ultimately showing how XPS can inform on the amount of reacted vs. unreacted dopant in the host material.	23
Figure 1.8	Basics of KP operation. Once the sample and the reference, which have different WF values (A), are brought into electrical contact, their Fermi levels align leading to the formation of a contact potential difference (CPD), (B). A charge-free state is reached by applying a nulling potential $V = -\text{CPD}$, and yielding the WF_{sample} . ^{73, 76}	24
Figure 1.9	Device architectures for $J - V$ measurements, where the organic semiconductor of thickness L is sandwiched between the	28

electrodes (left), or is deposited on pre-patterned electrodes separated by a distance L (center and right).

- Figure 2.1 Chemical structure of molecular n -dopants and PEIE previously used to decrease the work function of metal oxides (center and left). Chemical structure of electron-transporting materials C_{60} and P(NDI2OD-T2) (bottom right). 36
- Figure 2.2 Stability of the dimer-induced work function reduction to thermal annealing. Each data point corresponds to two ITO substrates, and four spots per substrate were analyzed by Kelvin probe in inert atmosphere. 38
- Figure 2.3 Stability of the dimer-induced work function reduction to solvent washing. Each data point corresponds to two ITO substrates, and four spots per substrate were analyzed by Kelvin probe in inert atmosphere. 39
- Figure 2.4 Side view of the structure of a diode manufactured to assess whether the reduction in the electrode work function induced by the n -dopants is retained upon deposition of an organic electron-transporting material. 40
- Figure 2.5 Semi-logarithmic plot of $J - V$ characteristics for devices with structure DSC-ITO (modified or unmodified)/ C_{60} (100 nm)/ MoO_x (10 nm)/Ag (150 nm). Indium tin oxide acts as the electron-injecting electrode in forward bias. 41
- Figure 2.6 Linear plot of $J - V$ characteristics for devices with structure DSC-ITO (modified or unmodified)/ C_{60} (100 nm)/ MoO_x (10 nm)/Ag (150 nm). Indium tin oxide acts as the electron-injecting electrode in forward bias. 42
- Figure 2.7 Current density – voltage characteristics of ITO/PEIE/ C_{60} (100 nm)/ MoO_x (10 nm)/Ag (150 nm) devices annealed at different temperatures and measured at room temperature in the dark. 44
- Figure 2.8 Current density – voltage characteristics of ITO/(IrCpCp*)⁺/ C_{60} (100 nm)/ MoO_x (10 nm)/Ag (150 nm) devices annealed at different temperatures and measured at room temperature in the dark. 44
- Figure 2.9 Semi-logarithmic plots of $J - V$ characteristics showing sample-to-sample variations for devices with structure DSC-cleaned ITO without modification/ C_{60} (200 nm)/ MoO_x (10 nm)/Ag (150 nm). The ITO acts as the electron-injecting electrode under forward bias. 45

Figure 2.10	Semi-logarithmic plots of $J - V$ characteristics showing sample-to-sample variations for devices with structure DSC-cleaned ITO modified with PEIE/C ₆₀ (200 nm)/MoO _x (10 nm)/Ag (150 nm). The ITO acts as the electron-injecting electrode under forward bias.	46
Figure 2.11	Semi-logarithmic plots of $J - V$ characteristics showing sample-to-sample variations for devices with structure DSC-cleaned ITO/(RuCp*mes) ⁺ /C ₆₀ (200 nm)/MoO _x (10 nm)/Ag (150 nm). The ITO acts as the electron-injecting electrode under forward bias.	46
Figure 2.12	Semi-logarithmic plots of $J - V$ characteristics showing sample-to-sample variations for devices with structure DSC-cleaned ITO/(IrCp*Cp) ⁺ /C ₆₀ (200 nm)/MoO _x (10 nm)/Ag (150 nm). The ITO acts as the electron-injecting electrode under forward bias.	47
Figure 2.13	Semi-logarithmic plots of $J - V$ characteristics showing effects of repeated cycling between +2 and -2 V for devices with structure DSC-cleaned ITO without modification/C ₆₀ (200 nm)/MoO _x (10 nm)/Ag (150 nm). The ITO acts as the electron-injecting electrode under forward bias.	47
Figure 2.14	Semi-logarithmic plots of $J - V$ characteristics showing effects of repeated cycling between +2 and -2 V for devices with structure DSC-cleaned ITO modified with PEIE/C ₆₀ (200 nm)/MoO _x (10 nm)/Ag (150 nm). The ITO acts as the electron-injecting electrode under forward bias.	48
Figure 2.15	Semi-logarithmic plots of $J - V$ characteristics showing effects of repeated cycling between +2 and -2 V for devices with structure DSC-cleaned ITO/(RuCp*mes) ⁺ /C ₆₀ (200 nm)/MoO _x (10 nm)/Ag (150 nm). The ITO acts as the electron-injecting electrode under forward bias.	48
Figure 2.16	Semi-logarithmic plots of $J - V$ characteristics showing effects of repeated cycling between +2 and -2 V for devices with structure DSC-cleaned ITO/(IrCp*Cp) ⁺ /C ₆₀ (200 nm)/MoO _x (10 nm)/Ag (150 nm). The ITO acts as the electron-injecting electrode under forward bias.	49
Figure 2.17	Linear plots of $J - V$ characteristics of devices with structure DSC-ITO (unmodified or (IrCp*Cp) ₂ -modified)/P(NDI2OD-T2) (300 ± 10 nm)/MoO _x (10 nm)/Ag (150 nm). ITO acts as the electron-injecting electrode in forward bias.	50
Figure 2.18	Linear plots of $J - V$ characteristics of devices with structure DSC-ITO (unmodified or modified)/P(NDI2OD-T2) (300 ± 10	51

nm)/MoO_x (10 nm)/Ag (150 nm). ITO acts as the electron-injecting electrode in forward bias.

- Figure 2.19 Graphical depiction of the electron transfer between the negatively charged surface of modified ITO and the solution-processed polymer P(NDI2OD-T2), with subsequent loss of monomer cations (RuCp*mes)⁺ or (IrCpCp*)⁺ and of reduced polymer chains during spin coating. As a consequence, the surface of ITO is not as negatively charged as before spin-coating. 51
- Figure 2.20 Work function modification of ITO and FTO of varying degrees of roughness using trimethyl-(4-(phosphonomethyl)-phenylammonium iodide and (RhCp*Cp)₂. 53
- Figure 2.21 XPS N 1s scans of ITO modified with trimethyl-(4-(phosphonomethyl)-phenylammonium iodide and (RhCp*Cp)₂. Possible structure associated with the species 54
- Figure 3.1 Molecular structures of the neutral dimeric dopant (1₂), neutral monomer (1), cationic monomer (1⁺), and of the ETMs C₆₀ and PTCBI. 67
- Figure 3.2 UPS spectra of piranha-cleaned FTO and FTO modified with layers of (RhCp*Cp)₂ (E_{kin} = kinetic energy; E_B = binding energy with respect to the Fermi level, E_F) (left). (b) XPS spectrum of FTO modified with a 10 nm-thick layer of (RhCp*Cp)₂ (right). 68
- Figure 3.3 XPS spectrum of modified FTO with a 1 nm-thick layer of (RhCp*Cp)₂. 69
- Figure 3.4 UPS spectra of FTO/C₆₀, FTO/10 nm (RhCp*Cp)₂/C₆₀ and FTO/5% doped C₆₀ (E_{kin} = kinetic energy, E_B = binding energy with respect to the Fermi level, E_F). The insets offer enlarged view of the UPS spectra at low binding energies, close to the E_F . The doping concentration of 5% is given as a molar percentage calculated from the evaporation rates. 71
- Figure 3.5 UPS spectra of FTO/PTCBI, FTO/10 nm (RhCp*Cp)₂/PTCBI and FTO/5% doped PTCBI (E_{kin} = kinetic energy, E_B = binding energy with respect to the Fermi level, E_F). The insets offer enlarged view of the UPS spectra at low binding energies, close to the E_F . The doping concentration of 5% is given as a molar percentage calculated from the evaporation rates. 72
- Figure 3.6 Electronic structure of triple-sublimed PTCBI, obtained via UPS (blue curve) and IPES (red curve). The optical band gap was 74

measured to be 1.7 eV; the ionization energy (5.87 eV) is similar to values reported in the literature (6.2 eV).¹²⁸

- Figure 3.7 UPS spectra of FTO/C₆₀ and (RhCp*Cp)₂ modified-FTO/C₆₀ with varying thickness of the (RhCp*Cp)₂ interlayer. 75
- Figure 3.8 UPS spectra of FTO/PTCBI and (RhCp*Cp)₂ modified-FTO/PTCBI with varying thickness of the (RhCp*Cp)₂ interlayer. 75
- Figure 3.9 XPS Rh 3d scans of FTO/1-10 nm (RhCp*Cp)₂/ETM and FTO/ETM coevaporated with (RhCp*Cp)₂. 77
- Figure 3.10 Smoothed NIR absorption spectra for pure ETM, 1₂-modified FTO/ETM annealed at increasing temperatures and 1₂ coevaporated with ETM. The doping concentration for coevaporated ETMs is calculated from the absorption peak at 1065 nm to be 15% for C₆₀ (left) and 17% for PTCBI (right). 78
- Figure 3.11 UV-vis-NIR absorption spectra for pure ETM, (RhCp*Cp)₂ modified-FTO/ETM annealed at increasing temperatures, and (RhCp*Cp)₂ coevaporated with ETM with a doping concentration of around 10%; ETM = C₆₀ (left), PTCBI (right). 79
- Figure 3.12 Raw NIR absorption spectra for pure ETM, 1₂-modified FTO/ETM annealed at increasing temperatures, and 1₂ coevaporated with ETM. The ETMs used were C₆₀ (left) and PTCBI (right). The doping concentrations for coevaporated ETMs are calculated from the deposition rates to be 13% for C₆₀ and 17% for PTCBI. 79
- Figure 3.13 Absorption of the reference box used to perform UV-vis-NIR absorption spectroscopy on samples containing (RhCp*Cp)₂. Since there are no absorption features of the reference box in the range of 1.04 eV to 1.44 eV, features in this range can be assigned to sub-bandgap features of the samples. Abrupt signal changes at 1.04 eV and 1.44 eV are artifacts of the spectrometer due to detector and grating changes. 80
- Figure 3.14 Current density – voltage characteristics for the best-performing solar cells fabricated using C₆₀ as ETM before and after deposition of (RhCp*Cp)₂ on FTO. 83
- Figure 3.15 Current density – voltage characteristics for the best-performing solar cells fabricated using PTCBI as ETM before and after deposition of (RhCp*Cp)₂ on FTO. 83

Figure 3.16	Current density – voltage characteristics for the best-performing solar cells fabricated using C ₆₀ and PTCBI as ETMs (left), and with PTCBI deposited on (RhCp* Cp) ₂ -modified FTO (right).	84
Figure 3.17	UV-vis spectra of 15-nm thick PTCBI films on glass before and after sequential spin-coating of acetonitrile and dimethylformamide.	86
Figure 4.1	Molecular structures of the neutral dimeric dopant (RhCp* Cp) ₂ , and of TBABH ₄ .	94
Figure 4.2	UPS spectra of piranha-cleaned FTO and FTO modified by dipping in solutions of (RhCp* Cp) ₂ for 1 min or 10 min, followed by three rinsing cycles with pure toluene. (E_{kin} = kinetic energy; E_B = binding energy with respect to the Fermi level, E_F).	96
Figure 4.3	XPS spectra of FTO modified by dipping in solutions of (RhCp* Cp) ₂ for 1 min (left) or 10 min (right). Spectra for sample 1 are similar to those for sample 2.	97
Figure 4.4	WF of pristine and modified FTO as a function of dipping time and concentration of TBABH ₄ solutions. After dipping, modified substrates were rinsed three times with pure acetonitrile. WF values were measured via Kelvin probe in air using gold as a reference. 75% of the sample data lie in the rectangular boxes, and horizontal lines within the boxes indicate the sample average. A minimum of four measurements was performed on each sample.	99
Figure 4.5	WF of pristine and modified FTO as a function of pressure and modification protocol (dipping/rinsing vs. dropcasting) using TBABH ₄ solutions. Unless specified otherwise, WF values were measured via Kelvin probe in air using gold as a reference. 75% of the sample data lie in the rectangular boxes, and horizontal lines within the boxes indicate the sample average. A minimum of four (two) measurements was performed on each sample analyzed via Kelvin probe (UPS).	100
Figure 4.6	UPS spectra of piranha-cleaned FTO and FTO modified by dipping in 10 mM TBABH ₄ solutions for 10 min, without rinsing, measured immediately or after 2 days. (E_{kin} = kinetic energy; E_B = binding energy with respect to the Fermi level, E_F). UPS was performed at a base pressure of 10 ⁻¹⁰ mbar.	100
Figure 4.7	Sheet resistance, resistivity and conductivity of C ₆₀ , and contact resistance of C ₆₀ with silver electrodes as a function of the surface treatment applied on DSC glass.	103

Figure 4.8	Resistance at the C ₆₀ /Ag contact plotted as a function of the conductivity of C ₆₀ , showing the effect of the surface treatments on both.	104
Figure 4.9	Semi-logarithmic plot of $J - V$ characteristics for devices with structure piranha cleaned-FTO (modified or unmodified)/C ₆₀ (200 nm)/BCP (10 nm)/Au (80 nm). In forward bias FTO acts as the electron-injecting electrode. Note $J - V$ characteristics for two different devices with TBABH ₄ -modified FTO is shown.	106
Figure 4.10	Semi-logarithmic plot of $J - V$ characteristics for devices with structure DSC-FTO (modified or unmodified)/C ₆₀ (200 nm)/BCP (10 nm)/Au (80 nm). In forward bias FTO acts as the electron-injecting electrode.	107
Figure 4.11	Current density – voltage characteristics for the best-performing solar cells fabricated using C ₆₀ as ETM before and after dipping FTO in 2 mM (RhCp* <i>Cp</i>) ₂ solutions, and rinsing three times with pure toluene, or in 10 mM TBABH ₄ solutions, and rinsing three times with pure acetonitrile.	110
Figure 5.1	Thermally activated reaction pathways of PCBCB molecules, where two benzocyclobutene groups can react together (top), and where a benzocyclobutene group reacts with the fullerene cage (bottom).	118
Figure 5.2	Molecular structures of the iridium dimer dopant (IrCp* <i>Cp</i>) ₂ and the crosslinker PMHBCB with the same benzocyclobutene moiety as the fullerene derivative.	120
Figure 5.3	UV-vis-NIR absorption spectra of solutions of PCBCB as a function of (IrCp* <i>Cp</i>) ⁺ content (molar percentage). The inset shows the appearance of the PCBCB radical anion at 1070 nm and the disappearance of neutral PCBCB at 330 nm.	121
Figure 5.4	UPS spectra of neat and doped (PCBCB) _n with (IrCp* <i>Cp</i>) ₂ (E_{kin} = kinetic energy; E_B = binding energy with respect to the Fermi level, E_F). Dimer content is reported as a function of molar percentage of monomer cations (IrCp* <i>Cp</i>) ⁺ relative to the host.	123
Figure 5.5	XPS spectra of doped (PCBCB) _n with (IrCp* <i>Cp</i>) ₂ . Dimer content is reported as a function of molar percentage of monomer cations (IrCp* <i>Cp</i>) ⁺ relative to the host.	124
Figure 5.6	Sheet resistance, resistivity and conductivity of (PCBCB) _n , and contact resistance of (PCBCB) _n with silver electrodes as a function of (IrCp* <i>Cp</i>) ⁺ content (molar percentage). The sheet	126

resistance of PCBM and resistance at the PCBM/Ag contact are reported for comparison.

- Figure 5.7 Sheet resistance, resistivity and conductivity of doped (PCBCB)_n, and contact resistance of doped (PCBCB)_n with silver electrodes as a function of crosslinker (molar) concentration. The concentration of (IrCp*Cp)⁺ in the fullerene derivative was kept constant at 3 mol % . 128
- Figure 5.8 Iridium elemental contribution in doped (PCBCB)_n films with 3 mol% (IrCp*Cp)₂ as prepared, and after spin-coating chlorobenzene or DMF on top of it. The elemental contribution of iridium is calculated from the area under the Ir 4f peaks in XPS spectra. The carbon elemental contribution in the same films is constant at around 70%, regardless of washing. 130
- Figure 5.9 Iridium elemental contribution in doped (PCBCB)_n films with 3 mol% (IrCp*Cp)₂ and 10 mol% PMHBCB, as prepared, and after spin-coating chlorobenzene or DMF on top of it. The elemental contribution of iridium is calculated from the area under the Ir 4f peaks in XPS spectra. The carbon elemental contribution in the same films is constant at around 60%, regardless of washing. 131
- Figure 5.10 Elemental contributions in doped (PCBCB)_n films with 3 mol% (IrCp*Cp)₂ and 10 mol% PMHBCB, as prepared, and after spin-coating chlorobenzene or DMF on top of it. The elemental contribution of carbon, oxygen, indium, tin and iridium are calculated from the area under the C 1s, O 1s, In 3d, Sn 3d and Ir 4f peaks in XPS spectra. 132
- Figure 5.11 Atomic concentration of iridium and ratio between Ir 4f and carbon C 1s peaks as a function of sputter depth and sputter time for (PCBCB)_n films containing 29 mol% (IrCp*Cp)⁺, deposited on ITO and covered by 20 nm of vacuum-deposited C₆₀. XPS depth profiling was performed on the samples as-prepared. 133
- Figure 5.12 Atomic concentration of iridium and ratio between Ir 4f and carbon C 1s peaks as a function of sputter depth and sputter time for (PCBCB)_n films containing 29 mol% (IrCp*Cp)⁺, deposited on ITO and covered by 20 nm of vacuum-deposited C₆₀. XPS depth profiling was performed on the samples after annealing at 185 °C for 90 min. 134
- Figure 5.13 Open-circuit voltage (*V*_{oc}) and fill factor (FF) for solar cells fabricated using as ETMs (PCBCB)_n, (PCBCB)_n containing 0.2 mol% of (IrCp*Cp)⁺ and PCBM. All solar cells were made using 137

tin oxide nanoparticles as a buffer layer between the fullerene derivative and FTO.

- Figure 5.14 Current density – voltage characteristics for the best-performing solar cells fabricated using as ETMs (PCBCB)_n, (PCBCB)_n containing 0.2 mol% of (IrCp*Cp)⁺ and PCBM. All solar cells were made using tin oxide nanoparticles as a buffer layer between the fullerene derivative and FTO. 138
- Figure 5.15 Current density – voltage characteristics for the best-performing solar cells fabricated using as ETMs (PCBCB)_n, (PCBCB)_n containing 1 mol% of crosslinker and a compact layer of SnO₂ covered with PCBM (reference). 139
- Figure 5.16 Current density – voltage characteristics for the best-performing solar cells fabricated with (PCBCB)_n, (PCBCB)_n + 0.2 mol% (IrCp*Cp)⁺, (PCBCB)_n + 1 mol% of crosslinker, and (PCBCB)_n containing both dopant and crosslinker as ETMs. 141
- Figure 5.17 Schematic of a typical degradation pattern of a solar cell containing organic semiconductors (hence representative of PSCs as well as OPVs), showing the burn-in and linear decay regimes. The lifetime of a solar cell is defined by the point at which the efficiency is 80% of what it originally was after the burn-in period. Adapted from the literature.¹⁷³ 142
- Figure 5.18 Stability comparison of non-encapsulated perovskite solar cells (PSCs) fabricated using as ETMs (PCBCB)_n or compact-layer SnO₂ coated with PCBM. PSCs were aged for 1800 h at 85 °C in the dark in inert atmosphere, and brought to atmosphere and room temperature for PCE measurement. An average of four devices per each data point is reported. The vertical line at 200 h marks the transition from burn-in to linear decay. 143
- Figure 5.19 Stability comparison of non-encapsulated perovskite solar cells (PSCs) fabricated using (PCBCB)_n and doped (PCBCB)_n as ETMs. PSCs were aged for 1800 h at 85 °C in the dark in inert atmosphere, and brought to atmosphere and room temperature for PCE measurement. An average of four devices per each data point is reported. The vertical line at 200 h marks the transition from burn-in to linear decay. 144
- Figure 5.20 Stability comparison of non-encapsulated perovskite solar cells (PSCs) fabricated using as ETMs (PCBCB)_n and (PCBCB)_n containing 1 mol% of PMHBCB crosslinker. PSCs were aged for 1800 h at 85 °C in the dark in inert atmosphere, and brought to atmosphere and room temperature for PCE measurement. An 145

average of four devices per each data point is reported. The vertical line at 200 h marks the transition from burn-in to linear decay.

- Figure 5.21 Stability comparison of non-encapsulated perovskite solar cells (PSCs) fabricated using as ETMs doped (PCBCB)_n and doped (PCBCB)_n containing 1 mol% of PMHBCB crosslinker. PSCs were aged for 1800 h at 85 °C in the dark in inert atmosphere, and brought to atmosphere and room temperature for PCE measurement. An average of four devices per each data point is reported. The vertical line at 200 h marks the transition from burn-in to linear decay. 146
- Figure 6.1 Proposed mechanism of *n*-doping of C₆₀ with tetrabutylammonium borohydride. 166

LIST OF SYMBOLS AND ABBREVIATIONS

AOB	Acridine orange base
CB	Conduction band
CB _{onset}	Conduction band onset
CV	Cyclic voltammetry
Cp	Cyclopentadienyl
Cp*	Pentamethylcyclopentadienyl
DI	Deionized water
DFT	Density functional theory
DSC	Detergent/solvent-cleaned
EA	Electron affinity
E_B	Binding energy
E_F	Fermi level
E_{kin}	Kinetic energy
ETM	Electron-transporting material
eV	Electron volt
E_{vac}	Vacuum level
FF	Fill factor
FTO	Fluorinated tin oxide
FWHM	Full width at half maximum
h	Hour
HOMO	Highest occupied molecular orbital
HOPG	Highly oriented pyrolytic graphite

HPLC	High-performance liquid chromatography
<i>IE</i>	Ionization energy
IMFP	Inelastic mean free path
IPES	Inverse photoemission spectroscopy
ITO	Indium tin oxide
<i>J</i>	Current density
<i>J_{sc}</i>	Short-circuit current
<i>j_o</i>	Reverse saturation current
k	Boltzmann constant
KP	Kelvin probe
Li-TFSI	Lithium bis(trifluoromethanesulfonyl)imide
LUMO	Lowest unoccupied molecular orbital
mes	Mesitylene, (i.e., 1,3,5-trimethylbenzene)
min	Minute
MV(0)	Neutral methyl viologen
NIR	Near-infrared
NMR	Nuclear magnetic resonance
OLEDs	Organic light-emitting diodes
OPVs	Organic photovoltaics
PMHBCB	poly(bicyclo[4.2.0]octa-1(6),2,4-trien-7-yl-hexanoyl methacrylate)
PCBM	Phenyl-C ₆₀ -butyric methyl ester
PCBCB	PhenylC ₆₁ butyric acid benzocyclobutene ester
PCE	Power conversion efficiency
PDI	Perylene diimide
PEI	Polyethylenimine

PEIE	Polyethylenimine, ethoxylated
PSCs	Perovskite solar cells
PTCBI	Perylene-3,4:9,10-tetracarboxylic bis(benzimidazole)
q	Absolute value of the charge of an electron
R _c	Contact resistance
R _s	Sheet resistance
R _t	Total resistance
s	Second
SECO	Secondary electron cut-off
spiro-OMeTAD	2,2',7,7'-Tetrakis(<i>N,N'</i> -di- <i>p</i> -methoxyphenylamino)-9,9'-spirobifluorene
SPO	Stabilized power output
T	Temperature
TMPMPAI	Trimethyl-(4-(phosphonomethyl)-phenylammonium iodide
TBABH ₄	Tetrabutylammonium borohydride
<i>t</i> BP	<i>Tert</i> -Butylpyridine
UHV	Ultra-high vacuum
UV	Ultraviolet
UPS	Ultra-violet photoelectron spectroscopy
V	Voltage
VB	Valence band
VB _{onset}	Valence band onset
V _{oc}	Open-circuit voltage
WF	Work function
XPS	X-ray photoelectron spectroscopy

Vis visible

vs. Versus

SUMMARY

This dissertation focuses on the use of the dimers formed by some 19-electron organometallic sandwich compounds to tune the electronic properties of transparent conductive oxides, particularly indium tin oxide (ITO) and fluorinated tin oxide (FTO), and organic electron-transporting materials (ETMs), specifically fullerene and perylene diimide derivatives used in perovskite solar cells (PSCs). The dimers reduce the work function (WF) of electrode materials by transferring electrons to the metal oxides, forming metal-organic monomeric cations electrostatically bound to the reduced electrode, or *n*-dope ETMs through a similar reaction. This dissertation is an investigation of the relationship between the processing method by which dimers are deposited on metal oxides or along with organic semiconductors, their ability to lower the WF of the electrode and/or to increase the electrical conductivity of ETMs, their chemical state in these doped materials, and the electrical behavior of the modified substrate in simple and complex optoelectronic devices. Moreover, the stability of the WF modification to solvent washing, temperature and processing route of ETM overlayers is explored. Two strategies to prevent washing of monomer cations and their diffusion are proposed: one entailing the combination of phosphonic acid and organometallic dimer modification of metal oxides; one entailing the use of a crosslinker in bulk-doped fullerene derivatives. The effect of the choice of surface-modification layer and ETM on charge collection in PSCs is assessed. The findings of this dissertation will contribute to the development of robust surface modification and doping approaches for the fabrication of efficient and stable optoelectronic devices.

CHAPTER 1. INTRODUCTION

The objective of this Ph.D. dissertation is to investigate the use of organometallic redox-active compounds as surface modifiers of transparent conductive oxides and as *n*-dopants for electron-transporting materials in perovskite solar cells. Following the introduction of the key terms used to describe the electronic structure of semiconductors, this chapter provides background information on *n*-dopants that have been used to increase the conductivity of organic semiconductors, or to modify the work function of electrodes. A brief overview of transparent conductive oxides and surface modification approaches used in optoelectronics follows, as well as a description of their principles of operation. The major experimental techniques that can be used to characterize surfaces and doping effects are discussed. Finally, an overview of the structure of this dissertation is provided.

1.1 Motivation and Significance

Our daily lives increasingly rely on commercial electronic products such as smart phones, computers, and TVs to exchange, generate and edit information. These products are composed among other parts of simpler electronic devices to turn them on and off (i.e., transistors), or to increase the luminosity of displays (i.e., light-emitting diodes). However, without electricity none of these devices would be able to operate. Growing energy needs, coupled with a fast-changing climate,¹ have stimulated the development of solar cells able to efficiently convert the most abundant renewable energy source, sunlight, into electricity at low costs.²⁻³ From a materials standpoint, semiconductors are central to the operation of the optoelectronic devices hereby mentioned. Inorganic semiconductors such as crystalline silicon have traditionally been the materials of choice;⁴⁻⁹ however, the discovery and

development of electrically conductive polymers¹⁰ has resulted in intensive research efforts on organic semiconductors and their incorporation in field-effect transistors (OFETs), light-emitting diodes (OLEDs), and photovoltaics (OPVs). The push towards organic electronics is partly motivated by the facile tunability of the materials properties of organic molecules through synthesis, and by their compatibility with roll-to-roll printing. Indeed, solution-processing could potentially enable the fabrication of large-area devices that are mechanically flexible and are light-weight, potentially reducing installation costs of commercial photovoltaic systems, which significantly contributes to their end-cost.³ In contrast, silicon-based electronics are limited in dimension to 30 cm-wide rigid wafers, fabricated using high-temperature methods. In both inorganic and organic semiconductor devices, electrical doping can be profitably used to increase electrical conductivity and to otherwise control the properties of the semiconductor. Doping consists of the introduction of external species (dopants), which either donate an electron (*n*-dopant) to or accept an electron (*p*-dopant) from the host material. In inorganic crystalline semiconductors, such as Si, a very small fraction of host atoms is replaced by atoms with one more (e.g., phosphorus) or one fewer (e.g., boron) valence electron than the host atom. In organic semiconductors, the dopants are typically redox-active molecules that are capable of forming host radical cations or anions through electron-transfer reactions. The choice of dopant for an organic semiconductor is critical to ensure that it can influence materials with a given electronic structure, without forming reaction by-products or migrating in the device under operation. It is possible to introduce the dopant by co-depositing it with the host (bulk doping) or by depositing at the interface between the host and another material, such as the electrode (interfacial doping). The latter can be effectively used to affect the

energetic alignment at the interface between the electrode and the organic semiconductor, enabling efficient charge collection in OPVs or injection in OLEDs. Many of the lessons learned from organic and silicon-based electronics research can be reapplied to lead halide perovskite solar cells (PSCs), which have rapidly developed over the last decade,¹¹ and have reached power conversion efficiencies above 23% as a single junction and of 28% in tandems with silicon solar cells.¹² Moreover, PSCs that retain 60% of their efficiency after 1000 h of exposure to light and air without encapsulation have also been reported in the literature, highlighting the potential of this technology.¹³ The perovskites in question are light-absorbing crystalline hybrid inorganic materials, $APbX_3$ [A = organic and/or inorganic cation, e.g., $CH_3NH_3^+$, Cs^+ ; X = Cl^- , Br^- , I^-], composed of earth-abundant elements, and can be processed by both vapor¹⁴ and solution methods.¹⁵ Similarly to organic molecules, the optoelectronic properties of these perovskites can be easily tuned by changing their composition.¹⁶⁻¹⁹ On the other hand, their high charge-carrier mobility values and low exciton binding energies are more typical of inorganic semiconductors. Organic semiconductors are often used as charge-selective layers in perovskite-based solar cells, and doping of these layers as well as interface engineering to form good electrical contact between the organic semiconductors and the electrodes, has been shown to improve the power conversion efficiency and the stability of these devices.²⁰⁻²⁴ Before covering different classes of dopants and surface modifiers, it is necessary to introduce the key terminology used to describe the electronic structure and properties of semiconductors.

1.2 Energy Level and Associated Terminology Definitions

1.2.1 Vacuum Level (E_{vac})

The vacuum level at infinity [$E_{vac}(\infty)$] is defined as the energy of an electron at rest at a distance that is sufficiently far from the solid surface that the electron is not affected by the electrostatic potential of the surface. $E_{vac}(\infty)$ is an invariant reference level; however, it is not experimentally accessible and has only theoretical implications.²⁵ The vacuum level of relevance to this dissertation, which is used to determine quantities such as the work function (WF), the ionization energy (IE), and the electron affinity (EA), can be defined as the local vacuum level, E_{vac} , which is the energy of an electron with zero kinetic energy (E_{kin}) with respect to the surface of a solid, but still affected by the electrostatic potential of the surface.²⁵⁻²⁷

1.2.2 Valence Band (VB)

Electrons in an atom display atomic orbitals represented by stationary electronic wave functions having quantized energy values. In a two-atom system, two valence-electron atomic orbitals, one from each atom, mix to form a chemical bond.²⁸ The latter results in two molecular orbitals: a bonding orbital, where the electron density between the two nuclei of the atoms increases, resulting in a lower energy level than the energy level of the individual valence-electron atomic orbitals; and an antibonding orbital, where the electron density between the nuclei of the two atoms decreases, resulting in a higher energy level than the energy level of the individual valence-electron atomic orbitals.²⁸ In a solid, a very large number of electrons interact, producing a large set of bonding orbitals with discrete energy values, and an analogous set of antibonding orbitals. These sets of bonding

and antibonding orbitals having discrete but very closely spaced energy levels are referred to as energy bands, and are commonly approximated as a continuous set of energy levels.²⁸ In an ideal crystalline solid, atoms are periodically arranged with electronic wave functions that significantly overlap causing molecular orbitals to acquire long-range crystalline symmetries. The existence of long range order opens up energy gaps where no electronic states exist. In non-ideal solids, defects are always present, introducing localized energy states within the bandgap that can act as traps or as electron-donating or electron-accepting states.²⁸ The VB is the highest filled band, and is fully occupied by electrons at absolute zero temperature. The occupied state of the VB with the highest energy is called the valence band maximum, or valence band onset (VB_{onset}).²⁹

1.2.3 Conduction Band (CB)

CB is the lowest energy empty band and is fully unoccupied by electrons at absolute zero temperature. The bottom edge of the CB, in other words, the unoccupied state with lowest energy, assuming the absence of trap states within the band gap, is called conduction band minimum or conduction band onset (CB_{onset}).²⁹

1.2.4 Fermi Level (E_F)

The distribution of energetic states within the relevant energy bands, known as the density of states, $N(E)$, is obtained by counting the number of energetic states available for an electron with energy between E and $E + \Delta E$ and can be defined as:

$$N(E) = \frac{1}{V} \frac{d\Omega(E)}{dE}, \quad (1)$$

where V is the volume and $\Omega(E)$ is the number of energy states.²⁸ The number of electrons occupying such energy states with an energy between E and $E + \Delta E$ can be calculated as:

$$n(E, T)dE = N(E)f(E, T)d(E), \quad (2)$$

where $f(E, T)$ is the probability of finding an electron with a given energy E . Since electrons are fermions, which are subatomic particles with half-integer spin that follow the Pauli exclusion principle,³⁰ in thermodynamic equilibrium they display an energy distribution that follows Fermi-Dirac statistics, with a probability function given by the expression:

$$f(E) = \frac{1}{1 + e^{\frac{E - E_F}{kT}}}, \quad (3)$$

where E_F is the Fermi level, k is Boltzmann constant, and T is the temperature.^{28, 30} In a metal, E_F lies within one band and at 0 K, E_F marks the boundary between occupied and unoccupied states.²⁷ In a semiconductor, E_F lies within the bandgap and does not correspond with an electronic level in the solid. In an intrinsic semiconductor, at equilibrium E_F is correlated with the intrinsic carrier concentration:

$$E_F = E_C + kT \ln \left(\frac{n_0}{N_C} \right) \quad (4)$$

$$E_F = E_V - kT \ln \left(\frac{p_0}{N_V} \right) \quad (5)$$

In the equations above, E_C (E_V) is the energy at the CB_{onset} (VB_{onset}), N_C (N_V) is the effective density of states per unit volume in the conduction (valence) band, and n_0 (p_0) is the equilibrium density of electrons (holes). Under non-equilibrium conditions (i.e., under

illumination), it is possible to express the non-equilibrium concentration of electrons (n) and of holes (p) in the semiconductor as the sum of the carrier density at equilibrium (n_0 for electrons, and p_0 for holes) and the electrons (δn) and holes (δp) generated because of the perturbation:

$$n = n_0 + \delta n \quad (6)$$

$$p = p_0 + \delta p \quad (7)$$

Excess free charge carriers in a semiconductor rapidly exchange energy leading to the formation of thermal distributions of electrons in the CB and holes in the VB. These thermal distributions are in quasi-static equilibrium and follow Fermi-Dirac statistics.²⁸ A semiconductor under illumination displays distinct quasi-Fermi levels for electrons in the CB and holes in the VB, such that:

$$n = n_0 + \delta n = n_i e^{\frac{F_N - E_i}{kT}} \quad (8)$$

$$F_N = E_C + kT \ln \left(\frac{n}{N_C} \right) \quad (9)$$

$$p = p_0 + \delta p = p_i e^{\frac{E_i - F_P}{kT}} \quad (10)$$

$$F_P = E_V - kT \ln \left(\frac{p}{N_V} \right) \quad (11)$$

In the equations above, F_N is the quasi-Fermi level for electrons, F_P is the quasi-Fermi level for holes, $n_i(p_i)$ is the intrinsic carrier concentration of electrons (holes), and E_i is the intrinsic E_F .

1.2.5 Work Function (WF)

WF is defined as the energy necessary to bring an electron from the E_F inside the material to the local vacuum level, E_{vac} , just outside the surface²⁷, as described by the following equation:

$$WF = E_{vac} - E_F \quad (12)$$

In other words, the WF can be thought of as the energy that would be required for an electron at the E_F to escape from the solid to free space. Given its relation to E_{vac} and E_F , WF depends on the density of states, doping concentration, temperature and carrier density of the material.²⁷ In addition, as discussed further below, the WF also depends on the electrostatic landscape at the surface of the material.

1.2.6 Ionization Energy (IE)

The solid-state IE is the minimum (positive) energy necessary to remove an electron from the filled states of a solid material and place it at E_{vac} . In an intrinsic semiconductor at absolute zero temperature, the electrons closest in energy to E_{vac} are those at the VB_{onset} (or at the highest-occupied molecular orbital, HOMO, in an organic semiconductor), therefore once E_{vac} and VB_{onset} are known, IE can be calculated:

$$IE = E_{vac} - VB_{onset} \quad (13)$$

Organic semiconductors typically used in optoelectronics have IE s of ca. 4.5 – 6.5 eV, while n -dopants tend to have $IE < 3.5$ eV.²⁷

1.2.7 Electron Affinity (EA)

The solid-state EA is the energy gained by adding an electron from E_{vac} to the lowest unoccupied state (i.e., the CB_{onset} or at the lowest-unoccupied molecular orbital, LUMO, in an intrinsic semiconductor at absolute zero temperature), hence once E_{vac} and CB_{onset} are known, EA can be calculated:

$$EA = E_{vac} - CB_{onset} \quad (14)$$

Organic semiconductors typically used in optoelectronics have EAs in the range of 2 – 4 eV, while p -dopants (discussed in section 1.3) tend to have $EA > 5.0$ eV. A more comprehensive discussion of EA can be found in the literature.²⁷

1.3 Semiconductors

By applying an electric field (E) to a material placed between two electrical contacts and measuring the resulting current density (J) across it, it is possible to define the conductivity (σ) as follows:

$$\sigma = \frac{J}{E} \quad (15)$$

The mobility (μ) indicates how fast charge carriers move in the electric field (E) applied to the material, and it is defined as the drift velocity (v) per unit electric field:

$$\mu = \frac{v}{E} \quad (16)$$

Equation 17 describes the relationship between conductivity and mobility, where n represents the density of charge carriers, and q is the elementary charge.

$$\sigma = n\mu q \quad (17)$$

Based on their electrical conductivity (σ), which is discussed more in detail in section 1.7.6, electronic materials can be classified (roughly) as insulators, semiconductors, or conductors. Insulators are characterized by $\sigma < ca. 10^{-8} \text{ S cm}^{-1}$, semiconductors by $ca. 10^{-8} \text{ S cm}^{-1} < \sigma < ca. 10^2 \text{ S cm}^{-1}$, and conductors by $\sigma > ca. 10^2 \text{ S cm}^{-1}$ at room temperature.

Organic semiconductors are characterized by a weak intermolecular overlap of the electronic wave functions; therefore, charge carriers tend to be localized on molecular units and charge transport occurs via tunneling or temperature-assisted hopping of charge carriers between sites. Due to the hopping transport, organic materials generally show mobility of often 10^{-5} to $10^{-2} \text{ cm}^2 \text{ V}^{-1} \text{ s}^{-1}$, which is much lower than the mobility of inorganic examples exhibiting band transport (10^{+3} to $10^{+4} \text{ cm}^2 \text{ V}^{-1} \text{ s}^{-1}$).³¹⁻³² Mobility in amorphous films of organic semiconductors is even lower since structural disorder leads to the formation of localized electronic states with a distribution of energy, which can be described as Gaussian, as shown in Figure 1.1 for the HOMO of the semiconductor. A similar depiction is also valid for the LUMO.³²

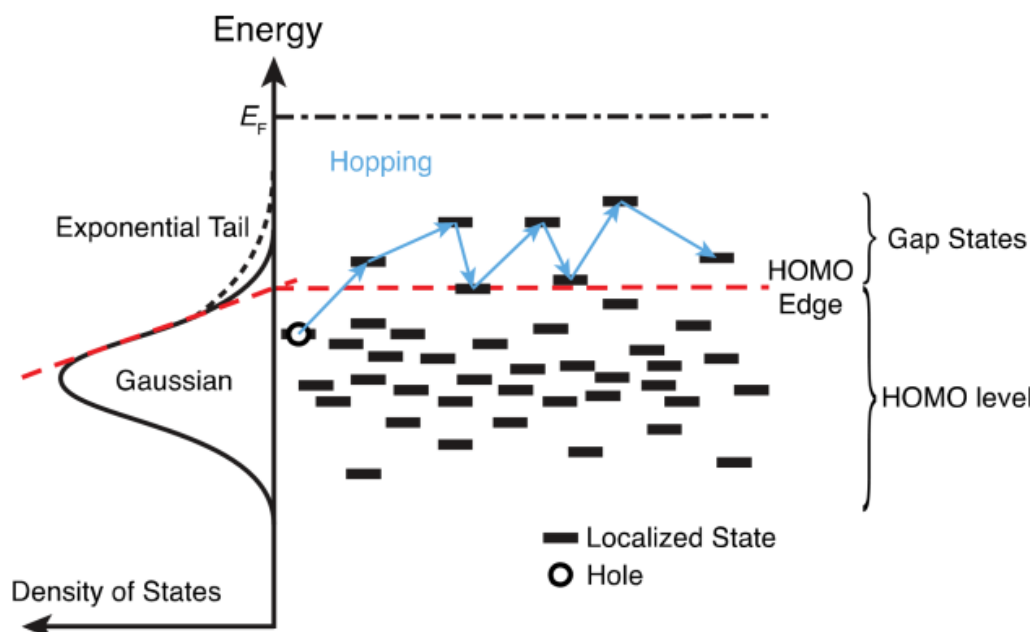


Figure 1.1 Representation of energetic disorder in an amorphous film of an organic semiconductor. The HOMO consists of a collection of energetically disordered localized states, which can be described by a Gaussian distribution. Charge carriers (holes) hop between these states. Figure adapted from the literature.³²

A strategy to increase the conductivity of organic semiconductors is to increase their carrier density; alternatively, materials with higher mobility can be chosen or designed. It is possible to increase the charge-carrier density either by injection from the electrodes or by addition of *n*- or *p*-dopants.³¹ Electrical doping consists in the addition of guest species to the host material, which alter the semiconductor's electrical properties by either donating electrons and filling empty states (*n*-dopants), or by accepting electrons from the host and creating holes (*p*-dopants). Previously, alkali metals and molecular compounds with very low *IEs* have been used as *n*-dopants; however, the former tend to diffuse in organic semiconductors, and the latter are highly air-sensitive and require constant handling in inert atmosphere. Alternatively, it is possible to use air-stable precursor molecules (e.g., organic

hydride-donors) where electrical doping is preceded by processes to obtain highly reducing species, leading to ease of synthesis and handling prior to device fabrication.

1.4 Redox-Active Organometallic Dimers

Among air-stable precursor molecules, dimers formed by some 19-electron organometallic sandwich compounds couple electron transfer with bond breaking, and can *n*-dope semiconductors with *EA* larger than 2.8 eV by transferring electrons to the acceptor and forming monomer cations, without the formation of any byproducts.³³⁻³⁴ Moreover, diffusion of monomer cations can be less likely than, for example, alkali metal ions, given the large size of the former. This dissertation focuses on the use of this type of *n*-dopants, and specifically (pentamethylcyclopentadienyl) (1,3,5-trimethyl-benzene) ruthenium dimer (RuCp*mes)₂, pentamethylcyclopentadienyl cyclopentadienyl iridium dimer (IrCp*Cp)₂, and pentamethylcyclopentadienyl cyclopentadienyl rhodium dimer (RhCp*Cp)₂.

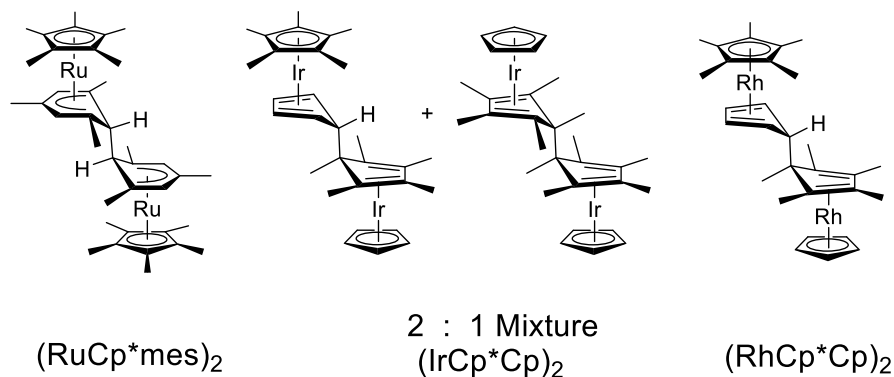


Figure 1.2 Chemical structure of molecular *n*-dopants used in this dissertation.

Two doping mechanisms are possible for these organometallic dopants.³³⁻³⁴ Dimers can undergo endergonic homolytic cleavage to 19-electron monomers, which quickly

transfer electrons to the acceptor material, if present, with $EA > 2.8$ eV, as illustrated by mechanism I in Figure 1.3. It is also possible for dimers to first endergonically transfer an electron to acceptors with suitable EA , then dissociate to a stable 18-electron monomer cation and a highly reactive 19-electron monomer, which can further transfer an electron to the acceptor, resulting in the formation of two monomer cations, as illustrated by mechanism II in Figure 1.3. For $(\text{RhCp}^*\text{Cp})_2$ both mechanisms are active, since its central C-C bond is relatively weaker than the one in ruthenium and iridium analogues, for which only mechanism II is active.³⁴ Regardless of the mechanism, the thermodynamics of doping depend on the oxidation potential of the 19-electron monomer $E(\text{M}^+/\text{M})$ and the free energy of dissociation of the central C-C dimeric bond, as discussed in chapter 2.

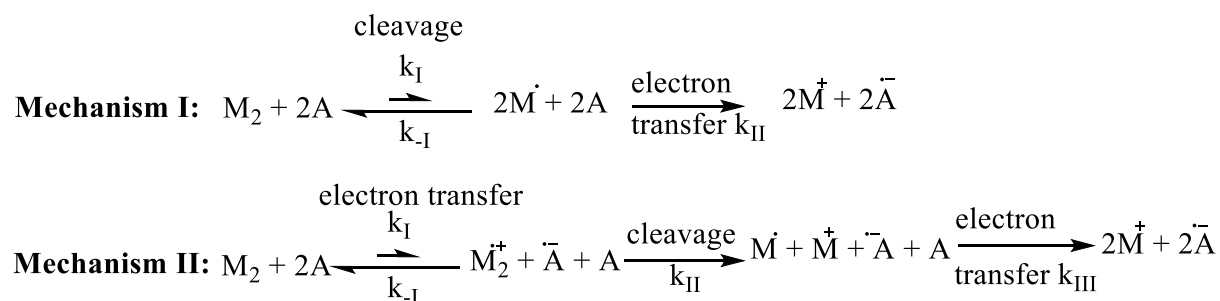


Figure 1.3 Two mechanisms by which electron transfer using organometallic dimers can take place.³³⁻³⁴

While the organometallic dimers in Figure 1.2 were used to dope small-molecule and polymer semiconductors with EA up to 2.8 eV, it was recently shown that photo-activation of $(\text{RuCp}^*\text{mes})_2$ can result in kinetically stable and efficient n -doping of electron acceptors (e.g., phenyldi(pyren-2-yl)phosphine oxide, POPy_2) with EA of 2.2 eV, which is beyond the thermodynamic reach of the dimer's effective reducing strength.³⁵ As a consequence

of *n*-doping using photoactivation, the conductivity of POPy₂ was increased by more than five orders of magnitude, leading to highly-efficient OLEDs.³⁵

1.5 Transparent Conducting Oxides (TCOs)

Optoelectronic devices (e.g., solar cells, light emitting diodes) require the use of electrodes with high optical transparency and high electrical conductivity to operate effectively. Transparent conducting oxides (TCOs) are a subgroup of transparent conducting electrodes (TCEs) that satisfy these requirements. Development of solar cells and of screen displays has further stimulated research on TCEs, leading to the investigation of flexible TCEs,³⁶⁻³⁸ as well as the development of surface modifiers to tune the electrode WF.³⁹⁻⁴² The TCOs of relevance to this dissertation are indium tin oxide (ITO), used in the context of diode fabrication in chapter 2, and fluorinated tin oxide (FTO), used as the electron-collecting electrode in PSCs in chapters 3-5. Both oxides have high optical transmission in the visible range ($\geq 90\%$); have medium-to-high WF, the exact value of which depends upon the cleaning method;⁴³ are relatively hard (5 – 6.5 Mohs hardness scale); and are commercially available as thin films typically deposited on glass or plastic substrates.⁴⁴

1.5.1 Indium Tin Oxide (ITO)

ITO ($\text{In}_2\text{O}_3:\text{Sn}$) is a highly electrically conductive TCO, owing its low resistivity ($1 - 2 \times 10^{-4} \Omega \text{ cm}$) to interstitial oxygen vacancies (V_o), which are formed when the polycrystalline material is annealed. Stoichiometric indium oxide (In_2O_3) has a valence band (VB) that is primarily O^{2-} 2p in character, and a conduction band (CB) that is primarily In 5s in character. The band gap of In_2O_3 is around 3.5 eV.⁴⁵ At low V_o

concentration, In 5s orbitals form shallow donor states just below the CB_{onset} ($\Delta E = 0.03$ eV). Moreover, the addition of tin forms another set of shallow states with Sn 5s character, as shown in Figure 1.4. These shallow states further decrease the barrier to conduction.⁴⁵⁻
⁴⁶ Given its high conductivity, ITO is an ideal TCO for high-resolution display applications where there is a need to keep the topography as smooth as possible. The latter can be achieved by depositing very thin films of the metal oxide without compromising its electrical properties.⁴⁴ ITO is commonly deposited via spray pyrolysis,⁴⁷ electron beam evaporation and sputtering techniques.^{44, 48} The concentration of indium in minerals on the earth's crust is low; therefore, indium is extracted as a by-product during the processing of the ores of other metals (e.g., zinc), driving the cost of the TCOs containing this element.

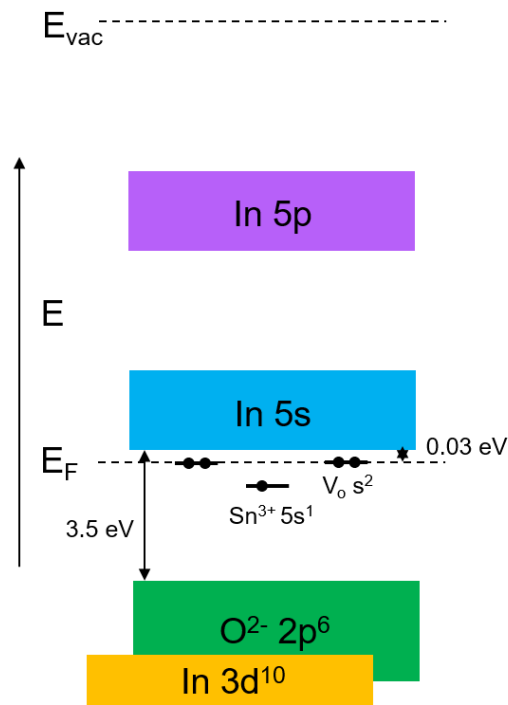


Figure 1.4 Energy diagram of ITO adapted from the literature.⁴⁵

1.5.2 Fluorinated Tin Oxide (FTO)

FTO ($\text{SnO}_2\text{:F}$) has a similar resistivity to ITO and is commonly prepared using chemical vapor deposition (CVD),⁴⁹ with the precursor trifluoroacetic acid as a fluorine source. By tuning the flow rate and flow ratio of the precursor it is possible to change the surface roughness and the fluorine doping level, respectively.⁵⁰ While the latter does not affect the optical transparency of FTO in the visible range,⁵¹⁻⁵² the introduction of fluorine has an impact on the electrical properties of the film, by replacing oxygen in the tin oxide lattice, and increasing the charge carrier concentration.^{50, 53-54} FTO is one of the most cost-effective TCOs to produce, since it does not contain expensive and rare elements (i.e., indium). Moreover, $\text{SnO}_2\text{:F}$ exhibits superior chemical durability and thermal stability compared to ITO, making FTO compatible with piranha cleaning and titanium dioxide sintering at temperature above 450 °C.⁴⁴ For these characteristics FTO has been widely used as electron-collecting electrode in dye-sensitized and perovskite solar cells.^{15, 55-56}

1.6 Surface Modification of Transparent Conducting Oxides

Tuning the WF of a substrate is particularly important to control the interface energetics of a semiconductor on top of an electrode. The interface can be modified to enhance the wettability of the substrate by the organic semiconductor, or to allow for a better energetic alignment in optoelectronic devices, decreasing the energetic barriers for charge injection or reducing charge collection losses, depending on the device. Typical optoelectronic devices require the presence of a low-WF metal for the collection or injection of electrons. Most low-WF metals (e.g., alkaline earth metals) are highly reactive with oxygen and water, and require encapsulation to maintain the low WF. Therefore, surface modifiers can be used to decrease the WF of electrodes such as ITO and FTO, who have medium-to-high WF, are stable and transparent. Phosphonic acids can form

monolayers on the surface of Lewis acidic metal oxides via coordination of the phosphoryl oxygen to the substrate surface followed by a heterocondensation reaction, or, if the metal oxide is weakly Lewis acidic (e.g., ITO), directly through heterocondensation without phosphoryl coordination.^{41, 57-58} This reactivity leads to the formation of up to three P-O-M bonds, where M is the metal oxide substrate. The dipole associated with P-O-M bonds (bond dipole) can reinforce or oppose the dipole of the substituents of the phosphonic acids. In the case of ITO, the bond dipole is oriented in a way that increases the WF. As a consequence, monolayers of phosphonic acids can effectively increase the WF of ITO by 1 eV but, to date, have only been shown to decrease the WF of the metal oxide by only 0.1 eV.^{41, 59} Another approach consists in the adsorption of polymers containing amines, such as polyethyleneimine (PEI) and its ethoxylated derivative (PEIE), on metals and metal oxides, the WF of which can be decreased by 1 eV due to the formation of an interface dipole between the polymers' amine groups and the conductive substrate.⁶⁰ However, PEI and PEIE are not the only surface modifiers that are not reliant on specific chemistry between the surface and the adsorbate, and that can effectively modify the WF of a large number of surfaces. Redox-active molecules, such as tetrakis(dimethylamino)ethylene (TDAE), neutral methyl viologen [MV(0)], and acridine orange base (AOB), can be electrostatically bound to the surface of electrodes where they transfer electrons to the surface, and form a large interface dipole. The latter leads to WF reductions of gold of 1.3 eV, 2.2 eV, and 1.9 eV in the case of thermally evaporated TDAE, MV(0) and AOB, respectively.⁶¹⁻⁶³ The use of TDAE was extended to ITO, whose WF was reduced by 0.9 eV upon formation of an interface dipole.⁶⁴ Nevertheless, use of these redox-active molecules (e.g., MV(0) and AOB) is limited to vacuum deposition and handling of some

of them, (e.g., TDAE) is not straightforward given their volatility and air-sensitivity. In contrast to MV(0) and AOB, the redox-active organometallic dimers discussed in section 1.4 can be deposited via solution and vacuum processing and can be handle in air for short periods of time (< 10 min). The WF of graphene can be decreased by 1.3 eV by solution processing of $(\text{RhCp}^*\text{Cp})_2$ for just a few seconds.⁶⁵ The WF of ZnO can reach values as low as 2.2 eV when $(\text{RuCp}^*\text{mes})_2$ is vacuum-deposited, forming $(\text{RuCp}^*\text{mes})^+$ cations on the oxide surface. This surface modification approach allows for alignment of the frontier levels of ZnO with an organic semiconductor deposited on top, inducing a seven-fold increase in radiative emission in a hybrid inorganic/organic structure.⁶⁶ Therefore, the use of dimers seems promising to modify metal oxides/organic semiconductor interfaces in various optoelectronic devices, including perovskite solar cells, where organic semiconductors are used as ETMs.

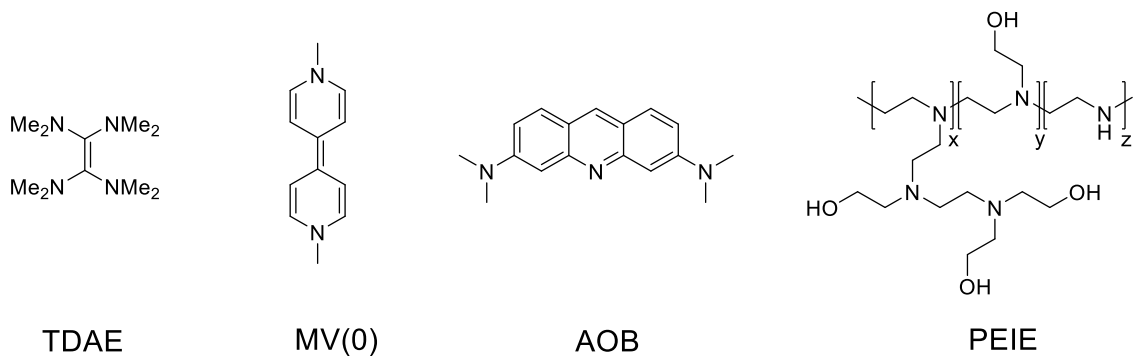


Figure 1.5 Chemical structure of TDAE, MV(0), AOB and PEIE.

1.7 Analytical Methods for Examining Surface Modifiers and Redox-Active Species

The following is a brief overview of the main characterization techniques that are employed in the later chapters of this dissertation to investigate the *n*-doping of surfaces and of bulk organic semiconductors.

1.7.1 Ultraviolet Photoelectron Spectroscopy (UPS)

UPS is a characterization technique used to probe the occupied states of metals (i.e., E_F) and semiconductors (i.e., E_F , VB/HOMO), by irradiating the material surface in ultra-high vacuum (UHV, pressure $< 10^{-8}$ Torr) with ultraviolet light. The UV source is commonly a helium discharge lamp, whose main emission lines are He I (21.22 eV) and He II (40.81 eV). These high-energy photons have sufficient energy to eject electrons from the occupied states near the surface with varying kinetic energies, E_{kin} . Some of the photoelectrons undergo scattering processes with other electrons on their way to the surface; inelastically scattered electrons lead to the formation of the secondary electron background, while those that can scatter elastically or that are unscattered are called primary electrons and provide useful information regarding their initial occupied state through their binding energy, E_B . The latter is correlated to E_{kin} through the following equation⁶⁷:

$$E_{kin} = h\nu - WF_{detector} - E_B, \quad (18)$$

where $h\nu$ is the energy of the UV radiation used. Those electrons with E_{kin} lower than the WF of the material itself are not detected, causing an abrupt decrease in intensity, called the secondary electron cut-off (SECO), which is the difference between the WFs of the sample and the detector.⁶⁸ The electrons that reach the detector with the highest E_{kin} are those emitted from the highest occupied states (i.e., VB_{onset} , HOMO), whose energy can be

calculated with respect to the E_F , which is set to $E_B = 0$ eV. From the SECO is possible to calculate the WF of the material, as described below and visually displayed in Figure 1.6:

$$WF_{sample} = h\nu - E_F - SECO, \quad (19)$$

where $h\nu$ is the energy of the incoming radiation. Therefore by adding the WF to the onset of the occupied states, it is possible to calculate the IE of the material. UPS is a surface-sensitive technique, since the inelastic mean free path (IMFP) of the photoexcited electrons, which is the average distance they can travel in the solid before they engage in an inelastic collision and lose their part of their E_{kin} , is typically less than 2 nm. The sensitivity of UPS to changes in the surface of metal oxides and organic semiconductors, led to its use in chapters 2-5.

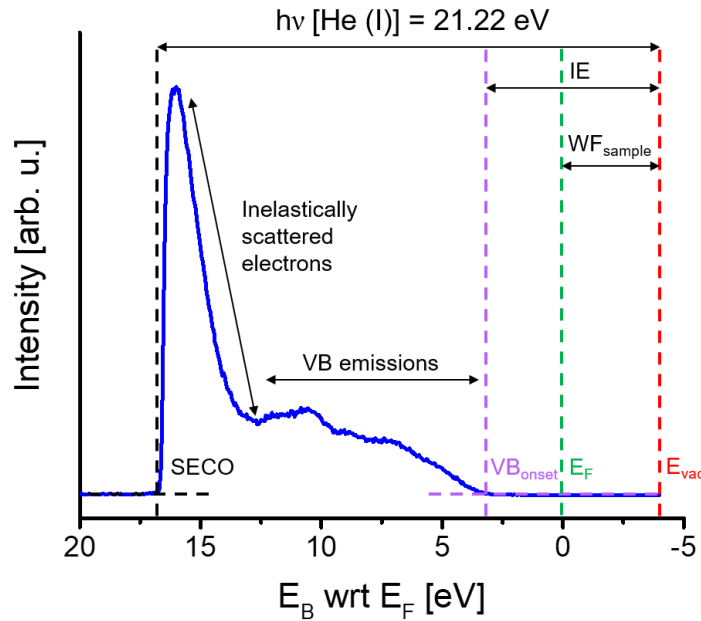


Figure 1.6 Sample UPS spectrum of ITO modified with a phosphonic acid (discussed in section 2.4), where the intensity is plotted as a function of the binding energy (E_B) with respect to the Fermi level (E_F , $E_B = 0$ eV). The secondary electron

cut-off (SECO), the valence band onset (VB_{onset}) and the ionization energy (IE) are clearly marked. The WF of the sample is calculated as the difference between the energy of the incident radiation [21.22 eV for He (I)] and the SECO (see equation 19).

1.7.2 Inverse Photoemission Spectroscopy (IPES)

IPES is a UHV characterization technique used to probe the unoccupied states of metals and semiconductors, by irradiating the material surface with a collimated beam of electrons with E_{kin} of 15 eV or less. Incoming electrons with E_{kin} larger than the WF of the sample, penetrate the surface and couple with high-lying unoccupied states of the material probed, to then radiatively decay to unoccupied states with lower energy. The photons emitted in the radiative decays are detected and provide information on the conduction band, LUMO, LUMO + 1, etc., of different semiconductors.^{32, 69} IPES is a surface-sensitive technique, probing the top 2 – 4 nm of the analyzed material given the larger IMFP compared to UPS. IPES can be performed in two modes: the fluorescent and the isochromat modes. In the former, the E_{kin} of the incoming electrons is fixed and photons with various energy are detected; in the latter, the energy of the incoming electrons is varied and the detector only collects photons with a fixed energy. The advantage of the isochromat mode – used in chapter 3 to investigate the unoccupied states of a perylene diimide derivative, and commonly used to analyze organic semiconductors – over the fluorescent one is the higher signal-to-noise ratio and the little-to-no sample damage, at the expense of the energy resolution.^{32, 69} By aligning IPES spectra, which provide information on the energy difference between the E_F and the CB_{onset} , and UPS spectra, which provide information on the energy difference between the E_{vac} and the E_F , the EA of the material can be calculated.^{32, 69}

1.7.3 X-ray Photoelectron Spectroscopy (XPS)

XPS is a UHV characterization technique that probes atomic core levels by irradiating the surface of conducting materials with high-energy x-rays, typically generated using Al-K α ($h\nu = 1486.6$ eV) or Mg-K α ($h\nu = 1253.6$ eV) as source lines.^{32, 70} The incident x-rays cause the ejection of inner shell electrons, which have a probability of escaping the material that decays exponentially with the distance of the atom in question from the surface, leading to an IMFP of *ca.* 10 nm. Once the emitted electrons reach an energy analyser, they are separated in terms of their kinetic energies, and are converted to binding energies, which are characteristics for a specific element, its chemical state, and chemical environment. Moreover, the number of ejected electrons is proportional to the number of atoms present. The XPS signals can then be corrected for the E_{kin} -dependent detector response and atomic ionization cross-sections to give ratios between different types of atoms, giving information on the chemical composition of surfaces and interfaces, as shown in chapters 2-5, with detection limits as low as 0.1% atom concentrations (although attenuation effects also have to be taken into account for atoms not located at the immediate surface).^{32, 70-71} In XPS spectra photoelectron peaks are superimposed on a background associated with inelastically scattered electrons, and signals originating from orbitals with an angular momentum quantum number larger than zero (i.e, p, d, f orbitals) appear as doublets due to spin-orbit coupling, as shown in Figure 1.7. These doublets have defined area ratios (1:2 for p orbitals, 2:3 for d orbitals and 3:4 for f orbitals), and an energy

separation dependent on the orbital and element the photoelectrons were ejected from.⁷² Other than the emitted photoelectrons, additional features can appear in XPS spectra such as those originating from the emission of Auger electrons; satellite peaks, which can be observed if the x-rays beam used to irradiate the sample is not monochromated; x-ray ghost lines due to x-ray anode contaminations; and plasmon loss peaks. For further reading, several references are provided.^{68, 70, 72}

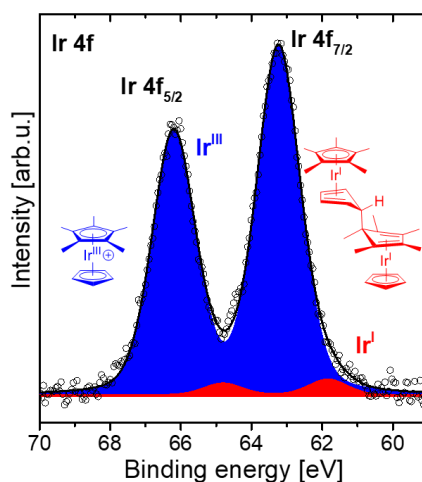


Figure 1.7 Sample XPS spectrum of phenylC₆₁butyric acid benzocyclobutene ester *n*-doped with (IrCp**Cp*)₂ (discussed in section 5.2.2), showing the Ir 4f ionization split into a doublet by spin-orbit coupling. The doublet is deconvoluted into two sets of peaks corresponding to iridium species with oxidation states +3 at higher E_B , and +1 at lower E_B , ultimately showing how XPS can inform on the amount of reacted vs. unreacted dopant in the host material.

1.7.4 Kelvin Probe (KP)

KP is a non-destructive technique that allows one to measure the WF of a material in the dark without exposure to UHV, by probing the contact potential difference (CPD) between the sample and a reference,⁷³ which is defined as:

$$CPD = WF_{sample} - WF_{reference} \quad (20)$$

When the material to be analysed is brought into electrical contact (through a wire) with the reference probe, their Fermi levels align leading to the formation of an electrical potential (CPD) between the sample and the reference probe. To reach a neutral state, a potential $V = -CPD$ is applied and WF_{sample} can be obtained, as depicted in Figure 1.8. Therefore, unlike UPS, which provides an absolute value of WF, KP is an indirect method of measuring WF as it requires calibration of the reference probe with a chemical inert material of known WF ($WF_{reference}$), such as gold or highly-oriented pyrolytic graphite (HOPG).⁷⁴ Given the finite size (mm^2) of the probe, WF values obtained using KP are averaged over a similar sample area, and are not sensitive to different crystal orientations at the surface,⁷³ whose WF can be adequately probed using UPS. However, since CPD measurements do not require pumping-down time, KP can be conveniently used to quickly screen the WF of several samples, as shown in chapters 2 and 4.⁷⁵ Moreover, it can also be used to investigate the WF of materials that are unstable to UHV or to hard UV irradiation, as discussed in chapter 4.

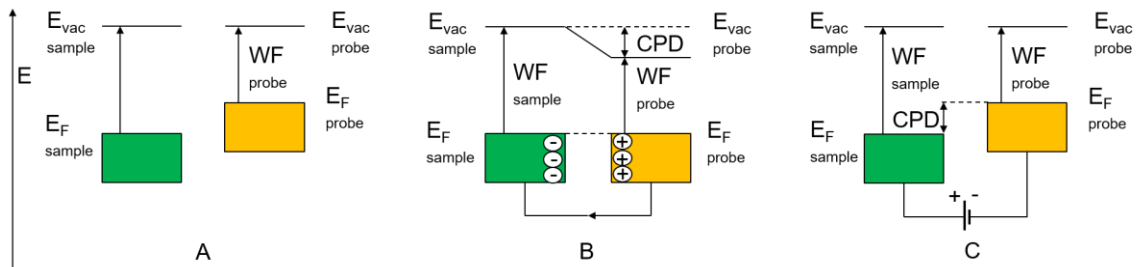


Figure 1.8 Basics of KP operation. Once the sample and the reference, which have different WF values (A), are brought into electrical contact, their Fermi levels align leading to the formation of a contact potential difference (CPD), (B). A charge-

free state is reached by applying a nulling potential $V = -CPD$, and yielding the WF_{sample} .^{73, 76}

1.7.5 Mobility Measurements Techniques

Charge mobility is a material property that can be measured using a range of techniques [e.g., time-of-flight (TOF) measurements, space-charge limited current (SCLC) measurements]. These methods operate over different length scales, require different sample geometries, and can involve different assumptions for their interpretations, which can sometimes make difficult to directly compare the obtained results. In time-of-flight experiments, the semiconductor is placed between a transparent electrode, such as ITO, and a metal electrode. The temperature of the sandwich structure is controlled and an electric field is applied in a specific direction to transport the carriers of interest. Excited states in the semiconductor are formed by shining a laser pulse through the ITO into the semiconductor, and such states then dissociate into electrons/hole pairs. Under the application of the electric field, photogenerated charge carriers of a given polarity move towards the metal electrode producing a transient current, which vanishes when the charges are collected. The mobility μ can be calculated using equation 16, where the drift velocity v by measuring the duration of the photocurrent, which is equal to the ratio of the semiconductor thickness and the duration of the photocurrent. At a given temperature, the natural logarithm of the mobility is proportional to the square root of the applied field, and variable-field experiments are used to extrapolate the “zero-field” mobility at that temperature.⁷⁷ Since the effective absorption length of the pulse that produces the photocarriers must remain small compared to thickness of the sample, and since the electric field in the sample is considered uniform, TOF measurements are carried out using thick

films of semiconductor and injection of carriers from the contacts needs to be minimized. However, in optoelectronic applications thin layers ($< 1 \mu\text{m}$) of semiconductors are used and charge injection or collection is desired. Therefore, instead of using TOF measurements it is possible to derive the mobility from current density-voltage ($J - V$) characteristics of thin organic films between electrodes, where the bias between two electrodes is varied and the current density across the organic semiconductor is measured. At low values of electric field, the $J - V$ curves are ohmic as discussed in more detail in section 1.7.6. By increasing the applied voltage so that the number of injected charge carriers is larger than those present in the bulk semiconductor due to thermal activation, a stationary space charge is established in the material and the $J - V$ curves become non-linear. In this regime, the current density can be described by the Mott-Gurney law:

$$J = \frac{9}{8} \varepsilon \varepsilon_0 \mu \frac{V^2}{L^3}, \quad (21)$$

where μ is the mobility of the charge carriers, L is the film thickness, ε is the permittivity of the semiconductor and ε_0 is the permittivity of free space. The mobility of charge carriers in a semiconductor, and the relationship between conductivity and mobility are defined in section 1.3, by equations 16 and 17, respectively.

1.7.6 *Electrical Conductivity Measurements*

The electrical conductivity (σ) of a thin film of an organic semiconductor can also be determined from $J - V$ measurements. When the voltage applied is low, few charge carriers per unit volume are injected and the current density across the organic semiconductor is dependent on the motion of thermally activated charge carriers present in

its bulk. Assuming that the density of charge carriers at and nearby the contacts with the electrodes is much higher than in the bulk of the semiconductor, the current density (J) can be described by Ohm's law:

$$J = \sigma \frac{V}{L}, \quad (22)$$

where the current density J is linearly proportional to the applied voltage V , and inversely proportional to the sample length L for different device structures for $J - V$ measurements.⁷⁸

In the ohmic region, the conductivity can be determined using the following equation:

$$\sigma = \frac{L}{RA}, \quad (23)$$

where A is the cross sectional area and R is the resistance of the organic semiconductor, obtained from the slope of the $I - V$ plot. The conductivity can be measured in different configurations. For example, the organic semiconductor can be deposited on the bottom electrode and the top electrode is subsequently evaporated, and the current density is measured perpendicularly to the substrate. Alternatively, the semiconductor can be deposited on an insulating substrate with pre-patterned electrodes, with a given spacing between them, called channel length (L); in this case, the current density is measured laterally to the substrate and the conductivity of the organic material can be determined using the following equation:

$$\sigma = \frac{L}{n w d R_t}, \quad (24)$$

where n is the number of channels, w is the width of the section where the organic material overlaps with the electrodes, d is the thickness of the organic semiconductor, and R_t is the total resistance obtained from the slope of the $I - V$ curves in the ohmic regime. To determine whether doping of organic semiconductors occurs, it is possible to find in the literature comparisons of current densities of pristine and doped samples at specific applied voltages even if outside of the ohmic regime.³³

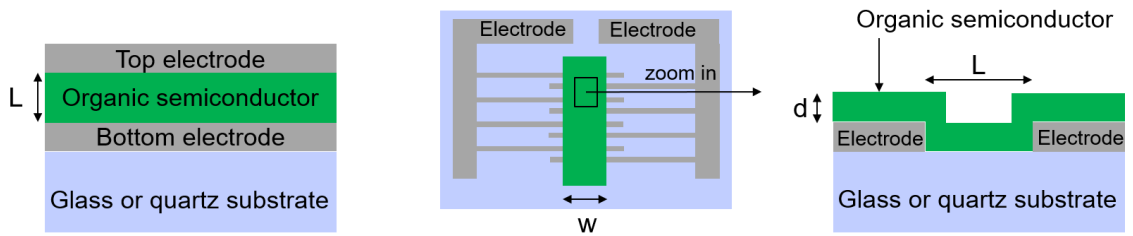


Figure 1.9 Device architectures for $J - V$ measurements, where the organic semiconductor of thickness L is sandwiched between the electrodes (left), or is deposited on pre-patterned electrodes separated by a distance L (center and right).

Four-point probe is another technique used to measure the resistivity, and calculate the conductivity, of bulk or thin-film of semiconductors. Four equally spaced metal tips (typically 1 mm apart) with finite radius are placed in contact with the semiconductor; a current I is supplied to the two outer probes, and a voltmeter measures the voltage drop V across the two inner probes.⁷⁹ In bulk samples (sample thickness, $t \gg$ probe spacing, s), considering that the current I injected by the first tip spreads spherically into a homogeneous and isotropic material, the resistivity ρ can be described as follows:

$$\rho = 2\pi s \frac{V}{I}, \quad (25)$$

where ρ is independent of the film thickness t . In thin films of semiconductors, the current can be assumed to spread cylindrically instead of spherically from the metal electrode, and ρ can be obtained as follows:

$$\rho = \frac{\pi t V}{\ln 2 I}, \quad (26)$$

where ρ is independent of the probe spacing s .⁷⁹ Unlike two-point probe measurements, using four-point probe provides conductivity values that are disentangled from the contact resistance between the metal tips and the semiconductor. In this dissertation, to prevent oxidation of doped species, conductivity measurements are often carried in inert atmosphere, as shown in chapters 4 and 5.

1.7.7 UV-vis-NIR Absorption Spectroscopy

Absorption spectroscopy is a useful tool for the characterization of materials used in optoelectronic applications. Absorption spectra are obtained by exposing the material to electromagnetic radiation with a given intensity (I_0). The material absorbs part of the radiation, and the incoming intensity is attenuated, as described by the Beer-Lambert law:

$$I = I_0 - \Delta I = I_0 e^{-\alpha x} \quad (27)$$

where I is the intensity of the transmitted radiation, ΔI represents is the attenuation in intensity, α is the absorption coefficient, which is material- and wavelength-dependent, and x is the path length of the radiation along which the attenuation takes place. ΔI is made of different contributions, originated by the interaction of light with the material, such as light-absorption, scattering, reflection, and interference. Most of the time, it is possible to minimize or ignore

all contributions but light absorption. The final absorption spectra are obtained by plotting over the range of wavelength of the incoming electromagnetic radiation, the absorbance (A) of the material, defined as:

$$A = \log_{10} \left(\frac{I_0}{I} \right) = -\log_{10}(T) = \frac{\alpha}{\ln(10)} x \quad (28)$$

where T is the transmittance, \log is the logarithm to base 10 and \ln is the logarithm to base e . Organic semiconductors tend to exhibit characteristic absorption features in the visible or infrared region, which are generally different from those of their radical anions, typically formed upon introduction of an n -dopant in sufficiently large quantities for the peak to be detected. However, radical anions of organic semiconductors tend to be highly air- and moisture-sensitive; therefore, n -doping studies in which the disappearance of the neutral features of the host material and the increase in absorbance of its radical anion are monitored, need to be performed in inert atmosphere. Doping and diffusion studies of semiconductors using UV-vis-NIR absorption spectroscopy are discussed at length in chapters 3 and 5.

1.8 Thesis Structure and Overview

This chapter serves as an introduction on the surface modifiers and n -dopants developed by the scientific community to improve electrical contact at electrode/semiconductor interfaces, and to improve the electrical conductivity of organic semiconductors in optoelectronic devices. The later chapters focus on furthering our understanding of organometallic dimers as surface modifiers of transparent conductive oxides and as n -dopants for electron-transporting materials used in efficient and stable PSCs. This thesis is the result of collaborative work with groups at the Georgia Institute of

Technology (Kippelen group – chapters 2, 4 and 5), at the University of Oxford (Snaith group – chapters 3, 4 and 5; Herz and Johnston groups – chapters 3 and 4; Riede group – chapter 3) and at the Humboldt University of Berlin (Koch group – chapters 3, 4 and 5).

Chapter 2 builds on previous work that established a correlation between the reducing strength of organometallic *n*-dopants and their ability to decrease the WF of metals and metal oxides.⁸⁰ The chapter has two goals: the first is to assess the stability to solvent washing and thermal stress of the WF modification of ITO induced by dimeric reductants; the second is to understand whether the transparent metal oxide can work as a low-WF electrode in simple sandwich devices. The electrical behavior of dimer-modified ITO is compared to that of bare or PEIE-modified ITO by fabricating diodes containing ETMs processed from vacuum or from solution. A combination of covalent tethering of phosphonic acids and reduction of ITO with the organometallic compounds is proposed as a robust surface modification strategy.

Chapters 3 and 4 explore the use of (RhCp*Cp)₂, processed from vacuum (chapter 3) and from solution methods (chapter 4), to modify the FTO/ETM interface, and to assess whether the modification and the processing route of the modifier have an impact on charge collection in PSCs. Various spectroscopic techniques described in chapter 1 are used to investigate electronic alignment at this interface, and *n*-doping of the ETM molecules in proximity of the modified electrode. Chapter 3 further focuses on comparing C₆₀ with a perylene diimide derivative, commonly used as a pigment in car paint, as vacuum-processible organic ETMs in PSCs. This body of work paves the way towards future studies assessing the impact of organic ETMs on the stability under thermal stress of PSCs. In chapter 4 C₆₀ is used as the ETM and (RhCp*Cp)₂ is compared with a metal-free

ammonium salt as WF modification layers on FTO capable of inducing interfacial *n*-doping of C₆₀.

Chapter 5 is a study of bulk *n*-doping of a fullerene derivative, phenylC₆₁butyric acid benzocyclobutene ester (PCBCB), which has been previously used as an insoluble ETM in PSCs,⁸¹ using the organometallic dimer (IrCp*₂Cp)₂. Diffusion of the latter under thermal stress in fullerene bilayers is explored, and the addition of a crosslinker is proposed as a strategy to prevent or limit diffusion, without negatively affecting the electrical conductivity of the host semiconductor. This chapter delves into whether there is a correlation between the introduction of the *n*-dopant and of the crosslinker in the ETM and solar cell stability.

Last, chapter 6 offers a summary of the findings reported throughout this dissertation, puts them in context with the literature and suggests future directions worth exploring.

CHAPTER 2. SURFACE MODIFICATION OF INDIUM TIN OXIDE WITH DIMERIC REDUCTANTS

2.1 Introduction

Materials with a low work function (WF) are used as electron-collecting electrodes in organic photovoltaics (OPVs) and perovskite solar cells (PSCs), electron-injecting electrodes in organic light-emitting diodes (OLEDs), and source and drain electrodes in *n*-channel organic field-effect transistors (OFETs). One of the requirements for at least one of the electrodes in OPVs and OLEDs is transparency to light. Conductive metal oxides, satisfy this requirement but most, including the widely used indium tin oxide (ITO), have a medium-to-high WF, which prevents ITO from being used as an electron-collecting or injecting electrode. For ITO to be used in this way, it is necessary to lower its work function; to do so dipoles that shift the vacuum level at the surface of the metal oxides can be introduced in several ways. Covalently tethering monolayer of phosphonic acids^{58, 82} to metal oxides leads to a somewhat small decrease in work function due to the partial cancellation of the bond dipole and the dipole of the substituents of the phosphonic acids.⁵⁹ WF reductions of more than 1 eV can be achieved by treating ITO in air with aqueous solutions of polyethyleneimine (PEI) and its ethoxylated derivative (PEIE), due to the formation of an interface dipole between the polymers' amine groups and the conductive substrate.⁶⁰ A less explored approach, which is in principle compatible with both solution and vacuum processing, consists of the reduction of metal oxide surfaces using molecular *n*-dopants. Reductants that have been applied to metal oxides, or in a related approach to metals such as gold, include tetrakis(dimethylamino)ethylene (TDAE), neutral methyl

viologen (MV(0)), acridine orange base (AOB).⁶¹⁻⁶³ Electron-transfer from strongly reducing species to the electrode results in a surface dipole between the negatively charged surface and a layer of dopant-derived cations. Recently, the Marder group has shown that the organometallic dimers of certain 19-electron sandwich compounds (effective redox potentials for the monomer cation/dimer couple, $E[M^+/0.5 M_2]$, estimated to be ca. -1.7 to -2.3 V vs. ferrocenium/ferrocene in tetrahydrofuran, THF)⁸³ are relatively air-stable and are much stronger reductants than TDAE ($E_{1/2}^{+/0} = -0.99$ V in acetonitrile, MeCN),⁸⁴⁻⁸⁵ MV(0) ($E_{1/2}^{+/0} = -1.25$ V in MeCN),⁸⁶ and AOB (+0.32 V in MeCN),⁸⁵⁻⁸⁶ and, as a consequence, lead to large reductions in WF.⁴⁰ The redox potential of TDAE and AOB were reported in the original publications vs. SCE and are here referenced vs. $FeCp_2^{+/0}$, according to a conversion reported in the literature.⁸⁵ $E(M^+/0.5 M_2)$ is the estimated redox potential for the overall half-reaction $M + e^- = 0.5 M_2$ and measures the overall reducing strength of the dimer, in other words the thermodynamic feasibility of electron transfer. Values were estimated using the following equation, where F is the Faraday constant, which describes the relationship between the overall reducing strength of the dimers, the free energy of dissociation of the dimer into monomers (ΔG_{diss}) obtained through M06/LANL2DZ/6-31G(d,p) DFT calculations, and the oxidation potential of the 19-electron monomer $E(M^+/M)$ determined by electrochemistry on hexafluorophosphate salts, $M^+PF_6^-$:

$$E(M^+/0.5M_2) = E(M^+/M) + 0.5 \frac{\Delta G_{diss}(M_2)}{2F} \quad (29)$$

This chapter examines the extent to which organometallic dopants $(IrCp^*Cp)_2$ and $(RuCp^*mes)_2$ can be used as solution-processable surface dopants of indium tin oxide, and

use polyethyleneimine as a benchmark modification treatment, since both the dimers and PEIE lead to work function reductions larger than 1 eV. If alternative and reliable surface treatments to tune the work function of metal oxides were established by leveraging the reducing power of the dimers, surface-modified materials could replace low work function metals belonging to group 1 and 2, such as calcium. Even though Ca is effectively used as an electron-injecting/collecting electrode in organic electronics, it is opaque, usually best deposited in vacuum and unstable upon exposure to oxygen, moisture and halide-containing materials. These disadvantages could be overcome by demonstrating that dimer-doped transparent, stable and commercially available materials (e.g., ITO) work as electron-injecting electrodes when organic semiconductors processed from vacuum or from solution are deposited on top of them. Surface modification of a wide range of materials, including ITO, using polyethylenimine (PEIE) proved that it is possible to substitute low work function metals with transparent metal oxides in OLEDs and OPVs. However, the use of PEIE has been limited to deposition from aqueous solutions, which could possibly be an issue when materials successively deposited onto an electrode are water-sensitive. In this context, by comparing organometallic dimer doping with PEIE treatment, it could be possible to establish complementary surface modification protocols compatible with a variety of materials and processing techniques. Investigation of the work function changes induced by treatment of metal oxides using organometallic dimers was performed by Dr. Anthony J. Giordano and is discussed at length in his dissertation.⁸⁰ The following sections were performed by the author to examine stability of the work function modification and its applicability to electron injection from the ITO electrode. Most of the results shown here were published in *ACS Applied Materials & Interfaces*, 2015, **7**, 4320-

4326, and were obtained in collaboration with Dr. Talha M. Khan from the Kippelen group at the Georgia Institute of Technology (assistance with vacuum deposition for diode fabrication).

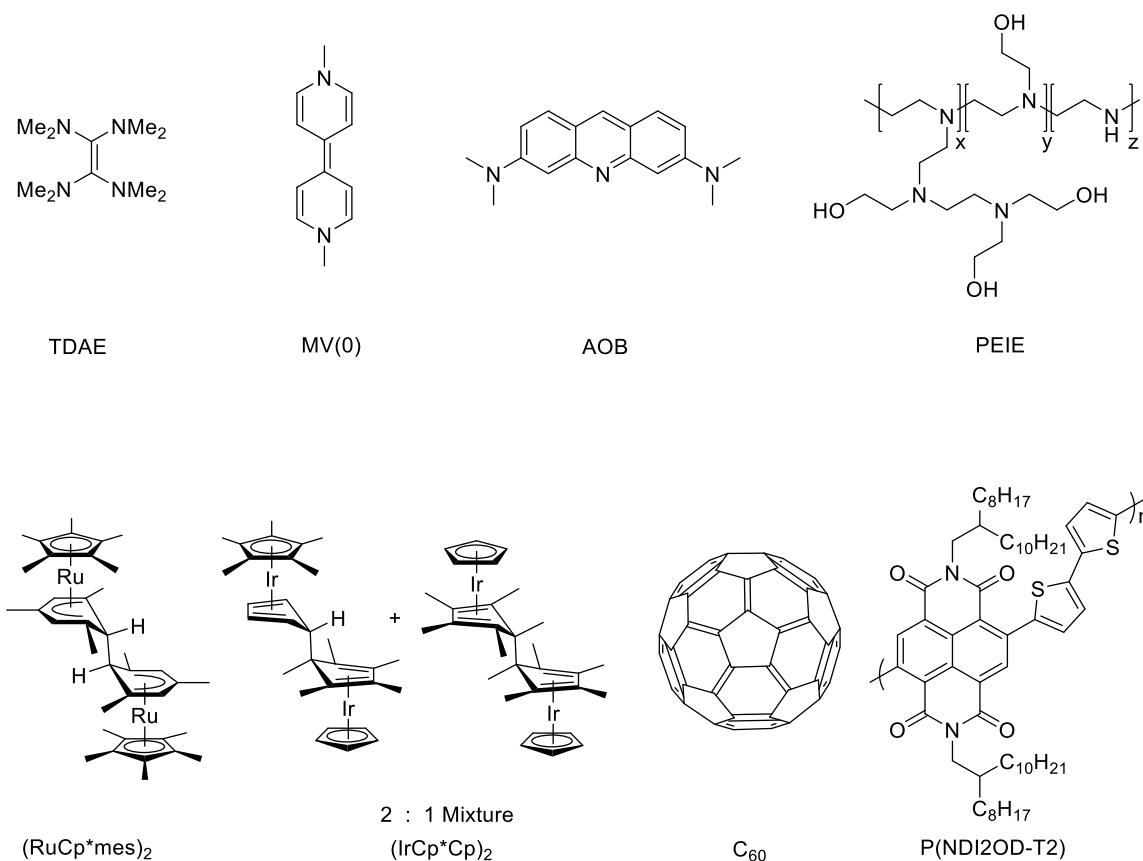


Figure 2.1 Chemical structure of molecular *n*-dopants and PEIE previously used to decrease the work function of metal oxides (center and left). Chemical structure of electron-transporting materials C₆₀ and P(NDI2OD-T2) (bottom right).

2.2 Stability of the Work Function Modification Induced by Organometallic Dopants

Effective work function modification methods need to be sufficiently robust to resist processing conditions commonly used in device fabrication: annealing and solvent washing

on top of the modified surface. For example, PEIE-modified ITO substrates do not experience any change in work function for temperature values lower than 190 °C, while PEI-modified ITO samples maintain their work function below 150 °C.⁶⁰ Moreover, PEIE-modified ITO surfaces experience work function changes of only 0.34 eV after being immersed in a glass beaker containing distilled water for 50 min, but the work function of the metal oxide recovers the pre-modification values after 50 min of exposure to ultrasonic bath in distilled water.⁶⁰ These observations are consistent with PEIE being physisorbed on ITO, and with the capability of the polymeric insulator to modify various conductors.

2.2.1 Stability of the Work Function Modification to Temperature

To investigate the thermal stability of the work function modification induced by redox-active dimers, ITO substrates were modified with $(\text{IrCp}^*\text{Cp})_2$ and $(\text{RuCp}^*\text{mes})_2$ and annealed for 10 min at different temperatures up to 150 °C in inert atmosphere. The work function values were measured at room temperature via Kelvin Probe in inert atmosphere. Only small variations ($|\Delta\text{WF}| < 0.25$ eV) were observed in the work function values of ITO treated with either $(\text{RuCp}^*\text{mes})_2$ or $(\text{IrCp}^*\text{Cp})_2$ in the temperature range explored, as shown in Figure 2.2.

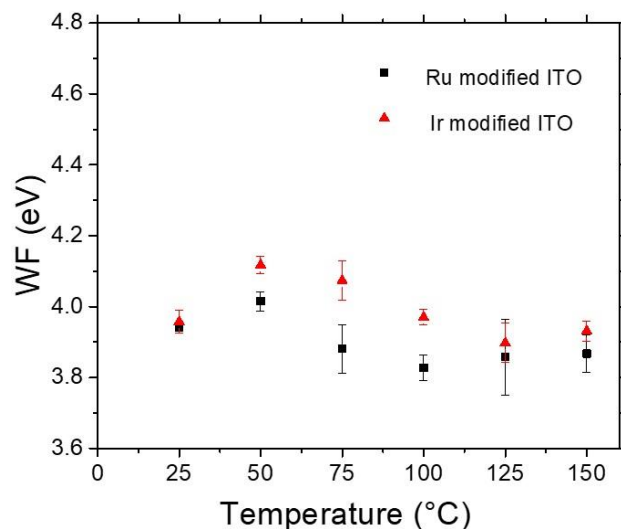


Figure 2.2 Stability of the dimer-induced work function reduction to thermal annealing. Each data point corresponds to two ITO substrates, and four spots per substrate were analyzed by Kelvin probe in inert atmosphere.

2.2.2 Stability of the Work Function Modification to Solvent Washing

Given that $(\text{RuCp}^*\text{mes})_2$ and $(\text{IrCp}^*\text{Cp})_2$ react with the metal oxide surface in a similar fashion (by transferring electrons to the surface and being oxidized to their monomer cations), and given their comparable thermal stability below 150 °C, stability to solvent washing was investigated solely for $(\text{IrCp}^*\text{Cp})_2$ -modified ITO. ITO surfaces were treated with dopant solution as detailed in section 2.6.1.2 and analysed in inert atmosphere as discussed in section 2.6.3. The work function modification of ITO using $(\text{IrCp}^*\text{Cp})_2$ is reasonably stable to solvent washing with toluene, chlorobenzene and *o*-dichlorobenzene, while the work function of modified ITO increases after spin-coating chloroform on it, as shown in Figure 2.3. To distinguish the effect of temperature and solvent washing, the substrates were not annealed after spin-coating, but solvent residues were removed with nitrogen. As expected, the work function of modified ITO increases when the metal oxide

is spin-coated with chloroform due to the presence of species such as water and hydrochloric acid in the solvent, and due to the reactivity of the solvent with the organometallic dimers³³ and with highly reducing species, such as low WF metal oxides.

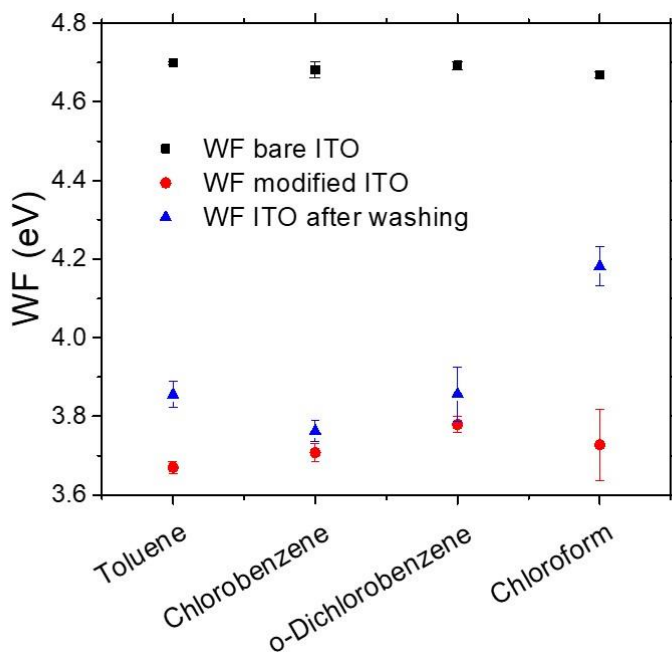


Figure 2.3 Stability of the dimer-induced work function reduction to solvent washing. Each data point corresponds to two ITO substrates, and four spots per substrate were analyzed by Kelvin probe in inert atmosphere.

2.3 Electrical Behavior of Surface-Modified ITO

Simple sandwich devices were fabricated to assess whether surface-modified ITO behaves as a low work function material and, therefore, as an electron-injecting electrode to an electron-transporting material (ETM) deposited via thermal evaporation in high vacuum (C_{60}) or via spin-coating from solution P(NDI2OD-T2). The two organic materials with high electron affinities (EA) equal to 4.0 eV for C_{60} ⁸⁷ and 3.9 eV for P(NDI2OD-T2),⁸⁸ were selected so that the barrier for electron injection estimated according to $\Delta E_{\text{inject}} = WF - EA$ is small. All devices were designed to be diodes, in other words to display a

preferential flow of current in a specific bias direction. The equation describing an ideal diode behavior is the following:

$$j = j_o(e^{\frac{qV}{nkT}} - 1), \quad (30)$$

where j_o is the reverse saturation current, V is the voltage, T is the temperature, k is the Boltzmann constant, q is the absolute value of the charge of an electron, and n is an ideality factor usually between 1 and 2. A layer of MoO_x was thermally evaporated on top of organic semiconductor to prevent the diffusion of atoms from the metal contact (Ag) into C_{60} or P(NDI2OD-T2) and reduce the leakage current, as well as favoring the collection of electrons from the semiconductor due to the high work function of MoO_x (WF = 5.5 eV). Each ITO substrate contained five devices, each with an effective area of ca. 0.1 cm^2 , but an average of three working devices per type (e.g., ITO/(RuCp*mes)⁺/C₆₀/MoO_x/Ag) of diode was obtained. The structure of the devices is schematically depicted below:

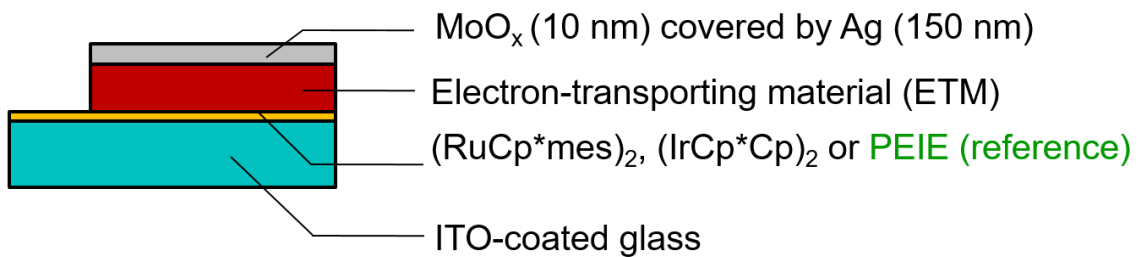


Figure 2.4 Side view of the structure of a diode manufactured to assess whether the reduction in the electrode work function induced by the n -dopants is retained upon deposition of an organic electron-transporting material.

2.3.1 Diode Fabrication with Vacuum-Deposited Organic Semiconductors

Figure 2.5 and Figure 2.6 show the current density-voltage ($J - V$) dark characteristics at room temperature of sandwich devices made of detergent/solvent-cleaned

(DSC) ITO (modified or unmodified)/C₆₀(100 nm)/MoO_x(10 nm)/Ag(150 nm). The $J - V$ curves can be understood in terms of the superimposition of diode and resistor electrical characteristics, the former describing electron injection and the latter leakage currents. As expected, the $J - V$ plot in the semi-logarithmic scale exhibit a diode behavior in forward bias for both modified and unmodified ITO substrates, Figure 2.5.

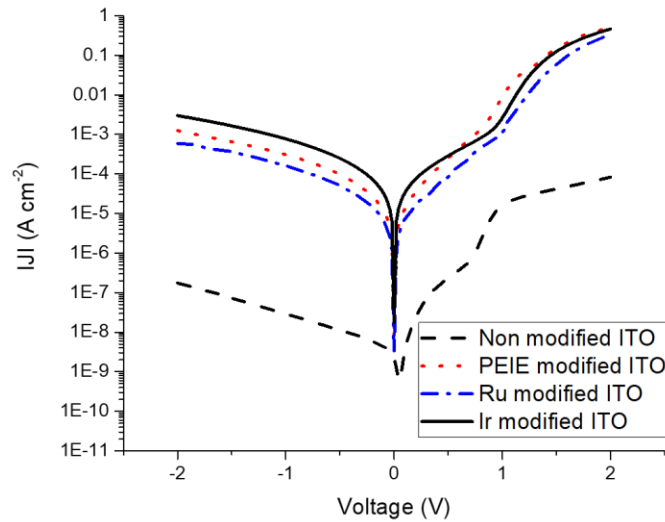


Figure 2.5 Semi-logarithmic plot of $J - V$ characteristics for devices with structure DSC-ITO (modified or unmodified)/C₆₀ (100 nm)/MoO_x (10 nm)/Ag (150 nm). Indium tin oxide acts as the electron-injecting electrode in forward bias.

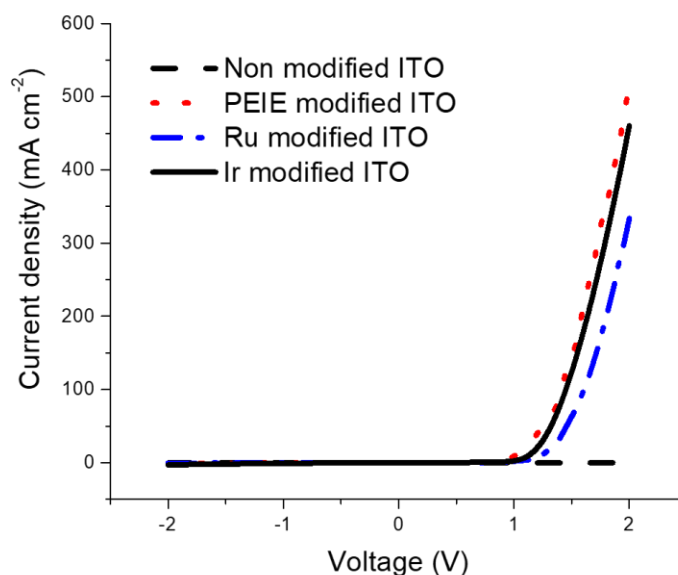


Figure 2.6 Linear plot of $J - V$ characteristics for devices with structure DSC-ITO (modified or unmodified)/ C_{60} (100 nm)/ MoO_x (10 nm)/Ag (150 nm). Indium tin oxide acts as the electron-injecting electrode in forward bias.

However, much higher current densities are measured when ITO is treated with the organometallic dimers compared to when the metal oxide surface is simply detergent/solvent-cleaned. Such difference in current injection suggests that the reduction in work function obtained via surface modification is retained upon deposition of the vacuum-deposited fullerene, and is indicative of the enhanced electron injecting behavior of the dimer-modified metal oxide in this architecture.

From Figure 2.5 and Figure 2.6 it is also evident that use of the dimers leads to similar electrical characteristics as are achieved using PEIE. The semi-logarithmic plot shows an increase of current density in reverse bias of several orders of magnitudes for diodes containing PEIE- or dimer-modified ITO relative to those containing pristine ITO. According to equation 30, for an ideal diode at large reverse bias ($V \ll 0$) the current density j is equal to $-j_o$. However, the current densities measured in reverse bias do not correspond

to the reverse saturation current of an ideal diode, j_0 , but to leakage currents. The observed increase in leakage currents could be related to different wetting conditions of the modified electrodes compared to unmodified ones and, therefore, to the morphology of the fullerene at the interface with ITO.

2.3.1.1 Stability of Diodes to Temperature

Diodes with a 100-nm thick layer of C_{60} were annealed at different temperatures and their dark $J - V$ characteristics were measured at room temperature, Figure 2.7 and Figure 2.8, to assess their thermal stabilities. Devices containing $(IrCp^*Cp)_2$ -modified ITO exhibit overlapping diode characteristics in forward bias, consistent with WF data in Figure 2.2, whereas current injection for devices made of PEIE-modified electrodes was observed at progressively lower voltages as the annealing temperature increased. Such decrease may be related to a possible interaction between PEIE and C_{60} .⁸⁹⁻⁹⁰ Devices containing $(RuCp^*mes)_2$ -modified electrodes stopped working after annealing at 50-75 °C.

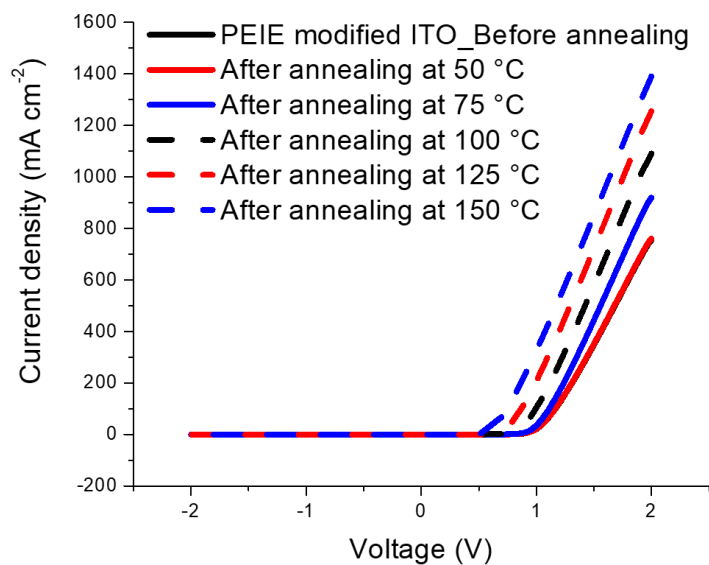


Figure 2.7 Current density – voltage characteristics of ITO/PEIE/C₆₀ (100 nm)/MoO_x (10 nm)/Ag (150 nm) devices annealed at different temperatures and measured at room temperature in the dark.

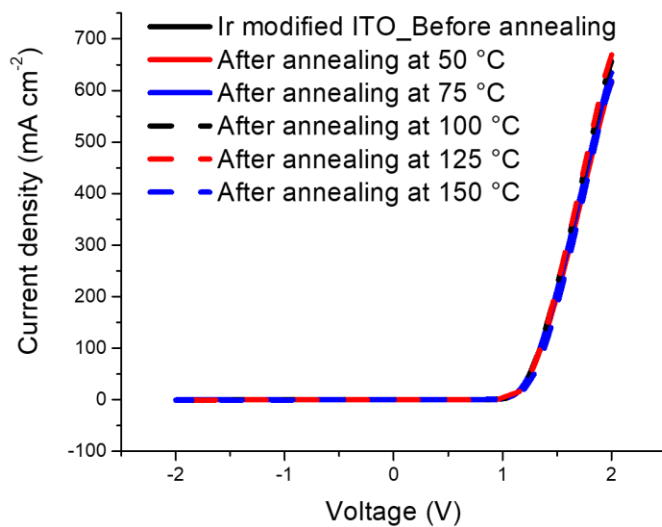


Figure 2.8 Current density – voltage characteristics of ITO/(IrCpCp*)+/C₆₀ (100 nm)/MoO_x (10 nm)/Ag (150 nm) devices annealed at different temperatures and measured at room temperature in the dark.

2.3.1.2 Stability of Diodes to Operation

Figure 2.9, Figure 2.10, Figure 2.11 and Figure 2.12 show the device-to-device variation for diodes with structures detergent/solvent-cleaned (DSC) ITO (modified or unmodified)/C₆₀ (200 nm)/MoO_x (10 nm)/Ag (150 nm). A higher average of working devices was obtained for this batch. While there is considerable variation of the leakage currents among devices, the diode currents dominating at forward biases of above 1 V are consistent and reproducible. These devices were repeatedly cycled between -2 V and +2 V and demonstrated to be stable to operation, as shown in Figure 2.13, Figure 2.14, Figure 2.15 and in Figure 2.16.

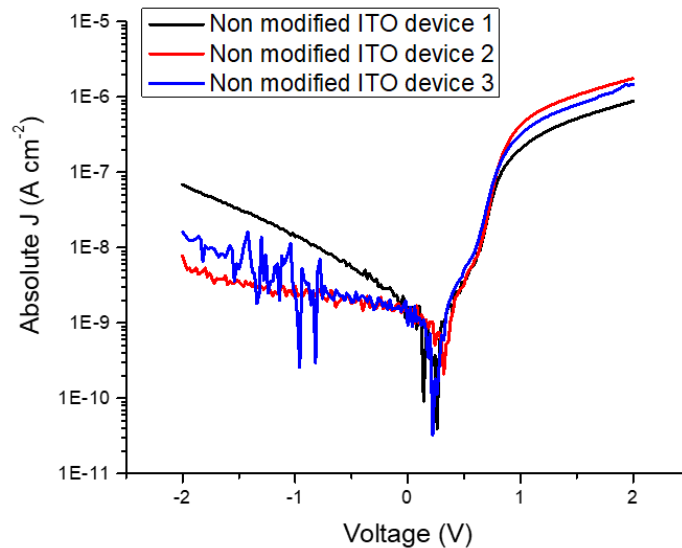


Figure 2.9 Semi-logarithmic plots of $J - V$ characteristics showing sample-to-sample variations for devices with structure DSC-cleaned ITO without modification/C₆₀ (200 nm)/MoO_x (10 nm)/Ag (150 nm). The ITO acts as the electron-injecting electrode under forward bias.

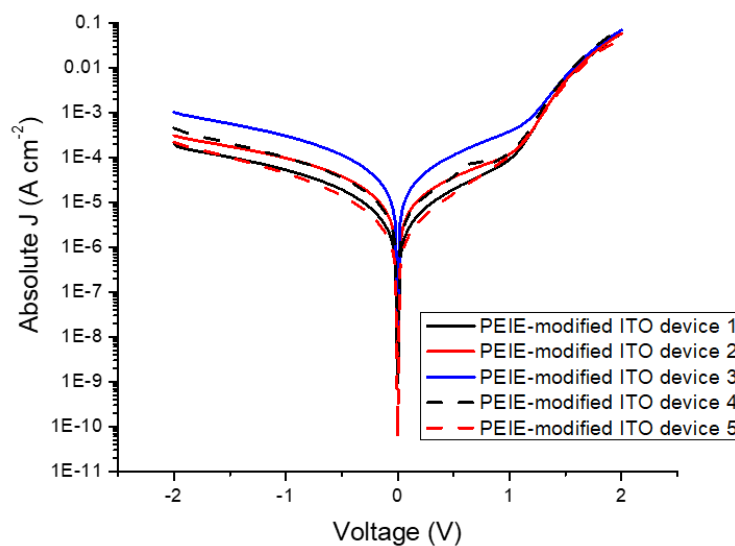


Figure 2.10 Semi-logarithmic plots of $J - V$ characteristics showing sample-to-sample variations for devices with structure DSC-cleaned ITO modified with PEIE/ C_{60} (200 nm)/ MoO_x (10 nm)/Ag (150 nm). The ITO acts as the electron-injecting electrode under forward bias.

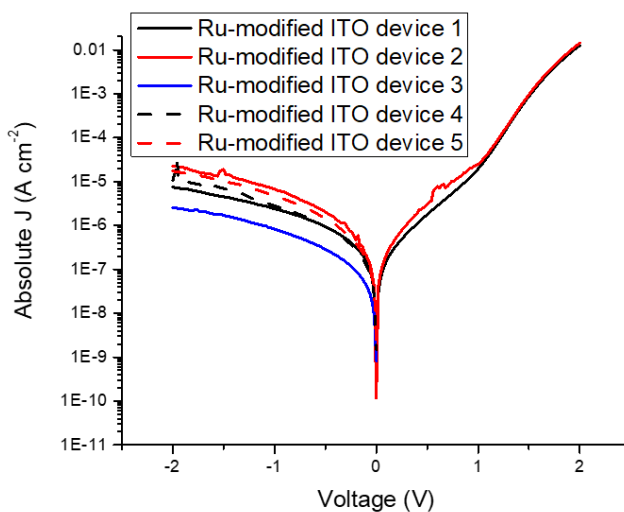


Figure 2.11 Semi-logarithmic plots of $J - V$ characteristics showing sample-to-sample variations for devices with structure DSC-cleaned ITO/ $(RuCp^*mes)^+/C_{60}$ (200 nm)/ MoO_x (10 nm)/Ag (150 nm). The ITO acts as the electron-injecting electrode under forward bias.

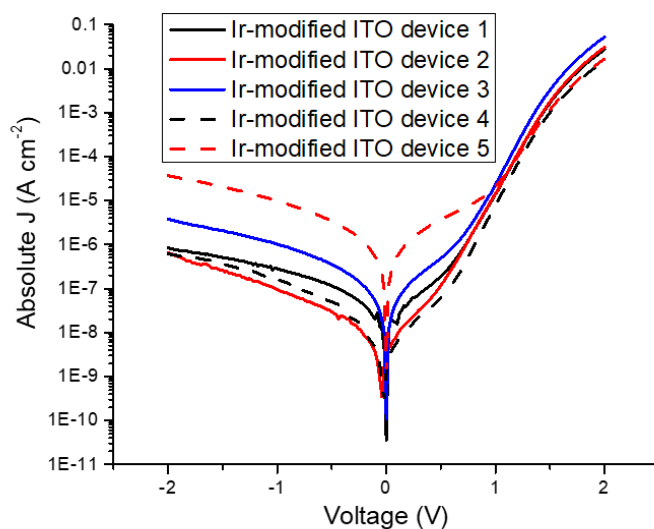


Figure 2.12 Semi-logarithmic plots of $J - V$ characteristics showing sample-to-sample variations for devices with structure DSC-cleaned ITO/(IrCp* Cp)⁺/C₆₀ (200 nm)/MoO_x (10 nm)/Ag (150 nm). The ITO acts as the electron-injecting electrode under forward bias.

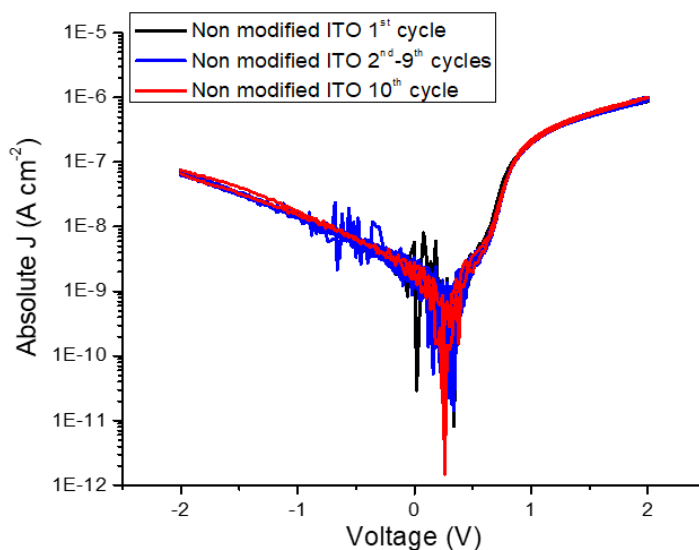


Figure 2.13 Semi-logarithmic plots of $J - V$ characteristics showing effects of repeated cycling between +2 and -2 V for devices with structure DSC-cleaned ITO without modification/C₆₀ (200 nm)/MoO_x (10 nm)/Ag (150 nm). The ITO acts as the electron-injecting electrode under forward bias.

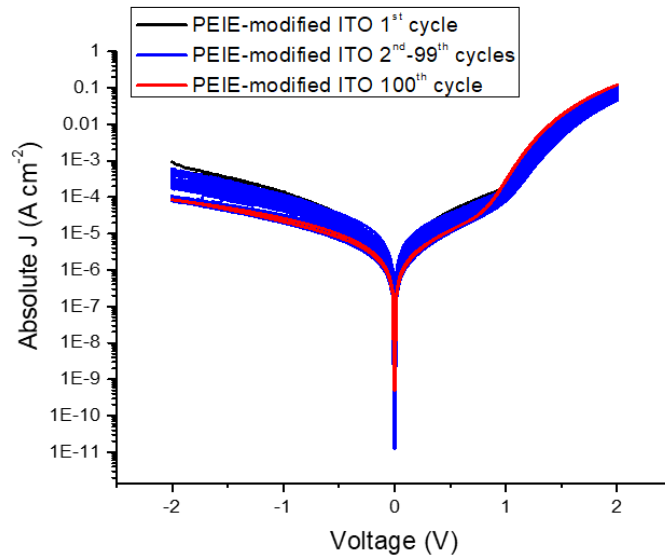


Figure 2.14 Semi-logarithmic plots of $J - V$ characteristics showing effects of repeated cycling between $+2$ and -2 V for devices with structure DSC-cleaned ITO modified with PEIE/ C_{60} (200 nm)/ MoO_x (10 nm)/Ag (150 nm). The ITO acts as the electron-injecting electrode under forward bias.

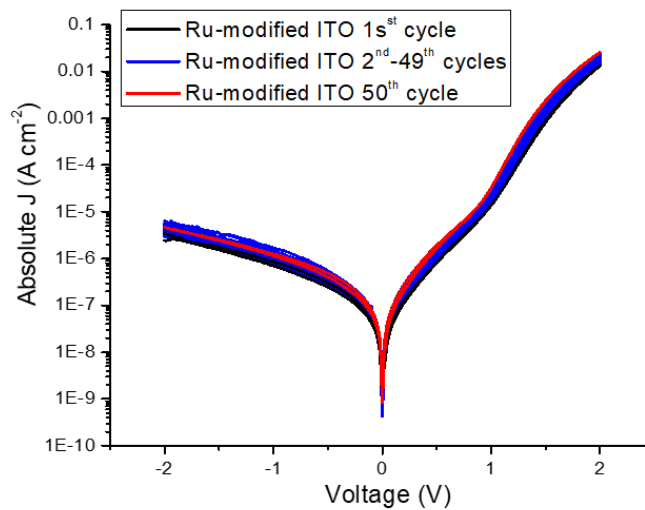


Figure 2.15 Semi-logarithmic plots of $J - V$ characteristics showing effects of repeated cycling between $+2$ and -2 V for devices with structure DSC-cleaned ITO/ $(RuCp^*mes)^+/C_{60}$ (200 nm)/ MoO_x (10 nm)/Ag (150 nm). The ITO acts as the electron-injecting electrode under forward bias.

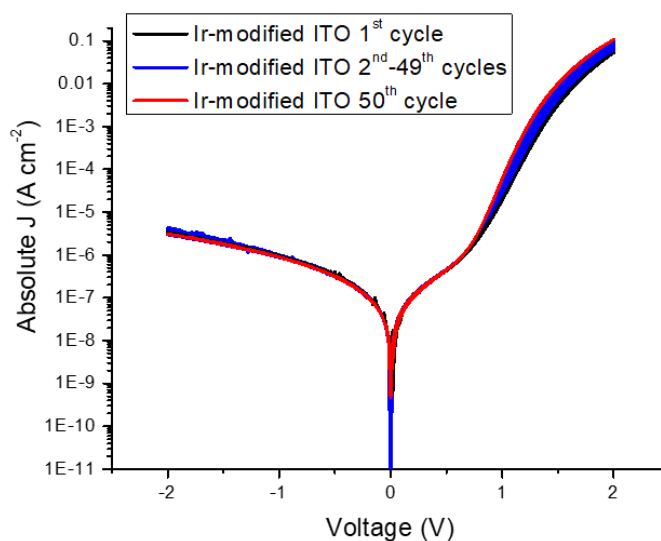


Figure 2.16 Semi-logarithmic plots of $J - V$ characteristics showing effects of repeated cycling between +2 and -2 V for devices with structure DSC-cleaned ITO/(IrCp* Cp)⁺/C₆₀ (200 nm)/MoO_x (10 nm)/Ag (150 nm). The ITO acts as the electron-injecting electrode under forward bias.

2.3.2 Diode Fabrication with Solution-Processed Organic Semiconductors

Instead of vacuum depositing C₆₀, an electron-transporting polymer P(NDI2OD-T2) was spin-coated on top of modified or unmodified ITO, and was covered with thermally evaporated MoO_x(10 nm) and Ag(150 nm). Modification of ITO with the dimers allowed for only slightly higher current density in forward bias ($J = 0.0012 \text{ mA cm}^{-2}$ for $V = 2 \text{ V}$) compared to devices with untreated ITO electrodes ($J = 0.0002 \text{ mA cm}^{-2}$ for $V = 2 \text{ V}$), Figure 2.17, which points towards post-modification work function values closer to those of unmodified ITO. Moreover, unlike for devices with vacuum-deposited C₆₀ as the electron-transport layer, a higher current injection was obtained when the ITO electrodes were modified with PEIE ($J = 22.5 \text{ mA cm}^{-2}$ for $V = 2\text{V}$) rather than with the dimers, Figure 2.18. It is possible that electron transfer occurred between the negatively charged

surface of modified ITO and the polymer, with subsequent monomer cation $(\text{RuCp}^*\text{mes})^+$ or $(\text{IrCpCp}^*)^+$ being lost with the negatively charged polymer chain during spin coating, as depicted in Figure 2.19.

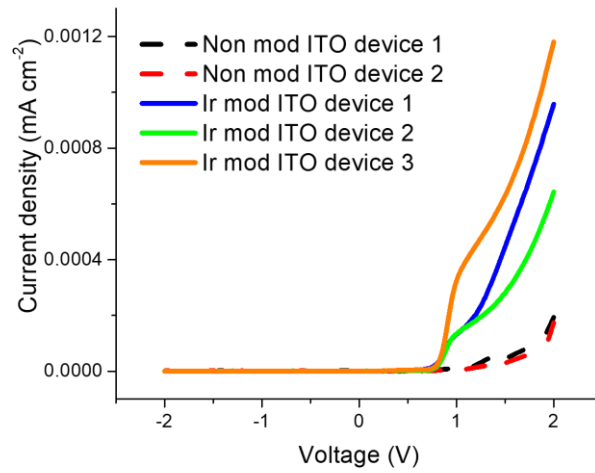


Figure 2.17 Linear plots of $J - V$ characteristics of devices with structure DSC-ITO (unmodified or $(\text{IrCp}^*\text{Cp})_2$ -modified)/P(NDI2OD-T2) (300 ± 10 nm)/ MoO_x (10 nm)/Ag (150 nm). ITO acts as the electron-injecting electrode in forward bias.

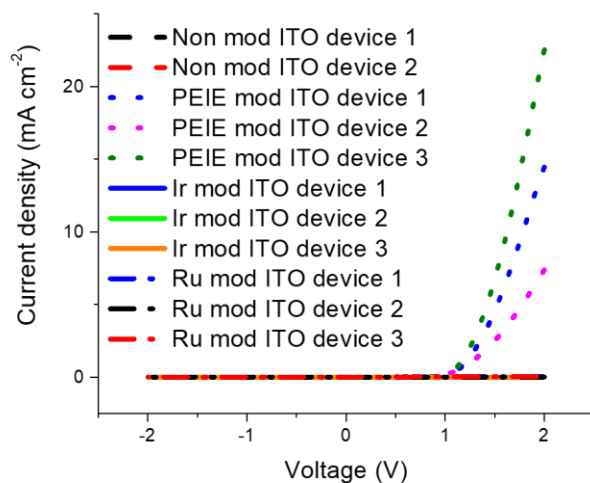


Figure 2.18 Linear plots of $J - V$ characteristics of devices with structure DSC-ITO (unmodified or modified)/P(NDI2OD-T2) (300 ± 10 nm)/ MoO_x (10 nm)/Ag (150 nm). ITO acts as the electron-injecting electrode in forward bias.

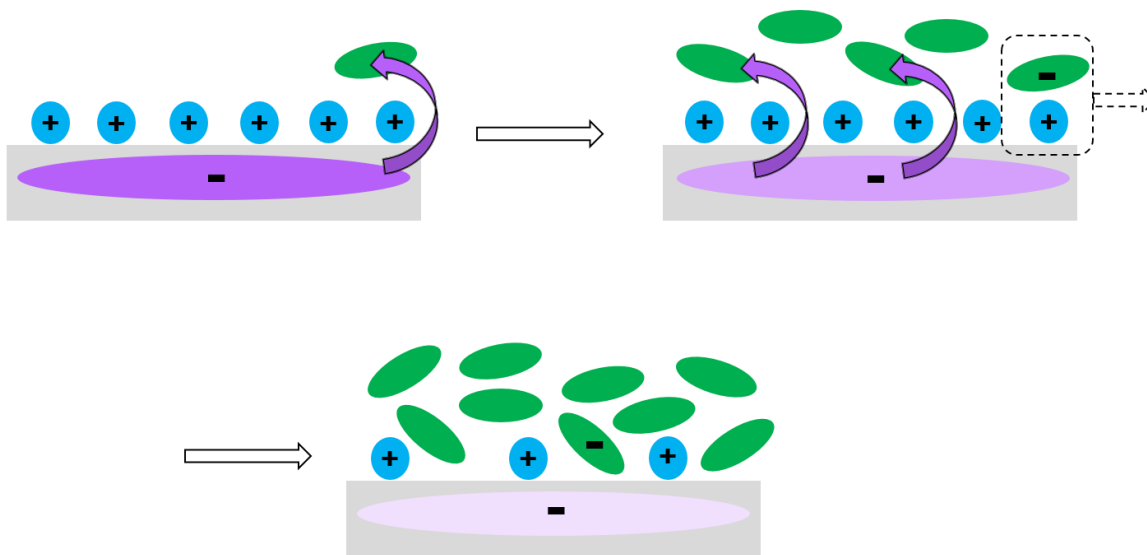


Figure 2.19 Graphical depiction of the electron transfer between the negatively charged surface of modified ITO and the solution-processed polymer P(NDI2OD-T2), with subsequent loss of monomer cations ($\text{RuCp}^*\text{mes}^+$ or IrCpCp^*) and of reduced polymer chains during spin coating. As a consequence, the surface of ITO is not as negatively charged as before spin-coating.

2.4 Phosphonic Acids to Prevent Dopant Washing During Solution Processing of Organic Semiconductors

Diodes with P(NDI2OD-T2) as the ETM indicated that PEIE-modified indium tin oxide works as a better electron-injecting electrode, showing current densities four orders of magnitude higher than dimer-modified ITO in forward bias ($V = 2V$). To further investigate how compatible the electrode surface treatment using dimers is with respect to solution processing of organic semiconductors, the metal oxide surface could be coated with phosphonic acids bearing a stable cation, such as an alkyl quaternary ammonium ion, counterbalanced by an anion. Trimethyl-(4-(phosphonomethyl)-phenylammonium iodide (TMPMPAI) was synthesized by the author, fully characterized and solution processed on ITO of varying degrees of roughness and on fluorinated tin oxide (FTO). Condensation and formation of monolayers of the phosphonic acid on the metal oxide surface were promoted by vacuum annealing for two hours at 140 °C. The metal oxide surface was then treated with $(RhCp^*Cp)_2$ which has a similar reducing strength to $(IrCp^*Cp)_2$ and $(RuCp^*mes)_2$; it was expected that electron transfer from the dimer to the metal oxide surface could take place, and that the monomer cation could be washed away with the iodide from the cationic phosphonic acid during spin-coating. Ultraviolet photoelectron spectroscopy (UPS) and Kelvin probe (KP) data shows an increase in work function upon depositing the phosphonic acid on ITO and FTO, as shown in Figure 2.20. UPS and KP data also shows large WF reductions after treating the phosphonic acid-covered metal oxides surface with $(RhCp^*Cp)_2$, in agreement with electron transfer from the dimer to ITO and FTO. However, x-ray photoelectron spectroscopy (XPS) indicate the absence of iodide on the surface before treatment with $(RhCp^*Cp)_2$. It is possible that during vacuum-

annealing TMPMPAI decomposed into methyl iodide and dimethylaminophosphonic acid, as shown in Figure 2.21. The XPS N1s scans show the presence of two nitrogen species, one at high binding energy (E_B) which could correspond to a cationic species, and one at low E_B which could be associated with the neutral phosphonic acid.

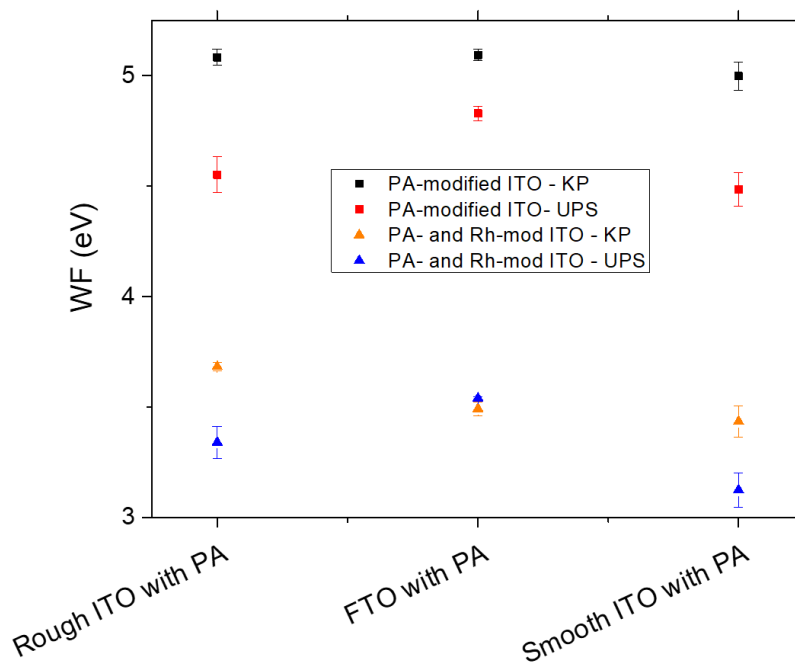


Figure 2.20 Work function modification of ITO and FTO of varying degrees of roughness using trimethyl-(4-(phosphonomethyl)-phenylammonium iodide and $(\text{RhCp}^*\text{Cp})_2$.

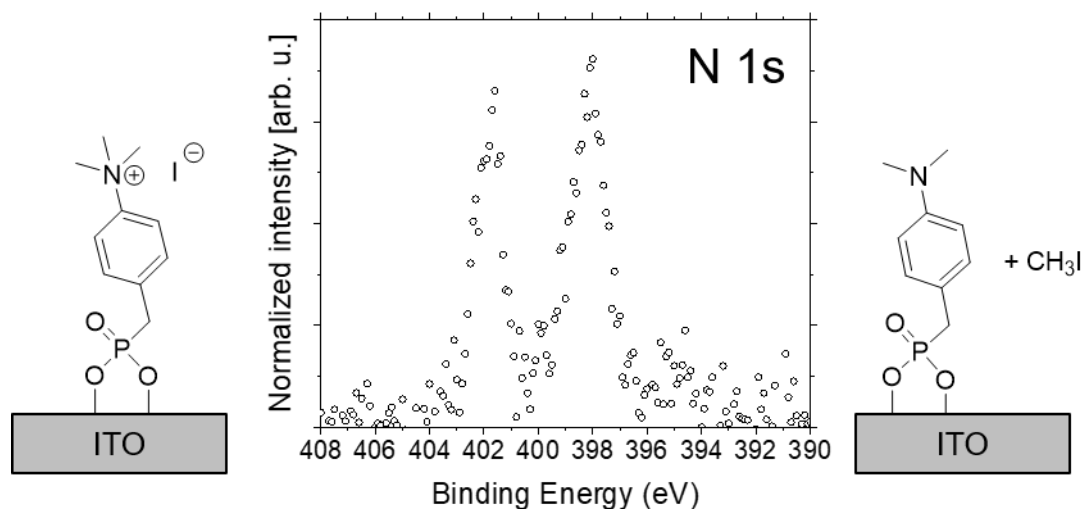


Figure 2.21 XPS N 1s scans of ITO modified with trimethyl-(4-(phosphonomethyl)-phenylammonium iodide and (RhCp* Cp)₂. Possible structure associated with the species

2.5 Conclusions

Chapter 2 demonstrated that the work function modification (> 1 eV) induced by treatment of ITO with the organometallic dimers (RuCp*mes)₂ and (IrCp*Cp)₂ is reasonably stable to annealing and solvent-washing with solvents commonly used in device fabrication, with the exception of chloroform, which tends to contain H₂O and HCl as impurities and even when dry and pure is more reactive with reductants than most solvents. For example, water could facilitate oxidation of the dimer-modified ITO via photoinduced electron transfer. The molecular *n*-dopants can be used to treat the surface of ITO and make the metal oxide behave as a low-WF electrode in simple diodes. Using these dimers to modify ITO results in similar electrical effects to using PEIE in diodes containing vacuum-deposited C₆₀ as an electron-transporting material. However, when similar diodes are fabricated by spin-coating an organic semiconductor of similar electron affinity to C₆₀, i.e. P(NDI2OD-T2), on top of dimer-modified ITO, the latter does not show similar electrical

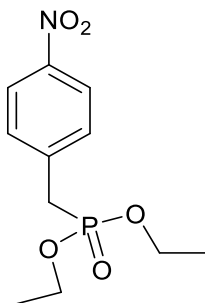
effects to using PEIE. Therefore, it seems reasonable to assume that an electron transfer could take place from the reduced ITO surface to the solution-processed semiconductor, which was washed away with monomer cations, resulting in a smaller WF reduction of the metal oxide and poor-electron injection in diodes with P(NDI2OD-T2). To tackle this issue a phosphonic acid with a cationic moiety, trimethyl-(4-(phosphonomethyl)-phenylammonium iodide, was synthesized and fully characterized. However, XPS data suggests loss of methyl iodide during processing of the compound on metal oxides. Future investigations could explore the potential of other processing routes of cationic phosphonic acids (sonication vs. vacuum annealing) and the impact of the phosphonic acid-assisted dimer-modification on electron injection in P(NDI2OD-T2)-containing diodes.

2.6 Experimental

2.6.1 Materials

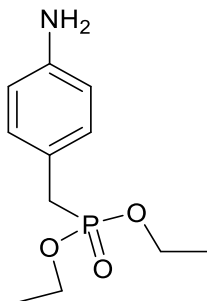
ITO-coated glass with an average sheet resistance of 15 Ω /sq was purchased from Colorado Concept Coatings LLC, Loveland, CO. A 35-40 wt% solution of PEIE (80% ethoxylated, $M_w = 70\,000\text{ g mol}^{-1}$) in water was purchased from Sigma-Aldrich and was further diluted with 2-methoxyethanol to a final concentration of 0.4 wt%. $(\text{IrCp}^*\text{Cp})_2$ and $(\text{RuCp}^*\text{mes})_2$ were synthesized according to previous reports.⁹¹⁻⁹²

2.6.1.1 Diethyl 4-nitrobenzylphosphonate⁹³



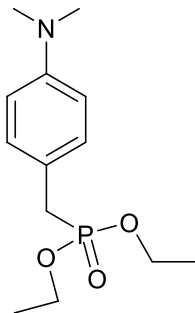
Triethyl phosphite (46.2 g, 278 mmol) was added to 1-(bromomethyl)-4-nitrobenzene (20.0 g, 92.6 mmol) in a 250 mL three-necked round-bottomed flask under inert atmosphere. The mixture was stirred and kept under nitrogen flow for 30 min prior to heating. The mixture was heated and refluxed at 130 °C (bath temperature) for 8 h. Once cooled down to room temperature, the crude product was dissolved in ethyl acetate and purified, first using a silica plug to remove excess triethyl phosphite. HCl (1 M aqueous solution) was added, and the product was extracted in dichloromethane to remove the impurity (4-diethylamino benzylphosphonate) and to yield a brown oil (2.83 g, 45%).⁹⁴ The ¹H NMR shifts were consistent with the literature.⁹³

2.6.1.2 Diethyl 4-aminobenzylphosphonate⁹³



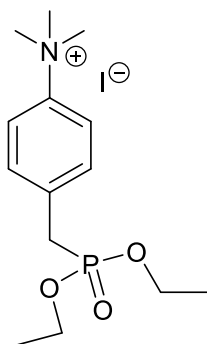
Diethyl 4-nitrobenzylphosphonate (2.83 g, 10.4 mmol) was dissolved in excess ethanol (90 mL, 1600 mmol) at room temperature. To the stirring solution, tin (II) chloride dihydrate (11.7 g, 51.8 mmol) was added in portions followed by the addition of concentrated aqueous HCl (3.8 g, 100 mmol). The reaction mixture was heated at reflux for 2 h, and cooled down to room temperature. The pH of the mixture was adjusted to 8-9 with the addition of NaOH solution (200 mL of a 1 M aqueous solution). The product was extracted in CH₂Cl₂ from the aqueous solution. The combined organic washings were combined, washed with water and brine, and dried over sodium sulfate. The solvent was removed under reduced pressure and the crude was purified by column chromatography in ethyl acetate to yield a pale orange-pink solid (2.17g, 77%). All glassware was washed with a KF solution after the reaction was completed to remove organo-tin residues. The ¹H NMR shifts were consistent with the literature.⁹³

2.6.1.3 Diethyl 4-(dimethylamino)benzylphosphonate⁹³



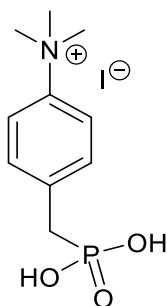
Solutions of diethyl 4-aminobenzylphosphonate (1.5 g, 6.2 mmol) and NaBH₄ (1.4 g, 37.2 mmol) were prepared in dry THF (24 mL) along with a solution of formaldehyde (37% in water, 1.9 mL) and 3 M H₂SO₄ (0.8 mL) in THF (24 mL). Half of the solution containing diethyl 4-aminobenzylphosphonate/NaBH₄ was added to the solution of formaldehyde/ H₂SO₄/THF. More 3 M H₂SO₄ solution (0.8 mL) was carefully added to the reaction mixture, followed by the addition of the other half of amine/NaBH₄ solution. The reaction mixture was stirred for 30 min at room temperature, and was then diluted with water (10 mL) and 1 M NaOH (20 mL). The aqueous layer was washed with diethyl ether, and the combined organic layers were washed with brine, dried over sodium sulfate, and filtered. Volatiles were removed under reduced pressure, and the product was purified by column chromatography in ethyl acetate to yield a yellow oil (0.94 g, 57%). ¹H NMR shifts were consistent with the literature.⁹³

2.6.1.4 Trimethyl-4-(diethylphosphonomethyl)phenylammonium iodide



To a solution of diethyl 4-(dimethylamino)benzyl phosphonate (0.3 g, 1.2 mmol) in nitromethane (6.5 mL), iodomethane (1.1 g, 8.0 mmol) was added. The obtained solution was stirred at room temperature for 60 h and then volatiles were removed under reduced pressure. The organic residue was washed with diethyl ether (3 x 10 mL) and then recrystallized from acetone and ether to give the product as crystals (0.3 g, 68%). ^1H NMR (300 MHz, CDCl_3): δ 7.96 (d, $J_{\text{H-H}} = 9$ Hz, 2H), 7.54 (dd, $J_{\text{H-H}} = 9, 3$ Hz, 2H), 4.08 (m, 4H), 4.01 (s, 9H), 3.20 (d, $J_{\text{H-P}} = 21$ Hz, 2H), 1.30 (t, $J_{\text{H-H}} = 6$ Hz, 6H). $^{13}\text{C}(^1\text{H})$ NMR (100.62 MHz, dimethyl sulfoxide- d_6): δ 145.65, 134.93 (d, $J_{\text{C-P}} = 8$ Hz), 131.03, 120.26, 61.50 (d, $J_{\text{C-P}} = 6$ Hz), 56.38, 31.28 (d, $J_{\text{C-P}} = 135$ Hz), 16.23 (d, $J_{\text{C-P}} = 5$ Hz). $^{31}\text{P}(^1\text{H})$ NMR (202.51 MHz, D_2O): δ 29.58. Anal. Calcd. for $\text{C}_{14}\text{H}_{25}\text{NO}_3\text{PI}$: C, 40.69; H, 6.10; N, 3.39; found C, 40.40; H, 6.08; N, 3.33. MS (ESI) m/z 271.2 ($\text{C}_{13}\text{H}_{22}\text{NO}_3\text{P}$).

2.6.1.5 Trimethyl-4-(phosphonomethyl)-phenylammonium iodide



Trimethyl-4-(diethylphosphonomethyl)phenylammonium iodide (0.2 g, 0.5 mmol) was added to dry carbon tetrachloride (0.8 g, 5 mmol) under nitrogen in a round-bottomed flask with external cooling. The mixture was stirred and iodotrimethylsilane (0.2 g, 1.1 mmol) was added dropwise using a glass syringe and steel hypodermic needle to maintain the temperature between 0-10 °C. The reaction mixture was evaporated under reduced pressure and the brown organic residue was treated with water (1 mL) to yield a crystalline solid (0.12 g, 69%). ¹H NMR (500 MHz, D₂O): δ 7.74 (d, *J*_{H-H} = 10 Hz, 2H), 7.51 (d, *J*_{H-H} = 10 Hz, 2H), 3.62 (s, 9H), 3.14 (d, *J*_{H-H} = 20 Hz, 2H). –OH resonances not observed. ¹³C(¹H) NMR (125.79 MHz, dimethyl sulfoxide-d₆): δ 146.53, 138.66, 132.83 (d, *J*_{C-P} = 6 Hz), 121.21 (d, *J*_{C-P} = 2.5 Hz), 58.47, 36.24 (d, *J*_{C-P} = 128 Hz). ³¹P(¹H) NMR (202.51 MHz, D₂O): δ 20.90. Anal. Calcd. for C₁₀H₁₇NO₃P(I)_{0.85}(I₃)_{0.15}: C, 30.39; H, 4.34; N, 3.54; I, 41.75; found C, 30.03; H, 4.57; N, 3.44, I, 41.50. MS (ESI) *m/z* 230.1 (C₁₀H₁₇NO₃P⁺), *m/z* 126.6 (I).

2.6.2 *Sample Preparation*

ITO substrates were scrubbed and then cleaned in sequential 20 min ultrasonic baths of detergent water, deionized (DI) water, acetone, and isopropanol at room

temperature. The substrates were then rinsed with isopropanol and dried off with nitrogen. The non-modified ITO substrates were then immediately used.

Detergent/solvent-cleaned (DSC) substrates were transferred to a nitrogen-filled glovebox (<0.1 ppm water and <0.5 ppm oxygen) and were treated with 2 mM solutions of $(\text{IrCp}^*\text{Cp})_2$ or $(\text{RuCp}^*\text{mes})_2$ in anhydrous and deoxygenated toluene for 1 min. The substrates were rinsed three times with toluene, dried with a flow of nitrogen, and immediately transferred under inert atmosphere to the glovebox containing the Kelvin Probe or to a vacuum thermal evaporation system for device fabrication.

Dimer-modified ITO substrates that were used for studies on the work function modification stability to solvent washing were transferred under inert atmosphere to a glovebox housing a spin-coater. 0.5 mL of toluene, chlorobenzene, *o*-dichlorobenzene, or chloroform were spin-coated on the modified-ITO samples at a speed of 800 rpm for 30 s and at an acceleration of 10000 rpm s⁻¹. Toluene and chlorobenzene were dried via distillation from calcium hydride and degassed via freeze-pump thawing. *o*-Dichlorobenzene and chloroform were obtained from nominally anhydrous bottles stored in a glove box.

2.6.3 *Surface Characterization*

Kelvin Probe analysis (Besocke Delta Phi) was performed in inert atmosphere, using a probe diameter of 3 mm. Highly ordered pyrolytic graphite (HOPG) was cleaved by using Scotch tape and its work function (4.6 eV) was measured at the beginning of each set of measurements and after analysing 2 samples. Measuring the work function of HOPG allows to account for instrumental drift. Four data points were collected for each ITO

substrate (2.54 cm × 2.54 cm) before and after modification, and average values and standard deviations were calculated.

2.6.4 Diode Fabrication

The ITO substrates were partially covered with Kapton tape and etched by exposure to a solution of aqua regia (3:1 concentrated hydrochloric acid/concentrated nitric acid) for 10 min at 80 °C. ITO on glass was cut into 2.54 cm × 2.54 cm substrates, which were subjected to sequential ultrasonic cleaning in detergent water, DI water, acetone, and isopropanol. Each ultrasonic bath lasted for 20 min at 45 °C. The PEIE solution (0.4 wt%) was spin-coated on top of the ITO substrates at a speed of 5000 rpm for 60 s and an acceleration of 1000 rpm s⁻¹; the spin-coated samples then were annealed at 100 °C for 10 min in air (the effective thickness of these PEIE layers has previously been found to be ca. 10 nm using spectroscopic ellipsometry).⁶⁰ Dimer modifications were carried out in the glovebox as described in section 2.6.1.2 and transferred to a vacuum thermal evaporation system (SPECTROS, K. J. Lesker). C₆₀ (100-200 nm), MoO_x (10 nm), and Ag (150 nm) were deposited sequentially through a shadow mask at a base pressure of 2 × 10⁻⁷ Torr on the unmodified, PEIE modified, or dimer-modified ITO substrates. In lieu of C₆₀, an electron-transporting polymer P(NDI2OD-T2) (M_w = 740 kg mol⁻¹, PDI = 4.3) was spin-coated on top of modified or unmodified ITO from a 20 mg/mL solution in anhydrous and oxygen-free toluene for 60 s, at a speed of 500 rpm and at an acceleration of 500 rpm/s. After annealing at 125 °C for 10 min, a 300 ± 10 nm thick polymer layer was obtained and covered with thermally evaporated MoO_x (10 nm) and Ag (150 nm), similarly to C₆₀-containing devices. The effective area of the diodes was 11.2 mm². Current density-voltage

($J - V$) curves were measured in a nitrogen-filled glovebox by using a source meter (2400 SourceMeter, Keithley Instruments Cleveland, OH) controlled by a LabVIEW program.

CHAPTER 3. MODIFICATION OF THE FLUORINATED TIN OXIDE/ELECTRON/TRANSPORTING MATERIAL INTERFACE IN PEROVSKITE SOLAR CELLS

3.1 Introduction

Perovskite solar cells (PSCs) are a promising photovoltaic technology, since the band gap of the light-absorbing perovskite can be easily modified by changing its composition,^{16, 95-97} and since solar cells efficiently converting absorbed light into electricity can be obtained through a variety of fabrication routes,¹⁴⁻¹⁵ at potentially low manufacturing costs.⁹⁸ The most efficient solar cells to date are fabricated in the *n-i-p* configuration, where the insoluble electron-transporting material (ETM) or *n*-layer, mesoporous titanium dioxide (*m*-TiO₂), is deposited on top of the transparent conductive oxide, fluorinated tin oxide (FTO), which lets sunlight shine towards the perovskite, processed on top of the ETM.⁹⁹ However, *m*-TiO₂ is unstable to UV-light exposure. and devices built on mesoporous titanium dioxide tend to show hysteretic behavior.¹⁰⁰ Moreover, deposition of *m*-TiO₂ requires calcination temperatures up to 500 °C, which are not compatible with flexible substrates and fabrication of tandem solar cells.¹⁰¹⁻¹⁰³ Replacing *m*-TiO₂ with fullerene derivatives, solution-processed at T < 120 °C or vacuum-deposited,¹⁰⁴⁻¹⁰⁵ leads to solar cells that are more stable to long-term illumination and exhibit a less pronounced hysteretic behavior. This can be attributed to efficient electron extraction from the perovskite to the fullerene layer.

Fullerene-based molecules do not induce a large density of defects at the perovskite/ETM interface, which would otherwise cause charge recombination.^{81, 106-108}

These findings further encouraged the investigation of other ETMs for PSCs based on reasonably conductive organic semiconductors with acceptable absorption for good transparency, and suitable energy levels for efficient electron extraction and cathode optimization.¹⁰⁹⁻¹¹¹ Among organic semiconductors perylene diimides (PDIs) and their derivatives are compounds of interest given their similar electron affinities to fullerenes, their processability through a variety of fabrication methods, and their mobilities, which are often of $10^{-3} \text{ cm}^2 \text{ V}^{-1} \text{ s}^{-1}$ or more.¹¹² By tuning the molecular structure of PDIs, it is possible to obtain inexpensive materials that are insoluble and sufficiently resistant to thermal stresses to be employed as pigments in car paint.¹¹³⁻¹¹⁴ PDIs were used in perovskite solar cells as hole-blocking layers in conjunction with fullerenes,¹¹⁵⁻¹¹⁷ as passivation layers on the surface of TiO_2 ,¹¹⁸ and as solution-processed ETMs,¹¹⁹ reaching power conversion efficiencies (PCEs) as high as 17.7%.¹²⁰ At the time of writing, *n-i-p* PSCs with vacuum-deposited perylene-based electron-transporting materials still lag behind in device performance (7.9%)¹²¹ compared to their solution-processed equivalents.¹²⁰

A potential strategy to obtain highly efficient PSCs fabricated on vacuum-deposited ETM is to improve charge collection, which depends on the electronic energy-level alignment at the interface between the electrode and the organic semiconductor once they are in contact. If the Fermi level (E_F) at the FTO/ETM interface does not end up being close to the lowest unoccupied molecular orbital (LUMO) of the ETM, substantial recombination could take place, given the large hole and electron densities close to the electrode. Therefore, the energy offset between the electron affinity (EA) of C_{60} or PDIs (3.9 – 4.0 eV)⁸⁷ and the work function (WF) of the FTO (4.6 eV) is potentially detrimental

to charge collection. To adjust energy alignment at the electrode interface/organic layer it is possible to pin the E_F of the electrode to the LUMO of the organic ETM by introducing interlayers, thus minimizing losses due to inadequate electron collection.⁶⁰ Depending on the interlayer, the molecules of ETM near the interface can be *n*-doped through an electron transfer, from the electrode or from the interlayer itself, to the ETM. Such interlayers can be introduced by treating the electrode with a strong reductant that creates a dipole by electron transfer to the electrode.⁶¹⁻⁶² As shown in chapter 2, dimers of nineteen-electron organometallic sandwich compounds are one class of reductants that have been used in this context, leading to a reduction of the WF of metals and metal oxides by more than 1 eV.^{40, 122} These organometallic dimers are also molecular *n*-dopants for organic semiconductors with EAs as low as 2.8 – 3.0 eV.³⁴ In both cases, these sandwich compounds can be processed from both solution and vacuum, and are moderately air-stable.

In this chapter a vacuum-deposited essentially insoluble PDI derivative, perylene-3,4:9,10-tetracarboxylic bis(benzimidazole) (PTCBI, Figure 3.1) – the condensation product of *o*-phenylene diamine and perylene-3,4:9,10-tetracarboxylic dianhydride – is compared to C₆₀ (Figure 3.1) as an ETM in *n-i-p* perovskite solar cells. Moreover, this chapter explores the use of one of the above mentioned dimers – pentamethylcyclopentadienyl cyclopentadienyl rhodium dimer (RhCp*₂)₂ (**12**, Figure 3.1) – as an interlayer between FTO and PTCBI to minimize electron-collection losses at the electron-selective contact. C₆₀ was adopted as a reference ETM, and changes in the electronic alignment (e.g., electrode WF and EA of organic semiconductor) were correlated with device performance characteristics. The results of this work have recently been published in *Molecular Systems Design and Engineering*, 2018, **3**, 741-747.¹²³ The

ultraviolet photoelectron and photoemission spectroscopy data were collected and analyzed in collaboration with Berthold Wegner from the Humboldt University of Berlin, Germany.

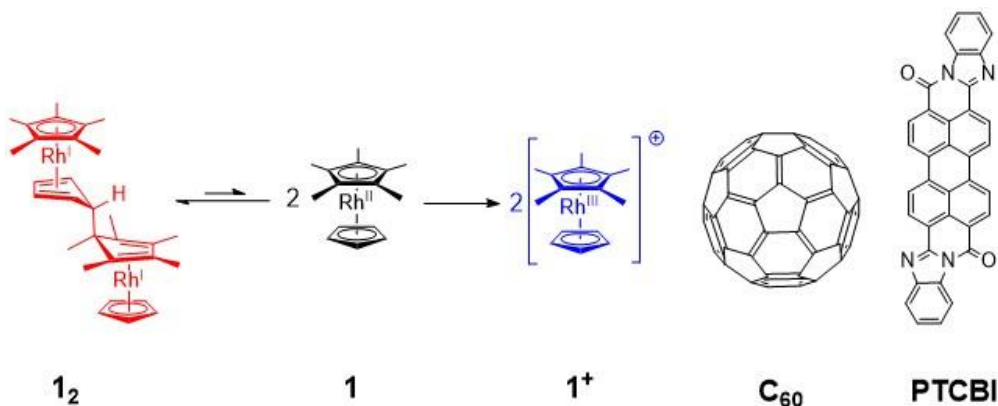


Figure 3.1 Molecular structures of the neutral dimeric dopant (1_2), neutral monomer (1), cationic monomer (1^+), and of the ETMs C₆₀ and PTCBI.

3.2 Surface Modification of FTO using Vacuum-Deposited (RhCp*₂Cp)₂

Layers of 1_2 of increasing thickness were vacuum-deposited on FTO, leading to a reduction of the metal oxide WF from 4.6 eV after piranha-cleaning to 3.3 eV when 10 nm of 1_2 are deposited, as shown by ultraviolet photoelectron spectroscopy (UPS) in Figure 3.2 (a). Upon modification of FTO with 1_2 , the secondary electron cut-off (SECO) of FTO shifts by up to 1.2 eV and the E_F position moves away from the valence band onset of the electrode by up to 0.4 eV. These observations suggest that the WF reduction is associated with the formation of an interface dipole at the FTO surface, and with electron transfer from the dopant to the electrode as seen for dimer-modified ITO in chapter 2.¹²² The shift in the valence band onset (VB_{onset}) relative to the Fermi level suggests that to a certain extent band bending is taking place. The x-ray photoelectron spectroscopy (XPS) spectra of dimer-modified FTO (Figure 3.2 and Figure 3.3) are consistent with this, showing a

Rh^{III} 3d species at 312.1 – 312.2 eV, which corresponds to the monomer cations 1⁺ formed when electrons are donated to the FTO (see further discussion of XPS core shifts in section 3.4.1).¹²² However, XPS reveals most of Rh 3d signal is associated with a Rh^I species at 310.8 – 310.9 eV, which corresponds to unreacted dimer 1₂. The ratio between Rh^{III} and Rh^I species increases slightly as more dopant is deposited on FTO, as shown in Table 3.2

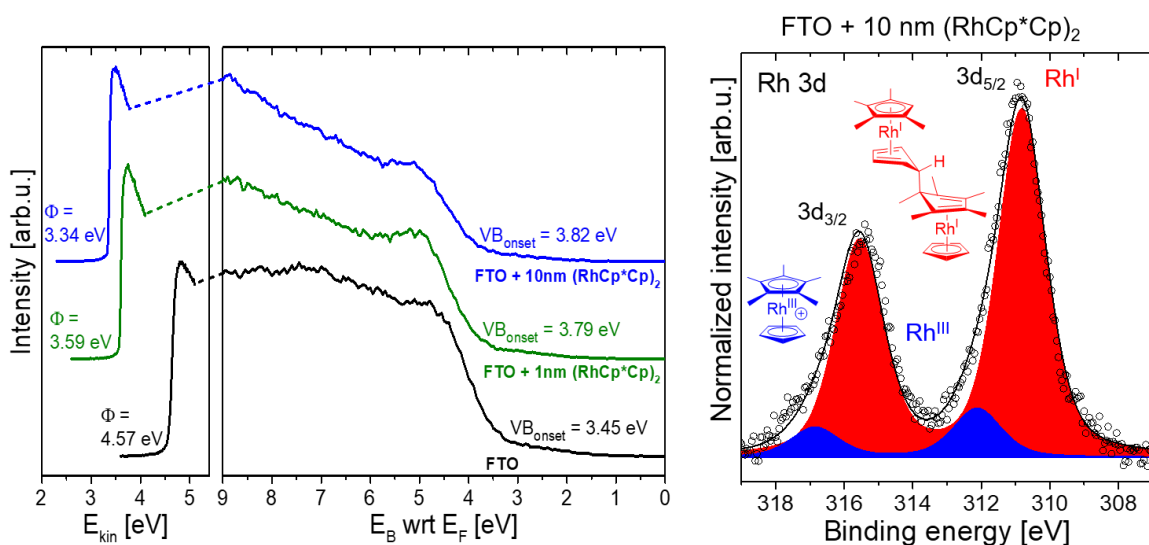


Figure 3.2 UPS spectra of piranha-cleaned FTO and FTO modified with layers of (RhCp*Cp)₂ (E_{kin} = kinetic energy; E_B = binding energy with respect to the Fermi level, E_F) (left). (b) XPS spectrum of FTO modified with a 10 nm-thick layer of (RhCp*Cp)₂ (right).

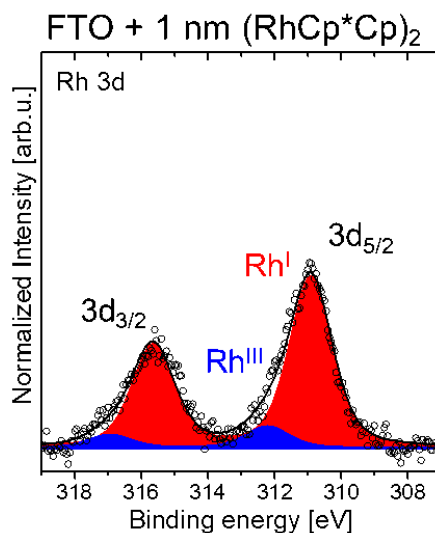


Figure 3.3 XPS spectrum of modified FTO with a 1 nm-thick layer of (RhCp* Cp)₂.

Table 3.1 XPS positions and peak ratios for (RhCp* Cp)₂-covered piranha-cleaned FTO. All values are in eV (except ratios). The position of the Rh^{III} 3d peaks was fixed to be at a distance of 1.3 eV from Rh^I 3d peaks to allow consistent fitting.¹²² ^aXPS core shifts are discussed at length in section 3.4.1. ^bFTO modified by dipping for 10 min in a 2 mM solution of (RhCp* Cp)₂ in toluene, followed by three rinsing cycles with pure toluene.

XPS positions ^a	Sn 3d _{5/2}	O 1s	C 1s	Rh ^I 3d _{5/2}	Rh ^{III} 3d _{5/2}
FTO	487.22	531.33	285.62	--	--
FTO + 1 nm (RhCp* Cp) ₂	487.27	531.32	286.17	310.91	312.21
FTO + 10 nm (RhCp* Cp) ₂	487.29	531.33	286.23	310.82	312.12
FTO + 10 min dipped (RhCp* Cp) ₂ ^b	487.23	-	286.23	309.72	311.02

Table 3.2 XPS peak ratios for (RhCp* Cp)₂-covered piranha-cleaned FTO. All values are in eV (except ratios). ^bFTO modified by dipping for 10 min in a 2 mM solution of (RhCp* Cp)₂ in toluene, followed by three rinsing cycles with pure toluene.

XPS ratios	Rh ^{III} /Rh ^I	Rh/Sn
FTO	--	--
FTO + 1 nm (RhCp* Cp) ₂	0.13	0.016
FTO + 10 nm (RhCp* Cp) ₂	0.14	0.035
FTO + 10 min dipped (RhCp* Cp) ₂ ^b	8.33	0.057

3.3 Electronic Alignment at the FTO/ETM Interface

To understand how (RhCp* Cp)₂ affects the energetic alignment at the FTO/ETM interface, vacuum-processible electron-transporting materials (ETMs) were used to avoid loss of soluble dimer molecules and/or ions from the substrate during deposition, as discussed in sections 2.3.2 and 2.4. C₆₀ and PTCBI were evaporated onto piranha-cleaned FTO and onto **1**₂-covered FTO. UPS shows that upon deposition of the ETMs on the metal oxide surface the WF decreases from 4.6 eV to 4.4 eV for C₆₀/FTO and to 4.3 eV for PTCBI/FTO, which is attributed to the push-back effect.^{26, 124-125} When FTO is modified with (RhCp* Cp)₂, the WF of the ETM-covered FTO shifts closer to the LUMO of the ETM (3.9 – 4.0 eV)⁸⁷ as shown in Figure 3.4 and in Figure 3.5.

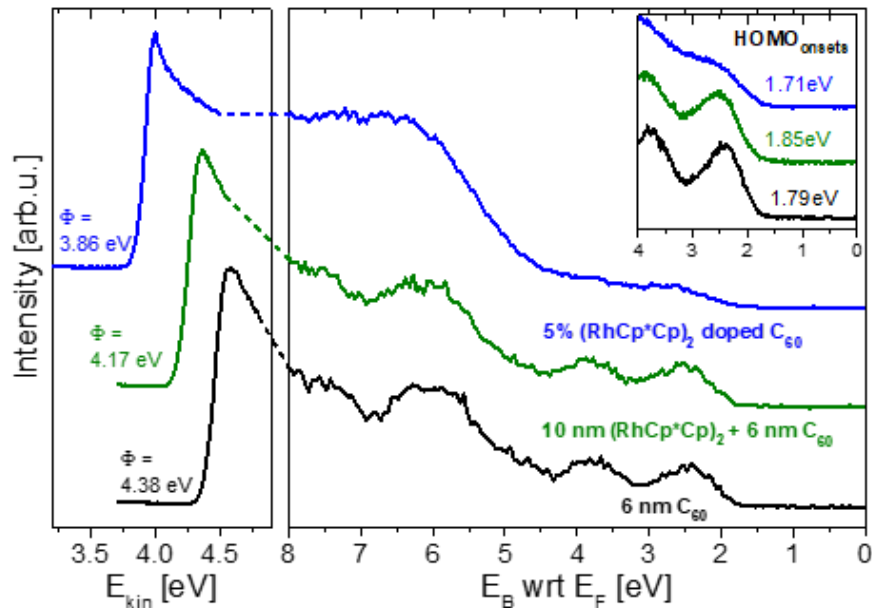


Figure 3.4 UPS spectra of FTO/ C_{60} , FTO/10 nm $(RhCp^*Cp)_2/C_{60}$ and FTO/5% doped C_{60} (E_{kin} = kinetic energy, E_B = binding energy with respect to the Fermi level, E_F). The insets offer enlarged view of the UPS spectra at low binding energies, close to the E_F . The doping concentration of 5% is given as a molar percentage calculated from the evaporation rates.

Table 3.3 XPS binding energies for C_{60} , bilayers of $(RhCp^*Cp)_2$ and C_{60} , and coevaporated C_{60} and dopant. ^aXPS core shifts are discussed at length in section 3.4.1.

XPS positions ^a	Sn 3d _{5/2}	C 1s	Rh ^I 3d _{5/2}	Rh ^{III} 3d _{5/2}
6 nm C_{60}	487.30	285.22	--	--
1 nm $(RhCp^*Cp)_2$ + 5 nm C_{60}	487.21	285.41	310.52	--
10 nm $(RhCp^*Cp)_2$ + 5 nm C_{60}	487.21	285.28	310.36	311.66
5% doped C_{60}	--	285.38	309.26	310.56

Table 3.4 XPS peak ratios for C₆₀, bilayers of (RhCpCp*)₂ and C₆₀, and coevaporated C₆₀ and dopant. The Rh/C ratio of 0.003 for the coevaporated ETM and dopant was used to calculate the actual doping concentration of 10%.**

XPS peak ratios	Rh ^{III} /Rh ^I	Rh/Sn
6 nm C ₆₀	--	--
1 nm (RhCp* <i>Cp</i>) ₂ + 5 nm C ₆₀	--	0.004
10 nm (RhCp* <i>Cp</i>) ₂ + 5 nm C ₆₀	0.02	0.002
5% doped C ₆₀	21.8	0.003

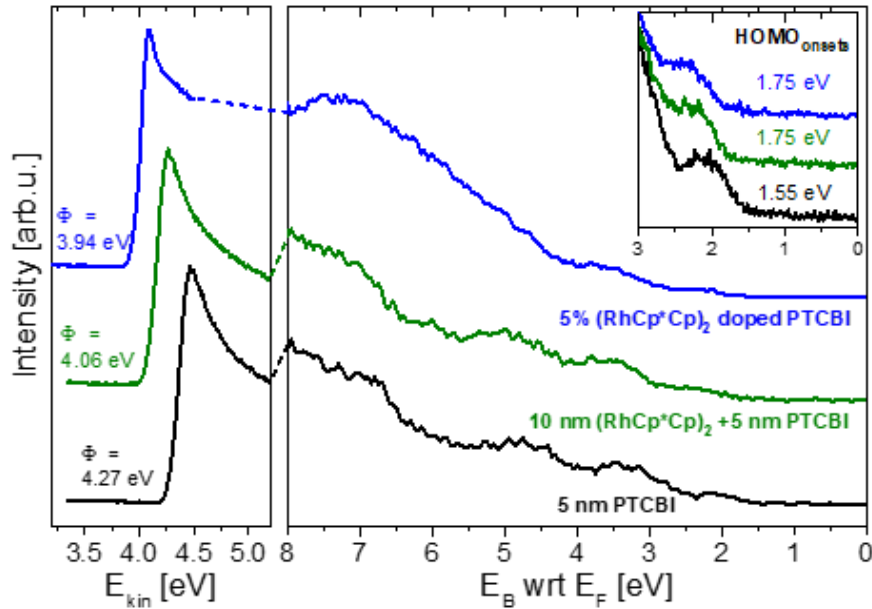


Figure 3.5 UPS spectra of FTO/PTCBI, FTO/10 nm (RhCpCp*)₂/PTCBI and FTO/5% doped PTCBI (E_{kin} = kinetic energy, E_B = binding energy with respect to the Fermi level, E_F). The insets offer enlarged view of the UPS spectra at low binding energies, close to the E_F . The doping concentration of 5% is given as a molar percentage calculated from the evaporation rates.**

Table 3.5 XPS binding energies for PTCBI, bilayers of (RhCpCp*)₂ and PTCBI, and coevaporated PTCBI and dopant. ^aXPS core shifts are discussed at length in section 3.4.1.**

XPS positions ^a	Sn 3d _{5/2}	C 1s	N 1s	Rh ^I 3d _{5/2}	Rh ^{III} 3d _{5/2}
5 nm PTCBI	487.14	285.23	398.90	--	--
1nm (RhCp* <i>Cp</i>) ₂ + 5 nm PTCBI	487.12	285.30	398.98	310.57	311.87
10 nm (RhCp* <i>Cp</i>) ₂ + 5 nm PTCBI	487.16	285.29	398.96	310.58	311.88
5% doped PTCBI	--	285.30	398.98	309.32	310.62

Table 3.6 XPS peak ratios for PTCBI, bilayers of (RhCpCp*)₂ and PTCBI, and coevaporated PTCBI and dopant. The Rh/N ratio of 0.04 for the coevaporated ETM and dopant was used to calculate the actual doping concentration of 8%.**

XPS ratios	Rh ^{III} /Rh ^I	Rh/Sn
5 nm PTCBI	--	--
1nm (RhCp* <i>Cp</i>) ₂ + 5 nm PTCBI	0.10	0.03
10 nm (RhCp* <i>Cp</i>) ₂ + 5 nm PTCBI	0.04	0.02
5% doped PTCBI	40.6	0.04

The electron affinity of PTCBI ($EA = E_{vac} - E_{CB}$, where E_{vac} is the vacuum level) was measured by inverse photoemission spectroscopy (IPES) to be 4.0 eV, Figure 3.6, which is similar to that of C₆₀.⁸⁷ UPS was performed prior carrying out IPES measurement. The resolution of the IPES setup is 1.3 eV and was determined from the broadening of the Fermi level of a gold reference. To account for this low resolution, the onset of the LUMO level measured by IPES was corrected by 700 meV assuming the full width at half maximum (FWHM) of the LUMO to be the same as the one of the HOMO, which was measured by UPS (600 meV). The correction was performed according to a previously described method.¹²⁶ These changes in WF suggest introducing the interlayer **1z** between the

electrode and the ETM leads to Fermi level pinning of FTO to the LUMO of the ETM. Note that energy-level bending can occur when the metal oxide/ETM interface is strongly Fermi level pinned; in other words the WF of modified FTO/ETM will not exactly align at 4.0 eV, as can be observed in Figure 3.7.¹²⁷ In the latter, the WF of FTO/1 nm (RhCp**Cp*)₂/5 nm C₆₀ is lower than that of FTO/10 nm (RhCp**Cp*)₂/6 nm C₆₀, but higher than 4.0 eV, in agreement with the model proposed by Oehzelt et al.¹²⁷ Note the different thickness of C₆₀ for these specific samples. Similarly, depositing a thicker amount of **12** between FTO and PTCBI causes the WF of the FTO/ETM to align close but not at the LUMO of PTCBI, Figure 3.8.

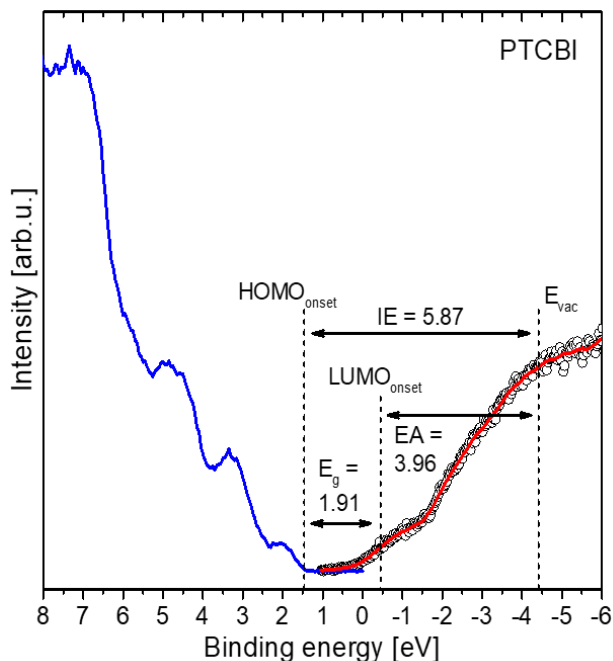


Figure 3.6 Electronic structure of triple-sublimed PTCBI, obtained via UPS (blue curve) and IPES (red curve). The optical band gap was measured to be 1.7 eV; the ionization energy (5.87 eV) is similar to values reported in the literature (6.2 eV).¹²⁸

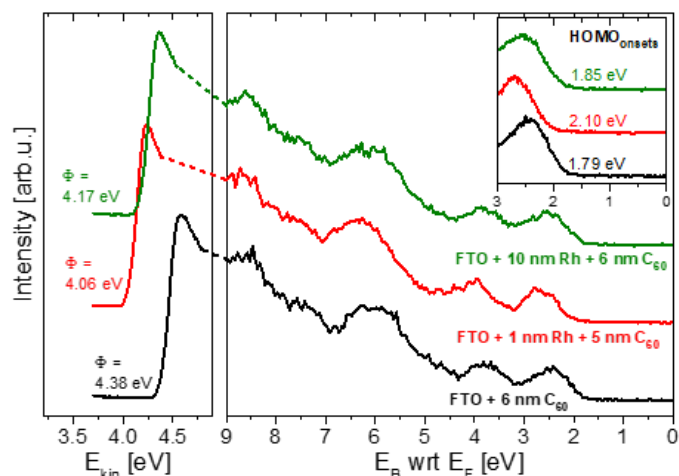


Figure 3.7 UPS spectra of FTO/C₆₀ and (RhCp* Cp)₂ modified-FTO/C₆₀ with varying thickness of the (RhCp* Cp)₂ interlayer.

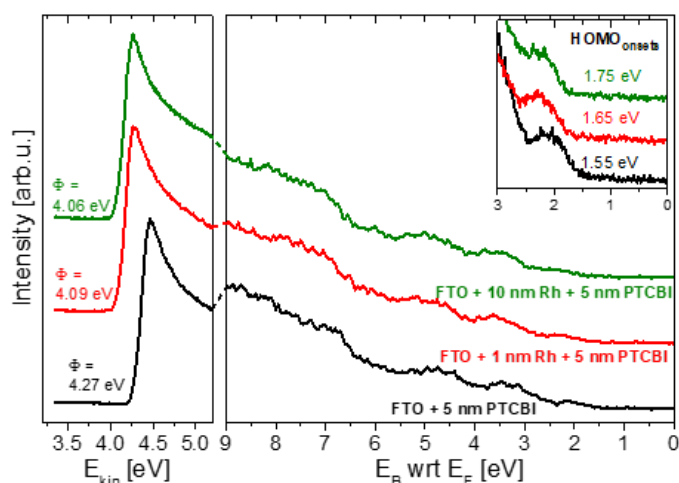


Figure 3.8 UPS spectra of FTO/PTCBI and (RhCp* Cp)₂ modified-FTO/PTCBI with varying thickness of the (RhCp* Cp)₂ interlayer.

3.4 Interfacial Doping of the ETM

Given the high electron affinities of C₆₀ and PTCBI and the effective doping strength of **12** (ca. -2.0 V vs. FeCp₂⁺⁰, from which an effective ionization energy of ca. 2.8 eV can be estimated),⁸³ it can be expected that upon deposition of these organic semiconductors on the **12**-covered electrode surface, the molecules near the interface will be *n*-doped by

unreacted **12** through an electron transfer. Additionally, since the WF of the modified FTO is lower than the *EA* of both ETMs, substrate-to-overlay charge transfer may occur to establish a common electro-chemical potential.¹²⁹⁻¹³⁰

To show that **12** does indeed *n*-dope these ETMs, **12** was coevaporated with PTCBI and C₆₀ (Figure 3.4 and Figure 3.5). Compared to modified FTO/ETM samples, coevaporation of (RhCp**Cp*)₂ with the ETM leads to a further reduction of the WF to 3.9 eV and to broadening of the valence band features of both C₆₀ and PTCBI, which are typical signatures of doping.¹³¹⁻¹³² XPS spectra confirm that the Rh 3d signal is mostly due to Rh^{III} species (reacted monomer cations, **1**⁺, see section 3.4.1) when (RhCp**Cp*)₂ is coevaporated with the ETM, and with Rh^I species (unreacted dimer **12**) when the ETM is deposited on **12**-modified FTO, as show in Figure 3.9.

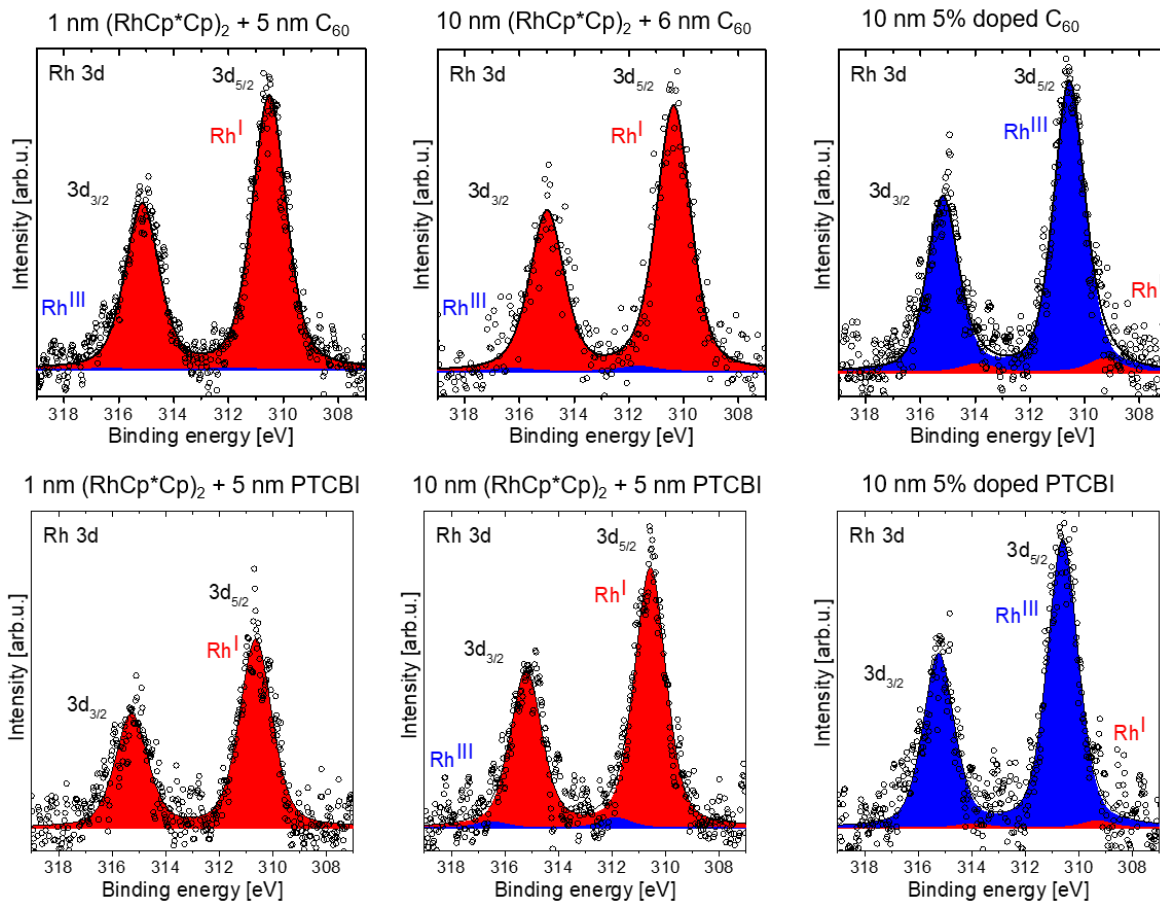


Figure 3.9 XPS Rh 3d scans of FTO/1-10 nm (RhCp*Cp)₂/ETM and FTO/ETM coevaporated with (RhCp*Cp)₂.

UV-vis-NIR spectroscopy on **1₂** coevaporated with C₆₀ shows the presence of an absorption peak at 1065 nm (1.16 eV), which is attributable to C₆₀^{•-} (Figure 3.10, Figure 3.11 and Figure 3.12).¹³³ A similar peak (at ca. 1120 nm, 1.11 eV) is observed when **1₂** is coevaporated with PTCBI, suggesting doping of the perylene derivative. In contrast, the NIR absorption peak is barely observed in the (RhCp*Cp)₂-treated FTO/ETM samples, although it becomes more pronounced after sequentially heating the same bilayer at 100, 150, 185 and 200 °C (at least 60 min at each temperature). The absorption in the NIR increases with annealing to final absorbance values that are comparable to those obtained with a nominal doping concentration of 0.6% in the case of C₆₀ and 1% for PTCBI,

calculated assuming that the dopant molecules are homogeneously dispersed throughout the ETMs. This increase suggests that annealing promotes the reaction of **1**₂ with the ETMs, perhaps allowing limited diffusion of the bulky **1**⁺ into the ETMs.

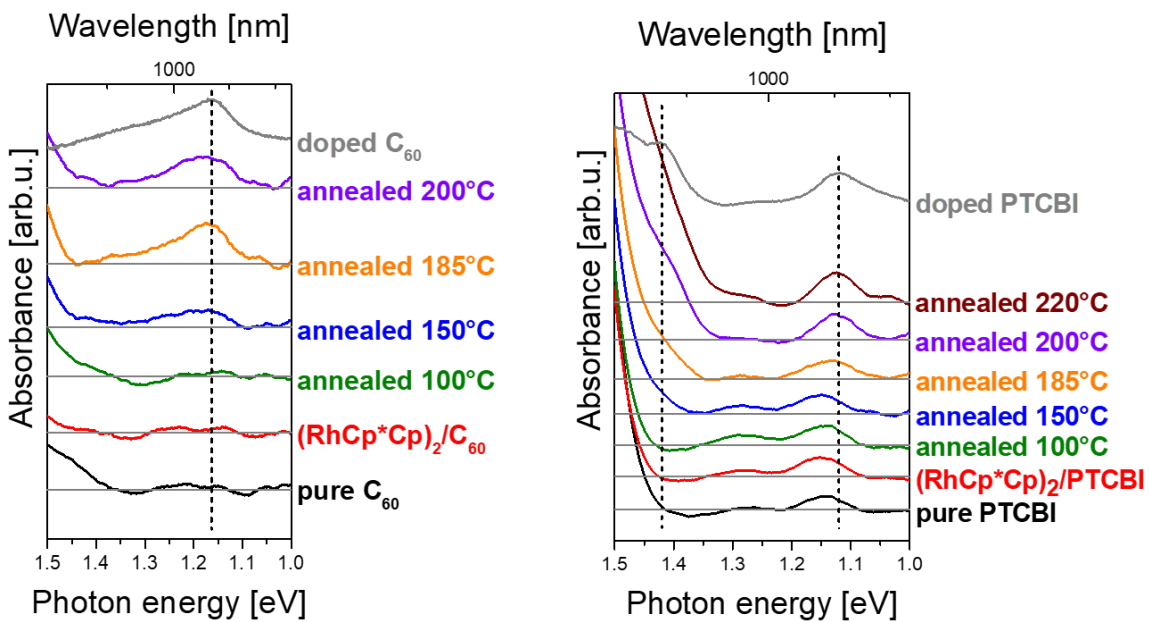


Figure 3.10 Smoothed NIR absorption spectra for pure ETM, **1**₂-modified FTO/ETM annealed at increasing temperatures and **1**₂ coevaporated with ETM. The doping concentration for coevaporated ETMs is calculated from the absorption peak at 1065 nm to be 15% for C₆₀ (left) and 17% for PTCBI (right).

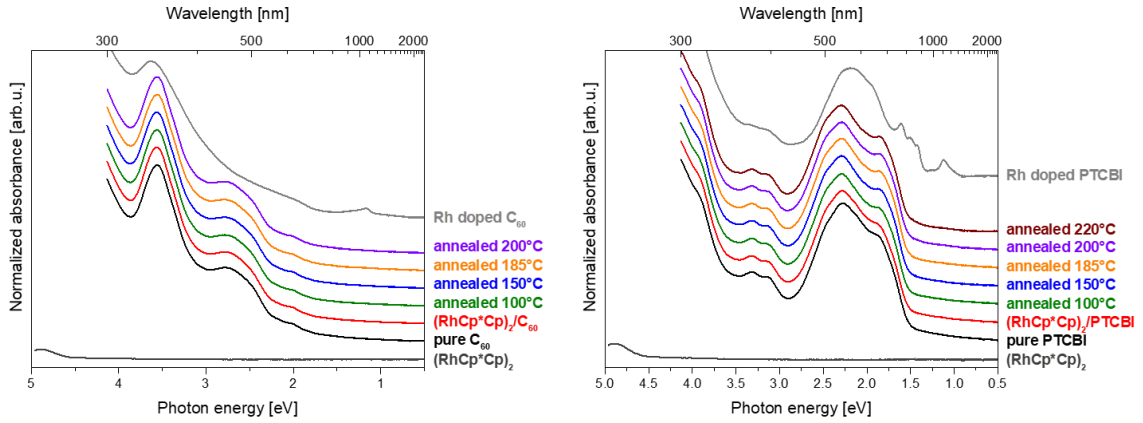


Figure 3.11 UV-vis-NIR absorption spectra for pure ETM, (RhCp* Cp)₂ modified-FTO/ETM annealed at increasing temperatures, and (RhCp* Cp)₂ coevaporated with ETM with a doping concentration of around 10%; ETM = C₆₀ (left), PTCBI (right).

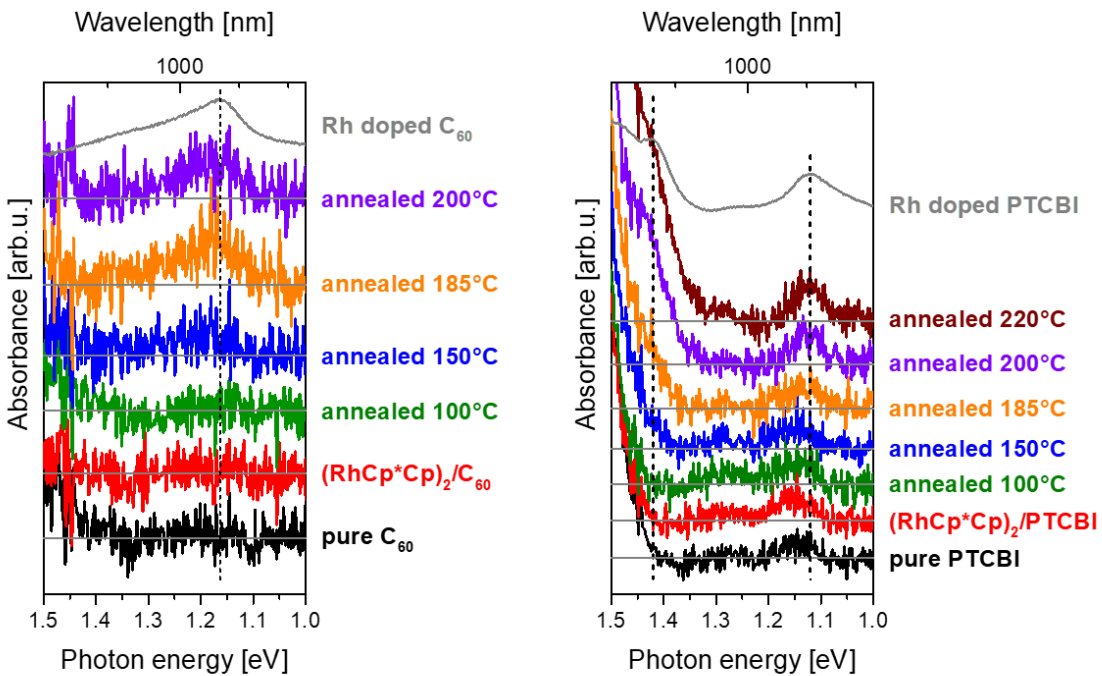


Figure 3.12 Raw NIR absorption spectra for pure ETM, 1₂-modified FTO/ETM annealed at increasing temperatures, and 1₂ coevaporated with ETM. The ETMs used were C₆₀ (left) and PTCBI (right). The doping concentrations for coevaporated ETMs are calculated from the deposition rates to be 13% for C₆₀ and 17% for PTCBI.

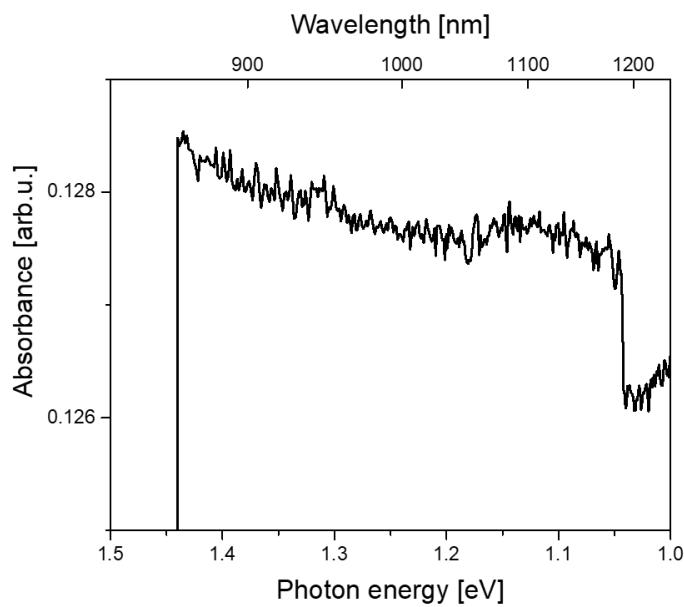


Figure 3.13 Absorption of the reference box used to perform UV-vis-NIR absorption spectroscopy on samples containing $(\text{RhCp}^*\text{Cp})_2$. Since there are no absorption features of the reference box in the range of 1.04 eV to 1.44 eV, features in this range can be assigned to sub-bandgap features of the samples. Abrupt signal changes at 1.04 eV and 1.44 eV are artifacts of the spectrometer due to detector and grating changes.

3.4.1 Discussion of the XPS Rh 3d Peak Assignment

The Rh 3d ionization is split into $3d_{5/2}$ and $3d_{3/2}$ peaks by spin-orbit coupling; the following discussion and the binding energy (E_B) reported in Table 3.1 – Table 3.6 are focused on the Rh $3d_{5/2}$ component but the trends apply equally to the Rh $3d_{3/2}$. In both the present study and previous work, two chemically distinct species are often present in $(\text{RhCp}^*\text{Cp})_2$ -containing samples, differing in Rh $3d_{5/2}$ (and $3d_{3/2}$) E_B by *ca.* 1.3 eV.^{65, 122} These are assigned to the unreacted neutral dimer, $(\text{RhCp}^*\text{Cp})_2$, and the monomer cation, RhCp^*Cp^+ , that is known to be formed on oxidation of the dimer,³⁴ with the lower E_B signal being assigned to the former, which is formally Rh^{I} , and the higher E_B signal to the latter, which is formally Rh^{III} . However, since this difference in E_B is relatively small (although

the formal oxidation states are 1+ and 3+, there is considerable covalency and charge delocalization onto the ligands in these species), differences in the immediate environment of the Rh species can have comparable effects on the E_B to the oxidation state; this has been seen in previous studies^{65, 122} and the present work.

Table 3.1 and Table 3.2 compare data for a dimer solution deposited on FTO, followed by washing with toluene to remove most of the unreacted $(\text{RhCp}^*\text{Cp})_2$, which leaves primarily Rh^{III} cations (originated from dopants that have transferred electrons to the oxide) covering most of the FTO surface, with data for thick evaporated layers of the dimer, where only a small fraction is expected to be oxidized to the cation. This illustrates that the E_{BS} depend on the details of the environment with both high- and low- E_B components, assigned to Rh^{III} and Rh^{I} respectively, being seen at lower E_B in the thin film. Table 3.3 – Table 3.6 indicate that similar Rh^{I} and Rh^{III} E_B for thick evaporated films in the presence of ETM overlayers can be measured as the uncovered thick layers in Table 3.1. On the other hand, for coevaporated dimer:ETM films, where owing to the high EA of the ETMs ($\gg 3$ eV) most of the dimer is expected to be converted to Rh^{III} monomer cations, the E_B for both Rh^{I} and Rh^{III} components are similar to, but a little lower than the corresponding values for the monolayer films on FTO, and considerable lower than those for the thick films. The differences in E_B for the two components between samples presumably arise from the large differences in chemical environments: in the monolayers on FTO the dopant molecules and ions are all in close proximity to the negatively charged oxide film, in coevaporated films the dopant species will likely be in close proximity to both neutral and negatively charged ETM molecules, and in the thick-film structures (both with and without ETM overlayers), most dopant species will be surrounded by neutral

dopant molecules. Monolayers of mostly RhCp* Cp^+ on FTO will be further discussed in chapter 4.

3.5 PTCBI as ETM in Perovskite Solar Cells and the Impact of FTO Surface Treatment with (RhCp* Cp)₂

Perovskite solar cells with *n-i-p* architecture were fabricated to assess the ability of PTCBI to act as an ETM for PSCs, and to assess the electrical consequence of introducing an interlayer between the electrode and the two ETMs. The architecture of the solar cells consisted of FTO (bare or modified with 10 nm of **12**)/ETM (C₆₀ or PTCBI)/CH₃NH₃PbI₃/spiro-OMeTAD/Ag. The average device performance parameters and stabilized power output (SPO) are shown in Table 3.7 while the current density – voltage (*J* – *V*) curves of the best-performing solar cells with evaporated CH₃NH₃PbI₃ are shown in Figure 3.14 for C₆₀ as ETM and in Figure 3.15 for PTCBI as ETM. SPO is defined as the power conversion efficiency (PCE) of devices held at their *J* – *V* determined maximum power point.

Table 3.7 Device performance parameters averaged over five solar cells with evaporated CH₃NH₃PbI₃.

ETM	J_{sc} (mA cm ⁻²)	V_{oc} (mV)	FF (%)	PCE (%)	SPO (%)
C ₆₀	17.1 ± 0.3	988 ± 6	55 ± 1	9.3 ± 0.3	9.5 ± 0.4
(RhCp* Cp) ₂ /C ₆₀	17.5 ± 0.2	994 ± 5	59 ± 1	10.1 ± 0.3	10.0 ± 0.3
PTCBI	17.4 ± 0.8	928 ± 21	54 ± 1	8.6 ± 0.7	6.8 ± 0.8
(RhCp* Cp) ₂ /PTCBI	19.9 ± 0.2	935 ± 7	56 ± 1	10.4 ± 0.1	9.2 ± 0.1

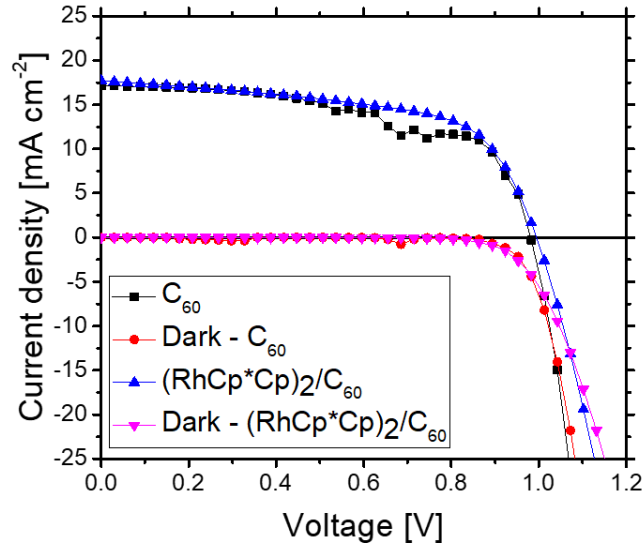


Figure 3.14 Current density – voltage characteristics for the best-performing solar cells fabricated using C_{60} as ETM before and after deposition of $(RhCp^*Cp)_2$ on FTO.

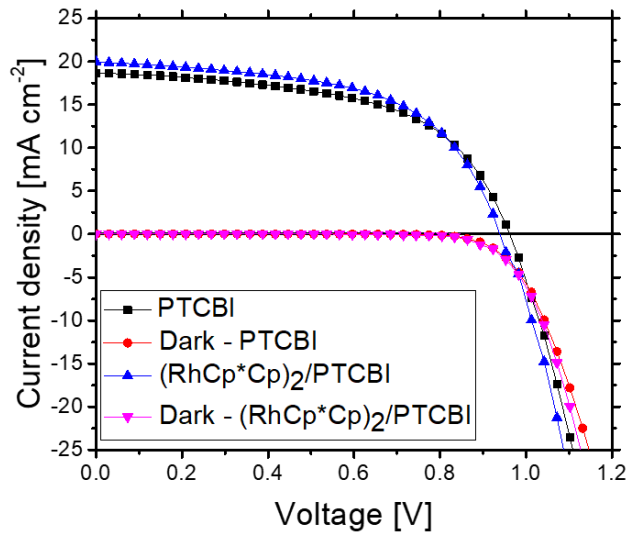


Figure 3.15 Current density – voltage characteristics for the best-performing solar cells fabricated using PTCBI as ETM before and after deposition of $(RhCp^*Cp)_2$ on FTO.

Interlayer-free solar cells fabricated using PTCBI as ETM exhibit similar short-circuit current (J_{sc}) and fill factor (FF), but lower open-circuit voltage (V_{oc}) and SPO, compared to devices fabricated with C_{60} . However, the deposition of the $(RhCp^*Cp)_2$

interlayer greatly improves the SPO of devices with PTCBI as ETM from an average of 6.8% to 9.2%. Their $J - V$ determined PCE also increases from an average of 8.6% to 10.4%. The increase in PCE is a result of both higher J_{sc} and FF, which suggests an improvement in the charge collection upon introduction of $(\text{RhCp}^*\text{Cp})_2$ at the FTO/ETM contact. Improvements in PCE and FF are also observed for C_{60} -based solar cells after the electrode/ETM interface is modified using **12**. However, changes in SPO are negligible upon interface modification in C_{60} devices. Solar cells fabricated with solution processed $\text{CH}_3\text{NH}_3\text{PbI}_3$ were also fabricated. The perovskite layer was processed from a methylamine/acetonitrile precursor solution,¹³⁴ as described in section 3.7.3.

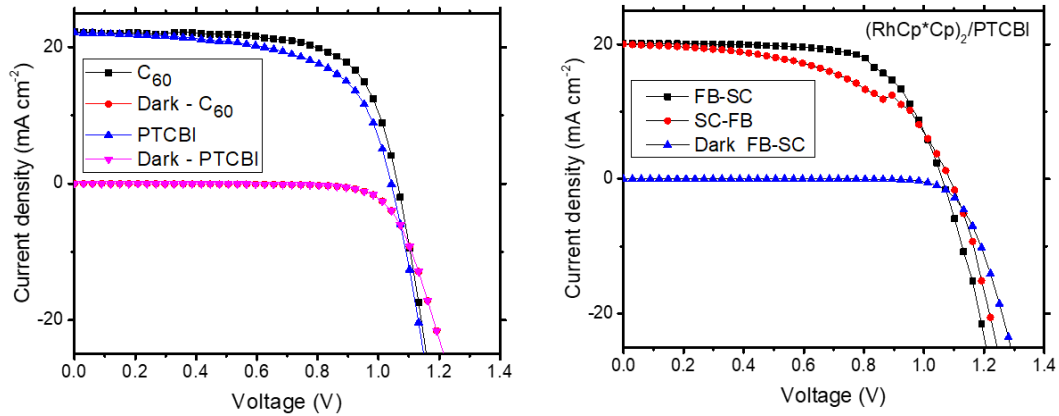


Figure 3.16 Current density – voltage characteristics for the best-performing solar cells fabricated using C_{60} and PTCBI as ETMs (left), and with PTCBI deposited on $(\text{RhCp}^*\text{Cp})_2$ -modified FTO (right).

Figure 3.16 shows the current density – voltage ($J - V$) curves for the champion devices with solution-processed $\text{CH}_3\text{NH}_3\text{PbI}_3$. FB stands for forward bias, and SC stands for short-circuit. Figure 3.17 shows the UV-vis spectra of PTCBI films on glass before and after sequential spin-coating of acetonitrile and dimethylformamide. Both C_{60} ¹³⁴ and PTCBI are insoluble in methylamine/acetonitrile preventing the formation of pinholes in

the ETM during active-layer deposition. The perovskite absorber processed from solution was annealed for 60 min at 100 °C to ensure its full crystallization. Moreover, annealing promotes more extensive interfacial doping of the ETM in the case of (RhCp**Cp*)₂-modified FTO, as shown by the absorption spectra in Figure 3.10 (similar to that seen for other *n*-doped PDI ETMs).¹¹⁹ Table 3.8 displays the device performance parameters of best-performing solar cells fabricated with solution-processed perovskite. With optimized processing conditions stabilized efficiencies up to 12.7% can be obtained using PTCBI as ETM, and up to 14.2% when the FTO/PTCBI interface is modified with **12**. The fill factor increases more dramatically (from 61% to 67%) with interface modification, when the ETM is doped and brought into ohmic contact with the FTO electrode,¹³⁵ than in the devices with vacuum-deposited CH₃NH₃PbI₃ (Table 3.7); the larger enhancement in FF may be associated with the increased level of interfacial doping of the ETM (Figure 3.10) associated with the thermal annealing step used in these devices. However, J_{sc} is somewhat decreased with the **12** interlayer.

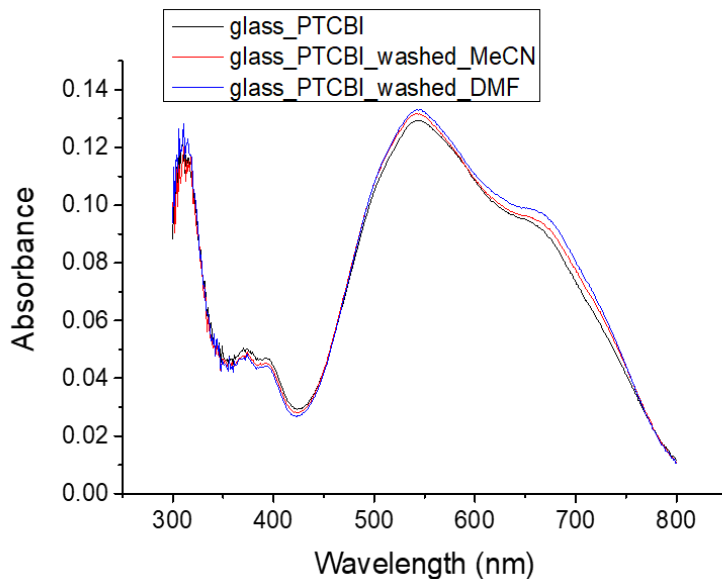


Figure 3.17 UV-vis spectra of 15-nm thick PTCBI films on glass before and after sequential spin-coating of acetonitrile and dimethylformamide.

Table 3.8 Device performance parameters of best-performing solar cells with solution-processed $\text{CH}_3\text{NH}_3\text{PbI}_3$.

ETM	J_{sc} (mA cm^{-2})	V_{oc} (V)	FF (%)	PCE (%)	SPO (%)
C_{60}	22.3	1.07	68	15.7	16
PTCBI	22.2	1.04	61	13.7	12.7
10 nm $(\text{RhCp}^*\text{Cp})_2/\text{PTCBI}$	20.1	1.07	67	14.6	14.2

3.6 Conclusions

The work in this chapter demonstrated that the organometallic dimer $(\text{RhCp}^*\text{Cp})_2$ can be successfully used to modify the FTO electrode/ETM interface in PSCs, by pinning the E_F of the electrode to the LUMO of the ETM and n -doping the molecules of organic semiconductor in proximity of the interface. Vacuum-deposition of $(\text{RhCp}^*\text{Cp})_2$ leads to a decrease in the WF of the FTO by more than 1 eV, since the dopant readily transfers electrons to the electrode and forms monomer cations on the metal oxide surface. However,

multilayers of unreacted dopant are present, some of which can react with nearby ETM molecules and moderately diffuse after sequential hour-long heating cycles at above 100 °C. This is the first time that the perylene derivative PTCBI is employed as an ETM in a PSC. *n-i-p* PSCs fabricated using this organic semiconductor on (RhCp**Cp*)₂-modified FTO lead to some of the highest power conversion efficiencies reported for PSCs with vacuum-deposited ETMs (up to 14.2%). However, solar cells fabricated using C₆₀ under comparable conditions still outperform those fabricated on PTCBI (16% vs. 12.7%). Nonetheless, the results are consistent with other recent studies¹¹⁹⁻¹²¹ in indicating that PDI-type molecules are promising ETMs for PSCs. Specifically, here we show that a vacuum-processible and essentially insoluble derivative can be useful in *n-i-p* devices; future investigations could explore the potential of other derivatives with these properties.

3.7 Experimental

3.7.1 Materials Synthesis and Purification

PTCBI was purchased from Sigma-Aldrich and it was purified in three cycles *via* thermal gradient sublimation prior to loading the material into the high-vacuum deposition system.¹³⁶ Triple-sublimed C₆₀ (purity > 99.9%, HPLC) was purchased from CreaPhys GmbH. (RhCp**Cp*)₂ was synthesized according to methods reported in the literature.^{34, 137}

3.7.2 Photoelectron Spectroscopy

The UPS, XPS and IPES spectra were recorded in a lab system consisting of an analysis chamber, with a base pressure of 10⁻⁹ mbar, connected to a load-lock chamber, with a base pressure of 5 × 10⁻⁸ mbar. UPS was performed using a helium-gas-discharge

lamp (21.218 eV) with low photon flux (attenuated by an aluminium filter) in order to avoid radiation damage of the samples. The secondary electron cut-off (SECO) spectra were measured with a bias of -10 V applied to the sample to clear the analyser work function. The excitation source for XPS measurements was non-monochromated Al K α (1486.7 eV). An Omicron EA125 hemispherical energy analyser was used to collect the spectra in normal emission geometry (energy resolutions for UPS and XPS measurements, determined from the Au Fermi edge and the Au 4f_{7/2} peak, were 180 meV and 1.2 eV, respectively). The error of XPS binding energies retrieved from curve fitting is estimated to be smaller than 50 meV, as obtained from procedures where binding energies were purposely offset. IPES measurements (incident electron energy range: 5-15 eV, NaCl-coated photocathode, SrF₂-window) were performed in the isochromat mode. All UPS, XPS and IPES spectra were recorded at room temperature.

3.7.3 Solar Cell Fabrication

Fluorinated tin oxide (FTO) coated glass sheets (Hartford Glass, 15 $\Omega \square^{-1}$) were etched using a 2 M HCl solution and zinc powder. After initial washing with Hellmanex™ III detergent, substrates were immersed for 90 min in a H₂SO₄:H₂O₂ 3:1 (v/v) piranha solution. The FTO substrates were rinsed with deionized water, and dried with compressed dry air. The substrates were deposited on a mask and loaded on a vacuum deposition chamber, where (RhCp**Cp*)₂, C₆₀ or PTCBI were sequentially deposited at 10⁻⁶ mbar at a rate of 0.1 $\text{\AA} \text{ s}^{-1}$. The samples were transferred to a different vacuum chamber for the coevaporation of PbI₂ and CH₃NH₃I at 10⁻⁶ mbar. Alternatively, a CH₃NH₃PbI₃ solution was prepared by bubbling dry methylamine gas into a black dispersion of perovskite precursors (1.00 CH₃NH₃I:1.06 PbI₂) in acetonitrile at a concentration of 0.5 M, until the

dispersion turned into a clear, light yellow solution as described in the literature.¹³⁴ The resulting $\text{CH}_3\text{NH}_3\text{PbI}_3$ solution in acetonitrile/methylamine was spin-coated onto the substrate at 2000 rpm for 45 s in a nitrogen-filled glovebox. The dense perovskite layers obtained from spin-coating were annealed at 100 °C for 60 min. After the substrates were cooled down to room temperature, the hole-transporting material 2,2',7,7'-tetrakis(*N,N'*-di-*p*-methoxyphenylamine)-9,9'-spirobifluorene (spiro-OMeTAD) was deposited from chlorobenzene with additives at a concentration of 30 mM for lithium bis(trifluoromethanesulfonyl)imide (Li-TFSI) and of 80 mM for *tert*-butylpyridine (*t*BP) via spin-coating at 2000 rpm for 45 s. 110 nm thick silver electrodes were thermally evaporated at 1×10^{-6} mbar through a shadow mask to create solar cells with a total active area of 0.0919 cm², as defined by the overlap between FTO and silver.

3.7.4 Current Density-Voltage Characterization

The current density–voltage (J – V) curves were measured (2400 Series SourceMeter, Keithley Instruments) in ambient conditions under simulated AM1.5 sunlight at (100 mW cm^{-2}) irradiance generated by an Abet Class AAB sun 2000 simulator, with the intensity calibrated with an NREL calibrated KG5 filtered Si reference cell. The mismatch factor was calculated to be less than 1%. The solar cells were masked with a metal aperture to expose a 0.0919 cm² active area for testing of both the current–voltage characteristics and stabilized power conversion efficiency (η_{MPP}). The devices were prebiased at 1.4 V for 5 s before initiating the reverse and forward scans. The scan rate was 0.38 V s⁻¹. Immediately after the J – V measurements, the η_{MPP} was measured without prebiasing. The devices were kept at the voltage defined at maximum power point, which

was determined from the J – V scans, for 50 s to measure the stabilized power conversion efficiency and current density.

3.7.5 *UV-vis-NIR Absorption Spectroscopy*

Absorbance spectra were measured with a Lambda 950 UV-vis-NIR spectrophotometer (PerkinElmer) in a controlled nitrogen atmosphere. The samples were prepared by depositing the respective materials onto solvent-cleaned quartz glass substrates via (co-) evaporation at 10^{-7} mbar. A baseline spectrum of clean quartz glass substrate was subtracted from the spectra before further analysis. To analyze the energy region in the optical gap of the ETMs, a background (taking into account Rayleigh scattering and arbitrary linear background) with the form $A = a + bE + cE^4$ was subtracted from the respective spectra; a , b and c are arbitrary fitting parameters, A is the absorbance and E is the photon energy. Data was smoothed using a 100-point second order Savitzky–Golay filter.

CHAPTER 4. INTERFACIAL DOPING OF C₆₀ AND ITS IMPLICATION FOR HIGH-PERFORMANCE PEROVSKITE SOLAR CELLS

4.1 Introduction

Fullerene-based molecules can replace TiO₂ and work as electron transporting materials (ETMs) in perovskite solar cells (PSCs), as discussed in chapter 3. One advantage of using organic ETMs is that these semiconductors can be easily doped, either in the bulk or interfacially, by using *n*-dopants, via vacuum deposition^{87, 133, 138-140} and/or solution mixing.¹⁴¹⁻¹⁴³ Via doping it is possible to increase the conductivity of semiconductors, and to obtain ohmic contact at the interface of semiconductors with metals or metal oxides. For example, building on previous research on organic photovoltaics, Bolink *et al.* improved charge extraction in PSCs by introducing a doped layer of charge selective materials [C₆₀ as the electron-transporting material (ETM), and *N,N,N',N'*-tetra([1,1'-biphenyl]-4-yl)-[1,1':4',1''-terphenyl]-4,4''-diamine (TaTm as the hole-transporting one (HTL)] directly in contact with the respective electrodes (electron- or hole- collecting).¹³⁵ It was also shown that recombination in solar cells can be reduced by leaving a thin layer of intrinsic charge selective materials directly in contact with the light-absorbing perovskite. Although power conversion efficiencies of above 20% were demonstrated using this double-layer charge-selective layer architecture, these solar cells are likely not to be stable because of the very high doping concentration (exceeding 30 wt% dopant content relative to C₆₀).¹³⁵

Interfacial doping could therefore be a viable strategy to increase the conductivity of the ETM close to the electrode, to pin the Fermi level of the electrode to the LUMO of the ETM, and minimize the introduction of species that could potentially diffuse under device operation. One approach to obtain interfacial doping of the ETM is to treat the electrode with a strong reductant that creates a dipole via an electron transfer to the electrode, thus lowering its WF, as shown in chapters 1 and 3. Depending on the reductant, the molecules of ETM near the interface can be *n*-doped through an electron transfer, from the low WF electrode or from the reductant itself, to the ETM. Chapter 3 highlighted how charge collection losses at the FTO/ETM interface, where the ETMs used were C₆₀ and derivatives of perylene diimides, can be minimized by introducing a thin layer (≤ 10 nm) of an organometallic *n*-dopant, pentamethylcyclopentadienyl cyclopentadienyl rhodium dimer, (RhCp**Cp*)₂.¹²³ The latter reacts to form its corresponding monomeric cation, which is sufficiently bulky to only diffuse to a limited extent, as shown in section 3.4. Nevertheless, vacuum-deposition of (RhCp**Cp*)₂ results in the deposition of large amounts of unreacted dimer. In this chapter, in order to optimize the amount of dopant used, to attempt to improve the surface coverage on FTO, and to reduce the likelihood of dopant migration, solution processing of (RhCp**Cp*)₂ was investigated. The use of the organometallic dimer is compared to that of a commercially available metal-free ammonium salt, tetrabutylammonium borohydride (TBABH₄). Non-redox active tetraalkylammonium salts (i.e., tetrabutylammonium fluoride) can dope fullerenes¹⁴⁴⁻¹⁴⁵ via a nucleophilic attack.¹⁴⁶ Sodium borohydride is known to react with C₆₀ via hydride transfer forming C₆₀H⁻, followed by deprotonation of water or alcohol, forming dihydrofullerenes (C₆₀H₂).¹⁴⁷⁻¹⁴⁸ Moreover, ammonium salts have been used to lower the work function of metals and metal

oxides.¹⁴⁹⁻¹⁵⁰ Kemerink *et al.* found that tertiary aliphatic amines and polyelectrolytes (e.g., aliphatic quaternary ammonium salts and sulfonic acid based polymers) show a similar behavior in modifying the WF of metals and metal oxides by formation of an interface dipole.¹⁵⁰ This surface treatment is governed by the attraction of the positive and negative part of the dipole towards the interface by an image dipole in the substrate. It was found that the WF modification depends on the relative size of the anion and cation and their respective ability to move. The smaller and more mobile ion generally resides closest to the substrate, with the larger ion forming an outer layer, resulting in a net dipole orientation away from or towards the surface modifier.¹⁵⁰ Among the compounds previously investigated by Kemerink *et al.*, TBABH₄ induced the largest WF reduction on the surface of gold, which was as large as 0.6 eV, measured through scanning Kelvin probe microscopy in a glovebox. In this chapter, solution-based surface treatments on FTO using (RhCp**Cp*)₂ and TBABH₄ are correlated to changes in conductivity of the ETM, C₆₀, both laterally and vertically, and with device performance characteristics of *n-i-p* PSCs, fabricated using C₆₀ as the ETM onto modified FTO as the bottom electrode. The following results were obtained in collaboration with Berthold Wegner from the Humboldt University of Berlin (UPS and XPS analysis), Xiaojia Jia from Georgia Tech (assistance with vacuum deposition for conductivity measurements and diode fabrication), and Dr. Jay B. Patel from the University of Oxford (assistance with vacuum deposition for perovskite solar cells fabrication).

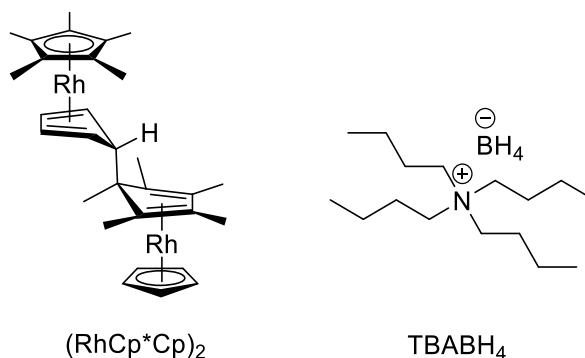


Figure 4.1 Molecular structures of the neutral dimeric dopant $(\text{RhCp}^*\text{Cp})_2$, and of TBABH_4 .

4.2 Surface Modification of FTO

4.2.1 Surface Modification of FTO using $(\text{RhCp}^*\text{Cp})_2$ Solutions

Dipping piranha-cleaned FTO substrates for an increasing amount of time in a 2 mM toluene solution of $(\text{RhCp}^*\text{Cp})_2$, and subsequently rinsing the surface of the metal oxide with pure toluene to remove unreacted dopant, causes the WF of FTO to decrease from 4.6 eV for unmodified FTO to 3.3 eV after a 10 min dip, as shown by UPS in Figure 4.2. Upon modification of FTO with solutions of $(\text{RhCp}^*\text{Cp})_2$, the secondary electron cut-off (SECO) of FTO shifts by up to 1.3 eV, similarly to what is observed when $(\text{RhCp}^*\text{Cp})_2$ is vacuum-deposited, and once again confirming the formation of an interface dipole at the FTO surface. Unlike for FTO covered with vacuum-deposited $(\text{RhCp}^*\text{Cp})_2$, whose Rh 3d signal was dominated by a Rh^{I} species corresponding to unreacted dimer, XPS spectra of FTO modified with solutions of $(\text{RhCp}^*\text{Cp})_2$, Figure 4.3, show that the predominant species on the surface is a Rh^{III} species at 310.5 – 311.0 eV. The latter is associated with the monomer cations $(\text{RhCp}^*\text{Cp})^+$ formed when electrons are donated to the FTO (see further discussion of XPS Rh 3d core shifts, largely dependent on the environment

surrounding the dopant molecules, in section 3.4.1). Notably, for one of the FTO samples modified for 1 min a Rh^I species was not detected, indicating that excess unreacted dopant does not adhere to the surface under these conditions. The ratio between Rh^{III} and Rh^I species decreases by more than an order of magnitude with increasing dipping time, as shown in Table 4.1. This suggests that dipping FTO substrates in dimer solutions for longer causes an increasing amount of unreacted dopant to be deposited on the surface of the metal oxide. However, the ratio between the total Rh 3d signal and the Sn 3d signal for solution-modified FTO does not change remarkably with increasing dipping time, and the ratio is larger than the one for FTO modified with vacuum-deposited (RhCp*₂Cp)₂, Table 3.1. The higher degree of reaction to form the Rh^{III} monomer cation may result from uniform coverage, rather than the island formation noted on evaporation of (RhCp*₂Cp)₂ on FTO. Therefore, XPS analysis suggests that solution-processing of the organometallic dimer leads to a higher coverage of the substrate surface. It seems reasonable to assume that when FTO is modified with (RhCp*₂Cp)₂, the WF of FTO covered by presumably only a fairly thin layer of C₆₀ shifts closer to the LUMO of C₆₀ (*EA* = 3.9 eV), as previously shown for vacuum-deposited (RhCp*₂Cp)₂/C₆₀ in Figure 3.7.

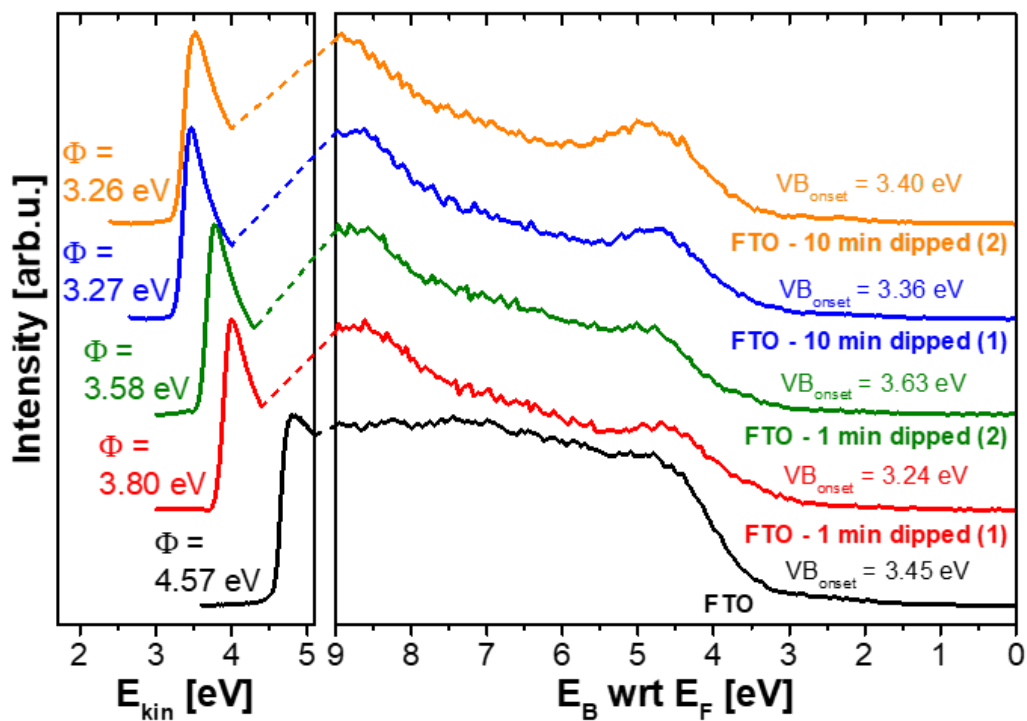


Figure 4.2 UPS spectra of piranha-cleaned FTO and FTO modified by dipping in solutions of $(\text{RhCp}^*\text{Cp})_2$ for 1 min or 10 min, followed by three rinsing cycles with pure toluene. (E_{kin} = kinetic energy; E_B = binding energy with respect to the Fermi level, E_F).

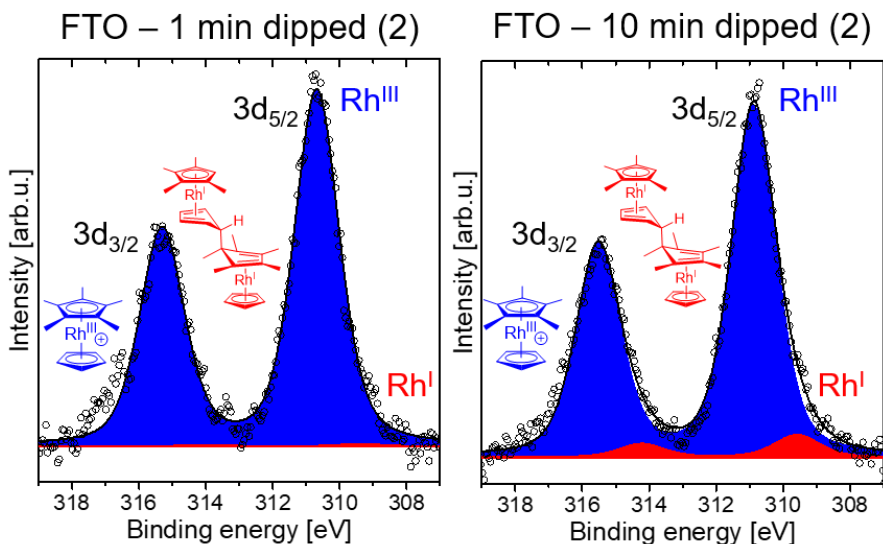


Figure 4.3 XPS spectra of FTO modified by dipping in solutions of $(\text{RhCp}^*\text{Cp})_2$ for 1 min (left) or 10 min (right). Spectra for sample 1 are similar to those for sample 2.

Table 4.1 XPS positions and peak ratios for $(\text{RhCp}^*\text{Cp})_2$ -covered piranha-cleaned FTO. FTO was modified by dipping in 2 mM solutions of the *n*-dopant for different amount of time, followed by three rinsing cycles with pure toluene. All values are in eV (except ratios). The position of the Rh^{III} 3d peaks was fixed to be at a distance of 1.3 eV from Rh^{I} 3d peaks to allow consistent fitting.¹²²

XPS positions	Sn 3d _{5/2}	C 1s	Rh ^I 3d _{5/2}	Rh ^{III} 3d _{5/2}	Rh ^{III} /Rh ^I	Rh/Sn
FTO	487.22	285.62	--	--	--	--
FTO 1 min dipped (1)	487.16	285.84	--	310.54	--	0.047
FTO 1 min dipped (2)	487.29	286.02	309.38	310.68	100	0.061
FTO 10 min dipped (1)	487.24	286.25	309.59	310.89	16.7	0.069
FTO 10 min dipped (2)	487.23	286.32	309.72	311.02	8.3	0.057

4.2.2 Surface Modification of FTO using TBABH_4 solutions

Changes in WF of FTO substrates dipped in TBABH_4 solutions in acetonitrile, and subsequently rinsed with pure CH_3CN to remove excess modifier, were not detected using UPS in ultra-high vacuum (10^{-10} mbar), regardless of the concentration of the modifier

solutions and the dipping time chosen. Moreover, no N 1s or B 1s peaks were detected via XPS, indicating little or no presence of TBABH₄ on the FTO surface. However, a decrease in the FTO WF of up to 0.6 eV, similar to what was previously reported for gold,¹⁵⁰ was measured using Kelvin probe in air, Figure 4.4, when the concentration of TBABH₄ and dipping time are increased to 10 mM and 10 min, respectively. To investigate whether the WF modification induced by treatment with TBABH₄ is stable in vacuum, the concentration and dipping time were kept constant. TBABH₄-modified FTO substrates were exposed for one hour to progressively lower pressure, resulting in an increase of the WF from 4.3 eV to 4.5 eV, as shown in Figure 4.5, suggesting that the WF-modification can be mostly preserved up to 10⁻⁶ mbar on the time scale explored. Instead of rinsing three times the FTO surface with pure acetonitrile, FTO substrates were simply dipped in 10 mM TBABH₄ solutions for 10 min (obtaining the so-called “TBABH₄ dropcast” samples), and analysed via UPS. The SECO of FTO shifted by 1.9 eV upon dropcasting TBABH₄ on top of the metal oxide, as reported in Figure 4.6. However, the WF increases from 2.7 eV to 3.2 eV after exposing the dropcast samples to 10⁻¹⁰ mbar for two days, and plateaus at 4.2 eV upon air exposure, Figure 4.5. XPS analysis, Table 4.3, confirms the presence of TBABH₄ on the surface of dropcast samples, as can be evidenced from the *ca.* 1:1 ratio between N 1s and B 1s, and a ratio of *ca.* 1:3 between a relatively high-binding energy C 1s signal and a lower-binding energy C 1s signal, consistent with the expected number of carbon atoms connected to the nitrogen atom in TBABH₄, Figure 4.1, and the carbon atoms connected to only carbon and hydrogen atoms. The ratio between C 1s and N 1s peaks is calculated to be 18, close enough to the theoretical value of 16. The deviation from the ideal value may be associated with the presence of adventitious carbon. Storing the

dropcast sample at 10^{-10} mbar for two days leads to a decrease in the ratio between C 1s and Sn 3d. These XPS and UPS TBABH₄-related data suggest that the ammonium salt could desorb, potentially with decomposition, from the FTO surface over time, causing the WF to approach pre-modification values. The reversibility of the WF modification of FTO using TBABH₄ seems consistent with physisorption, as proposed by Kemerink *et al.*¹⁵⁰ However, if C₆₀ were to be deposited on top of the TBABH₄-modified FTO, it seems reasonable to assume that the ammonium salt would not desorb and the induced WF reduction would be preserved. To do so, in the following sections, C₆₀ was vacuum deposited within 1 h from vacuum exposure at 10^{-6} mbar. Vacuum deposition of C₆₀ was chosen as the preferred processing method on top of solution-treated substrates, instead of spin-coating, to prevent washing off the surface modifiers, as was discussed for (RuCp*mes)₂ and (IrCp*Cp)₂ in section 2.4.

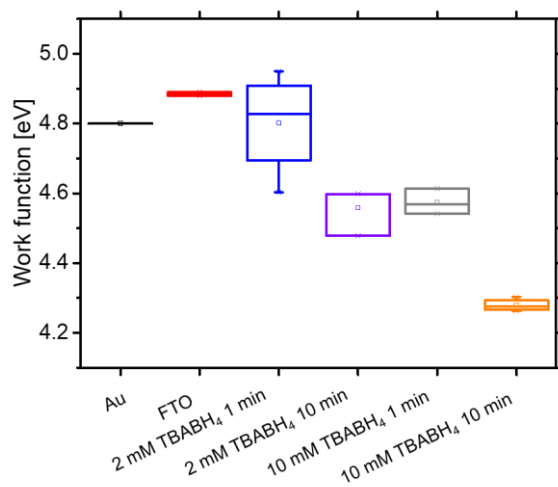


Figure 4.4 WF of pristine and modified FTO as a function of dipping time and concentration of TBABH₄ solutions. After dipping, modified substrates were rinsed three times with pure acetonitrile. WF values were measured via Kelvin probe in air using gold as a reference. 75% of the sample data lie in the rectangular boxes, and horizontal lines within the boxes indicate the sample average. A minimum of four measurements was performed on each sample.

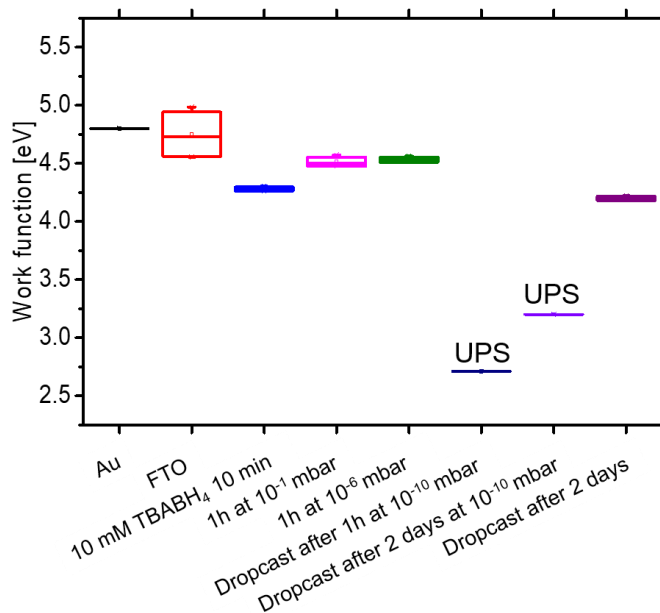


Figure 4.5 WF of pristine and modified FTO as a function of pressure and modification protocol (dipping/rinsing vs. dropcasting) using TBABH₄ solutions. Unless specified otherwise, WF values were measured via Kelvin probe in air using gold as a reference. 75% of the sample data lie in the rectangular boxes, and horizontal lines within the boxes indicate the sample average. A minimum of four (two) measurements was performed on each sample analyzed via Kelvin probe (UPS).

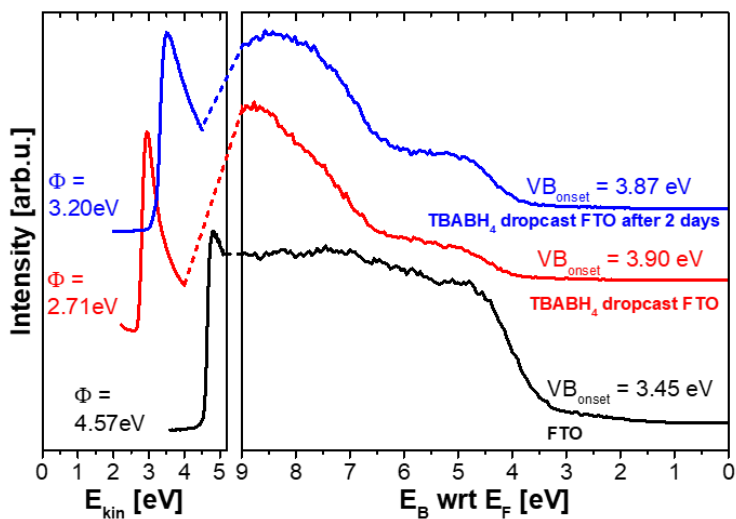


Figure 4.6 UPS spectra of piranha-cleaned FTO and FTO modified by dipping in 10 mM TBABH₄ solutions for 10 min, without rinsing, measured immediately or after 2 days. (E_{kin} = kinetic energy; E_B = binding energy with respect to the Fermi level, E_F). UPS was performed at a base pressure of 10^{-10} mbar.

Table 4.2 XPS positions for TBABH₄-dropcast FTO immediately analyzed after modification and analyzed after being stored for two days at 10⁻¹⁰ mbar. FTO was modified by dipping in 10 mM solutions of the ammonium salt for 10 min, without rinsing. All values are in eV.

XPS positions	Sn 3d _{5/2}	C 1s _{C-C}	C 1s _{C-N}	N 1s	B 1s
TBABH ₄ dropcast FTO	487.25	286.81	287.98	403.49	188.05
TBABH ₄ dropcast FTO after 2 days	487.24	286.79	287.96	403.93	188.20

Table 4.3 Peak ratios of XPS signals for TBABH₄-dropcast FTO immediately analyzed after modification and analyzed after being stored for two days at 10⁻¹⁰ mbar. FTO was modified by dipping in 10 mM solutions of the ammonium salt for 10 min, without rinsing.

Sample	C-C/C-N	C/N	N/B	C/Sn
TBABH ₄ dropcast FTO	2.8	18.4	1.0	6.8
TBABH ₄ dropcast FTO after 2 days	2.6	18.1	1.1	5.6

4.3 Impact of Surface Treatments on in-Plane Electrical Conductivity of C₆₀

In chapter 3 it was shown that the molecules of C₆₀ at the interface with FTO covered with vacuum-deposited (RhCp*₂Cp)₂ are *n*-doped through electron transfer from the modifier layer, which predominantly consists of unreacted dopant. Although XPS analysis, Table 4.1, suggests that there is not a lot of unreacted dopant on the surface of FTO when (RhCp*₂Cp)₂ is solution processed, *n*-doping at the modified FTO/C₆₀ interface is expected to take place because the dopant-treated electrode, with a WF much lower than the *EA* of the ETM, and C₆₀ will establish a common electrochemical potential through substrate-to-overlayer charge transfer. Analogous considerations are valid when FTO is treated with TBABH₄ solutions with or without triple rinsing, and subsequently coated with the

fullerene, since a WF as low as 2.7 eV can be obtained when TBABH₄ is dropcast on the metal oxide, Figure 4.6. If indeed interfacial *n*-doping were to take place, the lateral conductivity of C₆₀ would increase. To test this hypothesis, C₆₀ (100 nm) was deposited on detergent/solvent-cleaned (DSC) glass treated with 2 mM solutions of (RhCp**Cp*)₂ and 10 mM solutions of TBABH₄. On top of C₆₀, silver electrodes were deposited and transmission line measurements (discussed in section 4.7.4) were performed to measure the sheet resistance (*R_s*) of the ETM, and determine its conductivity (*σ*), its resistivity (*ρ*), and the resistance at the C₆₀/Ag contact (*R_c*), reported in Table 4.4 and Table 4.5.

Table 4.4 Sheet resistance of C₆₀ and resistance at the C₆₀/silver contact as a function of surface treatments on glass.

Surface treatment	<i>R_s</i> (Ω □ ⁻¹)	<i>R_c</i> (Ω)
None	$4.3 \times 10^{10} \pm 2.2 \times 10^{10}$	$3.9 \times 10^9 \pm 2.1 \times 10^9$
1 min (RhCp* <i>Cp</i>) ₂	$2.4 \times 10^8 \pm 1.1 \times 10^8$	$8.9 \times 10^6 \pm 6.4 \times 10^6$
10 min (RhCp* <i>Cp</i>) ₂	$8.3 \times 10^8 \pm 7.3 \times 10^7$	$3.7 \times 10^7 \pm 1.9 \times 10^7$
10 mM TBABH ₄ 10 min	$1.7 \times 10^9 \pm 1.1 \times 10^9$	$1.1 \times 10^8 \pm 7.4 \times 10^7$
TBABH ₄ dropcast	$6.3 \times 10^8 \pm 2.3 \times 10^8$	$7.4 \times 10^7 \pm 1.6 \times 10^7$

Table 4.5 Resistivity and conductivity of C₆₀ as a function of surface treatments on glass.

Surface treatment	<i>ρ</i> (Ω cm)	<i>σ</i> (S cm ⁻¹)
None	$2.2 \times 10^5 \pm 1.1 \times 10^5$	$5.5 \times 10^{-6} \pm 2.7 \times 10^{-6}$
1 min (RhCp* <i>Cp</i>) ₂	$1.2 \times 10^3 \pm 5.6 \times 10^2$	$1.0 \times 10^{-3} \pm 6.2 \times 10^{-4}$
10 min (RhCp* <i>Cp</i>) ₂	$4.2 \times 10^3 \pm 3.6 \times 10^2$	$2.4 \times 10^{-4} \pm 2.0 \times 10^{-5}$
10 mM TBABH ₄ 10 min	$8.7 \times 10^3 \pm 5.4 \times 10^3$	$1.4 \times 10^{-4} \pm 6.5 \times 10^{-5}$
TBABH ₄ dropcast	$3.2 \times 10^3 \pm 1.1 \times 10^3$	$3.5 \times 10^{-4} \pm 1.5 \times 10^{-4}$

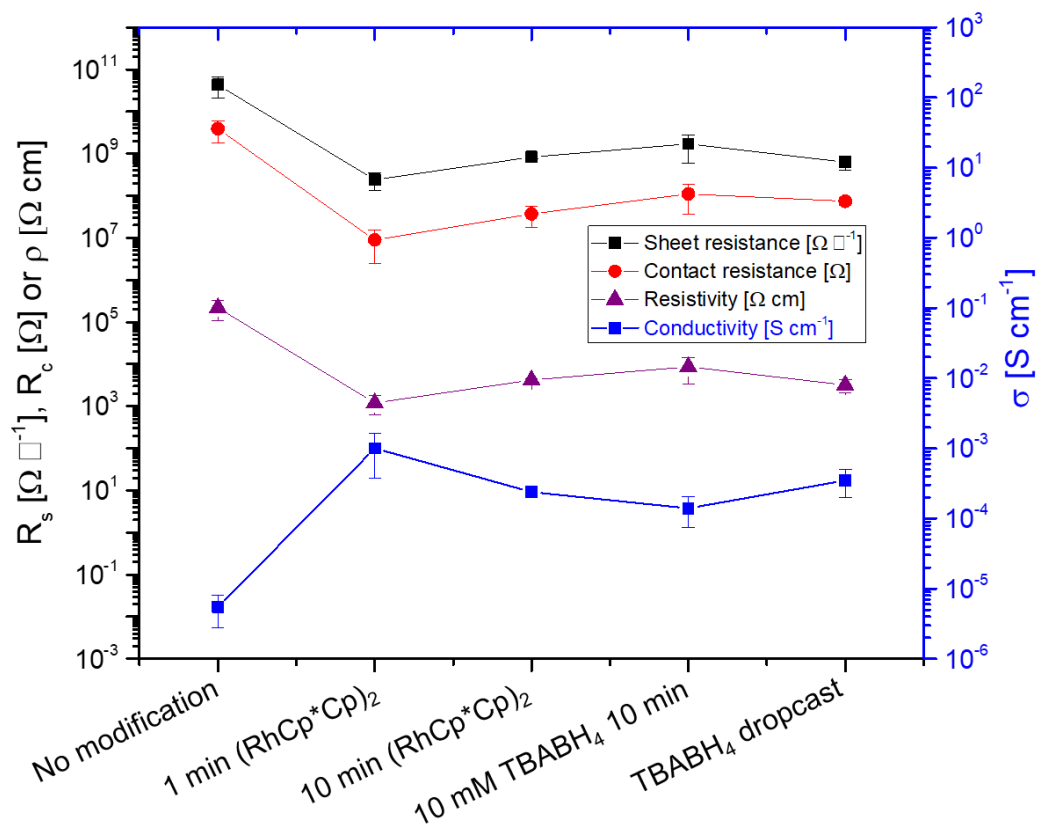


Figure 4.7 Sheet resistance, resistivity and conductivity of C₆₀, and contact resistance of C₆₀ with silver electrodes as a function of the surface treatment applied on DSC glass.

The conductivity of C₆₀ increases by up to two orders of magnitude when the DSC glass substrate is dipped for 1 min in a 2 mM solution of (RhCp*Cp)₂, Figure 4.7. Increasing dipping time to 10 min leads to a slight decrease in conductivity, which could be correlated with an increase in unreacted dimer present on the surface, as shown in the XPS spectra of dimer modified FTO in Figure 4.3. However, since glass is an insulator, electron transfer from the dimer to the substrate is unlikely to occur, and the observed changes in conductivity may be associated to unreacted dimer on glass entirely reacting

with the ETM; although excess dimer on the surface leads to lower conductivity, as shown in Figure 4.7. Treating glass with TBABH₄ solutions, with or without the rinsing step, yields similar conductivity values to those obtained when C₆₀ is deposited on top of glass dipped for 10 min in dimer solutions, corroborating the hypothesis that interface doping takes place. The resistance at the C₆₀/silver electrode contact decreases as the conductivity of C₆₀ increases, Figure 4.8, and contact resistance up to two orders of magnitude lower is achieved with a 1 min dimer treatment.

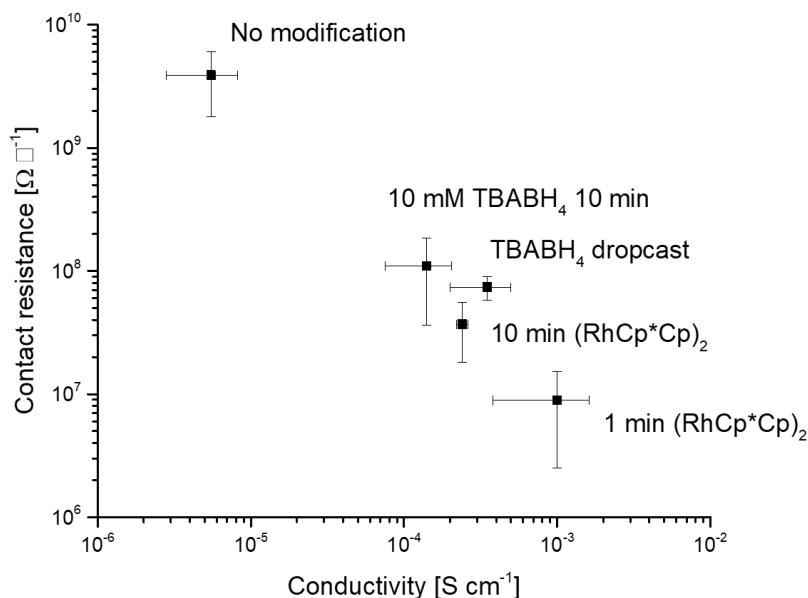


Figure 4.8 Resistance at the C₆₀/Ag contact plotted as a function of the conductivity of C₆₀, showing the effect of the surface treatments on both.

4.4 Through-Plane Electrical Behavior of Surface-Modified FTO

Simple sandwich devices were fabricated to assess whether surface-modified FTO behaves as a low WF material and, therefore, as an electron-injecting electrode to C₆₀. The architecture of the devices consisted of FTO (bare or modified)/C₆₀ (200

nm)/bathocuproine (BCP, 10 nm)/Au (80 nm), where BCP is used as a buffer layer to prevent the diffusion of metal atoms into C₆₀ and to reduce the leakage current.¹⁵¹ Figure 4.9 and Figure 4.10 show the current density-voltage ($J - V$) dark characteristics at room temperature of the sandwich devices. PEIE was used as a reference modifier, as previously shown in section 392.3 for the investigation of the electrical behavior of dimer-modified ITO. The $J - V$ curves can be understood in terms of the superimposition of diode and resistor electrical characteristics, the former describing electron injection and the latter leakage currents. The $J - V$ plot in the semi-logarithmic scale exhibit a diode behavior in forward bias for unmodified FTO substrates, Figure 4.9. However, upon treating the FTO with PEIE, TBABH₄, or (RhCp**Cp*)₂ solutions there is a large increase in the current density in reverse bias, and devices built on modified electrodes behave as resistors. This change in electrical behavior could be explained by both an increase in conductivity of C₆₀, discussed in section 4.3 and highlighted by a steeper current density slope around $V = 0$, and by the Fermi level of FTO being pinned to the LUMO of C₆₀. These two contributions lead to the formation of good electrical contacts at the FTO/C₆₀ interface. A similar observation was made by Zhou *et al.*, who showed how *n*-channel transistors fabricated using gold as source and drain electrodes become resistors when more than 1 nm of PEIE is deposited on the metal.⁶⁰

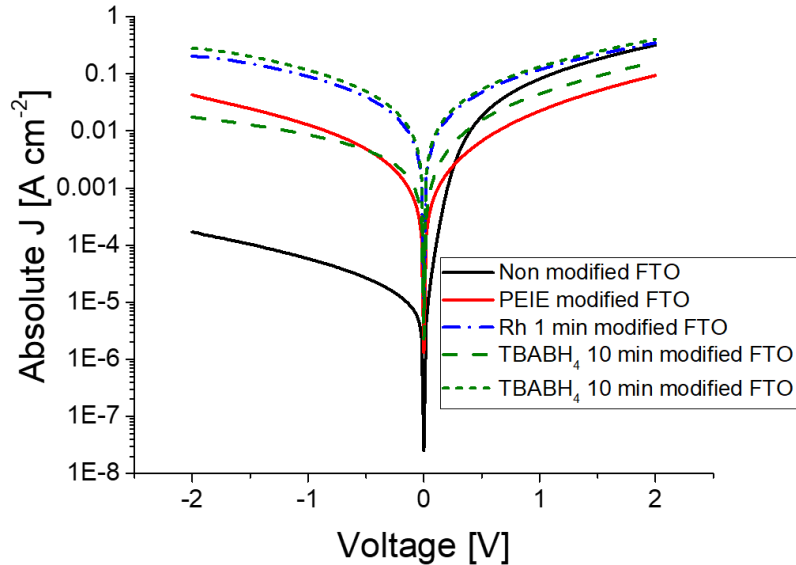


Figure 4.9 Semi-logarithmic plot of $J - V$ characteristics for devices with structure piranha cleaned-FTO (modified or unmodified)/C₆₀ (200 nm)/BCP (10 nm)/Au (80 nm). In forward bias FTO acts as the electron-injecting electrode. Note $J - V$ characteristics for two different devices with TBABH₄-modified FTO is shown.

Interestingly, 70% of the devices fabricated by dipping FTO in 10 mM TBABH₄ solutions for 10 min, followed by rinsing with pure acetonitrile, exhibit a similar electrical behavior to devices with (RhCp*₂Cp)₂-modified FTO. The remainder 30% of devices with TBABH₄ electrodes exhibit $J - V$ characteristics similar to devices with PEIE-modified FTO, as shown by the two different $J - V$ plots for TBABH₄-modified FTO in Figure 4.9. Increasing the amount of TBABH₄ on the FTO surface, by avoiding rinsing the metal oxide after dipping in 10 mM solutions, causes the devices to behave like those built on PEIE-modified FTO. Therefore, an explanation for the deviation in electrical behavior of devices where FTO is rinsed after the modification with TBABH₄, is that PEIE-like behavior is obtained when an excessively thick TBABH₄ layer, which is expected to act as an insulator,

is present between the FTO and C_{60} , limiting charge injection and collection. The excess $TBABH_4$ could stem from accidental non-uniformity in the rinsing protocol.

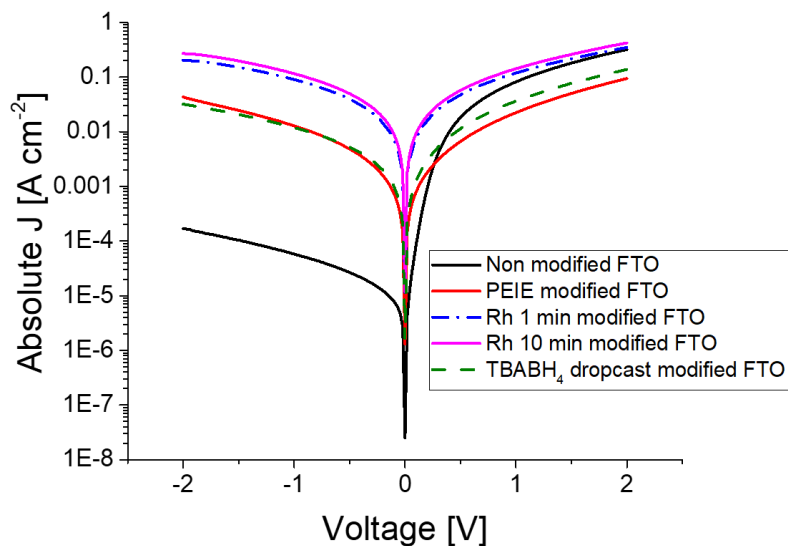


Figure 4.10 Semi-logarithmic plot of $J - V$ characteristics for devices with structure DSC-FTO (modified or unmodified)/ C_{60} (200 nm)/BCP (10 nm)/Au (80 nm). In forward bias FTO acts as the electron-injecting electrode.

Increasing the dipping time of FTO substrates in 2 mM $(RhCp^*Cp)_2$ solutions from 1 min to 10 min does not lead to appreciable differences in current density.

4.5 Impact of FTO Surface Treatments on Perovskite Solar Cells

Perovskite solar cells with $n-i-p$ architecture were fabricated to assess the impact of work function modification of FTO and interfacial doping of C_{60} with $(RhCp^*Cp)_2$ and $TBABH_4$. The architecture of the solar cells consisted of FTO (bare or modified)/ C_{60} /CH₃NH₃PbI₃/spiro-OMeTAD/Ag. The average device performance parameters are shown in Table 4.6, while the current density – voltage ($J - V$) curves of the best-performing solar cells with evaporated CH₃NH₃PbI₃ are shown in Figure 4.11.

Solar cells fabricated on top of FTO modified by dipping in $(\text{RhCp}^*\text{Cp})_2$ solutions for 1 min or 10 min exhibit similar factor (FF) and open-circuit voltage (V_{oc}), but higher short-circuit current (J_{sc}) and stabilized power conversion efficiency (SPO), compared to devices fabricated on unmodified FTO. SPO is defined as the power conversion efficiency (PCE) of devices held at their $J - V$ determined maximum power point. However, dipping FTO in rhodium-based dopant solution for 1 min greatly improves the SPO of devices from an average of 13.9% when FTO is unmodified to 15.6%, which corresponds to a 12% relative increase. Their $J - V$ determined PCE also increases from an average of 13.6% to 14.7%. The increase in J_{sc} , and the associated increase in PCE, suggest an improvement in the charge collection upon introduction of $(\text{RhCp}^*\text{Cp})_2$ at the FTO/ C_{60} contact, and is consistent with what previously observed in PSCs where FTO was covered in vacuum-deposited dimer,¹²³ reported in section 3.5. Increasing the amount of unreacted dopant by increasing dipping time from 1 min to 10 min does not seem to drastically affect J_{sc} , FF and V_{oc} ; however, slightly higher SPO and standard deviations are observed. It must be noted that the device fabrication protocol, section 4.7.5, does not include an annealing step that could further promote electron transfer from the unreacted dimer to C_{60} and perhaps dopant diffusion through the ETM, since the perovskite is evaporated.

Improvements in J_{sc} , FF and PCE are also observed after the electrode/ C_{60} interface is modified using TBABH₄. The highest average PCE and SPO, 15.1% and 15.0% respectively, were obtained by dipping the electrode in 10 mM solutions for 10 min and rinsing the surface with pure acetonitrile. In other words, modifying the surface with the optimized TBABH₄ conditions leads to an 8% increase in SPO relative to the control solar cells. Similarly to what was observed for solar cells with $(\text{RhCp}^*\text{Cp})_2$ -modified FTO, the

V_{oc} does not seem to be significantly affected by the TBABH₄ modification treatment. However, the J_{sc} , and to a lesser extent the FF, increase when the optimal dipping time and TBABH₄ concentration are used relative to the unmodified devices. These observations are consistent with an increase in the charge collection at the FTO/C₆₀ contact (higher J_{sc}), and suggest that surface modification does not impact recombination within the perovskite absorber (constant V_{oc}). Dropcasting FTO in 10 mM solutions of TBABH₄ leads to solar cells with a much lower average SPO (3.5%) compared to those fabricated on piranha-cleaned FTO (13.9%), largely because the perovskite absorber layer did not properly form on top of the dropcast substrate, yielding brown-yellow films. However, investigation of the perovskite morphology is beyond of the scope of this chapter.

Table 4.6 Device performance parameters averaged over twelve solar cells with evaporated CH₃NH₃PbI₃.

Surface treatment	J_{sc} (mA cm ⁻²)	V_{oc} (V)	FF (%)	PCE (%)	SPO (%)
None	19.2 ± 0.5	1.02 ± 0.01	70 ± 1	13.6 ± 0.3	13.9 ± 0.1
1 min (RhCp*Cp) ₂	20.2 ± 0.4	1.04 ± 0.01	71 ± 1	14.7 ± 0.4	15.6 ± 0.1
10 min (RhCp*Cp) ₂	20.1 ± 0.3	1.03 ± 0.02	71 ± 1	14.3 ± 0.5	14.7 ± 0.8
2 mM TBABH ₄ 1 min	19.9 ± 0.2	1.02 ± 0.01	70 ± 4	14.1 ± 1	14.9 ± 0.2
2 mM TBABH ₄ 10 min	19.3 ± 0.4	1.03 ± 0.01	71 ± 1	14.0 ± 0.2	14.3 ± 0.2
10 mM TBABH ₄ 10 min	20.3 ± 0.2	1.02 ± 0.01	74 ± 2	15.1 ± 0.3	15.0 ± 0.3
TBABH ₄ dropcast	7.6 ± 3.7	0.8 ± 0.2	50 ± 8	3.6 ± 2.4	3.5 ± 3.2

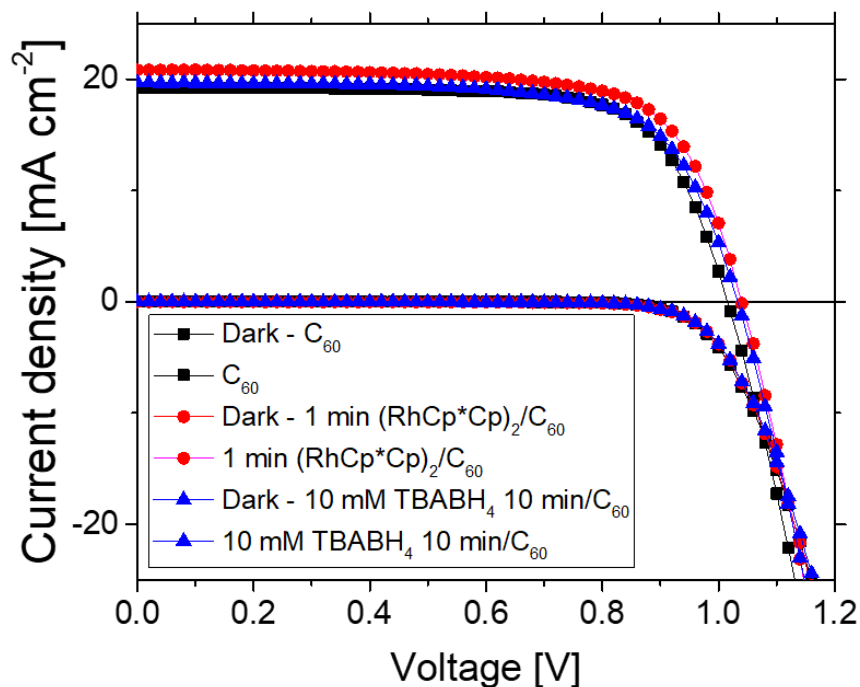


Figure 4.11 Current density – voltage characteristics for the best-performing solar cells fabricated using C_{60} as ETM before and after dipping FTO in 2 mM $(RhCp^*Cp)_2$ solutions, and rinsing three times with pure toluene, or in 10 mM $TBABH_4$ solutions, and rinsing three times with pure acetonitrile.

4.6 Conclusions

The work in this chapter demonstrated that the organometallic metallic dimer $(RhCp^*Cp)_2$ and the ammonium salt $TBABH_4$ can be used to modify the FTO electrode/ETM interface in PSCs, by n -doping the molecules of the organic semiconductor in proximity of the interface and by lowering the WF of the metal oxide so that it is similar or lower than the ETM electron affinity. Solution processing of $(RhCp^*Cp)_2$ leads to a decrease in the WF of the FTO by up to 1.3 eV, since the dopant readily transfers electrons to the electrode and forms monomer cations on the metal oxide surface. However, unlike when $(RhCp^*Cp)_2$ is vacuum deposited and multilayers of unreacted dopant are present,

the amount of unreacted dopant is minimized by shortening the dipping time to 1 min, potentially limiting diffusion of this species under device operation. Moreover, with solution processing of the reductant a higher coverage of the FTO surface is obtained in contrast to formation of islands of unreacted thermally-evaporated dimer. Work function reductions of up to 1.9 eV can be obtained by dropcasting multilayers of TBABH₄ by formation of an interface dipole, but the ammonium salt seems to desorb in ultra-high vacuum. Nevertheless, by limiting exposure of the TBABH₄-modified substrates to high vacuum for < 1 h, an increase in conductivity of C₆₀ of about two orders of magnitude can be measured, although even larger enhancement in conductivity can be obtained via a 1 min dip in (RhCp**Cp*)₂ solutions. *n-i-p* PSCs and simple C₆₀-based sandwich devices confirm that multilayers of surface modifiers hinder charge collection/injection. A 12% and 8% average increase in stabilized power conversion efficiency can be obtained by dipping FTO in solutions of (RhCp**Cp*)₂ or TBABH₄, reaching values as high as 15.7% and 15.3%, respectively.

4.7 Experimental

4.7.1 Materials Synthesis and Purification

(RhCp**Cp*)₂ was synthesized according to methods reported in the literature.^{34, 137} Tetrabutylammonium borohydride (TBABH₄) was purchased from Alfa Aesar and stored in inert atmosphere. Dry toluene and acetonitrile were obtained from a MBraun solvent purification system and freeze-pump-thawed to remove any oxygen present. The final water and oxygen content in the solvents was limited by that in the glovebox atmosphere (<0.5 ppm water and <50 ppm oxygen).

4.7.2 *Sample Preparation*

FTO was cut into 2.54 cm × 2.54 cm substrates (or 1 cm × 1 cm for UPS/XPS/Kelvin Probe studies), partially covered with tape and etched by exposure to a 2 M HCl solution and zinc powder. The FTO substrates were immersed for 90 min in a H₂SO₄:H₂O₂ 3:1 (v/v) piranha solution. The FTO substrates were rinsed with deionized water, and dried under a nitrogen flow. The non-modified FTO substrates were then immediately used.

Piranha-cleaned substrates were transferred to a nitrogen-filled glovebox, and were treated with 2 mM solutions of (RhCp**Cp*)₂ in anhydrous and deoxygenated toluene for 1 to 10 min, or with 2 mM – 10 mM solutions of TBABH₄ in anhydrous and deoxygenated acetonitrile for 1 to 10 min. To remove unreacted modifier, the treated substrates were rinsed three times with toluene or with acetonitrile – with only the exception of the TBABH₄-dropcast samples, which were not rinsed in any solvent – dried with a flow of nitrogen, and immediately transferred under inert atmosphere to the UPS/XPS analysis chamber or to a vacuum thermal evaporation system for device fabrication. The molarity of dimer solutions was kept constant at 2 mM, since further dopant additions led the compound to precipitate.

4.7.3 *Surface Characterization*

Kelvin Probe analysis (KP Technology Ltd.) was performed in air, using a gold tip with a diameter of 2 mm. The work function of a gold standard (4.8 eV) was measured at the beginning of each set of measurements and after analysing 2 samples. Measuring the work function of gold allows to account for instrumental drift. Four data points were

collected for each FTO substrate (1 cm × 1 cm) before and after modification, and average values and standard deviations were calculated. UPS and XPS measurements were carried as described in section 3.7.2.

4.7.4 Transmission Line Measurements

Glass was cut into 2.54 cm × 2.54 cm substrates, which were then scrubbed and cleaned in sequential 20 min ultrasonic baths of detergent water, deionized (DI) water, acetone, and isopropanol at room temperature. The substrates were then rinsed with isopropanol and dried off with nitrogen. Detergent/solvent-cleaned (DSC) glass was then modified following the procedure indicated in section 4.7.2. Modified and unmodified glass was immediately transferred without air exposure to a vacuum thermal evaporation system (SPECTROS, K. J. Lesker), for the deposition of C₆₀ (100 nm) and silver metal (100 nm). The Ag electrodes were deposited through a shadow mask to define fine metal lines, with a spacing between them linearly increasing from 600 to 2400 μm. Equation 31 below describes the relationship between the total resistance (R_t), the sheet resistance (R_s) of the C₆₀ films and C₆₀/silver contact resistance (R_c)¹⁵²:

$$R_t = 2R_c + \frac{R_s d_i}{w}, \quad (31)$$

where w is length of the Ag electrode and d_i is the spacing between electrodes. The data point collected were fitted with a regression line described by equation 31. The fit was considered valid only if the coefficient of determination (R^2) is higher than 0.95. Resistivity values were calculated by multiplying the sheet resistance by the thickness of the C₆₀ films, and conductivity values were calculated as the reciprocal for resistivity values.

4.7.5 Diode Fabrication

For PEIE control experiments, a PEIE solution (0.4 wt%) was spin-coated on top of piranha-cleaned FTO substrates at a speed of 5000 rpm for 60 s and an acceleration of 1000 rpm s⁻¹; the spin-coated samples then were annealed at 100 °C for 10 min in air, as previously specified in section 2.6.4 for PEIE on ITO. Modifications using (RhCp* Cp)₂ and TBABH₄ were carried out in the glovebox as described in section 4.7.2; the samples were then transferred to a vacuum thermal evaporation system (SPECTROS, K. J. Lesker) without air exposure. C₆₀ (200 nm), bathocuproine (BCP) (10 nm), and Au (80 nm) were deposited sequentially through a shadow mask at a base pressure of 2 × 10⁻⁷ Torr on the unmodified, PEIE-modified, TBABH₄-modified, or dimer-modified FTO substrates. The effective area of the devices obtained was 11.2 mm². Current density-voltage (*J* – *V*) curves were measured in a nitrogen-filled glovebox in the dark by using a source meter (2400 SourceMeter, Keithley Instruments Cleveland, OH) controlled by a LabVIEW program.

4.7.6 Solar Cell Fabrication

Modified and piranha-cleaned substrates were deposited on a mask and loaded into a vacuum deposition chamber, where 10 nm of C₆₀ were deposited at 10⁻⁶ mbar at a rate of 0.1 Å s⁻¹. In the same vacuum chamber, the samples were subsequently covered by a 450 nm-thick layer of CH₃NH₃PbI₃, obtained *via* the coevaporation of PbI₂ and CH₃NH₃I at 10⁻⁶ mbar. After the substrates were cooled down to room temperature, the hole-transporting material 2,2',7,7'-tetrakis(*N,N'*-di-*p*-methoxyphenylamine)-9,9'-spirobifluorene (spiro-OMeTAD) was deposited from chlorobenzene with additives at a concentration of 30 mM for lithium bis(trifluoromethanesulfonyl)imide (Li-TFSI) and of

80 mM for *tert*-butylpyridine (*tBP*) via spin-coating at 2000 rpm, 2000 rpm/s for 45 s. 110 nm thick silver electrodes were thermally evaporated at 1×10^{-6} mbar through a shadow mask to create solar cells with a total active area of 0.0919 cm², as defined by the overlap between FTO and silver. Current density-voltage characterization was carried out as specified in section 3.7.4.

CHAPTER 5. N-DOPING OF A FULLERENE THAT CAN BE THERMALLY INSOLUBILIZED AS AN ELECTRON-TRANSPORTING MATERIAL FOR METAL HALIDE PEROVSKITE SOLAR CELLS

5.1 Introduction

Fullerene derivatives are increasingly being used as electron-transporting materials (ETMs) for perovskite-based devices due to their favorable band alignment with perovskite absorbers. Additionally, the perovskite/C₆₀ interface has been shown to have a decreased defect density as compared to conventional oxide-based ETMs such as TiO₂.¹⁰⁴ Therefore, fullerene derivatives have been increasingly used as electron-transporting materials (ETMs). In chapter 3 and chapter 4 the perovskite layer was either vacuum-deposited or cast onto ETMs using an acetonitrile/methylamine solvent mixture,¹³⁴ which does not dissolve the organic ETMs. However, most fullerene-based materials are soluble in dimethylformamide (DMF), which is the most commonly employed solvent to process the perovskite absorbers. Therefore, shunting paths are created when perovskites are solution-processed from DMF onto fullerene layers, causing an increase in charge recombination. To circumvent this issue, the thickness of the ETM can be increased to more than 30 nm, so that only part of the layer is washed away by DMF, but this approach tends to lead to films containing pinholes.^{104, 153} Several strategies have been adopted to achieve a continuous and insoluble fullerene-based electron-transporting material (ETM), for both perovskite and organic photovoltaics (OPVs), where morphology control of fullerenes is critical. These strategies include the addition of a small UV-curable bis-amide

crosslinker,¹⁵⁴ thermally-activated crosslinking with commercially available poly(allylamine),¹⁵⁵ as well as grafting crosslinkable groups (e.g., styryl,¹⁵⁶ oxetane,¹⁵⁷ epoxides¹⁵⁸) on the fullerene.¹⁵⁹ By incorporating a benzocyclobutene moiety (BCB) in place of the methyl group of [6,6]-phenyl-C₆₀-butyric methyl ester (PCBM), a film made of fullerene oligomers (PCBCB)_n is obtained upon spin-coating and heating to 200 °C. BCBs are known to thermally open to form *o*-quinodimethane derivatives, which can then dimerize to form dibenzocyclooctanes. Accordingly, reactions of the type shown in Figure 5.1 (top) may be responsible for the insolubilization of PCBCB, leading to (PCBCB)_n.¹⁶⁰ Cycloaddition of quinodimethane intermediates with fullerenes has been observed in the literature,¹⁶¹ and thus another possible reaction pathway that insolubilizes PCBCB is that shown in Figure 5.1 (bottom). Experimentally, it was found that dimers of PCBCB (i.e., n = 2) are the major product of the thermally activated ring-opening reaction.¹⁶⁰ However, since (PCBCB)_n films are insoluble in DMF and chlorobenzene, it is reasonable to assume that larger oligomers can be formed as well.⁸¹ (PCBCB)_n has been used to prevent aggregation of fullerenes in OPVs under thermal aging at 150 °C,¹⁶⁰ and as an ETM in *n-i-p* perovskite solar cells,⁸¹ reaching stabilized power conversion efficiencies above 17%.¹⁰⁷

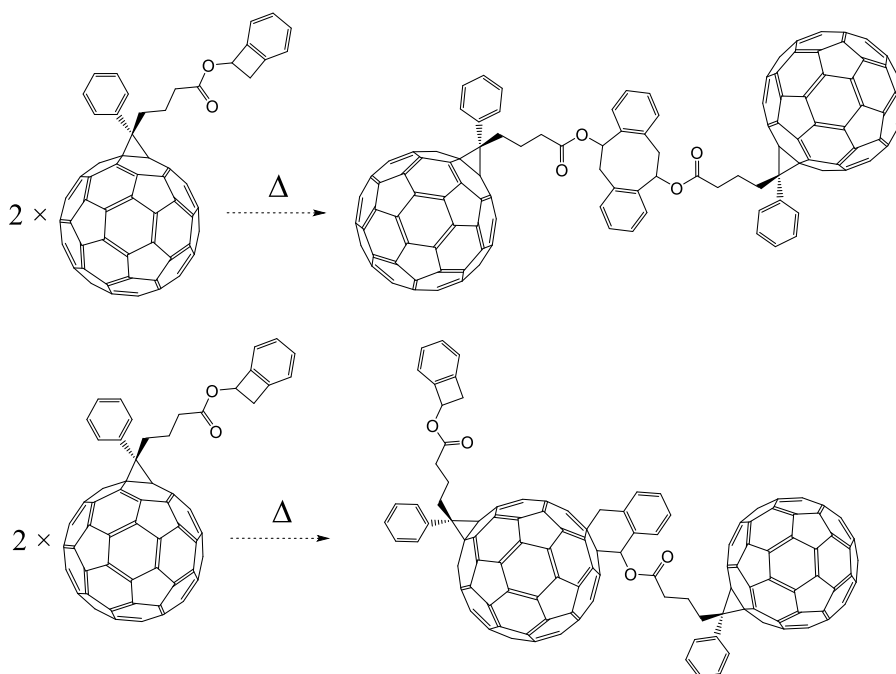


Figure 5.1 Thermally activated reaction pathways of PCBCB molecules, where two benzocyclobutene groups can react together (top), and where a benzocyclobutene group reacts with the fullerene cage (bottom).

By introducing an *n*-dopant in organic ETMs, it is possible to fill electronic traps and increase the number of charge carriers, therefore increasing the conductivity of the ETM.¹⁶² 1,3-Dimethyl-2,3-dihydro-1*H*-benzimidazol-2-yl (N-DMBI-H) derivatives have been used to *n*-dope C₆₀,¹⁵³ PCBM,¹⁶³ and a perylene diimide,¹¹⁹ leading to a decrease in the density of sites where trap-assisted recombination can occur, and to improvements not only in power conversion efficiency but also in the stability of perovskite solar cells (PSCs) under illumination.¹⁵³ However, while DMBI derivatives are attractive due to their air-stability, their doping mechanism involves a hydride transfer and the formation of side-products, which, at best, are species that dilute the semiconductor molecules. Moreover, N-DMBI derivatives in some cases requires activation by overnight thermal annealing after film deposition.^{142, 164-165} Organometallic dimers can dope electron acceptors with electron

affinities larger than 2.8 eV by transferring electrons to the acceptor and forming monomer cations, without the formation of any byproducts or needing overnight thermal activation.⁸⁷ To date, it has been assumed that, while possible, diffusion of monomer cations is less likely than, for example, alkali metal ions, given the large size of the former. However, while diffusion of organometallic *p*-dopants in organic semiconductors has been investigated,¹⁶⁶ little experimental data are available regarding the diffusion of organometallic dimers. Results presented in chapter 3 show that in bilayers made of organometallic dopant/ETM, (RhCp* Cp)⁺ could potentially diffuse into ETMs such as C₆₀ and PTCBI during the annealing process. In light of this, it is worthwhile assessing whether the network of oligomers formed via the thermal activation of BCB moieties, could be sufficient to prevent or limit the diffusion of (IrCp* Cp)⁺. While such a network of oligomers is sufficiently dense to prevent the dissolution of (PCBCB)_n in DMF, it may not be sufficient to prevent monomer cations from diffusing at the temperatures at which the perovskites are crystallized (up to 185 °C for 90 min). One strategy to increase connectivity between the oligomers and potentially limit dopant diffusion is to introduce a crosslinker into the (PCBCB)_n layer. This chapter explores solution doping of (PCBCB)_n using an iridium-based organometallic dimer, (IrCp* Cp)₂, shown in Figure 5.2. The iridium-based dopant has a similar effective reducing strength to (RuCp* mes)₂ and (RhCp* Cp)₂, previously used to dope C₆₀⁸³ and a perylene diimide derivative.¹²³ The crosslinker poly(bicyclo[4.2.0]octa-1(6),2,4-trien-7-yl-hexanoyl methacrylate), PMHBCB, was synthesized, and the effect of its addition as well as that of the iridium dimer on the conductivity of (PCBCB)_n films was investigated. Moreover, the stability of doping to solvent processing and thermal annealing is explored. These results are correlated to the

device performance parameters of PSCs as well as the stability of the devices. The following results were obtained in collaboration with Berthold Wegner and Dr. Thorsten Schultz from the Humboldt University of Berlin (UPS and XPS analysis), Xiaojia Jia from Georgia Tech (assistance with vacuum deposition for conductivity measurements), Dr. Raghunath R. Dasari, Dr. Yadong Zhang and Dr. Elena Longhi (synthetic assistance), Marie-Hélène Tremblay from Georgia Tech and Kelly Schutt from the University of Oxford (optimization of crosslinker concentration in PSCs, fabrication of *p-i-n* devices and solar cell thermal stability studies).

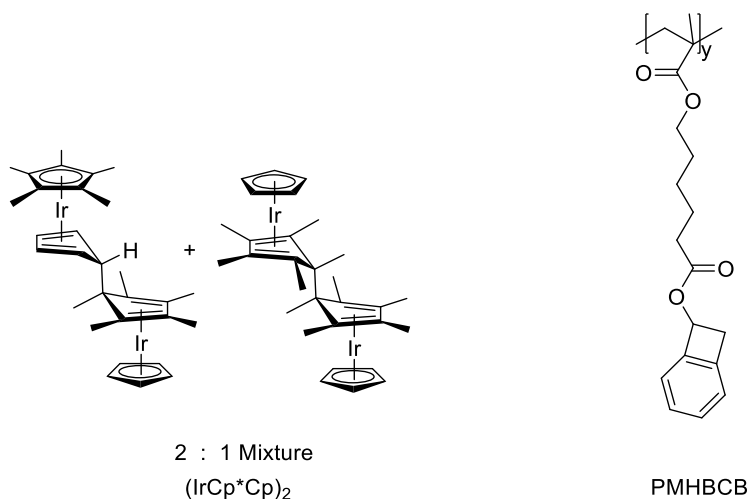


Figure 5.2 Molecular structures of the iridium dimer dopant (IrCp* Cp)₂ and the crosslinker PMHBCB with the same benzocyclobutene moiety as the fullerene derivative.

5.2 Doping of PCBCB using (IrCp* Cp)₂

5.2.1 Doping of PCBCB Solutions

Since the electron affinity of PCBCB is similar to that of PCBM ($EA = 3.7$ eV),¹⁶⁰ it is expected that (IrCp* Cp)₂ can dope PCBCB given the dopant effective reducing

strength (*ca.* -2.0 V vs. $\text{FeCp}_2^{+/0}$ in THF).⁸³ To confirm reduction of the acceptor in solution, UV-vis-NIR spectroscopy was performed. Figure 5.3 shows that as increasing molar concentration of dopant, the absorption peak corresponding to the neutral acceptor¹⁶⁰ at 330 nm decreases in intensity while the presence of a peak at 1070 nm becomes more evident. The latter corresponds to the fullerene radical anion.^{165, 167} Each dimer molecule donates one electron each to two acceptor molecules, hence the molecular percentages in the legend and in the rest of the chapter are reported in terms of iridium monomer cations, $(\text{IrCp}^*\text{Cp})^+$.

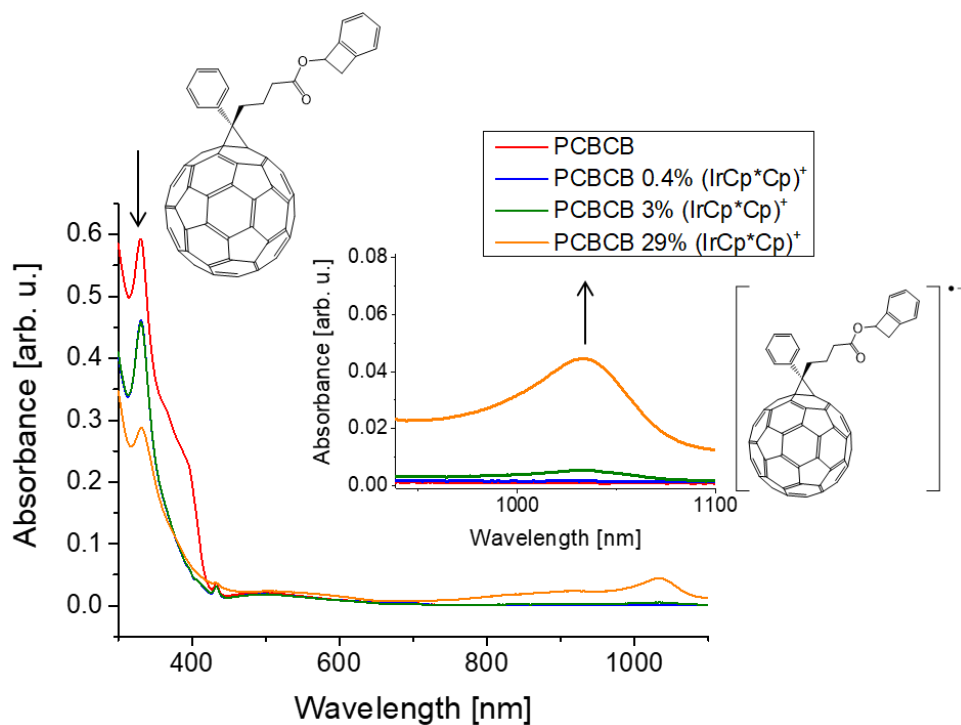


Figure 5.3 UV-vis-NIR absorption spectra of solutions of PCBCB as a function of $(\text{IrCp}^*\text{Cp})^+$ content (molar percentage). The inset shows the appearance of the PCBCB radical anion at 1070 nm and the disappearance of neutral PCBCB at 330 nm.

5.2.2 Doping of (PCBCB)_n Films

Films of PCBCB were spin-coated on piranha-cleaned FTO from blends of solutions of the host and (IrCp**Cp*)₂ in the desired molar ratios. The films were thermally insolubilized leading to the formation of oligomers (PCBCB)_n by heating at 200 °C for 10 min, and were characterized using UPS and XPS. FTO is a transparent conductive metal oxide used as electron-collecting electrode in PSCs. Figure 5.4 shows how the work function (WF) of (PCBCB)_n decreases by up to 0.6 eV and its Fermi level (E_F) progressively shifts further away from the HOMO of (PCBCB)_n with increasing addition of (IrCp**Cp*)₂, suggesting that the number of occupied states increases. At large dopant additions [i.e., 29 mol% (IrCp**Cp*)⁺], the HOMO features of the host material at low binding energy (E_B) become extremely broadened, which is a signature of *n*-doping in the solid state.

The Ir 4f ionization is split into 4f_{5/2} and 4f_{7/2} peaks by spin-orbit coupling; the following discussion and the E_B reported in Table 5.1 and in Figure 5.5 are focused on the Ir 4f_{7/2} component but the trends apply equally to the Ir 4f_{5/2}. In both the present study and previous work, two chemically distinct species are often present in (IrCp**Cp*)₂-containing samples, differing in Ir 4f_{7/2} (and 4f_{5/2}) E_B by *ca.* 1.4 – 1.3 eV.⁴⁰ These are assigned to the unreacted neutral dimer, (IrCp**Cp*)₂, and the monomer cation, (IrCp**Cp*)⁺, that is known to be formed on oxidation of the dimer,³⁴ with the lower E_B signal being assigned to the former, which is formally Ir^I, and the higher E_B signal to the latter, which is formally Ir^{III}. As expected, XPS indicates that most of (IrCp**Cp*)₂ reacts with (PCBCB)_n forming monomer cations, since peak deconvolution of the Ir 4f_{7/2} signal, Table 5.1 and Figure 5.5, shows large Ir^{III} contributions at 63.1 – 63.3 eV, and a small Ir^I peak at 61.8 – 61.9 eV. As

the doping concentration increases, the C 1s signal shifts to higher E_B , consistent with the expected shift of E_F away from the filled valence and core states on n -doping, and with the reduction of the fullerene-derivative to its radical anion, $(\text{PCBCB})_n^{\bullet-}$. On the other hand the ratio between Ir^{III} and Ir^{I} decreases slightly, indicating that more dopant is present in its unreacted form compared to lower doping concentrations.

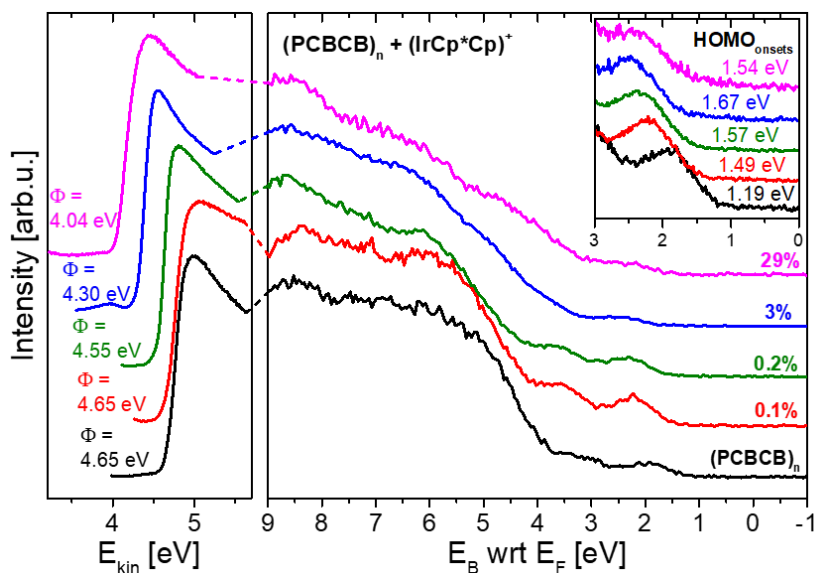


Figure 5.4 UPS spectra of neat and doped $(\text{PCBCB})_n$ with $(\text{IrCp}^*\text{Cp})_2$ (E_{kin} = kinetic energy; E_B = binding energy with respect to the Fermi level, E_F). Dimer content is reported as a function of molar percentage of monomer cations $(\text{IrCp}^*\text{Cp})^+$ relative to the host.

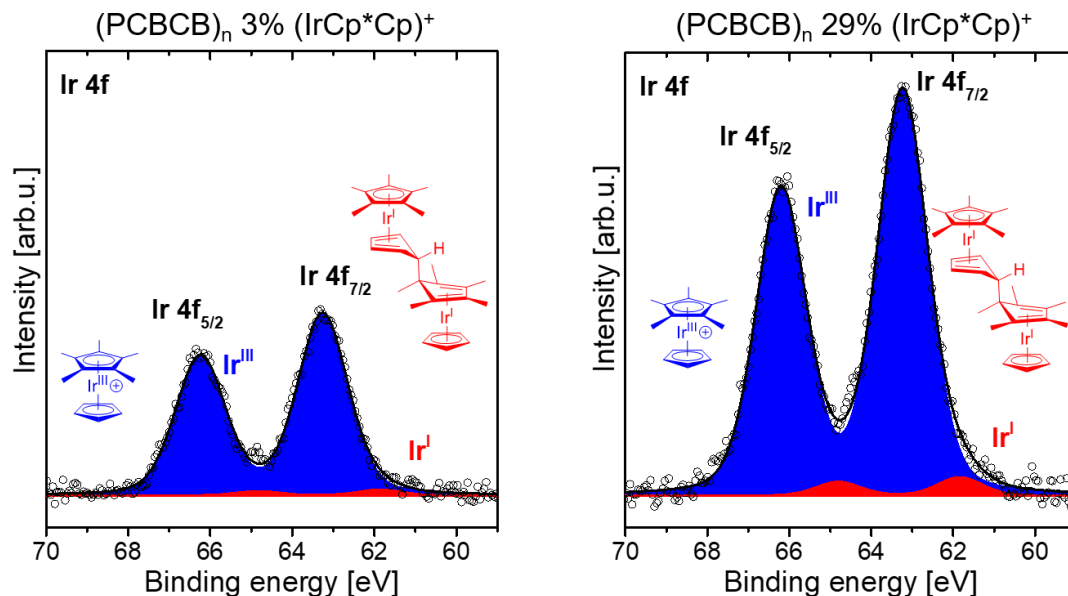


Figure 5.5 XPS spectra of doped $(\text{PCBCB})_n$ with $(\text{IrCp}^*\text{Cp})_2$. Dimer content is reported as a function of molar percentage of monomer cations $(\text{IrCp}^*\text{Cp})^+$ relative to the host.

Table 5.1 XPS positions and peak ratios for pristine or doped $(\text{PCBCB})_n$ films on FTO. All values are in eV (except ratios). All XPS signals were normalized to the one of Sn $3d_{5/2}$. $(\text{IrCp}^*\text{Cp})_2$ content is reported as a function of molar percentage of monomer cations $(\text{IrCp}^*\text{Cp})^+$ relative to the host.

XPS positions	Sn $3d_{5/2}$	C 1s	Ir^{I} $4f_{7/2}$	Ir^{III} $4f_{7/2}$	$\text{Ir}^{\text{III}}/\text{Ir}^{\text{I}}$
$(\text{PCBCB})_n$	487.27	284.64	--	--	--
$(\text{PCBCB})_n$ 0.2% $(\text{IrCp}^*\text{Cp})^+$	487.30	285.03	--	63.09	--
$(\text{PCBCB})_n$ 3% $(\text{IrCp}^*\text{Cp})^+$	487.28	285.29	61.86	63.26	34.5
$(\text{PCBCB})_n$ 29% $(\text{IrCp}^*\text{Cp})^+$	487.23	285.34	61.84	63.24	24.4

5.3 Electrical Conductivity Measurements

5.3.1 Impact of Doping on in-Plane Electrical Conductivity of $(\text{PCBCB})_n$

Since UV-vis-NIR absorption spectroscopy, UPS and XPS suggest that n -doping of PCBCB takes place in solution and in the solid state, transmission line measurements

(discussed in section 4.7.4) were performed to quantify the impact of dopant addition on the in-plane electrical conductivity of the thermally insolubilized fullerene product. Films of (PCBCB)_n or PCBM (50 nm) were spin-coated on detergent/solvent-cleaned (DSC) glass followed by annealing at 200 °C or 70 °C for 10 min, respectively. On top of the ETMs, silver electrodes were vacuum-deposited and the sheet resistance (R_s) of the ETMs was measured to determine their conductivity (σ), their resistivity (ρ), and the resistance at the ETM/Ag contact (R_c), which are reported in Table 5.2 and Table 5.3.

Table 5.2 Sheet resistance of (PCBCB)_n and resistance at the (PCBCB)_n/silver contact as a function of (IrCp* Cp)⁺ content (molar percentage). The sheet resistance of PCBM and resistance at the PCBM/Ag contact are reported for comparison.

Material	R_s ($\Omega \square^{-1}$)	R_c (Ω)
PCBM	$2.8 \times 10^{12} \pm 4.4 \times 10^{12}$	$8.2 \times 10^{10} \pm 6.9 \times 10^{10}$
(PCBCB) _n	$6.7 \times 10^{11} \pm 3.1 \times 10^{11}$	$5.4 \times 10^9 \pm 3.8 \times 10^9$
(PCBCB) _n 0.2% (IrCp* Cp) ⁺	$5.3 \times 10^9 \pm 2.9 \times 10^9$	$2.9 \times 10^7 \pm 2.4 \times 10^7$
(PCBCB) _n 3% (IrCp* Cp) ⁺	$1.0 \times 10^9 \pm 9.4 \times 10^8$	$1.6 \times 10^7 \pm 1.3 \times 10^7$
(PCBCB) _n 29% (IrCp* Cp) ⁺	$1.5 \times 10^8 \pm 3.7 \times 10^7$	$1.4 \times 10^6 \pm 1.0 \times 10^6$

Table 5.3 Resistivity and conductivity of (PCBCB)_n as a function of (IrCp* Cp)⁺ content (molar percentage). The resistivity and conductivity of PCBM are reported for comparison.

Material	ρ ($\Omega \text{ cm}$)	σ (S cm^{-1})
PCBM	$1.4 \times 10^7 \pm 2.2 \times 10^7$	$5.6 \times 10^{-7} \pm 5.0 \times 10^{-7}$
(PCBCB) _n	$3.4 \times 10^6 \pm 1.5 \times 10^6$	$3.7 \times 10^{-7} \pm 2.2 \times 10^{-7}$
(PCBCB) _n 0.2% (IrCp* Cp) ⁺	$2.6 \times 10^4 \pm 1.4 \times 10^4$	$4.5 \times 10^{-5} \pm 1.9 \times 10^{-5}$
(PCBCB) _n 3% (IrCp* Cp) ⁺	$5.1 \times 10^3 \pm 4.7 \times 10^3$	$3.3 \times 10^{-4} \pm 2.3 \times 10^{-4}$
(PCBCB) _n 29% (IrCp* Cp) ⁺	$7.6 \times 10^2 \pm 1.9 \times 10^2$	$1.4 \times 10^{-3} \pm 3.8 \times 10^{-4}$

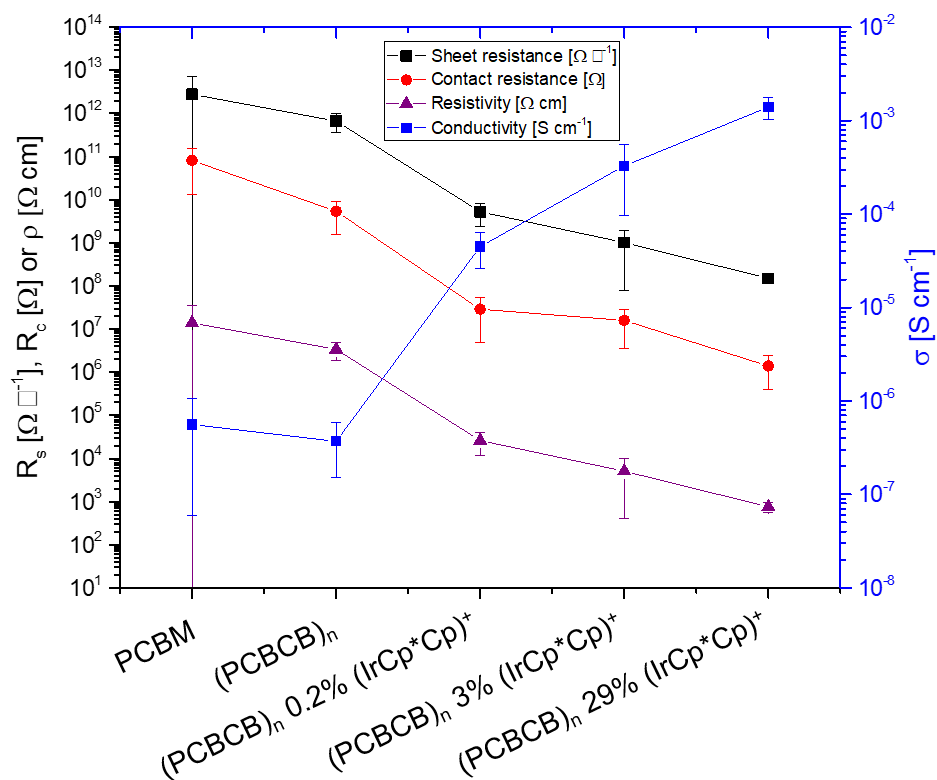


Figure 5.6 Sheet resistance, resistivity and conductivity of (PCBCB)_n, and contact resistance of (PCBCB)_n with silver electrodes as a function of (IrCp* Cp)⁺ content (molar percentage). The sheet resistance of PCBM and resistance at the PCBM/Ag contact are reported for comparison.

Figure 5.6 indicates that thermally insolubilized (PCBCB)_n has an in-plane conductivity comparable to that of PCBM; however, a slightly lower resistance at the (PCBCB)_n/silver contact is observed compared to that at the PCBM/Ag contact. Upon addition of the organometallic dimer the conductivity of (PCBCB)_n increases by up to four orders of magnitude, and the resistance at the (PCBCB)_n/Ag contact decreases by a similar extent. The increase in conductivity is consistent with the E_F shift away from the HOMO of the organic semiconductor, Figure 5.4, confirming *n*-doping.⁸⁷

5.3.2 Impact of Crosslinking on in-Plane Conductivity of Doped (PCBCB)_n

The crosslinker PMHBCB was synthesized via polymerization of a methacrylate monomer containing a BCB moiety using the radical initiator azobisisobutyronitrile (AIBN). To assess whether the introduction of the PMHBCB affects the in-plane electrical conductivity of doped (PCBCB)_n films, transmission line measurements were performed. The concentration of iridium monomer cations, (IrCp**Cp*)⁺, was kept constant at 3 mol% to be able to measure values in conductivity larger than those of undoped (PCBCB)_n and reliably determine the effect of PMHBCB addition, the concentration of which was increased up to 30 mol%. Figure 5.7 shows a ten-fold increase in the conductivity of doped (PCBCB)_n upon the addition of crosslinker. Further, increasing the crosslinker loading in (PCBCB)_n films from 1 mol% to 30 mol% does not lead to a significant increase in conductivity. However, when the concentration of PMHBCB is 20 mol%, the resistance at the fullerene-derivative/silver electrode contact seems to be the lowest; further addition of crosslinker leads to a large increase in *R_c*, approaching values close to those of doped (PCBCB)_n with no crosslinker.

Table 5.4 Sheet resistance of doped (PCBCB)_n and resistance at the doped (PCBCB)_n/silver contact as a function of crosslinker concentration. The (IrCpCp*)⁺ concentration was fixed to 3 mol%.**

Material	<i>R_s</i> (Ω □ ⁻¹)	<i>R_c</i> (Ω)
Doped (PCBCB) _n	$1.0 \times 10^9 \pm 9.4 \times 10^8$	$1.6 \times 10^7 \pm 1.3 \times 10^7$
Doped (PCBCB) _n + 1% crosslinker	$3.7 \times 10^7 \pm 3.6 \times 10^6$	$9.6 \times 10^5 \pm 4.9 \times 10^5$
Doped (PCBCB) _n + 10% crosslinker	$4.3 \times 10^7 \pm 5.8 \times 10^6$	$7.7 \times 10^5 \pm 1.8 \times 10^5$
Doped (PCBCB) _n + 20% crosslinker	$4.3 \times 10^7 \pm 7.1 \times 10^6$	$2.8 \times 10^5 \pm 2.2 \times 10^5$
Doped (PCBCB) _n + 30% crosslinker	$4.4 \times 10^7 \pm 2.9 \times 10^7$	$2.7 \times 10^6 \pm 6.4 \times 10^5$

Table 5.5 Resistivity and conductivity of (PCBCB)_n as a function of crosslinker concentration. The (IrCpCp*)⁺ concentration was fixed to 3 mol %.**

Material	ρ (Ω cm)	σ (S cm ⁻¹)
Doped (PCBCB) _n	$5.1 \times 10^3 \pm 4.7 \times 10^3$	$3.3 \times 10^{-4} \pm 2.3 \times 10^{-4}$
Doped (PCBCB) _n + 1% crosslinker	$1.9 \times 10^2 \pm 1.8 \times 10^1$	$5.5 \times 10^{-3} \pm 5.4 \times 10^{-4}$
Doped (PCBCB) _n + 10% crosslinker	$2.2 \times 10^2 \pm 2.9 \times 10^1$	$4.7 \times 10^{-3} \pm 6.8 \times 10^{-4}$
Doped (PCBCB) _n + 20% crosslinker	$2.1 \times 10^2 \pm 3.5 \times 10^1$	$4.8 \times 10^{-3} \pm 8.8 \times 10^{-4}$
Doped (PCBCB) _n + 30% crosslinker	$2.2 \times 10^2 \pm 1.5 \times 10^2$	$5.9 \times 10^{-3} \pm 3.4 \times 10^{-3}$

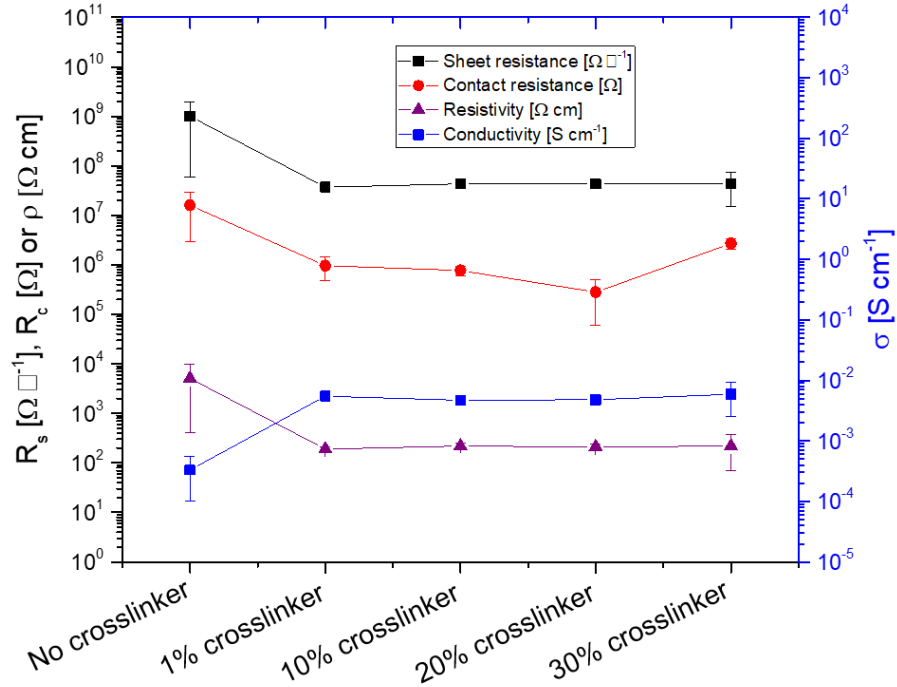


Figure 5.7 Sheet resistance, resistivity and conductivity of doped (PCBCB)_n, and contact resistance of doped (PCBCB)_n with silver electrodes as a function of crosslinker (molar) concentration. The concentration of (IrCpCp*)⁺ in the fullerene derivative was kept constant at 3 mol %.**

Previously reported 2D-GIWAXS analysis on PCBM, PCBCB and (PCBCB)_n films shows that upon formation of the oligomers via annealing, the crystallinity of the

films increases and the spacing between fullerene groups decreases slightly, leading to larger mobility values in $(\text{PCBCB})_n$ compared to PCBCB and PCBM.¹⁶⁰ Noting that pristine materials with high mobility do not always exhibit high conductivity,¹⁶⁸⁻¹⁷⁰ it is possible that the addition of crosslinker PMHBCB may lead to larger conductivity by leading to a more monodisperse array of inter-fullerene spacings. However, further experimental evidence is needed to validate this hypothesis.

5.4 Stability of Doping of $(\text{PCBCB})_n$ Films to Solvent Washing

Results presented in chapter 2 suggest that monomer cations $(\text{IrCpCp}^*)^+$, physisorbed on a negatively charged metal oxide surface, are washed away when an organic semiconductor is spin-coated on top of the metal oxide. Therefore, it is plausible to assume that $(\text{IrCpCp}^*)^+$ in bulk $(\text{PCBCB})_n$ could be washed away with low-molecular weight reduced fullerene oligomers by solvent processing on top of the doped ETM. To test this hypothesis films of doped $(\text{PCBCB})_n$ containing 3 mol% $(\text{IrCp}^*\text{Cp})^+$ were prepared and analyzed by XPS before and after spin-coating solvents commonly used in device fabrication, such as chlorobenzene and DMF. Figure 5.8 shows the iridium elemental contribution – calculated from the area under the Ir 4f peaks – in the films washed with chlorobenzene is not significantly different from the iridium content in non-washed samples. However, films washed with DMF contain less iridium than in the as-prepared ones. To assess whether the addition of the crosslinker PMHBCB could prevent the loss of iridium cations by possibly increasing the linkage between fullerene oligomers, XPS was performed on $(\text{PCBCB})_n$ films containing 10 mol% crosslinker and 3 mol% of $(\text{IrCp}^*\text{Cp})^+$. Figure 5.9 shows that the elemental contribution of iridium does not significantly change upon washing when PMHBCB is present in the films. The small variations in iridium

content in the samples containing PMHBCB can be accounted for by accidental coverage variations, as shown by the slight increase (decrease) in indium and tin (carbon) elemental contribution for the non-washed samples, Figure 5.10.

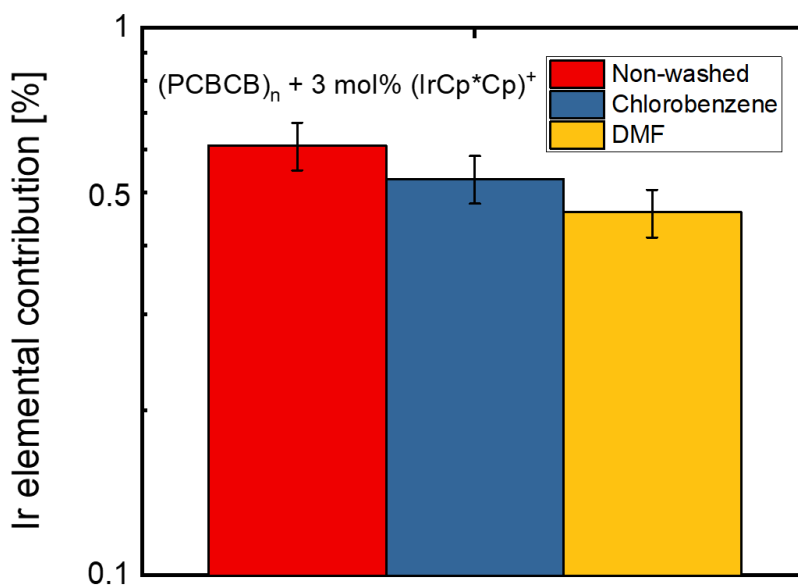


Figure 5.8 Iridium elemental contribution in doped (PCBCB)_n films with 3 mol% (IrCp*Cp)₂ as prepared, and after spin-coating chlorobenzene or DMF on top of it. The elemental contribution of iridium is calculated from the area under the Ir 4f peaks in XPS spectra. The carbon elemental contribution in the same films is constant at around 70%, regardless of washing.

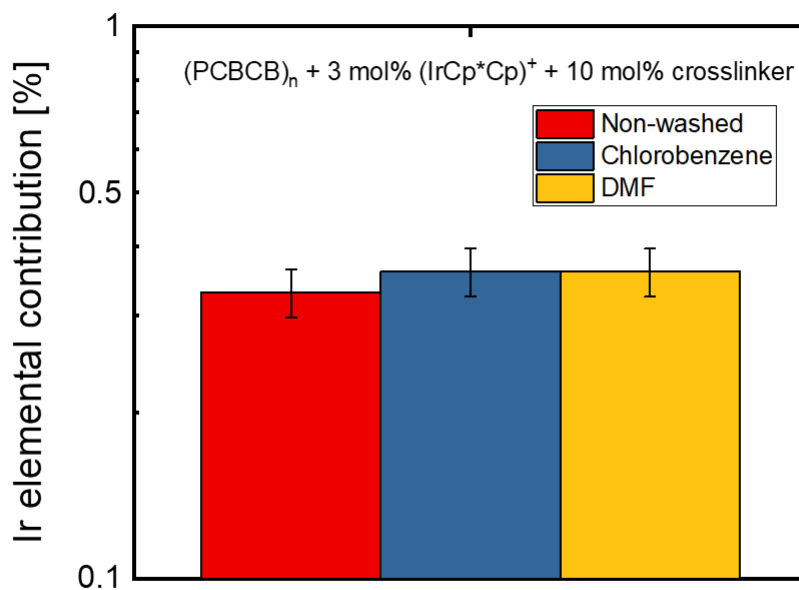


Figure 5.9 Iridium elemental contribution in doped (PCBCB)_n films with 3 mol% (IrCp*Cp)₂ and 10 mol% PMHBCB, as prepared, and after spin-coating chlorobenzene or DMF on top of it. The elemental contribution of iridium is calculated from the area under the Ir 4f peaks in XPS spectra. The carbon elemental contribution in the same films is constant at around 60%, regardless of washing.

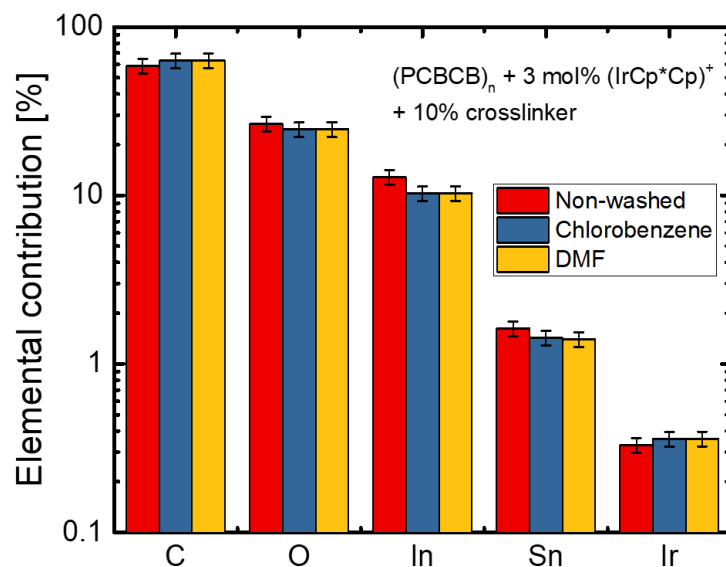


Figure 5.10 Elemental contributions in doped (PCBCB)_n films with 3 mol% (IrCp⁺Cp)⁺ and 10 mol% PMHBCB, as prepared, and after spin-coating chlorobenzene or DMF on top of it. The elemental contribution of carbon, oxygen, indium, tin and iridium are calculated from the area under the C 1s, O 1s, In 3d, Sn 3d and Ir 4f peaks in XPS spectra.

5.5 Diffusion Studies of (IrCp⁺Cp)⁺ in (PCBCB)_n upon Thermal Annealing

To assess whether the network of oligomers, formed via the thermal activation of BCB moieties, could potentially be sufficient to prevent or limit the diffusion of iridium monomer cations, films of (PCBCB)_n containing 29 mol% of (IrCp⁺Cp)⁺ were deposited on ITO substrates. The latter was chosen over FTO because of its lower root mean square surface roughness ($R_{\text{RMS}} = 0.1 \text{ nm}$ vs. 15 nm), which allows relatively easy monitoring of the concentration profile of iridium throughout the film thickness via XPS depth profiling. C₆₀ (20 nm) was vacuum-deposited on top of (PCBCB)_n, to prevent washing of the dopant, and to prevent the introduction of energy barriers for the dopants to diffuse, since C₆₀ and

(PCBCB)_n have similar *EA*,^{87, 160} and only differ little in their structure. Figure 5.11 shows the concentration profile of iridium throughout the as-made bilayer (no annealing). Most of the iridium present in the bilayer is located in the (PCBCB)_n.

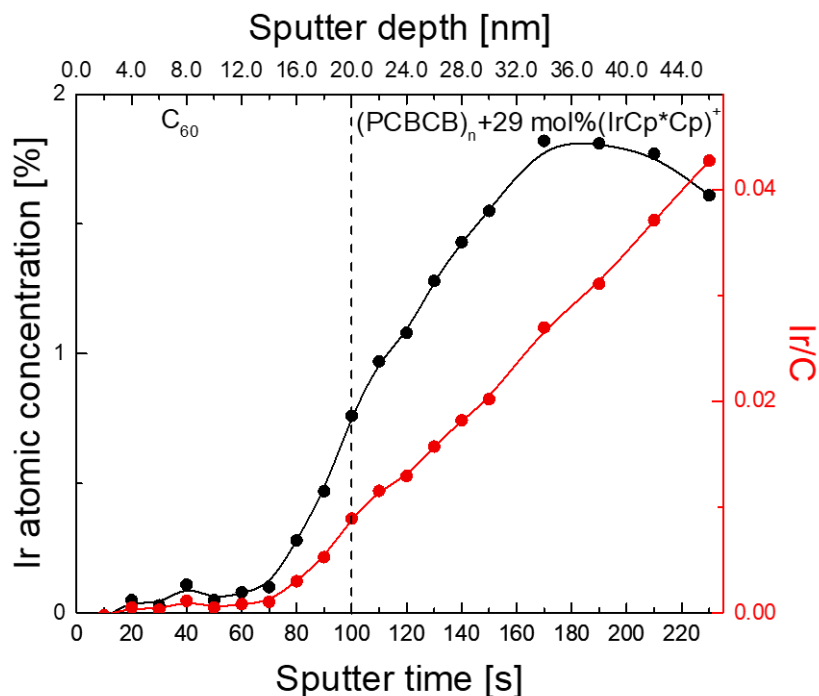


Figure 5.11 Atomic concentration of iridium and ratio between Ir 4f and carbon C 1s peaks as a function of sputter depth and sputter time for (PCBCB)_n films containing 29 mol% (IrCpCp*)⁺, deposited on ITO and covered by 20 nm of vacuum-deposited C₆₀. XPS depth profiling was performed on the samples as-prepared.**

Annealing the bilayer of doped (PCBCB)_n/C₆₀ at 185 °C for 90 min, which is the same annealing protocol used to crystallize the most stable perovskite material reported in the literature, formamidinium-cesium lead mixed halide perovskite^{97, 153} previously deposited on pristine (PCBCB)_n,¹⁰⁷ leads to a redistribution of the iridium content in the bilayer, as shown in Figure 5.12. There is clearly diffusion from the doped (PCBCB)_n layer into the C₆₀ overlayer.

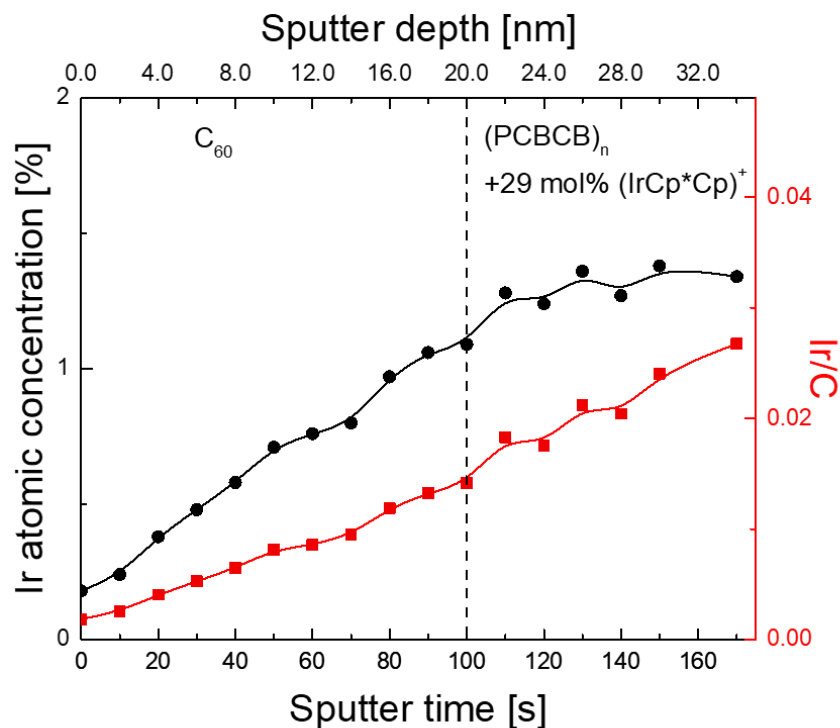


Figure 5.12 Atomic concentration of iridium and ratio between Ir 4f and carbon C 1s peaks as a function of sputter depth and sputter time for $(\text{PCBCB})_n$ films containing 29 mol% $(\text{IrCp}^*\text{Cp})^+$, deposited on ITO and covered by 20 nm of vacuum-deposited C_{60} . XPS depth profiling was performed on the samples after annealing at 185 °C for 90 min.

5.6 The Effect of Dopant and Crosslinker Addition to $(\text{PCBCB})_n$ ETMs in Perovskite Solar Cells (PSCs)

Perovskite solar cells with the *n-i-p* architecture were fabricated to assess the impact of *n*-doping and crosslinking between insoluble oligomers in $(\text{PCBCB})_n$. The architecture of the solar cells consisted of FTO/ETM/ $(\text{HC}(\text{NH}_2)_2)_{0.83}\text{Cs}_{0.17}\text{Pb}(\text{I}_{0.8}\text{Br}_{0.2})_3$ /spiro-OMeTAD/Ag, where $(\text{HC}(\text{NH}_2)_2)_{0.83}\text{Cs}_{0.17}\text{Pb}(\text{I}_{0.8}\text{Br}_{0.2})_3$ is a thermally stable formamidinium cesium lead mixed-halide perovskite,^{97, 107, 153} processed from solutions of DMF and dimethylsulfoxide (DMSO) in a ratio of 4:1. Since PCBCB is a derivative of PCBM, reference solar cells were fabricated using the latter as the organic ETM. However,

PCBM alone is largely washed away when the perovskite is solution-processed on top of it, which can be attributed to a higher solubility in DMF for PCBM than for C₆₀. Therefore, tin oxide nanoparticles (SnO₂ NPs) were introduced to prevent the formation of pinholes in the ETM, when the PCBM is washed. Nevertheless, previous work shows that when formamidinium cesium lead mixed-halide is chosen as the light-absorbing perovskite, SnO₂ NPs work as a buffer layer to improve the electronic contact between fullerenes and FTO.¹⁵³ To single out the impact of *n*-doping on device performance, SnO₂ NPs were used in all solar cells, even though (PCBCB)_n itself is insoluble. The light-absorbing perovskite was deposited using a protocol that requires annealing at 100 °C,¹⁷¹ instead of at 185 °C, in a trade off between attempting to limit dopant diffusion and thermal stability. However diffusion studies at 100 °C need to be performed. The device performance parameters averaged over thirteen solar cells per each type of ETM are shown in Table 5.6, and the current density – voltage (*J* – *V*) curves of the best-performing solar cells are shown in Figure 5.14. At the lowest doping concentration explored [0.2 mol% IrCp**Cp*]⁺, there is a small average increase in open-circuit voltage (*V*_{oc}) and in stabilized power output (SPO) compared to devices with pristine (PCBCB)_n. Once again, SPO is defined as the power conversion efficiency (PCE) of devices held at their *J* – *V* determined maximum power point. On average, the *V*_{oc} increases from 1.08 V to 1.11 V, and the SPO increases from 11.9% to 12.5%, for PSCs fabricated with (PCBCB)_n and doped (PCBCB)_n, respectively. The increase in *V*_{oc}, shown in Figure 5.13, suggests a reduction in the non-radiative recombination at the interface takes place, possibly because of faster charge extraction associated with an increased conductivity of the organic ETM. Variations in fill factor (FF) across devices with *n*-doped (PCBCB)_n are smaller compared to those in devices with

unmodified (PCBCB)_n, although a large increase in FF is not observed, possibly because some of the dopant is washed away by DMF, as shown in section 5.4. Further increasing the dopant content to 3 mol% (IrCp**Cp*)⁺ leads to lower V_{oc} , short-circuit current (J_{sc}) and PCE compared to solar cells with unmodified (PCBCB)_n. Therefore, a low doping level [0.2 mol% IrCp**Cp*)⁺] seems optimal to maximize device efficiency. From a practical standpoint, difficulties in controlling low concentrations of dopants and sensitivity of fullerene radical anions to moisture and oxygen levels can minimize the improvements in PCE. It must also be noted that solar cells fabricated with pristine and doped (PCBCB)_n exhibit on average higher PCE compared to devices containing PCBM (11.5%), when SnO₂ NPs are used as a buffer layer between the ETM and the FTO. Replacing SnO₂ NPs with a compact layer of tin oxide (*c*-SnO₂) covered with a very thin layer of PCBM leads to solar cells with $J - V$ determined PCE of 15.5%, considerably higher than the average PCE of solar cells using (PCBCB)_n with no buffer layer between FTO and the organic ETM (12.2%), as shown in Table 5.7. However, unlike SnO₂ NPs, *c*-SnO₂ functions well as an ETM even without PCBM.¹⁷² Hence, the reference solar cells with *c*-SnO₂/PCBM are not meant to provide a comparison between various fullerene-derivatives as ETMs; they rather provide an indication of the quality of the perovskite and other layers in the device architecture.

Table 5.6 Device performance parameters averaged over thirteen solar cells with solution-processed $(\text{HC}(\text{NH}_2)_2)_{0.83}\text{Cs}_{0.17}\text{Pb}(\text{I}_{0.8}\text{Br}_{0.2})_3$ as a function of the dopant concentration in $(\text{PCBCB})_n$ films. Reference devices were made with PCBM as the organic ETM. All solar cells were made using tin oxide nanoparticles as a buffer layer between the fullerene derivative and FTO.

mol% $(\text{IrCp}^*\text{Cp})^+$	J_{sc} (mA cm^{-2})	V_{oc} (V)	FF (%)	PCE (%)	SPO (%)
0	20.2 ± 0.9	1.08 ± 0.02	58 ± 5	12.5 ± 1.3	11.9 ± 0.8
0.2	20.5 ± 0.7	1.11 ± 0.01	62 ± 2	13.7 ± 0.7	12.5 ± 0.6
3	19.4 ± 1.7	1.10 ± 0.01	62 ± 2	13.1 ± 1.3	12.0 ± 0.8
PCBM	19.3 ± 1.4	1.07 ± 0.03	57 ± 7	11.5 ± 1.6	11.1 ± 0.3

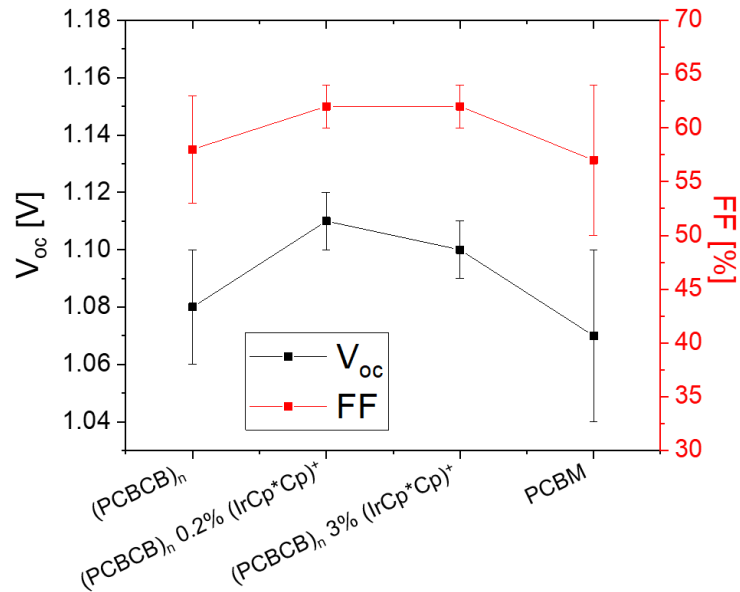


Figure 5.13 Open-circuit voltage (V_{oc}) and fill factor (FF) for solar cells fabricated using as ETMs $(\text{PCBCB})_n$, $(\text{PCBCB})_n$ containing 0.2 mol% of $(\text{IrCp}^*\text{Cp})^+$ and PCBM. All solar cells were made using tin oxide nanoparticles as a buffer layer between the fullerene derivative and FTO.

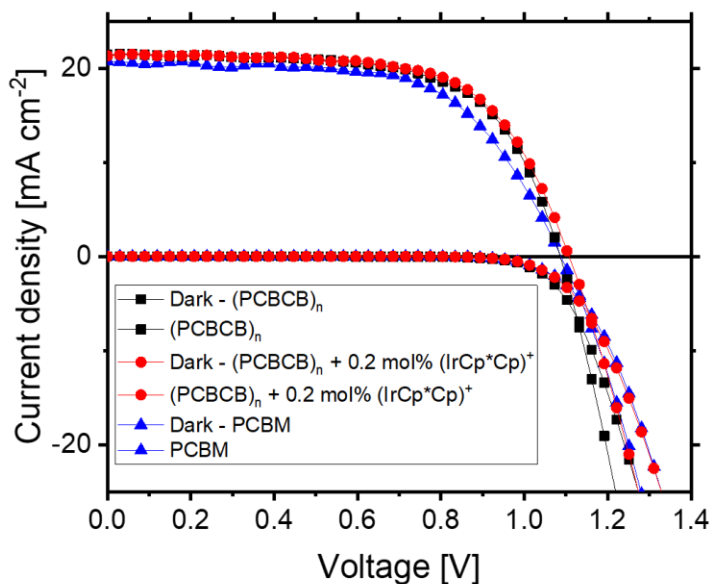


Figure 5.14 Current density – voltage characteristics for the best-performing solar cells fabricated using as ETMs $(PCBCB)_n$, $(PCBCB)_n$ containing 0.2 mol% of $(IrCp^*Cp)^+$ and PCBM. All solar cells were made using tin oxide nanoparticles as a buffer layer between the fullerene derivative and FTO.

The concentration of crosslinker PMHBCB in $(PCBCB)_n$ was varied and its impact on the electrical behavior of PSCs was assessed. The device performance parameters averaged over five solar cells for each type of ETM are shown in Table 5.7, and the $J - V$ curves of the best-performing solar cells are shown in Figure 5.15. Adding 1 mol% of crosslinker in films of $(PCBCB)_n$ leads to an increase in FF, and in PCE from an average of 12.2% for pristine $(PCBCB)_n$ to 13.7% for crosslinked $(PCBCB)_n$. The increase in FF seems to be consistent with the increase in conductivity, shown in Figure 5.7, upon addition of PMHBCB in doped films of $(PCBCB)_n$. Increasing the concentration of crosslinker above 1 mol% induces rapid degradation of device performance parameters, probably because the crosslinker dilutes out the concentration of conducting PCBCB oligomers.

Table 5.7 Device performance parameters averaged over five solar cells with solution-processed $(\text{HC}(\text{NH}_2)_2)_{0.83}\text{Cs}_{0.17}\text{Pb}(\text{I}_{0.8}\text{Br}_{0.2})_3$ as a function of the PMHBCB crosslinker concentration in $(\text{PCBCB})_n$ films. The reference solar cell was made using compact-layer SnO_2 covered with PCBM as the ETM.

mol% crosslinker	J_{sc} (mA cm^{-2})	V_{oc} (V)	FF (%)	PCE (%)
0	17.3 ± 0.2	1.08 ± 0.03	65 ± 3	12.2 ± 0.3
1	17.9 ± 0.3	1.09 ± 0.03	71 ± 2	13.7 ± 0.3
10	15.3 ± 1.2	1.10 ± 0.03	66 ± 2	11.1 ± 1.2
20	14.2 ± 0.8	1.05 ± 0.07	69 ± 5	10.2 ± 0.9
30	11.2 ± 1.3	1.11 ± 0.04	64 ± 3	8.0 ± 0.9
50	14.0 ± 0.6	1.11 ± 0.03	67 ± 2	10.4 ± 0.1
<i>c</i> - SnO_2/PCBM	18.1 ± 0.4	1.13 ± 0.01	75 ± 1	15.5 ± 0.3

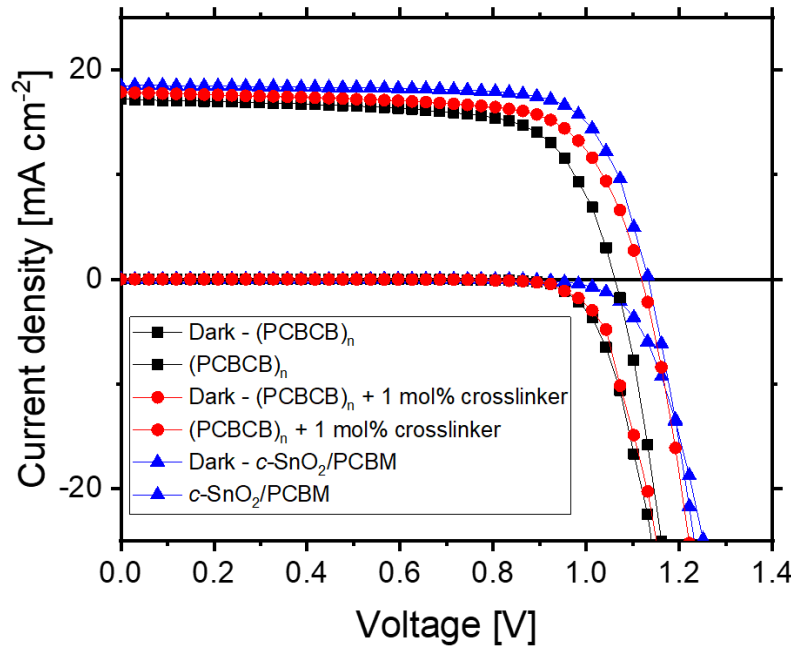


Figure 5.15 Current density – voltage characteristics for the best-performing solar cells fabricated using as ETMs $(\text{PCBCB})_n$, $(\text{PCBCB})_n$ containing 1 mol% of crosslinker and a compact layer of SnO_2 covered with PCBM (reference).

PSCs solar cells containing (PCBCB)_n with both the optimal concentration of dopant [0.2 mol% (IrCp*Cp)⁺] and the optimal concentration of crosslinker (1 mol% PMHBCB) were fabricated, and compared to solar cells with undoped (PCBCB)_n, doped (PCBCB)_n, and crosslinked (PCBCB)_n as ETM. The device performance parameters averaged over seven solar cells per each type of ETM are shown in Table 5.8, and the $J - V$ curves of the best-performing solar cells are shown in Figure 5.16. Adding both dopant and crosslinker to (PCBCB)_n leads to devices that exhibit lower FF, V_{oc} , J_{sc} and SPO compared to those with pristine (PCBCB)_n, doped (PCBCB)_n, and (PCBCB)_n containing only crosslinker. Conductivity measurements in section 5.3.2 show that the simultaneous addition of both (IrCp*Cp)₂ and PMHBCB is not detrimental to the in-plane conductivity of (PCBCB)_n; therefore, it is possible that the crystallization of the perovskite on this ETM is sub-optimal. Indeed, this hypothesis is supported by preliminary results showing that *p-i-n* solar cells fabricated using doped and crosslinked (PCBCB)_n exhibit PCEs above 16% and outperform those fabricated with undoped (PCBCB)_n, doped (PCBCB)_n and crosslinked (PCBCB)_n.

Table 5.8 Device performance parameters averaged over seven solar cells with solution-processed $(\text{HC}(\text{NH}_2)_2)_{0.83}\text{Cs}_{0.17}\text{Pb}(\text{I}_{0.8}\text{Br}_{0.2})_3$ and different ETMs. The reference solar cells were made using compact-layer SnO_2 covered with PCBM as ETM. 0.2 mol% $(\text{IrCp}^*\text{Cp})^+$ and 1 mol% PMHBCB were used in the films of $(\text{PCBCB})_n$ that were doped, crosslinked or both.

ETM	J_{sc} (mA cm^{-2})	V_{oc} (V)	FF (%)	PCE (%)	SPO (%)
$(\text{PCBCB})_n$	20.0 ± 0.5	1.03 ± 0.03	61 ± 4	12.7 ± 1.1	11.2 ± 2.3
Doped $(\text{PCBCB})_n$	19.6 ± 0.7	1.04 ± 0.01	63 ± 3	12.8 ± 0.8	12.3 ± 1.1
$(\text{PCBCB})_n$ + crosslinker	19.8 ± 0.7	1.03 ± 0.04	62 ± 2	12.6 ± 1.1	13.4 ± 1.0
Doped $(\text{PCBCB})_n$ + crosslinker	19.0 ± 0.5	0.99 ± 0.03	54 ± 5	10.3 ± 1.0	10.9 ± 0.4
$c\text{-SnO}_2/\text{PCBM}$	20.2 ± 0.4	0.97 ± 0.03	71 ± 2	14.0 ± 0.6	14.1 ± 0.3

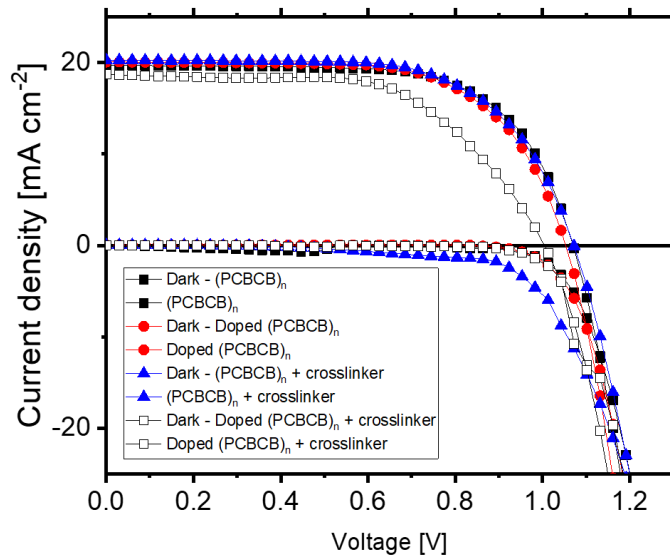


Figure 5.16 Current density – voltage characteristics for the best-performing solar cells fabricated with $(\text{PCBCB})_n$, $(\text{PCBCB})_n$ + 0.2 mol% $(\text{IrCp}^*\text{Cp})^+$, $(\text{PCBCB})_n$ + 1 mol% of crosslinker, and $(\text{PCBCB})_n$ containing both dopant and crosslinker as ETMs.

5.6.1 Stability of Perovskite Solar Cells upon the Introduction of *n*-Dopant and Crosslinker

Perovskite solar cells with the *n-i-p* architecture were aged in inert atmosphere at 85 °C in the dark, to investigate the impact on the device thermal stability of the choice of ETM, and of the introduction of (IrCp**Cp*)₂ and crosslinker in (PCBCB)_n films. The solar cell architecture was FTO/ETM/(HC(NH₂)₂)_{0.83}Cs_{0.17}Pb(I_{0.8}Br_{0.2})₃/spiro-OMeTAD/Cr/Au. Generally, it is possible to distinguish two regions in the degradation pattern of solar cells containing organic semiconductors: a first burn-in period, characterized by an exponential loss in efficiency whose magnitude and duration is dependent on the materials system,¹⁷³ followed by a linear decay. It is possible to define the device lifetime as the time at which the power conversion efficiency has reached 80% of its value post burn-in (*t*₈₀).

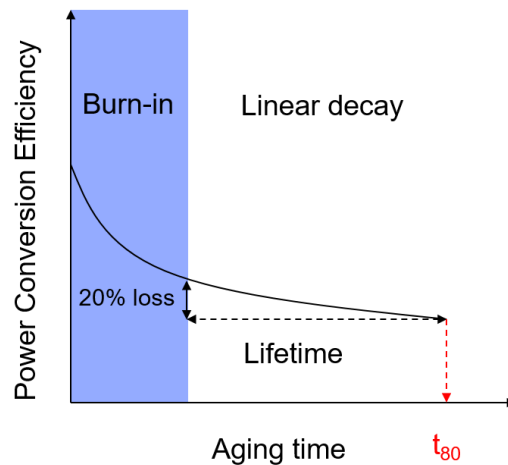


Figure 5.17 Schematic of a typical degradation pattern of a solar cell containing organic semiconductors (hence representative of PSCs as well as OPVs), showing the burn-in and linear decay regimes. The lifetime of a solar cell is defined by the point at which the efficiency is 80% of what it originally was after the burn-in period. Adapted from the literature.¹⁷³

The solar cells fabricated using organic ETMs exhibited a burn-in period over the first 200 h of aging. Figure 5.18 shows that solar cells fabricated using $(\text{PCBCB})_n$ as ETM exhibit a much severe burn-in compared to devices fabricated with a compact layer of SnO_2 covered with PCBM, the efficiency of which does not seem to decrease at all over the first 200 h. However, the lifetimes of $(\text{PCBCB})_n$ - and $c\text{-SnO}_2/\text{PCBM}$ -based devices are very similar ($t_{80} = 716$ h and 701 h respectively). These lifetime values are comparable to those reported in the literature for devices containing a similar perovskite absorbing layer,¹⁵³ and were obtained using linear regression fitting with a coefficient of determination (R^2) above 0.85.

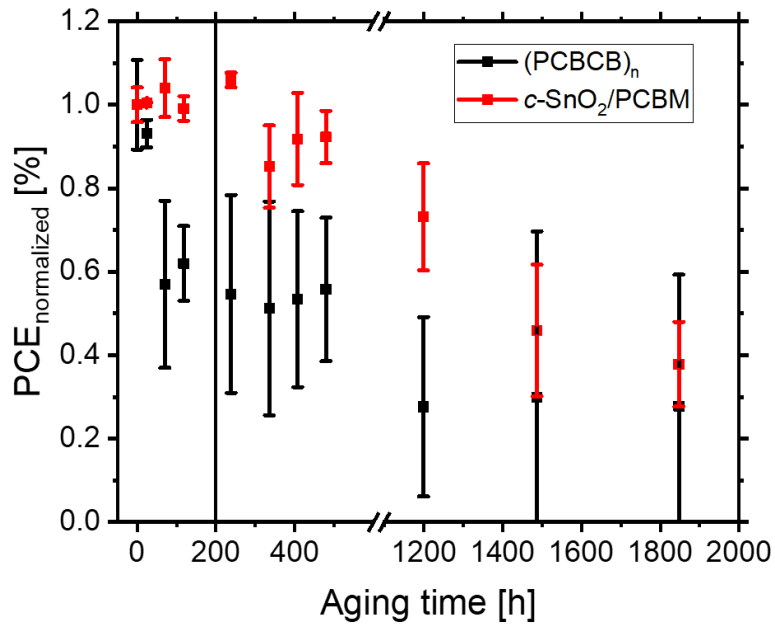


Figure 5.18 Stability comparison of non-encapsulated perovskite solar cells (PSCs) fabricated using as ETMs $(\text{PCBCB})_n$ or compact-layer SnO_2 coated with PCBM. PSCs were aged for 1800 h at 85 °C in the dark in inert atmosphere, and brought to atmosphere and room temperature for PCE measurement. An average of four devices per each data point is reported. The vertical line at 200 h marks the transition from burn-in to linear decay.

Figure 5.19 shows that doping $(\text{PCBCB})_n$ does not negatively affect device stability, which could point out that the dopant may not extensively diffuse at 85°C , which is a much lower temperature than the one used for diffusion studies in vacuum-deposited C_{60} in section 5.5, 185°C . Figure 5.20 shows that promoting connectivity among $(\text{PCBCB})_n$ oligomers with the addition of PMHBCB does not lead to improvements in thermal stability. However, the addition of the crosslinker in doped $(\text{PCBCB})_n$ films reduces the degradation in device performance during burn-in, although it does not seem to affect long-term degradation. It was not possible to confidently determine the lifetime of solar cells containing doped $(\text{PCBCB})_n$, crosslinked $(\text{PCBCB})_n$, and doped and crosslinked $(\text{PCBCB})_n$ given the poor R^2 (< 0.5) of the linear regression fit in the post burn-in regime.

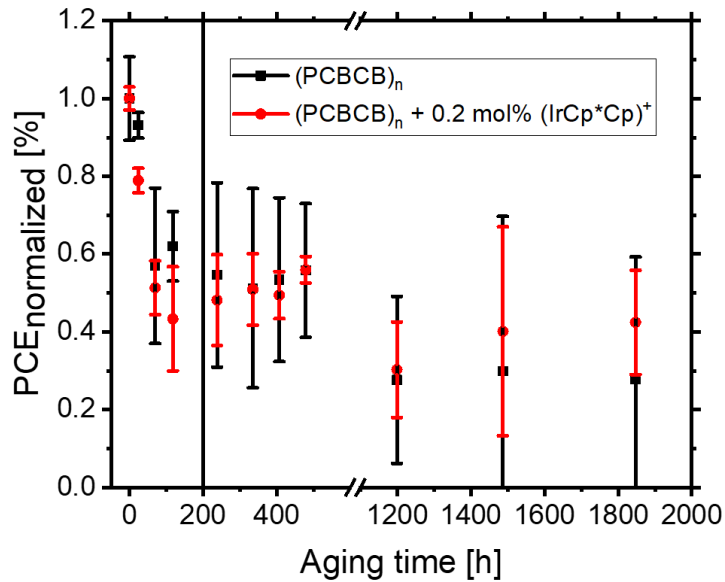


Figure 5.19 Stability comparison of non-encapsulated perovskite solar cells (PSCs) fabricated using $(\text{PCBCB})_n$ and doped $(\text{PCBCB})_n$ as ETMs. PSCs were aged for 1800 h at 85°C in the dark in inert atmosphere, and brought to atmosphere and room temperature for PCE measurement. An average of four devices per each data point is reported. The vertical line at 200 h marks the transition from burn-in to linear decay.

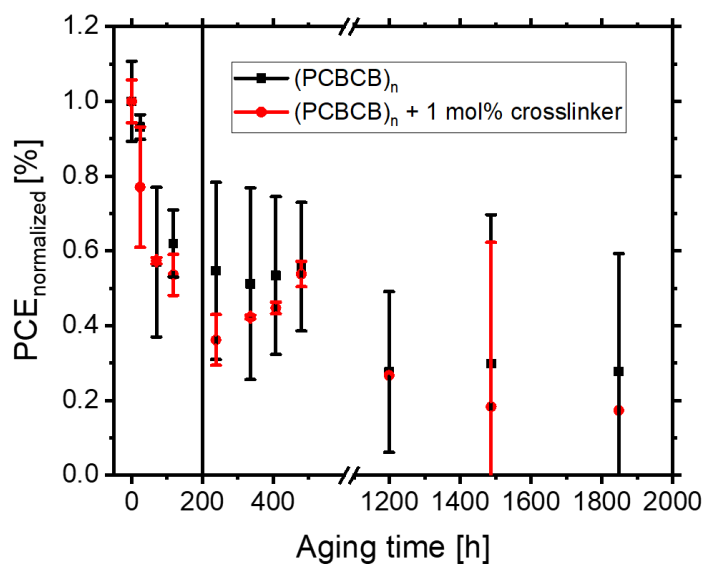


Figure 5.20 Stability comparison of non-encapsulated perovskite solar cells (PSCs) fabricated using as ETMs (PCBCB)_n and (PCBCB)_n containing 1 mol% of PMHBCB crosslinker. PSCs were aged for 1800 h at 85 °C in the dark in inert atmosphere, and brought to atmosphere and room temperature for PCE measurement. An average of four devices per each data point is reported. The vertical line at 200 h marks the transition from burn-in to linear decay.

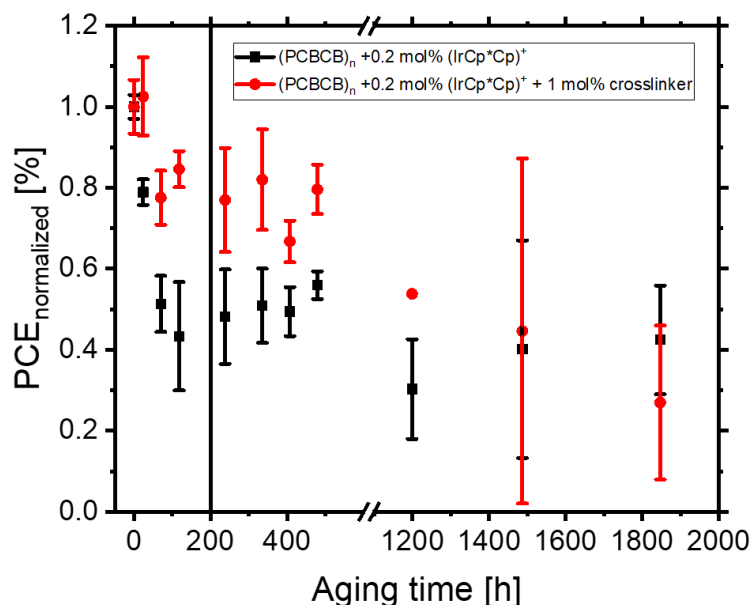


Figure 5.21 Stability comparison of non-encapsulated perovskite solar cells (PSCs) fabricated using as ETMs doped $(\text{PCBCB})_n$ and doped $(\text{PCBCB})_n$ containing 1 mol% of PMHBCB crosslinker. PSCs were aged for 1800 h at 85 °C in the dark in inert atmosphere, and brought to atmosphere and room temperature for PCE measurement. An average of four devices per each data point is reported. The vertical line at 200 h marks the transition from burn-in to linear decay.

5.7 Conclusions

$(\text{PCBCB})_n$ is an insoluble ETM compatible with solution-processing of perovskite from solvents like DMF. The work in this chapter demonstrated that $(\text{IrCp}^*\text{Cp})_2$ dopes the fullerene derivative by forming fullerene radical anions, $\text{PCBCB}^{\bullet-}$, and iridium monomer cations, $(\text{IrCp}^*\text{Cp})^+$. Doping insoluble films of $(\text{PCBCB})_n$ oligomers leads to an increase of the in-plane conductivity of the host material by four orders of magnitude. However, $(\text{IrCp}^*\text{Cp})^+$ can be washed away – together with low-molecular weight $\text{PCBCB}^{\bullet-}$ – by DMF spin-coated on top of the doped layer. Adding a crosslinker, PMHBCB, prevents washing of $(\text{IrCp}^*\text{Cp})^+$ and slightly increases the in-plane conductivity of the doped $(\text{PCBCB})_n$.

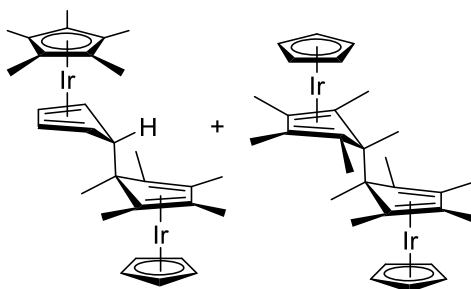
This is the first time that diffusion of $(\text{IrCp}^*\text{Cp})^+$ is clearly shown to take place in $(\text{PCBCB})_n/\text{C}_{60}$ bilayers heated at 185 °C. Adding the crosslinker to $(\text{PCBCB})_n$ may prevent the diffusion of the dopant, but further experimental evidence is needed to validate this hypothesis. Fabricating solar cells with low-doped $(\text{PCBCB})_n$ leads to an improvement in PCE associated with a small increase in V_{oc} , suggesting that the upward shift of the E_F upon doping leads a reduction in non-radiative recombination, possibly due to faster charge extraction in ETMs of increased conductivity. Fabricating solar cells using $(\text{PCBCB})_n$ with PMHBCB leads also to an improvement in PCE associated with an increase in FF. The latter suggests a possible increase in through-plane conductivity, which although not directly validated, seems consistent with in-plane conductivity studies. However, simultaneous incorporation of $(\text{IrCp}^*\text{Cp})_2$ and PMHBCB leads to a degradation of all device performance parameters. This electrical behavior could be associated with poor perovskite film formation, supported by fabrication of *p-i-n* solar cells exhibiting higher PCE when $(\text{PCBCB})_n$ is crosslinked and doped, as compared to pristine, doped or crosslinked $(\text{PCBCB})_n$. Unlike $(\text{PCBCB})_n$ -based PSCs, solar cells fabricated with *c*-SnO₂ covered with PCBM do not exhibit burn-in when aged at 85 °C in inert atmosphere. However, solar cells built with *c*-SnO₂/PCBM or $(\text{PCBCB})_n$ show very similar lifetimes ($t_{80} \sim 700$ h). The burn-in of $(\text{PCBCB})_n$ devices is reduced by introducing $(\text{IrCp}^*\text{Cp})_2$ and PMHBCB.

5.8 Experimental

5.8.1 Materials Synthesis

PCBCB and its precursors were synthesized following literature methods by the author and by Dr. Raghunath R. Dasari.^{160, 174} PCBM (Argos organics), 2,2',7,7'-tetrakis(*N,N'*-di-*p*-methoxyphenylamine)-9,9'-spirobifluorene (spiro-OMeTAD, Lumtec), formamidine iodide ((HC(NH₂)₂)I, GreatCell Solar), cesium iodide (CsI, Sigma-Aldrich), lead iodide (PbI₂, TCI Chemicals), lead bromide (PbBr₂, Alfa Aesar), and anhydrous solvents [DMF, DMSO, chlorobenzene, dichlorobenzene, anisole, toluene (Sigma-Aldrich)] were purchased.

5.8.1.1 Pentamethylcyclopentadienyl cyclopentadienyl iridium dimer⁹¹

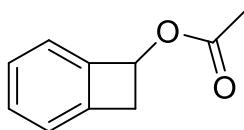


2 : 1 Mixture
(IrCp**Cp*)₂

To a suspension of sodium-potassium alloy absorbed onto silica gel (K₂Na-SG, 35%, Sigma Aldrich, 0.7 g, 2.45 mmol) in anhydrous and degassed tetrahydrofuran (60 mL), pentamethylcyclopentadienyl cyclopentadienyl iridium hexafluorophosphate (0.5 g, 0.93 mmol, synthesized following a previously reported procedure),⁹¹ was added in inert atmosphere. The reaction mixture was stirred for 1 h at room temperature. The obtained

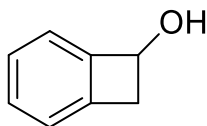
solution was cannulated into a Schlenk flask, through a frit containing celite, without oxygen exposure. After removal of THF under reduced pressure, the crude solid was extracted into dry and degassed toluene (20 mL). The solution was once again cannulated into a Schlenk flask, through a frit containing celite, without oxygen exposure. The solvent was removed under reduced pressure, and the solid was washed three times in dry, cold and oxygen-free hexanes to obtain a brown-yellow solid (0.3 g, 90%). K_2Na-SG was quenched by careful addition of isopropanol and ethanol until no hydrogen evolution is recorded. The 1H NMR shifts were consistent with the literature.⁹¹ The compound was synthesized by the author and Dr. Elena Longhi.

5.8.1.2 Bicyclo[4.2.0]octa-1,3,5-trien-7-yl acetate¹⁷⁵



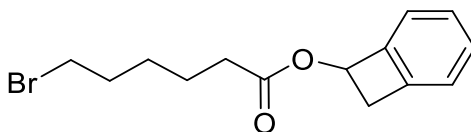
To refluxing (75 °C) and degassed vinyl acetate (0.80 L) were added dropwise a suspension of anthranilic acid (21.8 g, 159 mmol) in warm vinyl acetate (0.20 L) and amyl nitrite (186 mmol, 25 mL) under N_2 and stirring. The reaction was carried out for 30 min. The solvent was removed and the viscous brown oil was distilled to obtain a pale yellow liquid (2 g, 8%). 1H NMR shifts were consistent with the literature.¹⁷⁵

5.8.1.3 Bicyclo[4.2.0]octa-1,3,5-trien-7-ol¹⁷⁵



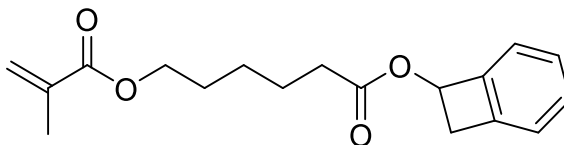
To a solution of bicyclo[4.2.0]octa-1,3,5-trien-7-yl acetate (1.3 g, 8 mmol) in methanol (8 mL) was added sodium carbonate (0.8 g, 7.7 mmol) in water (16.0 mL). The reaction mixture was stirred for 20 h at room temperature. The product was extracted in ether, the extracts were washed with water several times and dried over sodium sulphate. The solvent was removed, and a white solid product was obtained (1.24 g, 80%). ¹H NMR shifts were consistent with the literature.¹⁷⁵

5.8.1.4 Bicyclo[4.2.0]octa-1(6),2,4-trien-7-yl 6-bromohexanoate



To a solution of bicyclo[4.2.0]octa-1,3,5-trien-7-ol (0.65 g, 5.4 mmol) and 6-bromohexanoic acid (1.11 g, 5.7 mmol) in dry dichloromethane (20.0 mL) were added *N,N'*-dicyclohexylcarbodiimide (1.23 g, 6 mmol) and 4-dimethylaminopyridine (0.05g, 0.4 mmol) at room temperature under stirring. The reaction was carried out at room temperature for 2 h. The reaction mixture was filtered, and the solvent was removed. A yellow oil was obtained (2.45 g, 91%) after column chromatography using CHCl₃ and ethanol (100:1) as eluent. ¹H NMR (300 MHz, CDCl₃): δ 7.32 (m, 2H), 7.24 (m, 1H), 7.15 (d, *J*_{H-H} = 6 Hz, 1H), 5.92 (dd, *J*_{H-H} = 3.0, 1.5 Hz, 1H), 3.66 (dd, *J*_{H-H} = 15.0 Hz, 3.0 Hz, 1H), 3.40 (t, *J*_{H-H} = 6.0 Hz, 2H), 3.22 (dd, *J*_{H-H} = 15.0 Hz, 1.5 Hz, 1H), 2.38 (t, *J*_{H-H} = 6 Hz, 2H), 1.88 (p, *J*_{H-H} = 9.0 Hz, 2H), 1.69 (p, *J*_{H-H} = 6.0 Hz, 2H), 1.49 (m, 2H). ¹³C(¹H) NMR (100.62 MHz, dimethyl sulfoxide-d₆): δ 172.88, 144.05, 142.51, 130.00, 127.52, 123.33, 123.30, 71.02, 38.55, 34.97, 33.19, 31.86, 26.99, 23.55. Anal. Calcd. for C₁₄H₁₇BrO₂: C, 56.58; H 5.77; found: C, 56.44; H, 5.68. MS (ESI) *m/z* 319.03 [C₁₄H₁₇O₂BrNa (M+Na)⁺].

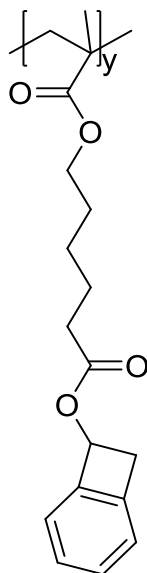
5.8.1.5 Bicyclo[4.2.0]octa-1(6),2,4-trien-7-yl 6-(methacryloyloxy)hexanoate



To a solution of methacrylic acid (1.05 g, 12.2 mmol) in dry DMF (10.0 mL) at room temperature, potassium carbonate (1.03 g, 18.3 mmol) and a solution of bicyclo[4.2.0]octa-1(6),2,4-trien-7-yl 6-bromohexanoate (0.9 g, 3.1 mmol) in DMF (2.0 mL) were added under nitrogen, and by preventing light exposure by wrapping the flask in aluminum foil. The reaction was monitored by thin layer chromatography. After 72 h the reaction was halted, the product was extracted in ether, and the extracts were washed with water at least three times. The organic residue was dried on Na₂SO₄, and the solvent was removed. A column was performed using a Biotage flash purification system (70% hexanes : 30% ethylacetate) without exposing the crude to light or heating. The organic phase was collected and the product extracted in water. The solvent was removed under reduced pressure. The product (0.46 g, 50% yield) and the starting material (250 mg, 0.86 mmol) bicyclo[4.2.0]octa-1(6),2,4-trien-7-yl 6-bromohexanoate were isolated. ¹H NMR (500 MHz, CDCl₃): δ 7.32 (td, *J*_{H-H} = 6.0, 0.5 Hz, 1H), 7.24 (m, 2H), 7.15 (d, *J*_{H-H} = 6.0 Hz, 1H), 6.09 (m, 1H), 5.92 (dd, *J*_{H-H} = 3.0, 1.5 Hz, 1H), 5.54 (m, 1H), 4.14 (t, *J*_{H-H} = 6.0 Hz, 2H), 3.66 (dd, *J*_{H-H} = 15.0 Hz, 3.0 Hz, 1H diastereotopic), 3.21 (d, *J*_{H-H} = 15.0 Hz, 1H diastereotopic), 2.38 (t, *J*_{H-H} = 6 Hz, 2H), 1.93 (s, 3H), 1.71 (m, 4H), 1.44 (m, 2H). ¹³C(¹H) NMR (125.81 MHz, CDCl₃): δ 173.54, 167.48, 144.26, 142.72, 136.45, 129.98, 127.54, 125.28, 123.53, 123.22, 71.51, 64.46, 38.95, 34.09, 28.33, 25.61, 24.56, 18.34. Anal.

Calcd. for C₁₈H₂₂O₄: C, 71.50; H 7.33; found: C, 71.46; H, 7.51. MS (ESI) *m/z* 303.15 [C₁₈H₂₃O₄ (M+H)⁺].

5.8.1.6 Poly(bicyclo[4.2.0]octa-1(6), 2, 4-trien-7-yl-hexanoyl metacrylate)



Bicyclo[4.2.0]octa-1(6),2,4-trien-7-yl 6-(methacryloyloxy)hexanoate (0.40 g, 1.32 mmol) and AIBN (2.0 mg, 0.012 mmol) were dissolved in dry benzene (6 ml) under nitrogen. The polymerization mixture was deoxygenated and was then heated up at 60 °C for 7 days without light exposure. The polymer was precipitated into methanol three times. After drying under vacuum, a white polymer was obtained in (0.32 g, 80%). ¹H NMR (500 MHz, CDCl₃): δ 7.28 (m, 1H), 7.20 (m, 2H), 7.11 (d, *J*_{H-H} = 10 Hz, 1H), 5.87 (s, 1H), 3.89 (s, br, 2H), 3.61 (dd, *J*_{H-H} = 15.0 Hz, 5.0 Hz, 1H diastereotopic), 3.17 (d, *J*_{H-H} = 15.0 Hz, 1H diastereotopic), 2.34 (s, br, 2H), 1.77 (m, br, 2H), 1.65 (m, br, 2H), 1.58 (s, 3H), 1.36 (s, br, 2H), 0.99 (s, br, 2H). ¹³C(¹H) NMR (125.81 MHz, CDCl₃): δ 177.45, 173.54, 144.43, 142.81, 130.07, 127.65, 123.69, 123.33, 71.60, 64.87, 54.24, 45.02, 39.05, 34.08, 27.99, 25.70, 24.62, 16.86. Anal. Calcd. for C₁₈H₂₂O₄: C, 71.50; H 7.33; found: C, 71.41; H, 7.36.

MS (MALDI) 302.53 g/mol. [C₁₈H₂₂O₄]. M_w = 581.4 kg/mol, PDI = 1.99 (determined via GPC in CHCl₃ at 35 °C). T_g = -10 °C, T_d = 210 °C. This reaction step was performed by Dr. Yadong Zhang, while the characterization of the compound was performed by the author.

5.8.2 *UV-vis-NIR Absorption Spectroscopy*

Absorbance spectra were measured with a Lambda 1050 UV-vis-NIR spectrophotometer (PerkinElmer) in a controlled nitrogen atmosphere. The solutions were prepared and sealed in the cuvettes in a glovebox. A baseline spectrum of dichlorobenzene was subtracted from the spectra before further analysis.

5.8.3 *Photoelectron Spectroscopy*

UPS and XPS measurements were carried as described in section 3.7.2. Depth profiling XPS measurements were performed using a JEOL JPS-9030 system with a monochromated Al K_α x-ray source (hν = 1486.6 eV). Argon with a pressure of 3 × 10⁻⁴ mbar was used as sputter gas, with low acceleration voltage and ion current (300 V and 3.5 mA) to minimize sputter damage. The resulting sputter rate was ~ 0.2 nm/s, as determined by measuring the step edge to the covered sample area by AFM after sputtering. For determination of atomic concentrations, sensitivity factors listed in the JEOL system were used.

5.8.4 *Transmission Line Measurements*

Transmission line measurements were carried out as specified in section 4.7.4. All films of the electron transporting materials [i.e., PCBM, (PCBCB)_n with and without

addition of dopant or crosslinker] had a thickness of 50 nm, measured via ellipsometry. To keep the thickness of the ETM constant, the final concentration of all fullerene derivative solutions, with and without the addition of *n*-dopant and/or crosslinker, was set to 30 mg/mL. For doping concentrations > 1 mol%, the concentration of (IrCp*Cp)₂ and PCBCB solutions was fixed to 17 mg/mL in chlorobenzene and 50 mg/mL in dichlorobenzene, respectively; for doping concentrations < 1 mol%, the concentration of (IrCp*Cp)₂ and PCBCB solutions was fixed to 2 mg/mL in chlorobenzene and 31 mg/mL in dichlorobenzene, respectively. 5 mg of crosslinker were dissolved in 1 mL of dichlorobenzene. All solutions were prepared, stirred for at least six hours, and spin-coated at 2000 rpm, 2000 rpm/s, for 45 s onto detergent/solvent-cleaned (DSC) glass substrates in a glovebox (<0.5 ppm water and <50 ppm oxygen), using degassed and anhydrous solvents. PCBM films – obtained from 30 mg/mL solutions in chlorobenzene – were annealed at 70 °C for 10 min, while PCBCB-based films were annealed at 200 °C for 10 min to promote crosslinking, yielding the fullerene insolubilized product (PCBCB)_n.¹⁶⁰ All films were immediately transferred without air exposure to a vacuum thermal evaporation system (SPECTROS, K. J. Lesker), for the deposition of silver metal (100 nm).

5.8.5 Solar Cell Fabrication

5.8.5.1 *n-i-p* Solar Cells for Optimization of Dopant Concentration

Fluorinated tin oxide (FTO) coated glass sheets (Hartford Glass, 15 Ω □⁻¹) were etched using a 2 M HCl solution and zinc powder. After initial washing with Hellmanex™ III detergent, substrates were immersed for 90 min in a H₂SO₄:H₂O₂ 3:1 (v/v) piranha solution. The FTO substrates were rinsed with deionized water, dried with compressed dry

air, and transferred into a nitrogen-filled glovebox for the deposition of the subsequent layers of the device. SnO₂ NPs were synthesized according to literature methods.^{153, 176} A solution of PCBM (7.5 mg/mL) in chlorobenzene was prepared, stirred for 12 h, filtered and spin-coated on top of the SnO₂ NPs for 45 s at 2000 rpm, 2000 rpm/s. PCBM was then annealed at 70 °C for 10 min. PCBCB (3 mg/mL) was dissolved in dichlorobenzene, while (IrCp**Cp*)₂ (1.6 mg/mL) was dissolved in chlorobenzene. Both solvents were degassed. All solutions were stirred for 12 h, mixed in desired ratios prior to deposition, spin-coated onto SnO₂ NPs for 45 s at 2000 rpm/s, 2000 rpm/s, and heated at 200 °C for 10 min. The perovskite layer was deposited using a 1.3 M precursor solution in anhydrous DMF:DMSO (4:1) of various salts [(HC(NH₂)₂)I, CsI, PbBr₂, PbI₂], stirred overnight at room temperature. 100 μL of the precursor solution were spin-coated on the ETMs at 1000 rpm for 10 s, followed by a step at 6000 rpm for 35 s, at 2000 rpm/s. After 40 s from the beginning of the spinning program, 80 μL of anisole were dropped on the spinning substrates. The perovskite films were annealed at 100 °C for 1 h. The hole-transporting material spiro-OMeTAD was deposited from chlorobenzene with additives at a concentration of 30 mM for lithium bis(trifluoromethanesulfonyl)imide (Li-TFSI) and of 80 mM for *tert*-butylpyridine (*t*BP) via spin-coating at 2000 rpm, 2000 rpm/s for 45 s. The hole-transporting layer was oxidized for 18 h prior to the electrode deposition. 110 nm thick silver electrodes were thermally evaporated at 1×10^{-6} mbar through a shadow mask to create solar cells with a total active area of 0.0919 cm², as defined by the overlap between FTO and silver. Current density-voltage characterization was carried out as specified in section 3.7.4.

5.8.5.2 *n-i-p* Solar Cells for the Optimization of Crosslinker Concentration in (PCBCB)_n and for Stability Studies

Fluorine doped tin oxide (FTO) coated glass substrates (Pilkington, TEC7) were etched in selected regions using a 2 M HCl solution and zinc powder. Substrates were cleaned with water, sequentially sonicated for 5 min in water, acetone and isopropyl alcohol, and then dried with a compressed nitrogen gun. The substrates were exposed to UV-ozone cleaning for 15 min. The SnO₂ compact layer was deposited as reported in the literature,¹⁷² and subsequently UV-ozone cleaned. All substrates (i.e., clean FTO and clean FTO/*c*-SnO₂) were transferred to a nitrogen-filled glovebox for the deposition of the other layers. A solution of PCBM (4.0 mg/mL) in chlorobenzene and dichlorobenzene in a ratio of 3:1 was prepared, stirred for 12 h and filtered. PCBM was spin-coated on top of the metal oxide for 20 s at 2000 rpm, 2000 rpm/s, and annealed at 100 °C for 10 min. PCBCB (30 mg/mL) and PMHBCB (12 mg/mL) were dissolved in dichlorobenzene, while (IrCp*Cp)₂ (2.4 mg/mL) was dissolved in chlorobenzene. All solutions were stirred for 12 h, filtered, and mixed in desired ratios prior to deposition, to yield a final concentration of PCBCB of 4.0 mg/mL. The prepared solutions were spin-coated for 20s at 2000 rpm/s, 2000 rpm/s, and heated at 200 °C for 10 min. The perovskite layer was deposited using a 1.3 M precursor solution in anhydrous DMF:DMSO (4:1) of various salts [(HC(NH₂)₂)I, CsI, PbBr₂, PbI₂], stirred overnight at room temperature and filtered using a 0.45 μm PTFE filter. 150 μL of the precursor solution were spin-coated on the ETMs at 1000 rpm for 10 s, followed by a step at 6000 rpm for 35 s, at 2000 rpm/s. After 30 s from the beginning of the spinning program, 400 μL of toluene were dropped on the spinning substrates. The perovskite films were annealed at 100 °C for 1 h. The hole-transporting material spiro-

OMeTAD was deposited and oxidized as reported in section 5.8.5.1. For the optimization of the crosslinker concentration, 110 nm thick silver electrodes were thermally evaporated at 1×10^{-6} mbar through a shadow mask to create solar cells with a total active area of 0.0919 cm², as defined by the overlap between FTO and silver. For stability studies, the silver electrode was replaced by 3 nm of chromium, followed by 80 nm of gold. Current density-voltage characterization was carried out as specified in section 3.7.4. Stability studies were carried out by storing the solar cells at 85 °C in inert atmosphere in the dark at open circuit conditions, and then bringing them to ambient temperature for current density-voltage characterization.

CHAPTER 6. CONCLUSIONS AND OUTLOOK

This dissertation focused on the use of the dimers formed by some 19-electron organometallic sandwich compounds to tune the electronic properties of transparent conductive oxides, particularly ITO and FTO, and organic electron-transporting materials (ETMs), specifically fullerene and perylene diimide derivatives. Whether deposited on an electrically conducting surface or in contact with an organic semiconductor with electron affinity (*EA*) larger than *ca.* 2.8 eV, these organometallic dimers transfer electrons and form stable 18-electron monomer cations. On a conducting surface this translates into the formation of an interface dipole from the electrostatic adsorption of the monomer cations on the reduced substrate. Although homolytic cleavage of the C-C bond in rhodium pentamethylcyclopentadienyl cyclopentadienyl dimer requires less energy compared to homolytic cleavage in the iridium- and ruthenium-based compounds, the three dimers explored in this work (IrCp^*Cp)₂, (RuCp^*mes)₂ and (RhCp^*Cp)₂ have similar effective reducing strength [i.e., $E(\text{M}^{+}/0.5 \text{ M}_2 \sim -2.0 \text{ V vs. FeCp}_2^{+/0})$]. Sub-monolayers of their monomer cations on the surface of metal oxides are found to result in large changes (> 1 eV) in work function (WF) (chapter 4 and previous reports^{40, 80, 122}), which are maintained not only after heating to at least 150 °C, but also after solvent washing, showing potential for application in device fabrication (chapter 2). Indeed, WF reduction leads to a lower electron-injection barrier in simple sandwich devices, ITO/modifier/C₆₀/MoO_x/Ag, where dimer-modified ITO behaves as the electron-injecting electrode in forward bias and C₆₀ is the vacuum-deposited ETM, as shown in chapter 2. The monomer cations present on the surface do not form a substantial insulating barrier to the flow of electrons into the device,

as demonstrated by the similar electrical behavior of dimer-modified ITO and ITO modified with polyethylenimine ethoxylated (PEIE). The latter is a polymer processed from aqueous solutions that can decrease the WF of various transparent conducting electrodes relevant to optoelectronics,⁶⁰ and that was used here as a reference surface modifier. Spectroscopic studies in chapter 3 reveal that the use of the dimer at the interface between the metal oxide (in this case, FTO) and ETMs with an *EA* of ca. 4.0 eV (i.e., C₆₀), pins the Fermi level of the electrode to the LUMO of the ETM and *n*-dopes the molecules of organic semiconductor in proximity of the interface (chapter 3); interfacial *n*-doping of the ETM leads to changes in in-plane conductivity of C₆₀ up to three orders of magnitude (chapter 4). Therefore, surface modification with the redox-active organometallic dimers is a promising strategy to obtain low-WF electrodes and compatibilize the inorganic materials with the organic overlayer in optoelectronic devices, as further corroborated by observations of similar WF reductions and electrical behaviors obtained in several laboratories.^{40, 66, 122-123} However, processing of the organometallic *n*-dopants on the electrode surface and processing of the organic semiconductor on the modified electrode are two factors to consider for optimizing electrical behavior in solar cells. These factors are discussed in the next two paragraphs.

Similar WF modifications ($\Delta WF \leq 1.3$ eV) can be obtained by tuning the thickness of (RhCp**Cp*)₂ vacuum-deposited on FTO between 1 and 10 nm and by varying the dipping time of the metal oxide in solutions of the same organometallic dimer between 1 and 10 min. Nevertheless, perovskite solar cells (PSCs) with CH₃NH₃I₃ and C₆₀ evaporated on top of vacuum-deposited (RhCp**Cp*)₂, chapter 3, seem to perform poorly compared to PSCs where FTO is modified with (RhCp**Cp*)₂ solutions, chapter 4. The former exhibit an

average stabilized power output (SPO) of 10%, while the latter exhibit a SPO of 14.7%. One of the reasons for such difference in stabilized efficiency could arise from the chemical state of the *n*-dopant on the surface of FTO. When it is vacuum-deposited, (RhCp**Cp*)₂ forms multilayers on the metal oxide and is present predominantly in his unreacted form. In contrast, solution processing of (RhCp**Cp*)₂ induces the formation of rhodium monomer cations, almost exclusively. The multilayers of unreacted dimer on FTO could slow down electron extraction and possibly lead to an increase in charge recombination. This hypothesis seems supported by two observations. First, increasing the dipping time of FTO in solutions of (RhCp**Cp*)₂, increases the amount of unreacted dopant present on the metal oxide surface by at least one order of magnitude, and solar cells fabricated with electrodes dipped longer show lower average SPO (14.7%) than those fabricated with FTO modified for shorter periods of time (15.6%). Second, by annealing bilayers of vacuum-deposited (RhCp**Cp*)₂ and fullerene or perylene diimide at progressively higher temperatures up to 220 °C, growth of the absorption peaks of the ETMs radical anions is observed, reaching values comparable to the absorption of ETMs at a nominal doping concentration of *ca.* 1%. This suggests that *n*-doping can be thermally activated, so that unreacted dimers in the multilayers transfer electrons to the ETMs, forming monomer cations and ETM radical anions. When an annealing step is included in the device fabrication, and as a consequence less unreacted dimer is present at the FTO/ETM interface, the stabilized efficiency of solar cells using PTCBI as ETM reaches up to 14.2%. As a comparison, the solar cells with PTCBI and vacuum-deposited dopant only reached 9.2% SPO. To establish definitively whether the presence of large quantities of unreacted dimer at the surface is detrimental to charge extraction, and leads to poorer stabilized efficiency than in solar cells with FTO

treated with $(\text{RhCp}^*\text{Cp})_2$ solutions, the latter would have to be fabricated in the same batch with PSCs using FTO modified with vacuum-deposited $(\text{RhCp}^*\text{Cp})_2$. Moreover, charge extraction and recombination studies using these modified electrodes, C_{60} or PTCBI, and $\text{CH}_3\text{NH}_3\text{I}_3$ would prove to be useful to understand the device data.

As previously mentioned, a second factor to be considered when optimizing electrical behavior in solar cells is the processing of the organic semiconductor on the dimer-modified electrode. ITO treated with $(\text{IrCp}^*\text{Cp})_2$ or $(\text{RuCp}^*\text{mes})_2$ solutions does not work as a low-WF electrode in simple sandwich devices in which the ETM is solution processed, instead of being vacuum deposited, as shown in chapter 2. In contrast, PEIE-modified ITO still behaves as an electron-injecting electrode in forward bias. It was initially assumed that the organometallic monomer cations were washed away during spin-coating with reduced molecules of the ETM, resulting in a smaller WF reduction of the metal oxide and poor-electron injection in diodes with solution-processed ETMs. Chapter 5 supports this assumption. Although iridium monomer cations $(\text{IrCp}^*\text{Cp})^+$ are not electrostatically bound to a surface as in chapter 2, they are dispersed within the bulk of phenyl C_{61} butyric acid benzocyclobutene ester (PCBCB). Washing doped films of thermally-insolubilized PCBCB, denoted here as $(\text{PCBCB})_n$, resulted in a 25% relative decrease in $(\text{IrCp}^*\text{Cp})^+$ content. Given the reactivity of the benzocyclobutene (BCB) moiety, the insoluble $(\text{PCBCB})_n$ is composed of oligomers of varying molecular weight; the iridium monomer cations are likely to be washed away with low-molecular weight $(\text{PCBCB})_n^-$ oligomers. In the following paragraphs, strategies are discussed that might help address the limitations described above: one to preserve the WF reduction of metal oxide

surfaces, and the other to prevent or at least limit the washing of organometallic monomer cations.

A combination of covalent tethering of phosphonic acids (PAs) and reduction of ITO with the redox-active *n*-dopants is proposed as a robust WF modification strategy in chapter 2. This approach entails tethering a monolayer of PA with a cationic moiety to metal oxides via condensation, and then treating the surface of the electrode with organometallic dimers. The *n*-dopants reduce the surface, and the monomer cations thereby formed would be washed away with the counter ion of the cationic moiety on the PA. As a result, the charge of the reduced surface is electrostatically balanced by the cationic PA bound on the electrode. Surface analysis highlights the need for a revision of PA processing routes explored so far on ITO, to preserve the cationic moiety from degradation. Future work should explore replacing vacuum annealing with dipping in PA solutions followed by sequential sonication in clean solvents, which was proven to be an effective way to obtain PA monolayers.¹⁷⁷⁻¹⁷⁸ Alternatively, PAs with alkylammonium groups could be replaced with more stable ones, cationic species such as those containing a substituted-pyridinium moiety and perhaps a tetraphenylphosphonium one. This combined surface modifier/dimer modification approach can potentially also be applied to other electrode materials relevant to optoelectronics; for example, gold, the WF of which has also been shown to be modified by redox-active dimers,⁸⁰ could be modified using a cationic thiol or cationic N-heterocyclic carbene, which bind well to the metal.¹⁷⁹⁻¹⁸¹

A second strategy to prevent or at least limit the washing of organometallic monomer cations consists of adding a polymeric crosslinker to organic semiconductors. Chapter 5 explores the use of a crosslinker PMHBCB, containing a BCB moiety in its repeating unit

since the host material PCBCB has the same group. By increasing the number of BCB units available, oligomers of the fullerene derivative seem to become connected, forming a network that prevents or at least significantly reduces washing of $(\text{IrCp}^*\text{Cp})^+$ in doped $(\text{PCBCB})_n$ films. Additionally, it was found that the crosslinker increases the in-plane conductivity of the doped $(\text{PCBCB})_n$ by an order of magnitude, possibly because the dense fullerene network formed upon addition of the crosslinker is characterized by a more monodisperse array of inter-fullerene spacings. This hypothesis is in line with a previous study on the crystallinity of PCBM and of PCBCB before and after thermal activation of BCBs;¹⁶⁰ 2D-GIWAXS analysis would be required on $(\text{PCBCB})_n$ films before and after the addition of the crosslinker to draw any further conclusions. It should be noted that the use of PMHBCB is specific to organic semiconductors bearing similar BCB moieties or that can react with the thermally activated BCB-derived diene.¹⁶¹ Another limitation of PMHBCB, as well as of PCBCB, is the high temperature required to activate crosslinking (200 °C for 10 min), which may not be compatible with materials that start degrading at or below 200 °C [i.e., $(\text{RhCp}^*\text{Cp})_2$, although $(\text{RhCp}^*\text{Cp})^+$ would be stable at these temperatures]. Nevertheless, it is possible to decrease the activation temperature to form *o*-quinodimethane intermediates by adding electron-donating groups to the cyclobutene ring.¹⁸²⁻¹⁸⁴ In alternative to the use of a crosslinker, BCB units can be incorporated into organometallic dimers, which can then be heated to react with organic semiconductors containing BCB units.¹⁸⁵ Instead of using heat as an activation source, UV-curable additives containing aryl azides or benzophenones could be used to prevent washing of organometallic dimers in a broader library of materials, without degrading the semiconductor properties.¹⁸⁶⁻¹⁸⁷ Crosslinking may not only be able to prevent washing of

monomeric cations, but could also prevent their diffusion. Chapter 5 clearly shows that $(\text{IrCp}^*\text{Cp})^+$ diffuses from $(\text{PCBCB})_n$ into a C_{60} overlayer upon heating at 185 °C for 90 min. The latter is the annealing protocol used to deposit the most stable perovskite material reported in the literature, a formamidinium cesium lead mixed-halide perovskite, characterized by highly ordered and textured crystals.^{97, 107, 153} It needs to be verified whether dopant diffusion would take place from $(\text{PCBCB})_n$ to the perovskite itself, and the threshold temperature for appreciable diffusion. Establishing correlations between diffusion, processing temperature and materials selection will help inform the development and use of the organometallic dimers not only in perovskite solar cells, where they could be compatibilized with the most stable perovskite absorbers, but in general in other optoelectronic applications, such as organic-light emitting diodes.

Redox-active *n*-dopants were used in the context of this dissertation to modify the WF of metal oxides by physisorption to the surface without the formation of a covalent linkage. Redox-active *p*-dopants [i.e., $\text{Mo}(\text{tfd})_3$ and its soluble analogues] can increase the WF of metals and metal oxides in a similar way.⁸⁰ Therefore, leveraging previously screened modification conditions for metal oxides and metals shown here and elsewhere,^{60, 80, 188} future research efforts could focus on expanding WF tuning with both *n*- and *p*-type redox-active species, as well as polymers like PEIE and small molecules like Magic Blue, to other electrode-relevant materials, such as silver nanowires (AgNWs) networks. The latter combine high electrical conductivity, optical transparency and flexibility, representing an attractive alternative to commonly used opaque and scarce metals or brittle metal oxides.¹⁸⁹⁻¹⁹⁰ High-quality non-modified AgNW transparent conductive electrodes can be deposited and have been used in high-efficiency perovskite solar cells.³⁷ Solution-

processed flexible polymer solar cells were fabricated using AgNWs instead of ITO. However, due to the lower WF of AgNWs anodes compared to ITO, flexible solar cells suffer from losses in open circuit voltage relative to those for analogous rigid cells as large as 0.3 V.³⁸ Reports of surface modification methods for AgNWs are available, but they often require multistep processing and they generally involve accepting a compromise between electrical conductivity and transmittance.¹⁹¹ Other surface modification methods have not yet been shown to lead to long-term stability of the modified-AgNWs, and do not establish robust methods to easily increase or decrease the WF.¹⁹² Hence, there is an interesting opportunity for redox-active organometallic compounds and other established surface modification methods⁶⁰ to bridge this gap.

The former are not the only surface modifiers explored in this work. Chapter 4 offers a comparison between $(\text{RhCp}^*\text{Cp})_2$ and commercially available, metal-free tetrabutylammonium borohydride, (TBABH_4) as WF-modification layer on FTO. Dropcasting multilayers of TBABH_4 on the metal oxide leads to WF reductions up to 1.9 eV, which are reversible in ultra-high vacuum. This behavior is consistent with physisorption on FTO and formation of an interface dipole at its surface, as suggested by Kemerink *et al.*¹⁵⁰ Moreover, conductivity measurements show that the ammonium salt can lead to an increase in the in-plane conductivity of C_{60} of more than an order of magnitude. It is known that sodium borohydride reacts with fullerenes via hydride transfer forming C_{60}H^- , which would be protonated to dihydrofullerene (C_{60}H_2).¹⁴⁷⁻¹⁴⁸ It may be possible that two separate phenomena take place when TBABH_4 is deposited at the interface between a conducting electrode and a fullerene. First, an interface dipole is formed upon physisorption of TBABH_4 on the substrate surface. Then, if more than a monolayer of the

ammonium salt is present on the surface, upon vacuum-deposition of C₆₀, a hydride transfer from excess (tetrabutylammonium) borohydride could lead to *n*-doping of the fullerene as follows:

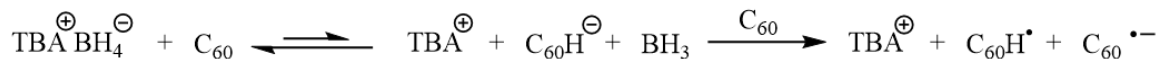


Figure 6.1 Proposed mechanism of *n*-doping of C₆₀ with tetrabutylammonium borohydride.

The proposed doping mechanism could be verified by detecting the formation of C₆₀ radical anions via UV-vis-NIR absorption spectroscopy in anhydrous chlorobenzene solutions of the organic semiconductor and TBABH₄. If the mechanism shown in Figure 6.1 were to be correct, *n*-doping of fullerenes using tetrabutylammonium borohydride would proceed similarly to *n*-doping with DMBI-H, and form C₆₀H_x byproducts, which can be detected via mass spectrometry. On the other hand, borohydride could potentially react not only with C₆₀, but also with any hydroxyl moieties on the surface of FTO, causing evolution of hydrogen and borane, and leaving behind negatively charged tin oxide, compensated by the tetrabutylammonium cations. Surface-sensitive infrared spectroscopy may be a useful tool to investigate attenuation of the SnO-H bond stretching-mode. Given that a relative increase in PSCs power conversion efficiencies of 8% [vs 12% with a (RhCp**Cp*)₂ treatment] can be obtained by simply treating the surface of FTO with TBABH₄ and subsequently vacuum-depositing C₆₀, it is worthwhile attempting to investigate the origin of the reactivity of this ammonium salt with the ETM and the metal oxide surface. Such investigation will further inform the design or direct application of readily available metal-free surface modifiers and dopants for highly efficient and stable optoelectronic devices.

Surface modifiers and *n*-dopants were used in this dissertation to improve electrical contact at the interface between the electron-collecting electrode and the ETM in PSCs. Specifically, C₆₀, PTCBI and (PCBCB)_n were chosen as the hole-blocking layers in solar cells with *n-i-p* architecture. PSCs fabricated with C₆₀ outperformed solar cells fabricated with PTCBI in terms of power conversion efficiency. However, this may not hold true if the growth of the organic semiconductors were to be controlled. By replacing vacuum deposition on room temperature FTO with organic molecular beam deposition on temperature controlled substrates, crystalline films could be obtained.¹⁹³⁻¹⁹⁴ Growing crystalline organic semiconductors may not only result in improved charge extraction, but also in improved light- and thermal stability of the solar cell, leading to reduced burn-in losses.¹⁹⁵⁻¹⁹⁸ Unlike ETMs which tend to photo-dimerize (i.e., C₆₀)¹⁹⁹⁻²⁰⁰ or are prone to bond disruption of the solubilizing side groups (i.e., PC₇₁BM),¹⁹⁸ perylene diimides show excellent photo-stability and weather fastness.²⁰¹ Therefore, future studies of organic ETMs within the context of PSCs should compare the stability of the devices upon light exposure and thermal stress. Additionally, investigation of the use of PTCBI, (PCBCB)_n and the redox-active organometallic species should be extended not only to PSCs fabricated in the *n-i-p* architecture but also to solar cells fabricated in the *p-i-n* configuration, where the perovskite is deposited on top of the hole-transporting material [i.e., poly(4-butylphenyldiphenylamine), also called poly-TPD]. For reasons that are not yet well understood, *p-i-n* perovskite solar cells seem to be more operationally stable than *n-i-p* ones; so far it seems that ion migration within the perovskite has a milder impact on the device performance in the planar *p-i-n* configuration.²⁰² Therefore, moving forward it is interesting to understand how organic (e.g., PEDOT:PSS, poly-TPD, fullerenes,

perylene) and inorganic (e.g., TiO₂, SnO₂) charge-selective layers affect the accumulation of ions at the interfaces with the perovskite in the long term. Finally, the hydrophobic nature of (PCBCB)_n could be of advantage in protecting the perovskite layer from moisture ingress in the *p-i-n* configuration,²⁰³ while it could play a detrimental effect on the crystallization of the perovskite in the *n-i-p* architecture, leading to the formation of smaller crystals.

Overall, the aim of this dissertation was to further our understanding of organometallic dimers as surface modifiers of electrode materials and as *n*-dopants for electron-transporting materials used in efficient and stable PSCs. Chapter 2 investigated the stability of the WF reduction induced by dimer treatment and the electrical behavior of the modified electrodes. Chapters 3 and 4 explored the relationship between processing of the organometallic dimer and charge collection in PSCs using organic ETMs. Chapter 5 focused on bulk doping of a fullerene derivative, washing and diffusion of dopant monomer cations. It has been shown that these dopants can play a variety of roles in improving overall device performance and/or stability in PSCs. Moreover, despite the focus on the applications of dimeric dopants to PSCs, many of the findings may also be relevant to other applications of transparent conducting electrodes and organic semiconductors.

APPENDIX A. LIST OF PUBLICATIONS

1. Pulvirenti, F.; Wegner, B.; Noel, N. K.; Mazzotta, G.; Hill, R.; Patel, Jay B.; Herz, L. M.; Johnston, M. B.; Riede, M. K.; Snaith, H. J.; Koch, N.; Barlow, S.; Marder, S. R., Modification of the Fluorinated Tin Oxide/Electron-Transporting Material Interface by a Strong Reductant and its Effect on Perovskite Solar Cell Efficiency. *Molecular Systems Design & Engineering* 2018, **3**, 741-747.
2. Giordano, A. J.; Pulvirenti, F.; Khan, T. M.; Fuentes-Hernandez, C.; Moudgil, K.; Delcamp, J. H.; Kippelen, B.; Barlow, S.; Marder, S. R., Organometallic Dimers: Application to Work-Function Reduction of Conducting Oxides. *ACS Applied Materials & Interfaces* 2015, **7**, 4320–4326.
3. McMeekin, D. P.; Wang, Z.; Rehman, W.; Pulvirenti, F.; Patel, J. B.; Noel, N. K.; Johnston, M. B.; Marder, S. R.; Herz, L. M.; Snaith, H. J., Crystallization Kinetics and Morphology Control of Formamidinium-Cesium Mixed-Cation Lead Mixed-Halide Perovskite via Tunability of the Colloidal Precursor Solution. *Advanced Materials* 2017, **29**, 16070391.
4. Hill, R.; Turren Cruz, S.; Pulvirenti, F.; Tress, W.; Wiegold, S.; Sun, S.; Nienhaus, L.; Bawendi, M.; Buonassisi, T.; Barlow, S.; Hagfeldt, A.; Marder, S. R.; Correa-Baena, J.-P., Phosphonic Acid Modification of the Electron Selective Contact: Interfacial Effects in Perovskite Solar Cells. *ACS Applied Energy Materials* (under review).
5. Noel, N. K.; Habisreutinger, S. N.; Pellaroque, A.; Pulvirenti, F.; Wenger, B.; Zhang, F.; Lin, Y.-H.; Reid, O. G.; Leisen, J.; Zhang, Y.; Barlow, S.; Kahn, A.; Marder, S. R.;

- Snaith, H. J.; Craig B. Arnold, Rand, B. P., Interfacial Charge-transfer Doping of Metal Halide Perovskites for High Performance Photovoltaics. (In preparation).
6. Pulvirenti, F.; Patel, J. B.; Wegner, B.; Jia, X.; Longhi, E.; Fuentes-Hernandez, C.; Kippelen, B.; Koch, N.; Johnston, M. B.; Herz, L.; Snaith, H. J.; Barlow, S.; Marder, S. R., Interfacial Doping of C₆₀ and its Implication for High-Performance Metal Halide Perovskite Solar Cells. (In preparation).
 7. Pulvirenti, F.; Tremblay, M.-H.; Schultz, T.; Wegner, B.; Schutt, K.; McMeekin, D. P.; Longhi, E.; Dasari, R.; Zhang, Y.; Snaith, H. J.; Koch, N.; Barlow, S.; Marder, S. R., Doping of a Thermo-Oligomerizing Fullerene Derivative for Solution-Processed Perovskite Solar Cells. (In preparation).
 8. Moudgil, K.; Pulvirenti, F.; Jucov, E. V.; Timofeeva, T.; Barlow, S.; Marder, S. R., Synthesis, Crystal Structures, and Reductive Dimerization of Pentaethyliridocenium Hexafluorophosphate. (In preparation).
 9. Pulvirenti, F.; Kosal, M. E., Development and Proliferation of Flexible and Wearable Electronics: Opportunities and Challenges for the U.S. Department of Defense. (In preparation).

REFERENCES

1. Gaffney, O.; Steffen, W., The Anthropocene Equation. *The Anthropocene Review* **2017**, *4* (1), 53-61.
2. Lewis, N. S.; Crabtree, G.; Nozik, A. J.; Wasielewski, M. R.; Alivisatos, P. *Basic Energy Sciences Workshop on Solar Energy Utilization*; 2005.
3. Fu, R.; Feldman, D.; Margolis, R. *U.S. Solar Photovoltaic System Cost Benchmark: Q1 2018*; National Renewable Energy Laboratory: Golde, CO, 2018.
4. Siffert, P.; Krimmel, E., *Silicon: Evolution and Future of a Technology*. Springer: Berlin, Heidelberg, 2013.
5. Bardeen, J.; Brattain, W. H., The Transistor, A Semi-Conductor Triode. *Physical Review* **1948**, *74* (2), 230-231.
6. Chapin, D. M.; Fuller, C. S.; Pearson, G. L., A New Silicon p-n Junction Photocell for Converting Solar Radiation into Electrical Power. *Journal of Applied Physics* **1954**, *25* (5), 676-677.
7. Jacoboni, C.; Canali, C.; Ottaviani, G.; Alberigi Quaranta, A., A Review of Some Charge Transport Properties of Silicon. *Solid-State Electronics* **1977**, *20* (2), 77-89.
8. Krames, M. R.; Shchekin, O. B.; Mueller-Mach, R.; Mueller, G.; Zhou, L.; Harbers, G.; Craford, M. G., Status and Future of High-Power Light-Emitting Diodes for Solid-State Lighting. *J. Display Technol.* **2007**, *3* (2), 160-175.
9. Zwanenburg, F. A.; Dzurak, A. S.; Morello, A.; Simmons, M. Y.; Hollenberg, L. C. L.; Klimeck, G.; Rogge, S.; Coppersmith, S. N.; Eriksson, M. A., Silicon Quantum Electronics. *Reviews of Modern Physics* **2013**, *85* (3), 961-1019.
10. Chiang, C. K.; Fincher, C. R.; Park, Y. W.; Heeger, A. J.; Shirakawa, H.; Louis, E. J.; Gau, S. C.; MacDiarmid, A. G., Electrical Conductivity in Doped Polyacetylene. *Physical Review Letters* **1977**, *39* (17), 1098-1101.
11. Kojima, A.; Teshima, K.; Shirai, Y.; Miyasaka, T., Organometal Halide Perovskites as Visible-Light Sensitizers for Photovoltaic Cells. *Journal of the American Chemical Society* **2009**, *131* (17), 6050-6051.
12. Laboratory, N. R. E. *Best Research-Cell Efficiencies*.
13. Wang, Z.; Lin, Q.; Chmiel, F. P.; Sakai, N.; Herz, L. M.; Snaith, H. J., Efficient Ambient-Air-Stable Solar Cells with 2D–3D Heterostructured Butylammonium–Caesium-Formamidinium Lead Halide Perovskites. *Nature Energy* **2017**, *2*, 17135.

14. Liu, M.; Johnston, M. B.; Snaith, H. J., Efficient Planar Heterojunction Perovskite Solar Cells by Vapour Deposition. *Nature* **2013**, *501*, 395.
15. Lee, M. M.; Teuscher, J.; Miyasaka, T.; Murakami, T. N.; Snaith, H. J., Efficient Hybrid Solar Cells Based on Meso-Superstructured Organometal Halide Perovskites. *Science* **2012**, *338* (6107), 643-647.
16. Eperon, G. E.; Stranks, S. D.; Menelaou, C.; Johnston, M. B.; Herz, L. M.; Snaith, H. J., Formamidinium Lead Trihalide: A Broadly Tunable Perovskite for Efficient Planar Heterojunction Solar Cells. *Energy & Environmental Science* **2014**, *7* (3), 982-988.
17. Noel, N. K.; Stranks, S. D.; Abate, A.; Wehrenfennig, C.; Guarnera, S.; Haghighirad, A.-A.; Sadhanala, A.; Eperon, G. E.; Pathak, S. K.; Johnston, M. B.; Petrozza, A.; Herz, L. M.; Snaith, H. J., Lead-Free Organic–Inorganic Tin Halide Perovskites for Photovoltaic Applications. *Energy & Environmental Science* **2014**, *7* (9), 3061-3068.
18. Eperon, G. E.; Paternò, G. M.; Sutton, R. J.; Zampetti, A.; Haghighirad, A. A.; Cacialli, F.; Snaith, H. J., Inorganic Caesium Lead Iodide Perovskite Solar Cells. *Journal of Materials Chemistry A* **2015**, *3* (39), 19688-19695.
19. Saliba, M.; Matsui, T.; Seo, J.-Y.; Domanski, K.; Correa-Baena, J.-P.; Nazeeruddin, M. K.; Zakeeruddin, S. M.; Tress, W.; Abate, A.; Hagfeldt, A.; Grätzel, M., Cesium-Containing Triple Cation Perovskite Solar Cells: Improved Stability, Reproducibility and High Efficiency. *Energy & Environmental Science* **2016**, *9* (6), 1989-1997.
20. Pellaroque, A.; Noel, N. K.; Habisreutinger, S. N.; Zhang, Y.; Barlow, S.; Marder, S. R.; Snaith, H. J., Efficient and Stable Perovskite Solar Cells Using Molybdenum Tris(dithiolene)s as p-Dopants for Spiro-OMeTAD. *ACS Energy Letters* **2017**, *2* (9), 2044-2050.
21. Hou, Y.; Du, X.; Scheiner, S.; McMeekin, D. P.; Wang, Z.; Li, N.; Killian, M. S.; Chen, H.; Richter, M.; Levchuk, I.; Schrenker, N.; Spiecker, E.; Stubhan, T.; Luechinger, N. A.; Hirsch, A.; Schmuki, P.; Steinrück, H.-P.; Fink, R. H.; Halik, M.; Snaith, H. J.; Brabec, C. J., A Generic Interface to Reduce the Efficiency-Stability-Cost Gap of Perovskite Solar Cells. *Science* **2017**, *358* (6367), 1192-1197.
22. Bin, Z.; Li, J.; Wang, L.; Duan, L., Efficient n-Type Dopants with Extremely Low Doping Ratios for High Performance Inverted Perovskite Solar Cells. *Energy & Environmental Science* **2016**, *9* (11), 3424-3428.
23. Zhou, H.; Chen, Q.; Li, G.; Luo, S.; Song, T.-b.; Duan, H.-S.; Hong, Z.; You, J.; Liu, Y.; Yang, Y., Interface Engineering of Highly Efficient Perovskite Solar Cells. *Science* **2014**, *345* (6196), 542-546.
24. Nguyen, W. H.; Bailie, C. D.; Unger, E. L.; McGehee, M. D., Enhancing the Hole-Conductivity of Spiro-OMeTAD without Oxygen or Lithium Salts by Using Spiro(TFSI)₂

in Perovskite and Dye-Sensitized Solar Cells. *Journal of the American Chemical Society* **2014**, *136* (31), 10996-11001.

25. Cahen, D.; Kahn, A., Electron Energetics at Surfaces and Interfaces: Concepts and Experiments. *Advanced Materials* **2003**, *15* (4), 271-277.

26. Ishii, H.; Sugiyama, K.; Ito, E.; Seki, K., Energy Level Alignment and Interfacial Electronic Structures at Organic/Metal and Organic/Organic Interfaces. *Advanced Materials* **1999**, *11* (8), 605-625.

27. Kahn, A., Fermi Level, Work Function and Vacuum Level. *Materials Horizons* **2016**, *3* (1), 7-10.

28. Fuentes-Hernandez, C., Charge Transport and Photogeneration in Organic Semiconductors: Photorefractives and Beyond. In *Photorefractive Organic Materials and Applications*, Blanche, P.-A., Ed. Springer International Publishing Switzerland, 2016.

29. Schwoerer, M.; Wolf, H. C., *Organic Molecular Solids*. Wiley-VCH Verlag GmbH & Co. KGaA: Weinheim, 2007.

30. Hill, T. L., *An Introduction to Statistical Thermodynamics*. Dover Publications, Inc.: New York, 1986.

31. Koehler, A.; Baessler, H., *Electronic Processes in Organic Semiconductors: An Introduction*. WILEY-VCH Verlag: Weinheim, 2015.

32. Man, G.; Endres, J.; Lin, X.; Kahn, A., Experimental Characterization of Interfaces of Relevance to Organic Electronics. In *The WSPC Reference on Organic Electronics: Organic Semiconductors*, 2016; pp 159-191.

33. Guo, S.; Kim, S. B.; Mohapatra, S. K.; Qi, Y.; Sajoto, T.; Kahn, A.; Marder, S. R.; Barlow, S., n-Doping of Organic Electronic Materials using Air-Stable Organometallics. *Advanced Materials* **2012**, *24* (5), 699-703.

34. Guo, S.; Mohapatra, S. K.; Romanov, A.; Timofeeva, T. V.; Hardcastle, K. I.; Yesudas, K.; Risko, C.; Brédas, J.-L.; Marder, S. R.; Barlow, S., n-Doping of Organic Electronic Materials using Air-Stable Organometallics: A Mechanistic Study of Reduction by Dimeric Sandwich Compounds. *Chemistry – A European Journal* **2012**, *18* (46), 14760-14772.

35. Lin, X.; Wegner, B.; Lee, K. M.; Fusella, M. A.; Zhang, F.; Moudgil, K.; Rand, B. P.; Barlow, S.; Marder, S. R.; Koch, N.; Kahn, A., Beating the Thermodynamic Limit with Photo-Activation of n-Doping in Organic Semiconductors. *Nature Materials* **2017**, *16*, 1209.

36. Langley, D.; Giusti, G.; Mayousse, C.; Celle, C.; Bellet, D.; Simonato, J.-P., Flexible Transparent Conductive Materials Based on Silver Nanowire Networks: A Review. *Nanotechnology* **2013**, *24* (45), 452001.

37. Bailie, C. D.; Christoforo, M. G.; Mailoa, J. P.; Bowring, A. R.; Unger, E. L.; Nguyen, W. H.; Burschka, J.; Pellet, N.; Lee, J. Z.; Grätzel, M.; Noufi, R.; Buonassisi, T.; Salleo, A.; McGehee, M. D., Semi-Transparent Perovskite Solar Cells for Tandems with Silicon and CIGS. *Energy & Environmental Science* **2015**, *8* (3), 956-963.
38. Yang, L.; Zhang, T.; Zhou, H.; Price, S. C.; Wiley, B. J.; You, W., Solution-Processed Flexible Polymer Solar Cells with Silver Nanowire Electrodes. *ACS Applied Materials & Interfaces* **2011**, *3* (10), 4075-4084.
39. Itoh, E.; Shirotori, T., Relationship between Work Function of Hole Collection Electrode and Temperature Dependence of Open-Circuit Voltage in Multilayered Organic Solar Cells. *Japanese Journal of Applied Physics* **2012**, *51* (2), 02BK14.
40. Giordano, A. J.; Pulvirenti, F.; Khan, T. M.; Fuentes-Hernandez, C.; Moudgil, K.; Delcamp, J. H.; Kippelen, B.; Barlow, S.; Marder, S. R., Organometallic Dimers: Application to Work-Function Reduction of Conducting Oxides. *ACS Applied Materials & Interfaces* **2015**, *7* (7), 4320-4326.
41. Hotchkiss, P. J.; Jones, S. C.; Paniagua, S. A.; Sharma, A.; Kippelen, B.; Armstrong, N. R.; Marder, S. R., The Modification of Indium Tin Oxide with Phosphonic Acids: Mechanism of Binding, Tuning of Surface Properties, and Potential for Use in Organic Electronic Applications. *Accounts of Chemical Research* **2012**, *45* (3), 337-346.
42. MacLeod, B. A.; Tremolet de Villers, B. J.; Schulz, P.; Ndione, P. F.; Kim, H.; Giordano, A. J.; Zhu, K.; Marder, S. R.; Graham, S.; Berry, J. J.; Kahn, A.; Olson, D. C., Stability of Inverted Organic Solar Cells with ZnO Contact Layers Deposited from Precursor Solutions. *Energy & Environmental Science* **2015**, *8* (2), 592-601.
43. Kugler, T.; Johansson, Å.; Dalsegg, I.; Gelius, U.; Salaneck, W. R., Electronic and Chemical Structure of Conjugated Polymer Surfaces and Interfaces: Applications in Polymer-Based Light-Emitting Devices. *Synthetic Metals* **1997**, *91* (1), 143-146.
44. Gordon, R. G., Criteria for Choosing Transparent Conductors. *MRS Bulletin* **2000**, *25*, 52-57.
45. Fan, J. C. C.; Goodenough, J. B., X-Ray Photoemission Spectroscopy Studies of Sn-Doped Indium-Oxide Films. *Journal of Applied Physics* **1977**, *48* (8), 3524-3531.
46. Mizuhashi, M., *Electrical Properties of Vacuum-Deposited Indium Oxide and Indium Tin Oxide Films*. 1980; Vol. 70, p 91-100.
47. Mochel, J. M. *Electrically Conducting Coatings on Glass and Other Ceramic Bodies*. 1951.
48. Holland, L.; Siddall, G., Reactive Sputtering and Associated Plant Design. *Vacuum* **1953**, *3* (3), 245-253.

49. Gao, Q.; Jiang, H.; Li, M.; Lu, P.; Lai, X.; Li, X.; Liu, Y.; Song, C.; Han, G., Improved Mechanical Properties of SnO₂:F Thin Film by Structural Modification. *Ceramics International* **2014**, *40* (2), 2557-2564.
50. Gao, Q.; Jiang, H.; Li, C.; Ma, Y.; Li, X.; Ren, Z.; Liu, Y.; Song, C.; Han, G., Tailoring of Textured Transparent Conductive SnO₂:F Thin Films. *Journal of Alloys and Compounds* **2013**, *574*, 427-431.
51. Andersson, A.; Johansson, N.; Bröms, P.; Yu, N.; Lupo, D.; Salaneck, W. R., Fluorine Tin Oxide as an Alternative to Indium Tin Oxide in Polymer LEDs. *Advanced Materials* **1998**, *10* (11), 859-863.
52. Jawalekar, S. R. Third International Workshop on Physics of Semiconductor Devices, Singapore, Jain, S. C.; Radhakrishna, S., Eds. World Scientific: Singapore, 1985; p 147.
53. Bruneaux, J.; Cachet, H.; Froment, M.; Messad, A., Correlation Between Structural and Electrical Properties of Sprayed Tin Oxide Films with and without Fluorine Doping. *Thin Solid Films* **1991**, *197* (1), 129-142.
54. Kim, H.; Park, H.-H., A Study on the Electrical Properties of Fluorine Doped Direct-Patternable SnO₂ Thin Films. *Ceramics International* **2012**, *38*, S609-S612.
55. Nazeeruddin, M. K.; Kay, A.; Rodicio, I.; Humphry-Baker, R.; Mueller, E.; Liska, P.; Vlachopoulos, N.; Graetzel, M., Conversion of Light to Electricity by cis-X₂bis(2,2'-Bipyridyl-4,4'-Dicarboxylate)Ruthenium(II) Charge-Transfer Sensitizers (X = Cl-, Br-, I-, CN-, and SCN-) on Nanocrystalline Titanium Dioxide Electrodes. *Journal of the American Chemical Society* **1993**, *115* (14), 6382-6390.
56. O'Regan, B.; Grätzel, M., A Low-Cost, High-Efficiency Solar Cell Based on Dye-Sensitized Colloidal TiO₂ Films. *Nature* **1991**, *353* (6346), 737-740.
57. Guerrero, G.; Mutin, P. H.; Vioux, A., Organically Modified Aluminas by Grafting and Sol-Gel Processes Involving Phosphonate Derivatives. *Journal of Materials Chemistry* **2001**, *11* (12), 3161-3165.
58. Paniagua, S. A.; Hotchkiss, P. J.; Jones, S. C.; Marder, S. R.; Mudalige, A.; Marrikar, F. S.; Pemberton, J. E.; Armstrong, N. R., Phosphonic Acid Modification of Indium-Tin Oxide Electrodes: Combined XPS/UPS/Contact Angle Studies. *The Journal of Physical Chemistry C* **2008**, *112* (21), 7809-7817.
59. Hotchkiss, P. J.; Li, H.; Paramonov, P. B.; Paniagua, S. A.; Jones, S. C.; Armstrong, N. R.; Brédas, J.-L.; Marder, S. R., Modification of the Surface Properties of Indium Tin Oxide with Benzylphosphonic Acids: A Joint Experimental and Theoretical Study. *Advanced Materials* **2009**, *21* (44), 4496-4501.
60. Zhou, Y.; Fuentes-Hernandez, C.; Shim, J.; Meyer, J.; Giordano, A. J.; Li, H.; Winget, P.; Papadopoulos, T.; Cheun, H.; Kim, J.; Fenoll, M.; Dindar, A.; Haske, W.;

Najafabadi, E.; Khan, T. M.; Sojoudi, H.; Barlow, S.; Graham, S.; Brédas, J.-L.; Marder, S. R.; Kahn, A.; Kippelen, B., A Universal Method to Produce Low-Work Function Electrodes for Organic Electronics. *Science* **2012**, *336* (6079), 327-332.

61. Bröker, B.; Blum, R.-P.; Frisch, J.; Vollmer, A.; Hofmann, O. T.; Rieger, R.; Müllen, K.; Rabe, J. P.; Zojer, E.; Koch, N., Gold Work Function Reduction by 2.2 eV with an Air-Stable Molecular Donor Layer. *Applied Physics Letters* **2008**, *93* (24), 243303.

62. Lindell, L.; Unge, M.; Osikowicz, W.; Stafström, S.; Salaneck, W. R.; Crispin, X.; de Jong, M. P., Integer Charge Transfer at the Tetrakis(dimethylamino)ethylene/Au Interface. *Applied Physics Letters* **2008**, *92* (16), 163302.

63. Li, F.; Zhou, Y.; Zhang, F.; Liu, X.; Zhan, Y.; Fahlman, M., Tuning Work Function of Noble Metals As Promising Cathodes in Organic Electronic Devices. *Chemistry of Materials* **2009**, *21* (13), 2798-2802.

64. Osikowicz, W.; Crispin, X.; Tengstedt, C.; Lindell, L.; Kugler, T.; Salaneck, W. R., Transparent Low-Work-Function Indium Tin Oxide Electrode Obtained by Molecular Scale Interface Engineering. *Applied Physics Letters* **2004**, *85* (9), 1616-1618.

65. Paniagua, S. A.; Baltazar, J.; Sojoudi, H.; Mohapatra, S. K.; Zhang, S.; Henderson, C. L.; Graham, S.; Barlow, S.; Marder, S. R., Production of Heavily n- and p-Doped CVD Graphene with Solution-Processed Redox-Active Metal–Organic Species. *Materials Horizons* **2014**, *1* (1), 111-115.

66. Schlesinger, R.; Bianchi, F.; Blumstengel, S.; Christodoulou, C.; Ovsyannikov, R.; Kobin, B.; Moudgil, K.; Barlow, S.; Hecht, S.; Marder, S. R.; Henneberger, F.; Koch, N., Efficient Light Emission from Inorganic and Organic Semiconductor Hybrid Structures by Energy-Level Tuning. *Nature Communications* **2015**, *6*, 6754.

67. O'Connor, D. J.; Sexton, B. A.; Smart, R. S. C., *Surface Analysis Methods in Materials Science*. 2nd ed.; Berlin; New York, 2003.

68. Huefner, S., *Photoelectron Spectroscopy: Principles and Applications*. Springer-Verlag: Berlin Heidelberg, 1995.

69. Woodruff, D. P.; Delchar, T. A., *Modern Techniques of Surface Science*. 2nd ed.; Cambridge University Press: Cambridge, 1994.

70. Moulder, J. F.; Chastain, J., *Handbook of X-Ray Photoelectron Spectroscopy: A Reference Book of Standard Spectra for Identification and Interpretation of XPS Data*. Physical Electronics Division, Perkin-Elmer Corporation: Eden Prairie, 1995.

71. https://www.xpsdata.com/Technique_limits_p1.pdf (accessed 02-22-2019).

72. Briggs, D.; Seah, M. P., *Practical Surface Analysis, Auger and X-ray Photoelectron Spectroscopy*. 2nd ed.; John Wiley & Sons: Chichester, 1990.

73. Subrahmanyam, A.; Kumar, C. S., *Kelvin Probe for Surface Engineering: Fundamentals and Design*. Ane Books Pvt Ltd: New Delhi, 2010.
74. Hansen, W. N.; Hansen, G. J., Standard Reference Surfaces for Work Function Measurements in Air. *Surface Science* **2001**, *481* (1), 172-184.
75. Kim, J. S.; Lagel, B.; Moons, E.; Johansson, N.; Baikie, I. D.; Salaneck, W. R.; Friend, R. H.; Cacialli, F., Kelvin Probe and Ultraviolet Photoemission Measurements of Indium Tin Oxide Work Function: A Comparison. *Synthetic Metals* **2000**, *111-112*, 311-314.
76. Schlaf, R. Tutorial on Kelvin Probe Measurements. <http://rsl.eng.usf.edu/Documents/Tutorials/TutorialsKelvinProbe.pdf> (accessed 02-22-2019).
77. Borsenberger, P. M.; Weiss, D. S., *Organic Photoreceptors for Imaging Systems*. Marcel Dekker: New York, 1993.
78. Shen, Y.; Hosseini, A. R.; Wong, M. H.; Malliaras, G. G., How To Make Ohmic Contacts to Organic Semiconductors. *ChemPhysChem* **2004**, *5* (1), 16-25.
79. Miccoli, I.; Edler, F.; Pfnur, H.; Tegenkamp, C., The 100th Anniversary of the Four-Point Probe Technique: The Role of Probe Geometries in Isotropic and Anisotropic Systems. *Journal of Physics: Condensed Matter* **2015**, *27* (22), 223201.
80. Giordano, A. J. Altering the Work Function of Surfaces: The Influential Role of Surface Modifiers for Tuning Properties of Metals and Transparent Conducting Oxides. Georgia Institute of Technology, 2014.
81. Wojciechowski, K.; Ramirez, I.; Gorisse, T.; Dautel, O.; Dasari, R.; Sakai, N.; Hardigree, J. M.; Song, S.; Marder, S.; Riede, M.; Wantz, G.; Snaith, H. J., Cross-Linkable Fullerene Derivatives for Solution-Processed n-i-p Perovskite Solar Cells. *ACS Energy Letters* **2016**, *1* (4), 648-653.
82. Paramonov, P. B.; Paniagua, S. A.; Hotchkiss, P. J.; Jones, S. C.; Armstrong, N. R.; Marder, S. R.; Bredas, J.-L., Theoretical Characterization of the Indium Tin Oxide Surface and of Its Binding Sites for Adsorption of Phosphonic Acid Monolayers. *Chemistry of Materials* **2008**, *20* (16), 5131-5133.
83. Mohapatra, S. K.; Fonari, A.; Risko, C.; Yesudas, K.; Moudgil, K.; Delcamp, J. H.; Timofeeva, T. V.; Bredas, J.-L.; Marder, S. R.; Barlow, S., Dimers of Nineteen-Electron Sandwich Compounds: Crystal and Electronic Structures, and Comparison of Reducing Strengths. *Chemistry – A European Journal* **2014**, *20* (47), 15385-15394.
84. Burkholder, C.; Dolbier, W. R.; Medebielle, M., Tetrakis(dimethylamino)ethylene as a Useful Reductant of Some Bromodifluoromethyl Heterocycles. Application to the Synthesis of New gem-Difluorinated Heteroarylated Compounds. *The Journal of Organic Chemistry* **1998**, *63* (16), 5385-5394.

85. Connelly, N. G.; Geiger, W. E., Chemical Redox Agents for Organometallic Chemistry. *Chemical Reviews* **1996**, *96* (2), 877-910.
86. Bockman, T. M.; Kochi, J. K., Isolation and Oxidation-Reduction of Methylviologen Cation Radicals. Novel Disproportionation in Charge-Transfer Salts by X-Ray Crystallography. *The Journal of Organic Chemistry* **1990**, *55* (13), 4127-4135.
87. Olthof, S.; Mehraeen, S.; Mohapatra, S. K.; Barlow, S.; Coropceanu, V.; Brédas, J.-L.; Marder, S. R.; Kahn, A., Ultralow Doping in Organic Semiconductors: Evidence of Trap Filling. *Physical Review Letters* **2012**, *109* (17), 176601.
88. Chen, Z.; Zheng, Y.; Yan, H.; Facchetti, A., Naphthalenedicarboximide- vs Perylenedicarboximide-Based Copolymers. Synthesis and Semiconducting Properties in Bottom-Gate N-Channel Organic Transistors. *Journal of the American Chemical Society* **2009**, *131* (1), 8-9.
89. Sun, Y.-P.; Liu, B.; Lawson, G. E., Photochemical Preparation of Highly Water-Soluble Pendant [60]Fullerene-Aminopolymers. *Photochemistry and Photobiology* **1997**, *66* (3), 301-308.
90. Miller, G. P., Reactions between Aliphatic Amines and [60]Fullerene: A Review. *Comptes Rendus Chimie* **2006**, *9* (7), 952-959.
91. Gusev, O. V.; Peterleitner, M. G.; Ievlev, M. A.; Kal'sin, A. M.; Petrovskii, P. V.; Denisovich, L. I.; Ustynyuk, N. A., Reduction of Iridocenium Salts [Ir(η^5 -C₅Me₅)(η^5 -L)]⁺ (L = C₅H₅, C₅Me₅, C₉H₇); Ligand-to-Ligand Dimerisation Induced by Electron Transfer. *Journal of Organometallic Chemistry* **1997**, *531* (1), 95-100.
92. Gusev, O. V.; Ievlev, M. A.; Peterleitner, M. G.; Peregudova, S. M.; Denisovich, L. I.; Petrovskii, P. V.; Ustynyuk, N. A., Reduction of Ruthenium Arenecyclopentadienyl Complexes Reactions Induced by Electron Transfer. *Journal of Organometallic Chemistry* **1997**, *534* (1), 57-66.
93. Gester, S.; Pietzsch, J.; Wuest, F. R., Synthesis of ¹⁸F-Labelled Stilbenes from 4-[¹⁸F]Fluorobenz-Aldehyde using the Horner–Wadsworth–Emmons Reaction. *Journal of Labelled Compounds and Radiopharmaceuticals* **2007**, *50* (2), 105-113.
94. van den Berg, O.; Sengers, W. G. F.; Jager, W. F.; Picken, S. J.; Wübbenhorst, M., Dielectric and Fluorescent Probes To Investigate Glass Transition, Melt, and Crystallization in Polyolefins. *Macromolecules* **2004**, *37* (7), 2460-2470.
95. Eperon, G. E.; Leijtens, T.; Bush, K. A.; Prasanna, R.; Green, T.; Wang, J. T.-W.; McMeekin, D. P.; Volonakis, G.; Milot, R. L.; May, R.; Palmstrom, A.; Slotcavage, D. J.; Belisle, R. A.; Patel, J. B.; Parrott, E. S.; Sutton, R. J.; Ma, W.; Moghadam, F.; Conings, B.; Babayigit, A.; Boyen, H.-G.; Bent, S.; Giustino, F.; Herz, L. M.; Johnston, M. B.; McGehee, M. D.; Snaith, H. J., Perovskite-Perovskite Tandem Photovoltaics with Optimized Band Gaps. *Science* **2016**, *354* (6314), 861-865.

96. Sutton, R. J.; Eperon, G. E.; Miranda, L.; Parrott, E. S.; Kamino, B. A.; Patel, J. B.; Hörantner, M. T.; Johnston, M. B.; Haghighirad, A. A.; Moore, D. T.; Snaith, H. J., Bandgap-Tunable Cesium Lead Halide Perovskites with High Thermal Stability for Efficient Solar Cells. *Advanced Energy Materials* **2016**, *6* (8), 1502458.
97. McMeekin, D. P.; Sadoughi, G.; Rehman, W.; Eperon, G. E.; Saliba, M.; Hörantner, M. T.; Haghighirad, A.; Sakai, N.; Korte, L.; Rech, B.; Johnston, M. B.; Herz, L. M.; Snaith, H. J., A Mixed-Cation Lead Mixed-Halide Perovskite Absorber for Tandem Solar Cells. *Science* **2016**, *351* (6269), 151-155.
98. Sivaram, V.; Stranks, S. D.; Snaith, H. J., Perovskite Solar Cells Could Beat the Efficiency of Silicon. *Scientific American* **2015**, *313*, 54-59.
99. Yang, W. S.; Park, B.-W.; Jung, E. H.; Jeon, N. J.; Kim, Y. C.; Lee, D. U.; Shin, S. S.; Seo, J.; Kim, E. K.; Noh, J. H.; Seok, S. I., Iodide Management in Formamidinium-Lead-Halide-Based Perovskite Layers for Efficient Solar Cells. *Science* **2017**, *356* (6345), 1376-1379.
100. Snaith, H. J.; Abate, A.; Ball, J. M.; Eperon, G. E.; Leijtens, T.; Noel, N. K.; Stranks, S. D.; Wang, J. T.-W.; Wojciechowski, K.; Zhang, W., Anomalous Hysteresis in Perovskite Solar Cells. *The Journal of Physical Chemistry Letters* **2014**, *5* (9), 1511-1515.
101. Kranz, L.; Abate, A.; Feurer, T.; Fu, F.; Avancini, E.; Löckinger, J.; Reinhard, P.; Zakeeruddin, S. M.; Grätzel, M.; Buecheler, S.; Tiwari, A. N., High-Efficiency Polycrystalline Thin Film Tandem Solar Cells. *The Journal of Physical Chemistry Letters* **2015**, *6* (14), 2676-2681.
102. Correa Baena, J. P.; Steier, L.; Tress, W.; Saliba, M.; Neutzner, S.; Matsui, T.; Giordano, F.; Jacobsson, T. J.; Srimath Kandada, A. R.; Zakeeruddin, S. M.; Petrozza, A.; Abate, A.; Nazeeruddin, M. K.; Grätzel, M.; Hagfeldt, A., Highly Efficient Planar Perovskite Solar Cells through Band Alignment Engineering. *Energy & Environmental Science* **2015**, *8* (10), 2928-2934.
103. Docampo, P.; Ball, J. M.; Darwich, M.; Eperon, G. E.; Snaith, H. J., Efficient Organometal Trihalide Perovskite Planar-Heterojunction Solar Cells on Flexible Polymer Substrates. *Nature Communications* **2013**, *4*, 2761.
104. Wojciechowski, K.; Leijtens, T.; Siprova, S.; Schlueter, C.; Hörantner, M. T.; Wang, J. T.-W.; Li, C.-Z.; Jen, A. K. Y.; Lee, T.-L.; Snaith, H. J., C60 as an Efficient n-Type Compact Layer in Perovskite Solar Cells. *The Journal of Physical Chemistry Letters* **2015**, *6* (12), 2399-2405.
105. Borchert, J.; Milot, R. L.; Patel, J. B.; Davies, C. L.; Wright, A. D.; Martínez Maestro, L.; Snaith, H. J.; Herz, L. M.; Johnston, M. B., Large-Area, Highly Uniform Evaporated Formamidinium Lead Triiodide Thin Films for Solar Cells. *ACS Energy Letters* **2017**, *2* (12), 2799-2804.

106. Shi, J.; Xu, X.; Li, D.; Meng, Q., Interfaces in Perovskite Solar Cells. *Small* **2015**, *11* (21), 2472-2486.
107. McMeekin, D. P.; Wang, Z.; Rehman, W.; Pulvirenti, F.; Patel, J. B.; Noel, N. K.; Johnston, M. B.; Marder, S. R.; Herz, L. M.; Snaith, H. J., Crystallization Kinetics and Morphology Control of Formamidinium–Cesium Mixed-Cation Lead Mixed-Halide Perovskite via Tunability of the Colloidal Precursor Solution. *Advanced Materials* **2017**, *29* (29), 1607039.
108. Patel, J. B.; Wong-Leung, J.; Van Reenen, S.; Sakai, N.; Wang, J. T. W.; Parrott, E. S.; Liu, M.; Snaith, H. J.; Herz, L. M.; Johnston, M. B., Influence of Interface Morphology on Hysteresis in Vapor-Deposited Perovskite Solar Cells. *Advanced Electronic Materials* **2017**, *3* (2), 1600470.
109. Zhu, Z.; Xu, J.-Q.; Chueh, C.-C.; Liu, H.; Li, Z. a.; Li, X.; Chen, H.; Jen, A. K.-Y., A Low-Temperature, Solution-Processable Organic Electron-Transporting Layer Based on Planar Coronene for High-performance Conventional Perovskite Solar Cells. *Advanced Materials* **2016**, *28* (48), 10786-10793.
110. Sun, C.; Wu, Z.; Yip, H.-L.; Zhang, H.; Jiang, X.-F.; Xue, Q.; Hu, Z.; Hu, Z.; Shen, Y.; Wang, M.; Huang, F.; Cao, Y., Amino-Functionalized Conjugated Polymer as an Efficient Electron Transport Layer for High-Performance Planar-Heterojunction Perovskite Solar Cells. *Advanced Energy Materials* **2016**, *6* (5), 1501534.
111. Zhao, D.; Zhu, Z.; Kuo, M.-Y.; Chueh, C.-C.; Jen, A. K.-Y., Hexaazatrinaphthylene Derivatives: Efficient Electron-Transporting Materials with Tunable Energy Levels for Inverted Perovskite Solar Cells. *Angewandte Chemie International Edition* **2016**, *55* (31), 8999-9003.
112. Hudej, R.; Bratina, G., Electrical Conductivity in Metal/3,4,9,10-Perylenetetracarboxylic Dianhydride/Metal Structures. *Journal of Applied Physics* **2003**, *93* (10), 6090-6094.
113. Zollinger, H., *Color Chemistry: Syntheses, Properties, and Applications of Organic Dyes and Pigments*. 3rd ed.; VHCA and Wiley-VCH: Zürich and Weinheim, 2003.
114. Langhals, H., Cyclic Carboxylic Imide Structures as Structure Elements of High Stability. Novel Developments in Perylene Dye Chemistry. *Heterocycles* **1995**, *40*, 477-500.
115. Calió, L.; Momblona, C.; Gil-Escrig, L.; Kazim, S.; Sessolo, M.; Sastre-Santos, Á.; Bolink, H. J.; Ahmad, S., Vacuum Deposited Perovskite Solar Cells Employing Dopant-Free Triazatruxene as the Hole Transport Material. *Solar Energy Materials and Solar Cells* **2017**, *163*, 237-241.
116. Min, J.; Zhang, Z.-G.; Hou, Y.; Ramirez Quiroz, C. O.; Przybilla, T.; Bronnbauer, C.; Guo, F.; Forberich, K.; Azimi, H.; Ameri, T.; Spiecker, E.; Li, Y.; Brabec, C. J., Interface Engineering of Perovskite Hybrid Solar Cells with Solution-Processed Perylene–

Diimide Heterojunctions toward High Performance. *Chemistry of Materials* **2015**, *27* (1), 227-234.

117. Kaltenbrunner, M.; Adam, G.; Głowacki, E. D.; Drack, M.; Schwödiauer, R.; Leonat, L.; Apaydin, D. H.; Groiss, H.; Scharber, M. C.; White, M. S.; Sariciftci, N. S.; Bauer, S., Flexible High Power-per-Weight Perovskite Solar Cells with Chromium Oxide–Metal Contacts for Improved Stability in Air. *Nature Materials* **2015**, *14*, 1032.

118. Zhang, M.; Li, T.; Zheng, G.; Li, L.; Qin, M.; Zhang, S.; Zhou, H.; Zhan, X., An Amino-Substituted Perylene Diimide Polymer for Conventional Perovskite Solar Cells. *Materials Chemistry Frontiers* **2017**, *1* (10), 2078-2084.

119. Kim, S. S.; Bae, S.; Jo, W. H., A Perylene Diimide-Based Non-Fullerene Acceptor as an Electron Transporting Material for Inverted Perovskite Solar Cells. *RSC Advances* **2016**, *6* (24), 19923-19927.

120. Zhang, H.; Xue, L.; Han, J.; Fu, Y. Q.; Shen, Y.; Zhang, Z.; Li, Y.; Wang, M., New Generation Perovskite Solar Cells with Solution-Processed Amino-Substituted Perylene Diimide Derivative as Electron-Transport Layer. *Journal of Materials Chemistry A* **2016**, *4* (22), 8724-8733.

121. Huang, J.; Gu, Z.; Zuo, L.; Ye, T.; Chen, H., Morphology Control of Planar Heterojunction Perovskite Solar Cells with Fluorinated PDI Films as Organic Electron Transport Layer. *Solar Energy* **2016**, *133*, 331-338.

122. Akaike, K.; Nardi, M. V.; Oehzelt, M.; Frisch, J.; Opitz, A.; Christodoulou, C.; Ligorio, G.; Beyer, P.; Timpel, M.; Pis, I.; Bondino, F.; Moudgil, K.; Barlow, S.; Marder, S. R.; Koch, N., Effective Work Function Reduction of Practical Electrodes Using an Organometallic Dimer. *Advanced Functional Materials* **2016**, *26* (15), 2493-2502.

123. Pulvirenti, F.; Wegner, B.; Noel, N. K.; Mazzotta, G.; Hill, R.; Patel, J. B.; Herz, L. M.; Johnston, M. B.; Riede, M. K.; Snaith, H. J.; Koch, N.; Barlow, S.; Marder, S. R., Modification of the Fluorinated Tin Oxide/Electron-Transporting Material Interface by a Strong Reductant and its Effect on Perovskite Solar Cell Efficiency. *Molecular Systems Design & Engineering* **2018**, *3* (5), 741-747.

124. Vázquez, H.; Dappe, Y. J.; Ortega, J.; Flores, F., Energy Level Alignment at Metal/Organic Semiconductor Interfaces: “Pillow” Effect, Induced Density of Interface States, and Charge Neutrality Level. *The Journal of Chemical Physics* **2007**, *126* (14), 144703.

125. Kahn, A.; Koch, N.; Gao, W., Electronic Structure and Electrical Properties of Interfaces between Metals and π -Conjugated Molecular Films. *Journal of Polymer Science Part B: Polymer Physics* **2003**, *41* (21), 2529-2548.

126. Krause, S.; Casu, M. B.; Schöll, A.; Umbach, E., Determination of Transport Levels of Organic Semiconductors by UPS and IPS. *New Journal of Physics* **2008**, *10* (8), 085001.

127. Oehzelt, M.; Koch, N.; Heimel, G., Organic Semiconductor Density of States Controls the Energy Level Alignment at Electrode Interfaces. *Nature Communications* **2014**, *5*, 4174.
128. Hill, I. G.; Kahn, A.; Soos, Z. G.; Pascal, J. R. A., Charge-Separation Energy in Films of π -Conjugated Organic Molecules. *Chemical Physics Letters* **2000**, *327* (3), 181-188.
129. Wang, H.; Amsalem, P.; Heimel, G.; Salzmann, I.; Koch, N.; Oehzelt, M., Band-Bending in Organic Semiconductors: The Role of Alkali-Halide Interlayers. *Advanced Materials* **2014**, *26* (6), 925-930.
130. Amsalem, P.; Niederhausen, J.; Wilke, A.; Heimel, G.; Schlesinger, R.; Winkler, S.; Vollmer, A.; Rabe, J. P.; Koch, N., Role of Charge Transfer, Dipole-Dipole Interactions, and Electrostatics in Fermi-Level Pinning at a Molecular Heterojunction on a Metal Surface. *Physical Review B* **2013**, *87* (3), 035440.
131. Lüsse, B.; Riede, M.; Leo, K., Doping of Organic Semiconductors. *physica status solidi (a)* **2013**, *210* (1), 9-43.
132. Arkhipov, V. I.; Heremans, P.; Emelianova, E. V.; Bäessler, H., Effect of Doping on the Density-of-States Distribution and Carrier Hopping in Disordered Organic Semiconductors. *Physical Review B* **2005**, *71* (4), 045214.
133. Li, F.; Werner, A.; Pfeiffer, M.; Leo, K.; Liu, X., Leuco Crystal Violet as a Dopant for n-Doping of Organic Thin Films of Fullerene C60. *The Journal of Physical Chemistry B* **2004**, *108* (44), 17076-17082.
134. Noel, N. K.; Habisreutinger, S. N.; Wenger, B.; Klug, M. T.; Hörantner, M. T.; Johnston, M. B.; Nicholas, R. J.; Moore, D. T.; Snaith, H. J., A Low Viscosity, Low Boiling Point, Clean Solvent System for the Rapid Crystallisation of Highly Specular Perovskite Films. *Energy & Environmental Science* **2017**, *10* (1), 145-152.
135. Momblona, C.; Gil-Escrig, L.; Bandiello, E.; Hutter, E. M.; Sessolo, M.; Lederer, K.; Blochwitz-Nimoth, J.; Bolink, H. J., Efficient Vacuum Deposited p-i-n and n-i-p Perovskite Solar Cells Employing Doped Charge Transport Layers. *Energy & Environmental Science* **2016**, *9* (11), 3456-3463.
136. Forrest, S. R., Ultrathin Organic Films Grown by Organic Molecular Beam Deposition and Related Techniques. *Chemical Reviews* **1997**, *97* (6), 1793-1896.
137. Gusev, O. V.; Denisovich, L. I.; Peterleitner, M. G.; Rubeshov, A. Z.; Ustynyuk, N. A.; Maitlis, P. M., Electrochemical Generation of 19- and 20-Electron Rhodocenium Complexes and Their Properties. *Journal of Organometallic Chemistry* **1993**, *452* (1), 219-222.
138. Haddon, R. C.; Hebard, A. F.; Rosseinsky, M. J.; Murphy, D. W.; Duclos, S. J.; Lyons, K. B.; Miller, B.; Rosamilia, J. M.; Fleming, R. M.; Kortan, A. R.; Glarum, S. H.;

Makhija, A. V.; Muller, A. J.; Eick, R. H.; Zahurak, S. M.; Tycko, R.; Dabbagh, G.; Thiel, F. A., Conducting Films of C60 and C70 by Alkali-Metal Doping. *Nature* **1991**, 350 (6316), 320-322.

139. Nollau, A.; Pfeiffer, M.; Fritz, T.; Leo, K., Controlled n-Type Doping of a Molecular Organic Semiconductor: Naphthalenetetracarboxylic Dianhydride (NTCDA) Doped with Bis(ethylenedithio)-Tetrathiafulvalene (BEDT-TTF). *Journal of Applied Physics* **2000**, 87 (9), 4340-4343.

140. Li, F.; Pfeiffer, M.; Werner, A.; Harada, K.; Leo, K.; Hayashi, N.; Seki, K.; Liu, X.; Dang, X.-D., Acridine Orange Base as a Dopant for n Doping of C60 Thin Films. *Journal of Applied Physics* **2006**, 100 (2), 023716.

141. Naab, B. D.; Zhang, S.; Vandewal, K.; Salleo, A.; Barlow, S.; Marder, S. R.; Bao, Z., Effective Solution- and Vacuum-Processed n-Doping by Dimers of Benzimidazoline Radicals. *Advanced Materials* **2014**, 26 (25), 4268-4272.

142. Wei, P.; Oh, J. H.; Dong, G.; Bao, Z., Use of a 1H-Benzoimidazole Derivative as an n-Type Dopant and To Enable Air-Stable Solution-Processed n-Channel Organic Thin-Film Transistors. *Journal of the American Chemical Society* **2010**, 132 (26), 8852-8853.

143. Gregg, B. A.; Chen, S.-G.; Branz, H. M., On the Superlinear Increase in Conductivity with Dopant Concentration in Excitonic Semiconductors. *Applied Physics Letters* **2004**, 84 (10), 1707-1709.

144. Li, C.-Z.; Chueh, C.-C.; Ding, F.; Yip, H.-L.; Liang, P.-W.; Li, X.; Jen, A. K.-Y., Doping of Fullerenes via Anion-Induced Electron Transfer and Its Implication for Surfactant Facilitated High Performance Polymer Solar Cells. *Advanced Materials* **2013**, 25 (32), 4425-4430.

145. Chueh, C.-C.; Li, C.-Z.; Ding, F.; Li, Z. a.; Cernetic, N.; Li, X.; Jen, A. K. Y., Doping Versatile n-Type Organic Semiconductors via Room Temperature Solution-Processable Anionic Dopants. *ACS Applied Materials & Interfaces* **2017**, 9 (1), 1136-1144.

146. Weber, C. D.; Bradley, C.; Lonergan, M. C., Solution Phase n-Doping of C60 and PCBM using Tetrabutylammonium Fluoride. *Journal of Materials Chemistry A* **2014**, 2 (2), 303-307.

147. Li, Y.-J.; Wang, G.-W.; Li, J.-X.; Liu, Y.-C., Cycloaddition Reactions of Hydrofullerenes with Cyano-Substituted Alkenes under Basic Conditions. *New Journal of Chemistry* **2004**, 28 (8), 1043-1047.

148. Guo, Y.; Li, W.; Yan, J.; Moosa, B.; Amad, M. a.; Werth, C. J.; Khashab, N. M., Fullerene-Catalyzed Reduction of Azo Derivatives in Water under UV Irradiation. *Chemistry – An Asian Journal* **2012**, 7 (12), 2842-2847.

149. Hyun, G.; Shin, D.; Lee, H.; Yi, Y., Enhancing the Performance of Inverted Organic Photovoltaics using Cathode Interlayers Based on Solution-Processable

Tetrabutylammonium Halides. *physica status solidi (RRL) – Rapid Research Letters* **2017**, *11* (10), 1700250.

150. van Reenen, S.; Kouijzer, S.; Janssen, R. A. J.; Wienk, M. M.; Kemerink, M., Origin of Work Function Modification by Ionic and Amine-Based Interface Layers. *Advanced Materials Interfaces* **2014**, *1* (8), 1400189.

151. Yoo, S.; Domercq, B.; Kippelen, B., Efficient Thin-Film Organic Solar Cells Based on Pentacene/C60 Heterojunctions. *Applied Physics Letters* **2004**, *85* (22), 5427-5429.

152. Cohen, S. S., Contact Resistance and Methods for its Determination. *Thin Solid Films* **1983**, *104* (3), 361-379.

153. Wang, Z.; McMeekin, D. P.; Sakai, N.; van Reenen, S.; Wojciechowski, K.; Patel, J. B.; Johnston, M. B.; Snaith, H. J., Efficient and Air-Stable Mixed-Cation Lead Mixed-Halide Perovskite Solar Cells with n-Doped Organic Electron Extraction Layers. *Advanced Materials* **2017**, *29* (5), 1604186.

154. Rumer, J. W.; Ashraf, R. S.; Eisenmenger, N. D.; Huang, Z.; Meager, I.; Nielsen, C. B.; Schroeder, B. C.; Chabinyo, M. L.; McCulloch, I., Dual Function Additives: A Small Molecule Crosslinker for Enhanced Efficiency and Stability in Organic Solar Cells. *Advanced Energy Materials* **2015**, *5* (9), 1401426.

155. Song, S.; Hill, R.; Choi, K.; Wojciechowski, K.; Barlow, S.; Leisen, J.; Snaith, H. J.; Marder, S. R.; Park, T., Surface Modified Fullerene Electron Transport Layers for Stable and Reproducible Flexible Perovskite Solar Cells. *Nano Energy* **2018**, *49*, 324-332.

156. Hsieh, C.-H.; Cheng, Y.-J.; Li, P.-J.; Chen, C.-H.; Dubosc, M.; Liang, R.-M.; Hsu, C.-S., Highly Efficient and Stable Inverted Polymer Solar Cells Integrated with a Cross-Linked Fullerene Material as an Interlayer. *Journal of the American Chemical Society* **2010**, *132* (13), 4887-4893.

157. Cheng, Y.-J.; Cao, F.-Y.; Lin, W.-C.; Chen, C.-H.; Hsieh, C.-H., Self-Assembled and Cross-Linked Fullerene Interlayer on Titanium Oxide for Highly Efficient Inverted Polymer Solar Cells. *Chemistry of Materials* **2011**, *23* (6), 1512-1518.

158. Drees, M.; Hoppe, H.; Winder, C.; Neugebauer, H.; Sariciftci, N. S.; Schwinger, W.; Schäffler, F.; Topf, C.; Scharber, M. C.; Zhu, Z.; Gaudiana, R., Stabilization of the Nanomorphology of Polymer–Fullerene “Bulk Heterojunction” Blends using a Novel Polymerizable Fullerene Derivative. *Journal of Materials Chemistry* **2005**, *15* (48), 5158-5163.

159. Wantz, G.; Derue, L.; Dautel, O.; Rivaton, A.; Hudhomme, P.; Dagron-Lartigau, C., Stabilizing Polymer-Based Bulk Heterojunction Solar Cells via Crosslinking. *Polymer International* **2014**, *63* (8), 1346-1361.

160. Deb, N.; Dasari, R. R.; Moudgil, K.; Hernandez, J. L.; Marder, S. R.; Sun, Y.; Karim, A.; Bucknall, D. G., Thermo-Cross-Linkable Fullerene for Long-Term Stability of Photovoltaic Devices. *Journal of Materials Chemistry A* **2015**, *3* (43), 21856-21863.
161. Gügel, A.; Belik, P.; Walter, M.; Kraus, A.; Harth, E.; Wagner, M.; Spickermann, J.; Müllen, K., The Repetitive Diels-Alder Reaction: A New Approach to [60]Fullerene Maindashchain Polymers. *Tetrahedron* **1996**, *52* (14), 5007-5014.
162. Walzer, K.; Maennig, B.; Pfeiffer, M.; Leo, K., Highly Efficient Organic Devices Based on Electrically Doped Transport Layers. *Chemical Reviews* **2007**, *107* (4), 1233-1271.
163. Kim, S. S.; Bae, S.; Jo, W. H., Performance Enhancement of Planar Heterojunction Perovskite Solar Cells by n-Doping of the Electron Transporting Layer. *Chemical Communications* **2015**, *51* (98), 17413-17416.
164. Wei, P.; Menke, T.; Naab, B. D.; Leo, K.; Riede, M.; Bao, Z., 2-(2-Methoxyphenyl)-1,3-dimethyl-1H-benzoimidazol-3-ium Iodide as a New Air-Stable n-Type Dopant for Vacuum-Processed Organic Semiconductor Thin Films. *Journal of the American Chemical Society* **2012**, *134* (9), 3999-4002.
165. Naab, B. D.; Guo, S.; Olthof, S.; Evans, E. G. B.; Wei, P.; Millhauser, G. L.; Kahn, A.; Barlow, S.; Marder, S. R.; Bao, Z., Mechanistic Study on the Solution-Phase n-Doping of 1,3-Dimethyl-2-aryl-2,3-dihydro-1H-benzoimidazole Derivatives. *Journal of the American Chemical Society* **2013**, *135* (40), 15018-15025.
166. Dai, A.; Wan, A.; Magee, C.; Zhang, Y.; Barlow, S.; Marder, S. R.; Kahn, A., Investigation of p-Dopant Diffusion in Polymer Films and Bulk Heterojunctions: Stable Spatially-Confined Doping for All-Solution Processed Solar Cells. *Organic Electronics* **2015**, *23*, 151-157.
167. Konarev, D. V.; Drichko, N. V.; Graja, A., Optical Absorption Spectra of Chemically Generated C60 and C70 Anions. *J. Chim. Phys.* **1998**, *95* (10), 2143-2156.
168. Liu, J.; Qiu, L.; Alessandri, R.; Qiu, X.; Portale, G.; Dong, J.; Talsma, W.; Ye, G.; Sengrian, A. A.; Souza, P. C. T.; Loi, M. A.; Chiechi, R. C.; Marrink, S. J.; Hummelen, J. C.; Koster, L. J. A., Enhancing Molecular n-Type Doping of Donor-Acceptor Copolymers by Tailoring Side Chains. *Advanced Materials* **2018**, *30* (7), 1704630.
169. Nava, D.; Shin, Y.; Massetti, M.; Jiao, X.; Biskup, T.; Jagadeesh, M. S.; Calloni, A.; Duò, L.; Lanzani, G.; McNeill, C. R.; Sommer, M.; Caironi, M., Drastic Improvement of Air Stability in an n-Type Doped Naphthalene-Diimide Polymer by Thionation. *ACS Applied Energy Materials* **2018**, *1* (9), 4626-4634.
170. Shi, K.; Zhang, F.; Di, C.-A.; Yan, T.-W.; Zou, Y.; Zhou, X.; Zhu, D.; Wang, J.-Y.; Pei, J., Toward High Performance n-Type Thermoelectric Materials by Rational Modification of BDPPV Backbones. *Journal of the American Chemical Society* **2015**, *137* (22), 6979-6982.

171. Jeon, N. J.; Noh, J. H.; Kim, Y. C.; Yang, W. S.; Ryu, S.; Seok, S. I., Solvent Engineering for High-Performance Inorganic–Organic Hybrid Perovskite Solar Cells. *Nature Materials* **2014**, *13*, 897.
172. Anaraki, E. H.; Kermanpur, A.; Steier, L.; Domanski, K.; Matsui, T.; Tress, W.; Saliba, M.; Abate, A.; Grätzel, M.; Hagfeldt, A.; Correa-Baena, J.-P., Highly Efficient and Stable Planar Perovskite Solar Cells by Solution-Processed Tin Oxide. *Energy & Environmental Science* **2016**, *9* (10), 3128-3134.
173. Peters, C. H.; Sachs-Quintana, I. T.; Kastrop, J. P.; Beaupré, S.; Leclerc, M.; McGehee, M. D., High Efficiency Polymer Solar Cells with Long Operating Lifetimes. *Advanced Energy Materials* **2011**, *1* (4), 491-494.
174. Kraus, G. A.; Wu, T., A Three-Component Reaction between Benzynes, the Enolate of Acetaldehyde, and Unsaturated Esters and Dihydroisoquinolines. *Tetrahedron* **2010**, *66* (3), 569-572.
175. Bubb, W.; Sternhell, S., Proton N.M.R. Spectra of 1-Substituted Benzocyclobutenes (Bicyclo[4,2,0]octa-1,3,5-trienes). *Australian Journal of Chemistry* **1976**, *29* (8), 1685-1697.
176. Zhang, Y.; Li, L.; Zheng, J.; Li, Q.; Zuo, Y.; Yang, E.; Li, G., Two-Step Grain-Growth Kinetics of Sub-7 nm SnO₂ Nanocrystal under Hydrothermal Condition. *The Journal of Physical Chemistry C* **2015**, *119* (33), 19505-19512.
177. Timpel, M.; Nardi, M. V.; Krause, S.; Ligorio, G.; Christodoulou, C.; Pasquali, L.; Giglia, A.; Frisch, J.; Wegner, B.; Moras, P.; Koch, N., Surface Modification of ZnO(0001)–Zn with Phosphonate-Based Self-Assembled Monolayers: Binding Modes, Orientation, and Work Function. *Chemistry of Materials* **2014**, *26* (17), 5042-5050.
178. Timpel, M.; Nardi, M. V.; Ligorio, G.; Wegner, B.; Pätzelt, M.; Kobin, B.; Hecht, S.; Koch, N., Energy-Level Engineering at ZnO/Oligophenylene Interfaces with Phosphonate-Based Self-Assembled Monolayers. *ACS Applied Materials & Interfaces* **2015**, *7* (22), 11900-11907.
179. Vigderman, L.; Manna, P.; Zubarev, E. R., Quantitative Replacement of Cetyl Trimethylammonium Bromide by Cationic Thiol Ligands on the Surface of Gold Nanorods and Their Extremely Large Uptake by Cancer Cells. *Angewandte Chemie International Edition* **2012**, *51* (3), 636-641.
180. Bock, C.; Pham, D. V.; Kunze, U.; Käfer, D.; Witte, G.; Wöll, C., Improved Morphology and Charge Carrier Injection in Pentacene Field-Effect Transistors with Thiol-Treated Electrodes. *Journal of Applied Physics* **2006**, *100* (11), 114517.
181. Kim, H. K.; Hyla, A. S.; Winget, P.; Li, H.; Wyss, C. M.; Jordan, A. J.; Larrain, F. A.; Sadighi, J. P.; Fuentes-Hernandez, C.; Kippelen, B.; Brédas, J.-L.; Barlow, S.; Marder, S. R., Reduction of the Work Function of Gold by N-Heterocyclic Carbenes. *Chemistry of Materials* **2017**, *29* (8), 3403-3411.

182. Oppolzer, W., Intramolecular Cycloaddition Reactions of ortho-Quinodimethanes in Organic Synthesis. *Synthesis* **1978**, 1978 (11), 793-802.
183. Endo, T.; Koizumi, T.; Takata, T.; Chino, K., Synthesis of Poly(4-vinylbenzocyclobutene) and its Reaction with Dienophiles. *Journal of Polymer Science Part A: Polymer Chemistry* **1995**, 33 (4), 707-715.
184. Dobish, J. N.; Hamilton, S. K.; Harth, E., Synthesis of Low-Temperature Benzocyclobutene Cross-Linker and Utilization. *Polymer Chemistry* **2012**, 3 (4), 857-860.
185. Moudgil, K. Design and Development of Dimeric Sandwich Compounds as *n*-Dopants for Organic Electronics. Georgia Institute of Technology, 2016.
186. Png, R.-Q.; Chia, P.-J.; Tang, J.-C.; Liu, B.; Sivaramakrishnan, S.; Zhou, M.; Khong, S.-H.; Chan, H. S. O.; Burroughes, J. H.; Chua, L.-L.; Friend, R. H.; Ho, P. K. H., High-Performance Polymer Semiconducting Heterostructure Devices by Nitrene-Mediated Photocrosslinking of Alkyl Side Chains. *Nature Materials* **2009**, 9, 152.
187. Virkar, A.; Ling, M.-M.; Locklin, J.; Bao, Z., Oligothiophene Based Organic Semiconductors with Cross-Linkable Benzophenone Moieties. *Synthetic Metals* **2008**, 158 (21), 958-963.
188. Choi, S.; Fuentes-Hernandez, C.; Wang, C.-Y.; Khan, T. M.; Larrain, F. A.; Zhang, Y.; Barlow, S.; Marder, S. R.; Kippelen, B., A Study on Reducing Contact Resistance in Solution-Processed Organic Field-Effect Transistors. *ACS Applied Materials & Interfaces* **2016**, 8 (37), 24744-24752.
189. Song, M.; Park, J. H.; Kim, C. S.; Kim, D.-H.; Kang, Y.-C.; Jin, S.-H.; Jin, W.-Y.; Kang, J.-W., Highly Flexible and Transparent Conducting Silver Nanowire/ZnO Composite Film for Organic Solar Cells. *Nano Research* **2014**, 7 (9), 1370-1379.
190. Beiley, Z. M.; Christoforo, M. G.; Gratia, P.; Bowring, A. R.; Eberspacher, P.; Margulis, G. Y.; Cabanetos, C.; Beaujuge, P. M.; Salleo, A.; McGehee, M. D., Semi-Transparent Polymer Solar Cells with Excellent Sub-Bandgap Transmission for Third Generation Photovoltaics. *Advanced Materials* **2013**, 25 (48), 7020-7026.
191. Gaynor, W.; Burkhard, G. F.; McGehee, M. D.; Peumans, P., Smooth Nanowire/Polymer Composite Transparent Electrodes. *Advanced Materials* **2011**, 23 (26), 2905-2910.
192. Wang, D.; Zhou, W.; Liu, H.; Ma, Y.; Zhang, H., Performance Improvement in Flexible Polymer Solar Cells Based on Modified Silver Nanowire Electrode. *Nanotechnology* **2016**, 27 (33), 335203.
193. Yamashita, A.; Hayashi, T., Organic Molecular Beam Deposition of Metallophthalocyanines for Opto-Electronics Applications. *Advanced Materials* **1996**, 8 (10), 791-799.

194. Pick, A.; Klues, M.; Rinn, A.; Harms, K.; Chatterjee, S.; Witte, G., Polymorph-Selective Preparation and Structural Characterization of Perylene Single Crystals. *Crystal Growth & Design* **2015**, *15* (11), 5495-5504.
195. Beiley, Z. M.; Hoke, E. T.; Noriega, R.; Dacuña, J.; Burkhard, G. F.; Bartelt, J. A.; Salleo, A.; Toney, M. F.; McGehee, M. D., Morphology-Dependent Trap Formation in High Performance Polymer Bulk Heterojunction Solar Cells. *Advanced Energy Materials* **2011**, *1* (5), 954-962.
196. Heumueller, T.; Mateker, W. R.; Sachs-Quintana, I. T.; Vandewal, K.; Bartelt, J. A.; Burke, T. M.; Ameri, T.; Brabec, C. J.; McGehee, M. D., Reducing Burn-in Voltage Loss in Polymer Solar Cells by Increasing the Polymer Crystallinity. *Energy & Environmental Science* **2014**, *7* (9), 2974-2980.
197. Heumueller, T.; Mateker, W. R.; Distler, A.; Fritze, U. F.; Cheacharoen, R.; Nguyen, W. H.; Biele, M.; Salvador, M.; von Delius, M.; Egelhaaf, H.-J.; McGehee, M. D.; Brabec, C. J., Morphological and Electrical Control of Fullerene Dimerization Determines Organic Photovoltaic Stability. *Energy & Environmental Science* **2016**, *9* (1), 247-256.
198. Cha, H.; Wu, J.; Wadsworth, A.; Nagitta, J.; Limbu, S.; Pont, S.; Li, Z.; Searle, J.; Wyatt, M. F.; Baran, D.; Kim, J.-S.; McCulloch, I.; Durrant, J. R., An Efficient, "Burn in" Free Organic Solar Cell Employing a Nonfullerene Electron Acceptor. *Advanced Materials* **2017**, *29* (33), 1701156.
199. Roubelakis, M. M.; Vougioukalakis, G. C.; Nye, L. C.; Drewello, T.; Orfanopoulos, M., Exploring the Photoinduced Electron Transfer Reactivity of Aza[60]Fullerene Iminium Cation. *Tetrahedron* **2010**, *66* (48), 9363-9369.
200. Meletov, K. P.; Arvanitidis, J.; Christofilos, D.; Kourouklis, G. A.; Davydov, V. A., Raman Study of the Temperature-Induced Decomposition of the Fullerene Dimers C120. *Chemical Physics Letters* **2016**, *654*, 81-85.
201. Li, C.; Wonneberger, H., Perylene Imides for Organic Photovoltaics: Yesterday, Today, and Tomorrow. *Advanced Materials* **2012**, *24* (5), 613-636.
202. Correa-Baena, J.-P.; Saliba, M.; Buonassisi, T.; Grätzel, M.; Abate, A.; Tress, W.; Hagfeldt, A., Promises and Challenges of Perovskite Solar Cells. *Science* **2017**, *358* (6364), 739-744.
203. Meng, X.; Bai, Y.; Xiao, S.; Zhang, T.; Hu, C.; Yang, Y.; Zheng, X.; Yang, S., Designing New Fullerene Derivatives as Electron Transporting Materials for Efficient Perovskite Solar Cells with Improved Moisture Resistance. *Nano Energy* **2016**, *30*, 341-346.